Fibre Reinforcement in Load Carrying Concrete Structures

Thesis for the degree of philosophiae doctor

Åse Lyslo Døssland
Trondheim, February 2008

Norwegian University of Science and Technology
Faculty of Engineering Science and Technology
Department of Structural Engineering

NTNU

NTNU
Norwegian University of Science and Technology

Thesis for the degree of philosophiae doctor

Faculty of Engineering Science and Technology
Department of Structural Engineering

ISBN 978-82-471-6924-7 (electronic ver.)
ISBN 978-82-471-6910-0 (printed ver.)
ISSN 1503-8181

Doctoral Thesis at NTNU, 2008:50

Printed by NTNU Trykk

Abstract

Fibre reinforcement can provide an alternative to conventional steel bars in order to improve the efficiency and working conditions on construction sites and in the prefabrication industry. Through the fibres ability to bridge cracks they improve the structural behaviour of the concrete by increased shear, moment and punching resistance, increased dowel effect, reduced crack spacing and crack widths, increased flexural stiffness and increased ductility in compression. A main reason for limited use of FRC in load-carrying structures seems to be the lack of accepted design guidelines.

The principal aim of this research project is to improve the current knowledge of the mechanical and structural behaviour of fibre reinforced concrete, focusing on practical applications. An experimental study is carried out where the following parameters are investigated: fibre volume, fibre length, steel versus synthetic fibres, size effect, influence of conventional reinforcement, self compacting versus vibrator compacted concrete, casting process and type of structural element.

Most of the test series were evaluated through calculations and finite element analysis (FEA) and compared with available design rules. Generally the agreement was good, both with discrete and smeared crack approach. This shows that FEA is an appropriate tool to determine the contribution of fibres to the load bearing capacity. Moreover, the results of the test series implied that the theoretical framework that exists today describes the behaviour of fibre reinforced structures relatively well, and that the design rules which are developed is satisfactory.

Sammendrag

Bruk av fiber som erstatning for vanlig slakkarmering i betongkonstruksjoner er svært aktuelt på grunn av større krav til rasjonell utførelse, samt HMS-forhold for jernbindere og mangel på arbeidskraft. Fiberarmering i plasstøpte betongkonstruksjoner er i Norge i dag hovedsakelig begrenset til stålfiberarmering i golv på grunn og påstøp og i spesialutførelser som sprøytebetong. En viktig årsak til at bruk av fiberarmering er såpass begrenset er at en mangler generelt aksepterte regler for beregning og utførelse av fiberbetong.

PhD prosjektet har hatt som hovedmål å øke kunnskapen om bruk av fiberbetong, både med hensyn på utførelse og dimensjonering. Det eksperimentelle arbeidet har i hovedsak vært finansiert gjennom et utvikingsprosjekt der intensjonen har vært å utvikle retningslinjer for dimensjonering og utførelse av stålfiberarmert betong som igjen kan legges til grunn for godkjenning fra byggherrer og bygningsmyndigheter. I tillegg har PhD prosjektet omfattet syntetiske makro fiber, og følgende forsøksserier er utført:

<u>Heftegenskaper - Uttrekksforsøk</u>
Uttrekksforsøk av enkeltfiber med ulik betongfasthet, innstøpingslengde og fibertype (syntetisk makro fiber, stålfiber med endekroker). Forsøksserien viste blant annet at syntetiske fiber oppnår maks uttrekkskraft med høyere uttrekkslengder enn stålfiber. Det var tydelig at økt betongfasthet forbedret heften mellom fiber og betong. Dessuten understreket uttrekksforsøkene at endekrokene på stålfibrene utgjør hovedbidraget til uttrekksmotstanden.

Fiberorientering - Konstruksjonselement av vibrert betong og SKB

Vegg og plateelement med selvkomprimerende (SKB) og vibrert stålfiberarmert betong. Små bjelker ble saget ut fra elementene og testet for å finne bøyestrekkfasthet og restfasthet etter opprissing. Formålet med forsøksserien var å undersøke fiberorienteringen gjennom elementene. Spesielt for plata med SKB var orienteringen jevn og gunstig. For de andre elementene viste den store spredningen i resultatene at fiberorienteringen varierte betraktelig. Forsøkene viste dessuten at middelspenningen i fibrene var høyere med SKB enn med vibrert betong selv om fastheten var tilnærmet lik.

Bjelkeprøving - moment og skjærbrudd

16 bjelker med planlagt moment- eller skjærbrudd ble testet. Parametere som ble undersøkt var vanlig vibrert betong kontra SKB, fibervolum, fiberlengde og innflytelse av tradisjonell armering. For momentkapasiteten var effekten av stålfibrene dobbelt så stor for den selvkomprimerende som for den ordinære betongen, noe som skyldes stor ensretting av fibrene i underkant av bjelketverrsnittet. Det var liten forskjell i skjærkapasitet mellom bjelkene med vibrert betong og de tilsvarende bjelkene med SKB. Forsøksresultatene var i god overensstemmelse med dimensjoneringsreglene.

Syntetiske fiber

36 små bjelker ble saget fra vegg og plateelement med ulike fibertyper og konsentrasjoner. Formålet var å sammenligne restfastheten for SKB med syntetiske fiber og SKB med stålfiber. Resultatene viste at syntetiske fiber kan overføre strekkspenninger over betongrissene på samme måte som stålfiber, men siden maksimal spenning blir oppnådd ved høyere rissvidder kan kapasiteten til betong med syntetiske makro fiber kun utnyttes når det blir tolerert relativt høye verdier for maksimal rissvidde.

Størrelseseffekt

Bøyeprøving av 9 bjelker med tre ulike dimensjoner ble utført for å undersøke størrelseseffekt av stålfiberarmert betong. Tre bjelker var armert med 1 % fiber, tre med 0,3 % fiber, og tre var armert både med 1 % fiber og kamstål. Effekten av økende tverrsnittshøyde på bøyestrekkfastheten tilsvarte vanlig armert betong. For bjelkene med 1 % fiber minket maksimal last og duktilitet relativt til last ved opprissing med økende tverrsnittshøyde.

Plater med punktlast

13 plater med dimensjon 1,2 x 0,15 x 3,6 m fritt opplagte på to render ble pålastet med en punktlast i midten. Formålet var å undersøke effekten av ulike fibertyper og armeringsforhold med hensyn til rissfordeling, duktilitet og maksimal last, og å kontrollere om fibrene kunne overføre lasten fra midten av platen til armeringsstengene som var plasserte nært langsidene av platen. Resultatene indikerte at maksimum avstand mellom armeringsstengene i henhold til standard dimensjoneringsregler for vanlig betong kan økes ved bruk av fiber. Videre viste fibertelling at fibrene hadde en hovedorientering langsetter platen, noe som tyder på at fibrene hadde rettet seg parallelt med flyteretningen til betongen.

Fiber som skjærarmering i hulldekkelement

12 fritt opplagte hulldekkeelement med dimensjon 4 x 1,2 x 0,32 m ble belastet med en linjelast 800 mm fra opplegg for å undersøke om fibrene kunne øke skjærkapasiteten til elementene. Produksjonsteknisk og med tilslaget som var tilgjengelig viste det seg å være vanskelig å oppnå god komprimering av betongen rundt spennstålet. Konsekvensen var at kapasitetsøkningen var neglisjerbar fordi det oppstod uttrekksbrudd av spenntauene før skjærkapasiteten var oppnådd. Den eneste fordelen med fibertilsetningen var derfor økt duktilitet.

Fullskala lastforsøk på dekker

Fullskala lastforsøk på tre dekker ble gjennomført i et betonghus på Rena militærleir der hele huset var utført med stålfiberarmert SKB. Forsøkene viste at fiber kan erstatte all tradisjonell armering i lastbærende dekker med relativt korte spenn.

Støpemetode

Fire veggelement av fiberarmert SKB ble støpt med pumpe og neddykket slange ved Contigas elementfabrikk i Moss. Formålet var å prøve om det var mulig å produsere en stabil SKB for pumping med det tilgjengelige tilslaget, å kontrollere om det ville oppstå fiberblokkering i rør/pumpe, og undersøke fiberfordeling og -orientering gjennom veggene. Tre fibertyper ble brukt, to typer stålfiber med endekroker og en type makro syntetisk fiber, og fibervolumet var 0,6 %. I en av veggene ble slangen ført frem og tilbake, noe som resulterte i en mer gunstig fiberorientering. Resultatene viste at fiberkonsentrasjonen minket noe med økende avstand til slangen, noe som indikerer at betongen var på grensen til separasjon. Betongens flyteretning var mer konstant i denne forsøksserien enn for veggelementene som var støpt med tobb gjennom trakt fra toppen av forskalingen.

Forsøk sammenlignet med teori

Resultatene ble evaluert vha håndberegninger og elementanalyser og sammenlignet med tilgjengelige dimensjoneringsregler, og generelt sett var overensstemmelsen god. Dette viser at det teoretiske rammeverket som eksisterer i dag i hovedsak kan beskrive oppførselen til fiberarmerte betongkonstruksjoner godt, og at dimensjoneringsreglene som er utviklet er tilfredsstillende.

Acknowledgements

First of all I would like to express my sincere gratitude to my supervisor Professor Terje Kanstad for giving me the opportunity to work on this research project. Much appreciation is given for his professional support, permanent encouragement and enthusiasm; always focusing on possibilities and solutions instead of problems and limitations.

The thesis is founded by a Norwegian industrial research project, and I would like to thank all participants for making my experimental study possible: Bekaert, Contiga, Con-Form, Dr. techn. Olav Olsen, Forsvarsbygg, Norbetong, Norcem, Norconsult, NTNU, Skanska Norge, Sintef, Unicon and Veidekke. Special credit is given to Jørn Injar for taking initiative and enabling all experiments that were performed at Contigas factory in Moss.

The research is partly financed by COIN – The Concrete Innovation Centre – which is a centre for research based innovation with funding from the Norwegian Research Council and industrial partners. The financial support is greatly acknowledged.

I am grateful to all my colleagues in the concrete group at the Department of Structural Engineering at NTNU and the concrete group at SINTEF Technology and Society. In particular Senior researcher Erik Thorenfeldt who contributed with valuable comments to the outcome of the research project, Kåre Johansen for his help and expertise regarding concrete mix design and Prof. Karl Vincent Høiseth for continuous encouragement and for valuable discussions.

The experiments of this study could not have been performed without the help and technical expertise of the laboratory personnel; Helge Rødsjø, Svein

Lorenzen, Kjell Kristiansen, Ove Loraas, Johan Jørgen Sandnes and Terje Pettersen. The good humour and atmosphere at the laboratory made the work more enjoyable and will be remembered with appreciation.

I would like to express my gratitude to the thesis committee members for their interest on my work. Moreover, I'm thankful to Prof. Joost Walraven for organizing my research stay at TU Delft. A warm thank goes to Eleni Lappa and Petra Schumacher for making my stay in Delft so pleasant and memorable, and also for valuable technical comments.

Special thanks go to Helge Nilsen for giving me a challenging and unforgettable summer job as a concreter when I had just started my civil engineer study. This gave me a foundation and interest for concrete structures which I have benefited from throughout my time as a PhD student.

I want to thank my parents, family and friends for the support they provided. Ida, Rebekka, Kristian, Marco, Ole, Justin, Katrin, Eivind, Ingunn, Madli, Dag Abel, Ann Karin, Dag, Mona, Kjersti, Ingvild – there were too many to mention on this list, thank you for making my time at in Trondheim a pleasant one.

My final thanks go to my boyfriend Nikolai for his unconditional support, encouragement and patience in the final stage of this work.

Åse Lyslo Døssland
February 2008

Table of contents

Notations

Roman Capital Letters

A_c	Concrete cross section	[mm^2]
A_f	Area of the cross-section of a single fibre	[mm^2]
A_s	Steel cross-section	[mm^2]
A_{sv}	Stirrup cross-section	[mm^2]
E_c	E-modulus of concrete	[N/mm^2]
E_s	E-modulus of steel	[N/mm^2]
F	Force	[kN]
F_a	Anchorage capacity (pull-out model)	[kN]
F_{max}	Maximum force	[kN]
F_u	Load at failure	[kN]
G_f	Fracture energy of concrete	[mm]
L	Member length	[mm]
L_d	Damage zone length	[mm]
M	Moment	[kNm]
M_{cr}	Cracking moment	[kNm]
M_{max}	Moment at maximum load	[kNm]
M_L	Plastic moment	[kNm]
N	Normal force	[kN]
N_f	Number of steel fibres per unit area.	[-]
V	Shear capacity	[kN]
V_c	Contribution of concrete to the total shear capacity	[kN]
V_s	Shear contribution from stirrups	[kN]
V_f	Shear contribution from fibres	[kN]
W_f	Fibre content	[kg/m^3]

Roman Lower Case Letters

a	Shear span	[m]
b	Width of cross-section	[mm]
b_w	Minimum width of cross-section	[mm]
c	Clear concrete cover on the bar	[mm]
d	Effective height of a cross-section	[mm]
d_f	Fibre diameter	[mm]
e	Eccentricity	[mm]
f_{bf}	Bonding strength for fibres (pull-out model)	[N/mm^2]
f_c	Concrete compressive strength	[N/mm^2]
f_c*	Concrete compr. strength at the most compressed side (CDZ model)	[N/mm^2]

f_{ct}	Concrete tensile strength	[N/mm^2]
$f_{ft,eq}$	Average equivalent bending strength	[N/mm^2]
$f_{t,res}$	Residual strength of concrete after cracking	[N/mm^2]
f_{sy}	Yield strength of steel	[N/mm^2]
h	Height of cross-section	[mm]
h_{cr}	Crack band width	[mm]
k	Proportionality factor	[-]
k_n	Factor to determine characteristic values depending on number of tests	[-]
l	Span	[mm]
l_f	Fibre length	[mm]
n	Number of cracks	[-]
p_e	Size factor	[-]
s	Bar spacing	[mm]
s_{rm}	Average crack spacing	[mm]
s_n	Standard deviation	[-]
v_f	Volume ratio of fibres	[-]
w	Crack width	[mm]
w_c	Localized deformation (CDZ model)	[-]
x,y,z	Cartesian coordinate system	[-]

Greek letters

α	Fibre orientation factor	[-]
α_{fd}	Filling degree (CDZ model)	[-]
β	Share of uni-directed fibres	[-]
ε	Strain	[-]
ε_0	Strain at maximum stress (CDZ model)	[-]
ε_c	Compressive strain	[-]
ε_s	Tensile strain	[-]
ε^{el}	Elastic strain	[-]
ε^{in}	Inelastic strain	[-]
ε_s	Steel strain	[-]
ϕ	Reinforcement diameter	[mm]
η	Factor which indicates how much of the fibre forces that acts in one direction	[-]
λ	Ratio between fibre length and diameter l_f/d_f	[-]
ρ	Reinforcement ratio	[-]
ρ_f	Section ratio of fibres	[-]
σ	Stress	[N/mm^2]
$\sigma_{f,average}$	Average stress in fibres	[N/mm^2]
σ_c	Concrete compressive stress	[N/mm^2]
σ_f	Fibre bridging stress	[N/mm^2]

$\sigma_{f,average}$	Average bridging stress in fibres	[N/mm^2]
$\sigma_{f,max}$	Maximum bridging stress in fibres	[N/mm^2]
σ_s	Steel stress	[N/mm^2]
τ	Shear resistance	[N/mm^2]
ω	Share of plane-orientated fibres	[-]

1 Introduction

1.1 Background

Fibre reinforcement can provide an alternative to conventional steel bars in order to improve the efficiency and working conditions on construction sites and in the prefabrication industry. Although fibres most often are used for non-structural applications to control plastic and drying shrinkage, they can also be applied to reduce or in some cases even replace ordinary reinforcement bars. The labour cost makes roughly 40% of the total cost of a concrete building [Löfgren, 2005], where a main part is related to the reinforcement work. The reduced labour can in some cases offset the increased material costs when fibres are used as replacement for conventional bars, especially in Norway where the recruitment of construction workers is particularly low. Moreover, the physically hard reinforcement work often leads to health complaints and an early retirement age. Fibres combined with self compacting concrete (SCC) is furthermore a very promising concept which improves the working conditions further, both with respect to efficiency and to health and safety benefits, since the heavy and noisy vibration work is avoided.

From a structural aspect, the main reason for adding fibres is to improve the fracture characteristics and structural behaviour through the fibres ability to bridge cracks. Fibre bridging over the cracks leads to increased shear, moment and punching resistance, increased dowel effect, reduced crack spacing and crack widths, increased flexural stiffness and increased ductility in compression.

The use of fibre reinforcement for structural applications is in Norway mainly limited to slabs on ground and sprayed concrete for rock support. Although extensive research has been done over the years to evaluate the

effect of fibres, existing standardised tests and design methods have not always been consistent in its treatment. A main reason for limited use of fibre reinforced concrete (FRC) in load-carrying structures seems to be the lack of accepted design guidelines. A more general utilization of fibre reinforced concrete in structural concrete structures require more detailed design rules, combined with guidance regarding choice of fibre types, concrete composition, execution rules and test methods.

1.2 Scope of the research

The principal aim of this research project is to improve the current knowledge of the mechanical and structural behaviour of fibre reinforced concrete, focusing on practical applications. An experimental study is carried out, and the results are compared with available design rules and with finite element analysis. Further, the connection between casting method and fibre orientation is investigated, since the behaviour of fibre reinforced structures strongly depends on the orientation and distribution of fibres.

The experimental investigations in this thesis are financially supported by the Norwegian industrial research project ”Industrialisation of cast in place concrete – Steel fibre reinforced concrete”, chaired by the contractor Veidekke ASA. This has been a Norwegian joint programme with 14 partners (Consultants, material suppliers, contractors, building owners, government agencies, universities and research institutes), with the main objective to develop nationally accepted guidelines for design and execution of fibre reinforced structures. Hence, a secondary objective of the experimental program has been to support these design guidelines.

1.3 Outline of the thesis

A theoretical background for this work is given in chapter 2 and 3 while the experimental study is presented in chapter 4 to 10. Chapter 2 describes fibre characteristics, concrete mix design and also the mechanics of crack propagation. Moreover, a summary of mechanical properties and testing methods is presented, considering compressive, tensile, shear and pull-out behaviour. Fibre orientation and fibre distribution is also treated, including both theoretical orientation models and fibre orientation in practice; the latter by describing the factors which imposes a pronounced fibre orientation in a particular direction. A number of approaches are available for structural analysis of fibre reinforced concrete both in the ultimate and in the serviceability limit state. Chapter 3 describes some of these methods considering both flexural and shear design and also including finite element modelling. Further, design methods for fibre reinforced concrete in the serviceability limit state are reviewed.

A series of pull-out tests is presented in chapter 4, where three main factors are investigated; compression strength, fibre type and cast in length. Chapter 5 focuses on fibre orientation based on bending tests on beams sawn from different structural elements made with vibrator compacted concrete (VCC) and self compacting concrete (SCC). Chapter 6 studies the effect of steel fibres on the shear and flexural behaviour based on four point bending tests on beams made with VCC and SCC. A comparison with different available design rules are presented together with finite element analyses. In chapter 7 the influence of synthetic fibres and steel fibres on the flexural behaviour is compared, and size effect of fibre reinforced concrete beams is treated in chapter 8. Chapter 9 examines the effect of different fibre types and reinforcement ratios in slabs exposed to concentrated loads, particularly in order to control if fibres are able to transfer large stresses which enables increased maximum spacing between reinforcement bars. Chapter 10 presents the results of three different field tests. Firstly, steel fibres are used as shear reinforcement in prestressed

hollow core units. Secondly, full scale load testing is carried out on three slabs in a fibre reinforced concrete building. The last field test covers a series of SCC walls cast with tube, with the objective to study the connection between casting method and fibre orientation. Chapter 11 summarises results and experiences gained from the experimental study and presents the final conclusions.

	Chapter nr								
Parameters	4	5	6	7	8	9	10.1	10.2	10.3
Compression strength	x	(x)							
Fibre volume		x	x	x	x	x	x		
Fibre length	x		x			x	x		x
Steel versus synthetic	x			x		x			x
Size effect					x				
Influence of reinfo. bars			x		x	x		x	
SCC versus VCC		x	x						
Casting process		x	x	x		x		(x)	x
Type of structural element		x		x					

Figure 1.1: An overview of parameters investigated in the experiments, which are described in the following chapters: 4. Pull-out tests, single fibres. 5. Beams sawn from plates and walls with VCC and SCC. 6. Beams designed for moment- and shear failure (VCC/SCC). 7. Synthetic/steel fibres, beams sawn from wall/plate elements. 8. Scale effect. FRC beams with different cross-section heights. 9. Simply supported slabs (fibres + bars) with concentrated load. 10.1. Prestressed hollow core elements with steel fibres. 10.2. Full scale loading on three slabs in FRC building. 10.3. SCC wall elements cast with tube.

2 Fibre reinforced concrete

2.1 General – development and use of FRC

Research on fibre reinforced concrete has been conducted since the 1960's [Shah and Skarendahl 1985]. During the 1970s the commercial use of this material began to increase, particularly in Europe, Japan and USA [Clarke, Vollum et al. 2007]. Common application areas today are shotcrete, pavements, industrial floors, precast elements and various kinds of repairs [Carlswärd 2006].

The addition of randomly distributed steel fibres increases the cracking resistance of concrete, i.e. the fracture toughness, ductility, impact resistance, fragmentation and spalling resistance [Shah and Skarendahl 1985]. However, since fibres generally are distributed through the cross section it is not possible to achieve the same area of reinforcement with fibres as with conventional bars. Hence, for normal fibre contents, the concrete exhibits a softening response.

Fibres are primarily used as replacement for conventional reinforcement in non-structural applications in order to control early thermal contraction cracking and drying shrinkage cracking. However, the use of fibres for structural applications as part of the overall structural design is continuously increasing. In some types of structures with relatively low reliability levels for structural safety such as slabs on grade, foundations and walls, fibres can replace ordinary reinforcement completely. Furthermore, in load carrying structures in general, fibre reinforcement may be used in combination with conventional or prestressed reinforcement.

Although economical issues has been the main limiting factor for practical use of SFR, it is presently a more interesting alternative due to lack of

skilled concrete workers and need for industrialisation of the construction industry [Kanstad & Døssland 2004].

2.2 Fibres – material, geometries and physical properties

A wide range of fibre types exists, which are made of different materials and with various geometries. Some types of fibres are mainly used to improve the toughness and reduce crack widths, while others are used to reduce plastic shrinkage cracking or to avoid spalling of concrete during fire [Löfgren 2005]. Commonly used materials are steel, glass, carbon, polyvinyl alcohol (PVA), polypropylene, (PP) and cellulose. The fibres come in many different shapes and sizes; PP-fibres can for instance be twisted, fibrillated or monofilament. Macro fibres are often characterized by their aspect ratio, i.e the length to diameter (or equivalent diameter) ratio. Most steel fibres are round in cross-section with diameters between 0.4 and 0.8mm and lengths ranging between 25 and 60mm [Clarke, Vollum et al. 2007]. The draft BS EN 14889-1 [British Standard institution 2006] classifies steel fibres into fibre groups as follows:

Group I	Cold-drawn wire
Group II	Cut sheet
Group III	Melt extract
Group IV	Shaved cold drawn wire
Group V	Milled from blocks

To enhance the bonding between fibre and concrete matrix, the fibres are often deformed, i.e. by end-hooks or end knobs, or they can be crimped (wave shaped) or twisted.

This work focuses on fibres used for structural applications, and for this purpose slender high strength steel fibres are considered to be most efficient. Further, synthetic fibres are becoming more attractive since they can offer similar post-crack ductility to steel fibres.

2.3 Concrete mix design of fibre reinforced concrete

2.3.1 Concrete mix design - VCC with fibres

Fibres affect the workability of the concrete, and at high fibre dosages it is often necessary to increase the filler content or the sand-to-coarse aggregate ratio in the mix composition in order to obtain an optimum packing density. If the maximum fibre volume is reached for a maximum grain size and aspect ratio, the probability for fibre balling increases. Moreover, the volume of coarse aggregate should not be too high compared to the total aggregate volume.

The mix design of SFRC can be based on the same volume design procedures as for plain concrete, where the fibres are considered as additional coarse aggregates in the mixture. With fibres, a larger internal surface needs to be moistened by cement paste, thus it is recommended to increase the cement weight in SFRC compared to plain concrete. Consequently, the surface area of the relevant fibre type should be considered in the design phase. Moreover, limiting the maximum grain size improves the workability and decreases the probability of fibre clustering. [Kooiman, 2000].

2.3.2 Concrete mix design – SCC with fibres

Self compacting concrete (SCC) is flowable and fills formwork and densely reinforced areas without vibration. With fibre reinforced SCC, further improvements can be obtained with respect to working conditions, time-saving and reduced labour costs. However, extended preliminary investigations are often required as regards to mix design.

The slump flow decreases with increasing fibre volume and fibre length [Groth 2000a]. Similar to VCC, adjustments in the mix design can be done to account for fibres, and most often it is necessary to carry out test mixes

to ensure that the concrete maintain self compactability. The components of fibre reinforced self compacting concrete (FRSCC) have to be homogenously distributed to avoid sinking particles, fibre clustering and blocking [Grünewald 2004], and it is important to aim at a smooth grading curve without gap grading [Thorenfeldt, Fjeld et al 2006].

Nemegeer [1999] studied the passing ability of FRSCC with the J-ring in combination with the slump flow test in order to determine the bar spacing required to avoid blocking. He found that a bar spacing of about two times the fibre length was required to avoid blocking. The recommendations for bar-spacing proposed by Groth [2000b] also include the aspect ratio and the volume of fibres. However, the composition of the FRSCC was not considered [Table 2.1].

s/l_f	L_f/d_f [-]	Max m_f [kg/m^3]
≥3	80	30
	65	60
≥2	65	30
	45	60
≥1.5	45	30

Table 2.1: Guidelines for assessment of blocking of SFRSCC where s=(minimum) gap distance between re-bars, l_f=fibre length, d_f=fibre diameter and m_f=fibre amount. [Groth 2000b]

Grünewald carried out an extensive study to optimise the mixture composition of FRSCC. The following criteria were applied to judge the self-compactability; a slump flow larger than 600mm, no segregation of the fibres, and a homogenous distribution of FRSCC on the flow table. In the study, 11 reference mixes with maximum aggregate size of 16mm were composed according to the Japanese method [Okamura and Ouchi 1999], proportioned at the upper level of self-compactability. Different fibre types were tested, and the maximum fibre contents obtained were 140, 100, 60

and 60 kg/m^3 for Dramix 45/30, Eurosteel 50/50, Dramix 65/40 and Dramix 80/60 respectively. With lower maximum aggregate sizes, even higher maximum fibre contents were reached. However, the study indicated that although the maximum fibre content depends on the mixture composition, the upper limit is a fibre characteristic, which for instance results in an upper limit of 80kg/m^3 for Dramix 80/60.

The results were calibrated with a method for predicting the maximum fibre content based on the CBI concept 'risk of blocking' [Peterson et al. 1998]. With the CBI method, the minimum amount of paste is calculated based on the aggregate's grading curve, its nature (natural or crushed) and by using a "risk curve", where the "risk of blocking" has to remain below 1:

Risk of blocking : $\sum_{i=1}^{n} \frac{n_{ai}}{n_{abi}} = \sum_{i=1}^{n} \frac{V_{ai}}{V_{abi}} \leq 1$

where n_{ai} = aggregate contribution of group i to blocking [-]
n_{abi} = blocking volume ratio of group i [-]; $n_{abi}=V_{abi}/V_t$
V_t = total volume of the concrete mix [m^3]
V_{ai} = aggregate volume of group i [m^3]
V_{abi} = blocking volume of aggregate group i [m^3]

Further, the blocking volume ratio n_{abi} is determined as a function of the bar spacing to fraction diameter of the aggregates c/d_f.

In Grünewald [2004] the CBI concept was adjusted by replacing the bar spacing to aggregate fraction diameter ratio c/d_f with the ratio of fibre length L_f to aggregate fraction diameter. The experimental study lead to maximum fibre factor $(v_f \cdot L_f/d_f)_{max}$:

Maximum fibre factor= (0.781-MFC)/0.211

where the maximum fibre content (MFC) depends on the kind of aggregates (crushed or nature), the volume of each fraction and the fibre length.

$$MFC = \sum_{i=1}^{n} \frac{n_{ai}}{n_{a,mfi}} = \sum_{i=1}^{n} \frac{V_{ai}}{V_{a,mfi}}$$

The contribution of aggregate group i to the maximum fibre content (n_{ai}) is equal to the volume of each fraction (V_{ai}) and has to be divided by the blocking volume ($V_{a,mfi}$) which is equal to the MFC-ratio $n_{a,mfi}$. The characteristic points of $n_{a,mfi}$ were varied to obtain a high correlation with the experimental results on the maximum fibre factor [Figure 2.1]. Hence, the content and distribution of the aggregates determine the maximum fibre content.

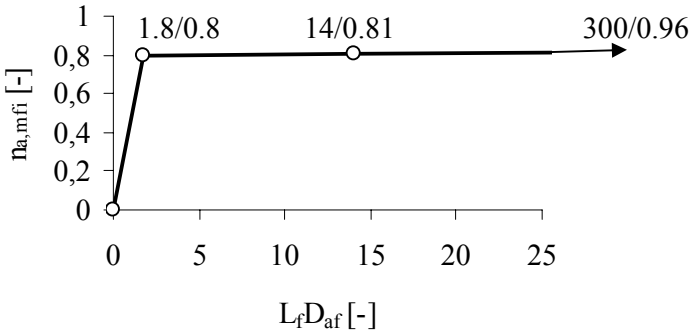

Figure 2.1: Relation between the ratio fibre length to equivalent aggregate diameter L_f/D_{af} and the MFC-ratio $n_{a,mfi}$. [Grünewald 2004]

In addition to the filling ability, Grünewald found that steel fibres affect the passing ability and segregation resistance significantly. The required bar spacing for non-blocking was increased with increasing fibre content. Hence, to optimise the mixture composition of FRSCC, the filling ability and segregation resistance have to be balanced and the geometrical effect of the fibres on the packing density has to be taken into account. [Grünewald and Walraven 2003], [Grünewald 2004] and [Grünewald and Walraven 2005].

2.4 Mechanics of crack formation and propagation

The main benefit of fibres is their ability to transfer stresses across a crack, and consequently enhancing the toughness and ductility of the concrete as well as the absorption capacity under impact [Clarke, Vollum et al. 2007].

Concrete is a heterogeneous material with pores and micro-cracks caused by shrinkage and thermal strains, which have been restrained by coarse aggregates and boundary conditions. During loading, the matrix transfers part of the load to the fibres before any macro-cracks are initiated. Hence, it is theoretically possible to increase the strength of the material by adding fibres. Yet, for the relatively limited fibre volumes that usually are added to conventional concrete, the fibre reinforcement does not cause any pronounced improvement of strength. This is related to the low tensile strain capacity of the cementitious matrix and also to the increased porosity that the fibre addition may induce. [Löfgren 2005]

Provided that fibre rupture is avoided (depending on the tensile strength of the fibres) debonding between fibre and concrete starts on the shortest embedded lengths until full debonding occurs. The initial micro cracks will then start to grow and eventually lead to a macro crack which covers several micro cracks [Kooiman 2000]. The bridging of fibres across cracks provides a post-crack tensile strength to the concrete as illustrated in Figure 2.2. In addition to debonding and fibre pull-out, other mechanics like matrix spalling and plastic deformation of the fibre might be present, which will be discussed further in chapter 2.5.4. A detailed overview of the mechanics of crack formation is given by Löfgren (2005).

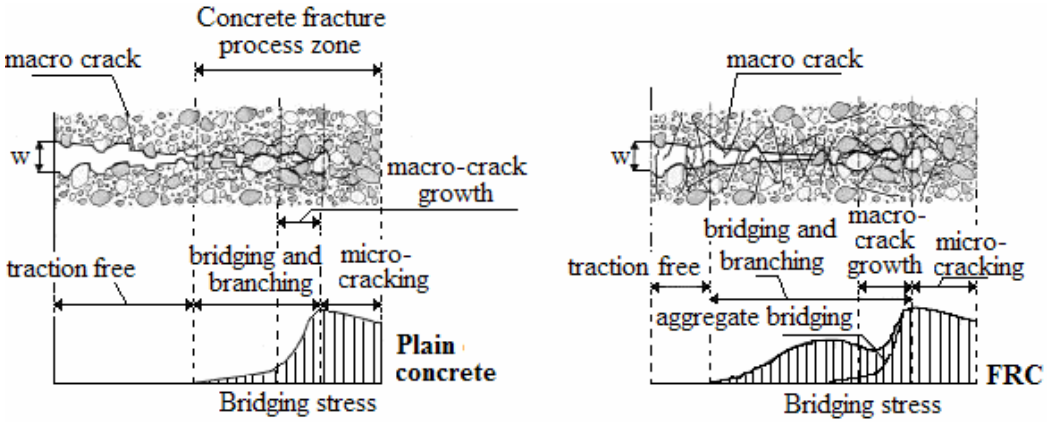

Figure 2.2: Schematic description of the stress-crack opening relationship for plain concrete and for FRC [Löfgren 2005].

Depending on the amount of fibres crossing the crack and on the fibre-matrix bonding, the post-crack stress can be larger than the cracking load, resulting in a so called strain hardening behaviour where multiple cracking occurs [Figure 2.3]. However, for normal fibre dosages (<1%) the material exhibit strain softening behaviour, i.e the damage localises immediately after initiation of the first crack.

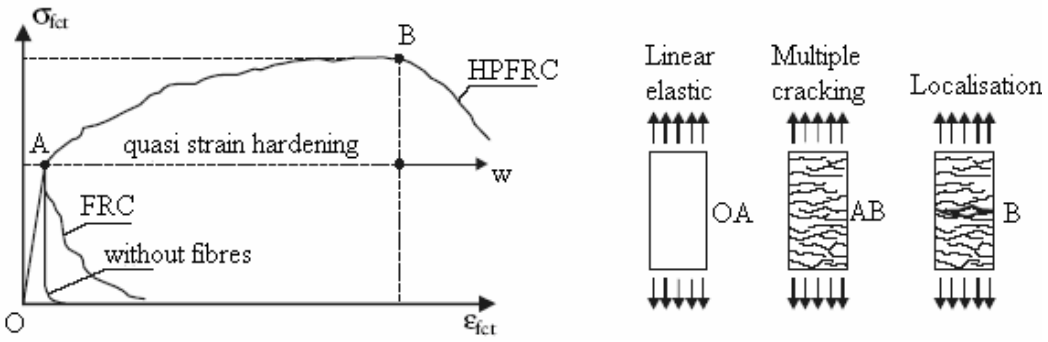

Figure 2.3: Definition of high performance fibre reinforced concrete [Kooiman 2000].

2.5 Mechanical properties and testing methods

Different test methods are available to estimate the mechanical properties of fibre reinforced concrete. The reliability of the methods described in this section is dependent on whether the difference in fibre orientation between specimen and structure are accounted for, since the wall-effect can be pronounced in the test specimens. The influence of wall-effect is primarily depending on the relation between fibre length and specimen size. Other aspects that influence the reliability of the methods are production and storage of specimen. One example regarding production of specimens for bending tests is given in Figure 2.4, which illustrates recommend casting methods aiming on avoiding weakness zones with unfavourable fibre orientation.

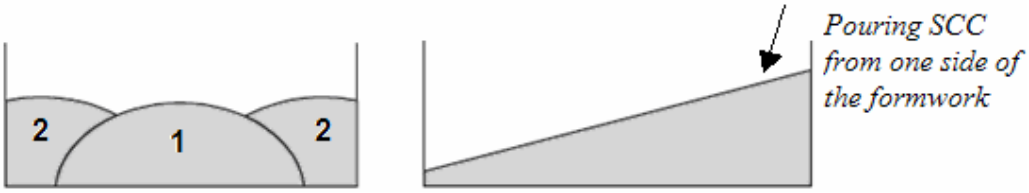

Figure 2.4: Filling method of beam specimens for FRVCC and FRSCC [Grünewald 2004].

2.5.1 Compression

Moderate concentrations of fibres do not influence the compressive strength significantly. However, fibre addition causes a less brittle failure. Failure of concrete in compression is related to failure in tension, as tensile stresses act perpendicular to the direction of the compressive load. The tensile stresses cause growth of the pre-existing micro cracks in the concrete, which eventually are bridged by mortar cracks as the stress continues to increase. [Schumacher 2006]

In a fracture mechanics based Compressive Damage Zone (CDZ) model proposed by Markeset (1993), the failure is distinguished into two modes. After reaching a stress of $0.75f_{cc}$, longitudinal cracking is initiated in a limited part of the specimen, the so-called damage zone. The second failure mode occurs after reaching the tensile stress, when lateral deformations within the longitudinal tensile cracks forms a shear band as the adjoining parts start sliding relative to each other. The effect of fibres in the presence of cracks is mainly based on preventing these lateral deformations, which results in a more ductile response [Kooiman 2000].

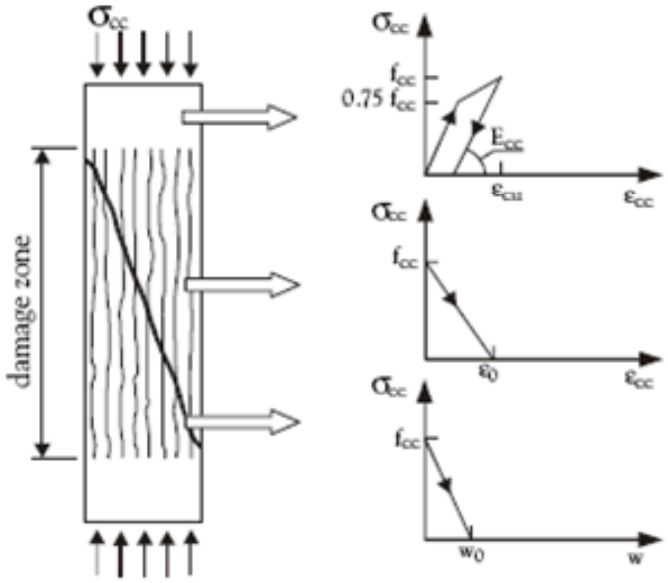

Figure 2.5: The CDZ model for plain concrete in uni-axial compression [Markeset, 1993]

The CDZ model is a constitutive macro-mechanical model which can be used to calculate the stress-strain relation of concrete in compression. The model has also been extended for additional confinement of the compressive zone with stirrup reinforcement. An overview is given in Schumacher (2006). Based on her research, Schumacher also proposed an extended CDZ model to steel fibre reinforced self-compacting concrete (SFRSCC).

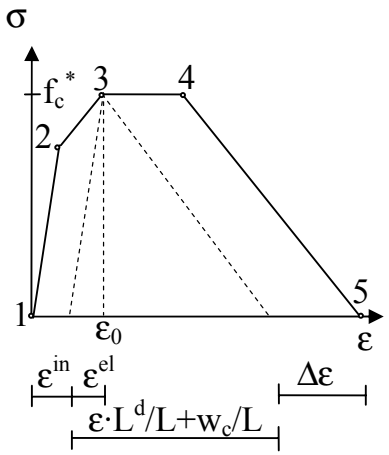

Point	σ	ε
1	0	0
2	$(2\alpha_{fd}-1)f_c^*$	$(2\alpha_{fd}-1)f_c^*/E_c$
3	f_c^*	ε_0
4	f_c^*	$\varepsilon_0 + \Delta\varepsilon$
5	0	$(\varepsilon_0-f_c^*/E_c)\cdot(1+2\alpha_{fd}k\cdot L_d/L)$ $+w_c/L+\Delta\varepsilon$

Figure 2.6: Average stress-strain relationship in the extended CDZ model by Schumacher (2006).

All points in Figure 2.6 can be calculated from the following parameters:

Filling degree	$\alpha_{fd} = 0.9$ for NSSCC
Nominal compression strength	$f_c^* = f_c - 1430(e/h)^2 + 380(e/h)$
Youngs modulus	$E_c = 0.9 \cdot 9500 f_c^{*(1/3)}$
Strain at maximum stress	$\varepsilon_0 = 0.7 f_c^{0.31} \cdot 0.8 - 7.5(e/h)^2 + 4.7e/h$
Proportionality factor	$k = 3.5 + 10 V_f l_f/d_f + 60e/h$
Localized deformation	$w_c = 0.7$ for NSSC
Damage zone length/total length	$L_d/L = 0.8 - 0.2 V_f l_f/d_f - e/h$

These parameters are determined by curve-fitting from several series of deformation-controlled compressive tests described in Schumacher (2006). Here e/h is the eccentricity versus cross section height, V_f the fibre volume and l_f/d_f the fibre length/diameter. The additional strain Δε takes into account confinements provided by stirrup-reinforcement or other boundary conditions. In her beam experiments, Schumacher accounted for the confining action of the loading platen in the region with the maximum moment by adding a strain Δε and by increasing the concrete compressive strength.

The compressive strength for FRC can be determined by simple standard tests, either on concrete cylinders or cubes [RILEM 2003]

2.5.2 Tension

The fibres influence the tensile behaviour of the concrete. It is mainly the ductility which is affected, not the tensile strength, and the influence is strongly dependent on the fibre content and fibre type. For engineered cementitious composites (ECC), the fibre concentration can be large enough to increase the tensile strength considerably, but for the moderate fibre content that can be applied in ordinary concrete the effect on the peak stress can be neglected.

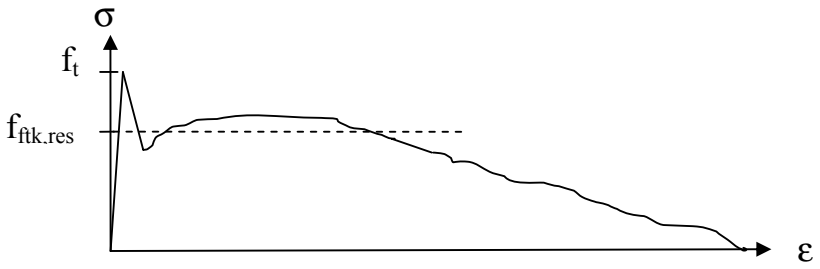

Figure 2.7: Typical tensile behaviour for SFRC. The value of the post-crack stress after cracking is called the residual strength $f_{ftk,res}$. Different approaches exists for modelling the post cracking stress.

It is when concrete is exposed to bending that the fibres come fully into effect as the softening response leads to a redistribution of stresses which imposes a new state of equilibrium across the cross-section after cracking. As a result, the maximum moment capacity may exceed the maximum moment of plain concrete [Kooiman 2000].

Uni-axial tensile test

The post-crack response of strain softening FRC can be determined directly in terms of stress-crack opening relation with the uni-axial tensile tests (UTT) as described in the recommendations by RILEM (2001). This test is

conducted as a displacement controlled tensile test on a notched cylindrical specimen where both ends are fixed with respect to rotation. However, the applicability of this test method is relative low due to the complex test setup. The uni-axial tensile test is time-consuming and difficult to carry out, and it demands highly trained and experienced personnel. It is therefore more economical to determine the post-crack indirectly by bending or splitting-tests without compromising on the reliability of the method. The uni-axial tensile test is ideal for determining the basic σ–ω relationship which is used in advanced design procedures. For development work on fibres and for assessing the influence of fibre type and dosage the beam test is more suitable [Clarke, Vollum et al. 2007].

Three point bending test

In the three-point bending test (3PBT) proposed by RILEM (2002), the tensile behaviour is evaluated in terms of the load bearing capacity at a certain deflection or crack mouth opening. Notched beams of dimensions 150x150mm cross-section with a minimum length of 550 mm are used as standard test specimens [RILEM 2002]. The advantage of the notch is that the crack forms in a predefined position and not in the weakest section. Consequently, notched beam tests tend to give higher values of flexural strength than un-notched beam tests but with a higher coefficient of variation [Clarke, Vollum et al. 2007].

Wedge splitting test

In the wedge splitting test (WST) a cube or cylinder is split from one side by a wedge. The load is applied in a deformation controlled way, and the crack opening displacement is measured on top of the specimen. The method does not require sophisticated test equipment. The UTT, WST and 3PBT were compared in a study carried out by Löfgren (2005). It was found that the scatter of the WST was somewhat lower than for the two other methods, although the scatter in general was large for all methods. This can mainly be explained by the variation in number of fibres crossing the cracks [Löfgren 2005]. Despite the fact that the test method is time- and cost-efficient with good reproducibility, it is still not widely applied.

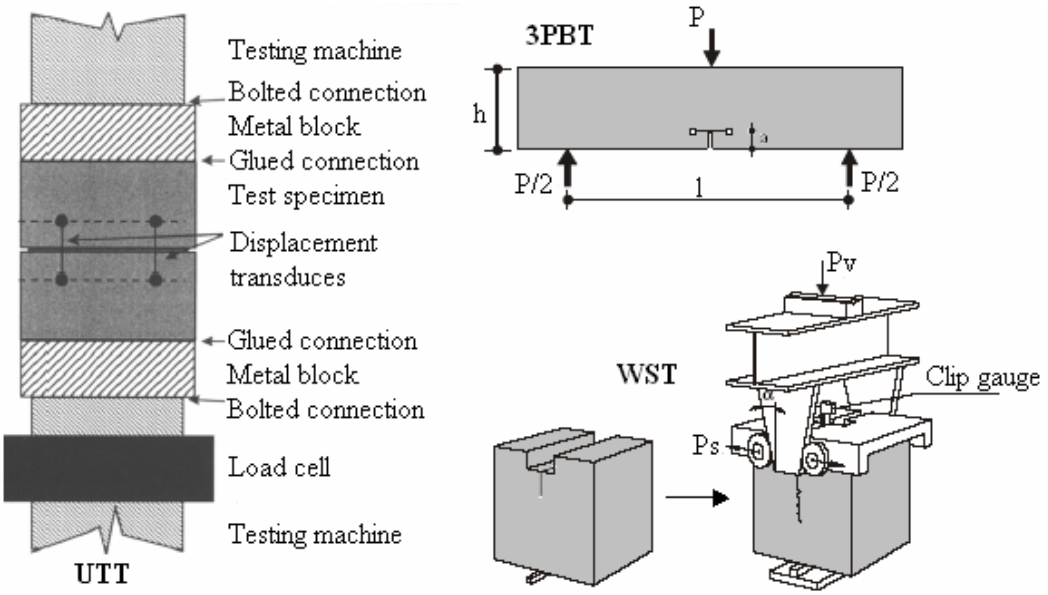

Figure 2.8: Test setup for the uni-axial tensile test (UTT) [Rilem 2001], three point bending test (3PBT) [Kooiman 2000] and wedge splitting test (WST) [Van Mier 1997]

Four point bending test

The JCI bending test is used in the design guidelines for Dramix steel fibres [Nemegeer 1997] and a corresponding method is also recommended by the Norwegian design rule draft [Thorenfeldt et al. 2006]. In this test, 150 x 150 x 600 mm long un-notched beams are loaded to failure under four point bending across a span of 450mm as illustrated in Figure 2.9. A constant bending moment occurs in the section between the two upper point loads. The deflections in the middle are measured and from this the toughness and the equivalent flexural strength can be calculated.

The advantage with the four point un-notched bending test is that it incorporates the effect of variation in the material's strength [Kooiman 2000] since the first crack will appear at the weakest section. One disadvantage is that the position of the crack cannot be predicted, which makes it hard to measure the crack opening deflections.

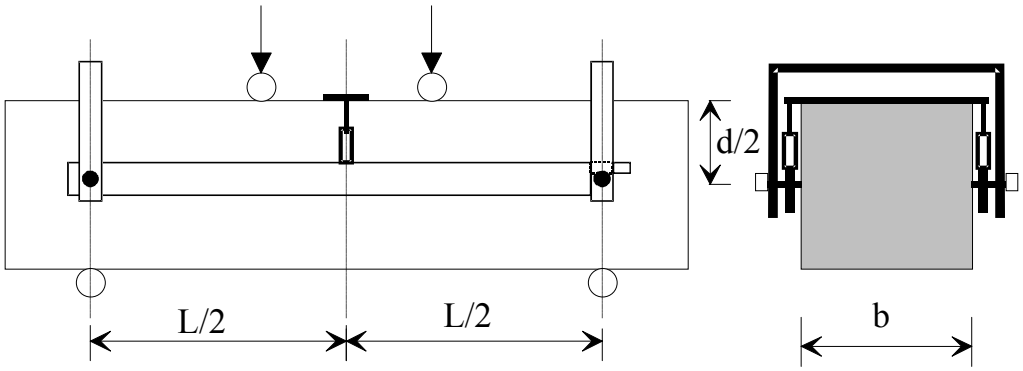

Figure 2.9: 4-point bending. Rig for deflection measurements. L=450mm, d=150mm, b=150 [Thorenfeldt et al. 2006]

In this thesis, the four point bending test is used to determine the tensile behaviour, based on the recommendations in the Norwegian design rule draft. The load is applied with a constant deformation rate at 0.1 mm/min. The residual strength after cracking is taken as $f_{res}=0.37f_{t,eq}$, where $f_{ft,eq}$ is the average equivalent bending strength recorded between 0.5 and 2.5mm deflection:

$$f_{ft,eq}= F_{(\delta 12)}L/(bd^2)$$

where L, b and d is given in Figure 2.9 and $F_{(\delta 12)}$ is the average load between the deflections $\delta_1=0.5$ and $\delta_2=2.5$ mm which can be calculated from the area under the load-deflection curve in this interval. The factor 0.37 expresses the difference between the tensile stress in the uncracked section and the equivalent tensile stress in the cracked section. This is based on the assumption that the depth of the compressive zone in the cracked stage is 1/10 which results in a ratio between the section modulus in the uncracked and cracked state of 0.37 [Kooiman 2000].

The fibre orientation is considered by cutting a block from the beam specimen and counting the fibres crossing the cross-section. The block is taken from the middle part of the beam between the twin loads at a minimum distance from the crack of $2/3l_f$, where l_f is the length of the fibre.

Fibre counting is done on both sawn sections on the block (corresponding to the longitudinal direction of the beam), and the average value is taken.
The method is based on test specimens sawn from plate- or wall elements, depending on the structural elements in which it is intended to use fibre reinforcement. The advantage is that wall effects are reduced, i.e. the fibres tendency to orientate parallel to the walls of the formwork, and that the test results are more representative for the real structure. A drawback of the method is cut-off fibres on the sides of the beams which have reduced pull-out resistance due to reduced anchorage as illustrated in Figure 2.10. The estimated fibre orientation based on fibre counting on sawn-out blocks does not consider that some fibres may be ineffective due to reduced anchorage.

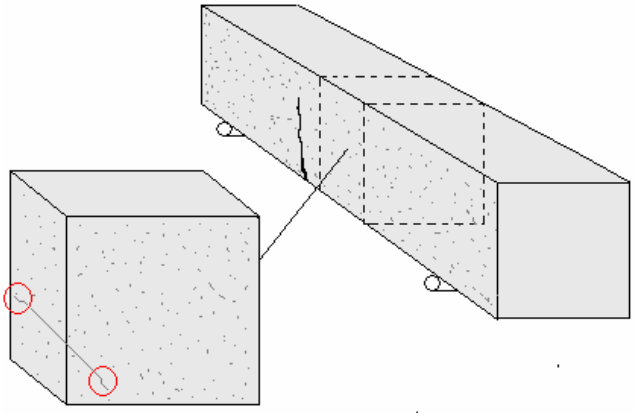

Figure 2.10: Sawn surface – example of cut-off fibres without anchorage.

Testing of sprayed concrete [EN 14488 2006]

To determine the flexural behaviour of fibre reinforced sprayed concrete, special testing methods exists. According to the European Standard [EN 14488 2006] the flexural strengths (first peak, ultimate and residual) are determined by 4-point bending of specimens with dimensions 125 x 75 x 550, and the energy absorption capacity is determined from FRC slab specimens. [Figure 2.11] The loads are applied at a rate of 0.25 and 1.0 mm/min for the beam and slab respectively, and the flexural behaviour is determined from the load-deflection curves. It should however be noted that it is not recommendable to characterize FRC by its energy absorption only, since it does not relate the contribution of fibres to crack widths or

deflections. Especially if synthetic fibres are used it should be considered that the maximum pull-out resistance might be reached at relatively large crack widths.

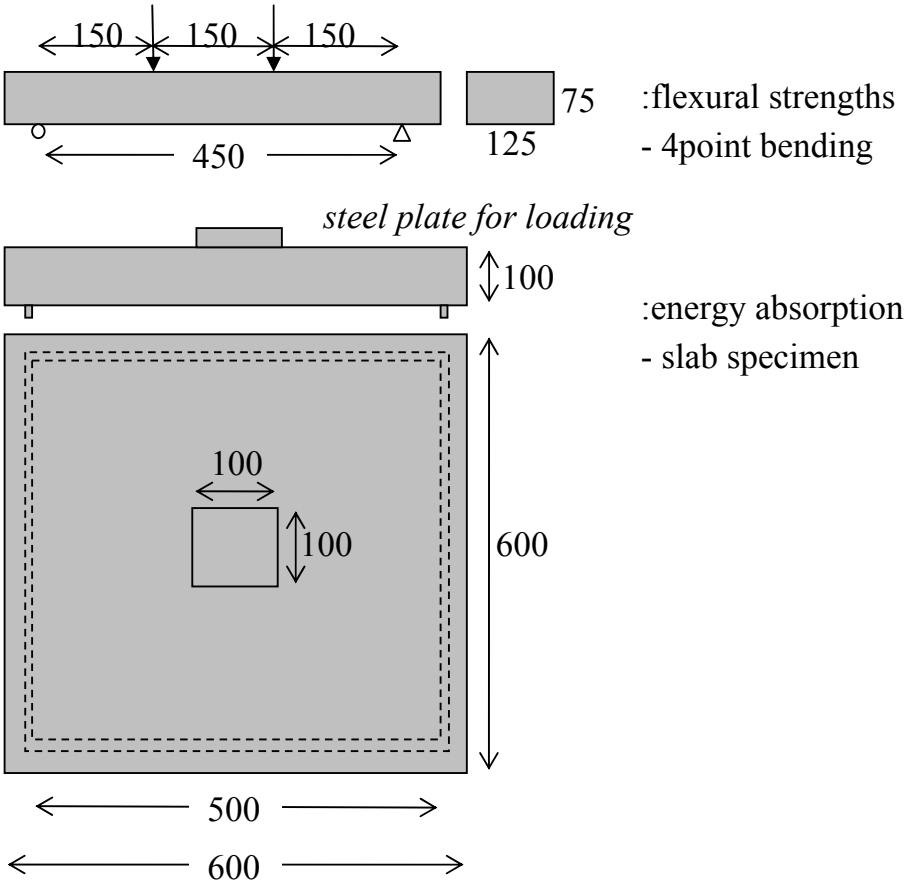

Figure 2.11: Loading of test specimen for testing of sprayed concrete according to EN 14488.

2.5.3 Shear

Fibres can be used as shear reinforcement as a replacement of stirrups in beams and similar structural applications. Numerous tests have indicated that the addition of steel or synthetic fibres significantly increase the shear strength of concrete structures and transform the failure mode from a

brittle-fracture to a more ductile one [Voo and Foster 2006]. As soon as the matrix cracks, the fibres are activated, resulting in a pronounced toughening behaviour due to fibre pull-out [Löfgren 2005]. The shear transfer capacity can be significantly increased, depending on fibre quantities [Barrigan 2002]. Moreover, the punching shear resistance can be increased considerably with fibres [Shaaban and Gesund 1994].

Determining the shear behaviour of fibre reinforced concrete is challenging due to the large number of parameters involved, e.g. shear span to depth ratio, scale effect, type of fibre, fibre content and orientation, bonding between fibre and concrete and also contribution from any longitudinal reinforcement bars placed to sustain high flexural moments [Uomoto et al. 1986]. Several methods exist for determining the shear capacity. The post-crack shear resistance is often based on post cracking tensile stresses determined from uni-axial tensile tests [e.g. Casanova (1997)], or equivalent post-crack flexural strengths determined from standardized beam tests [e.g. Nemegeer 1996, RILEM 2003]. Different methods for determining the shear capacity will be presented and discussed in section 3.4.

2.5.4 Pull-out

After cracking, the fibres transmit tensile stresses over the crack into the surrounding concrete. To avoid brittle failure, fibre pull-out has to be the dominating mechanism. Fibre fracture is not desirable. A potential fibre rupture depends mainly on the fibre strength, matrix strength, embedment length, fibre geometry and the inclination angle to the crack plane. Obviously, it is of major importance to choose a suitable fibre-concrete combination to minimize the probability for fibre rupture and at the same time keep the adhesion high enough to ensure a sufficient residual strength after cracking. Pull-out tests are fundamental to characterize the behaviour of FRC, and can be used to optimise the fibre-matrix combination. Together with knowledge about the orientation and distribution of fibres,

the pull out tests can also be used to estimate the average tension over a crack in a structure. A number of models are developed for this purpose, and one of them will be briefly presented later in this section.

The pull-out process is simplified divided into different stages where the following mechanisms are governing [Robins et al 2002]:

1) Mechanical adhesion as a shear bond at the fibre-matrix interface (bonded phase)
2) Frictional shear bond along the fibre-matrix interface when the fibre slips from the matrix (de-bonded phase)

The mechanical bond is the governing mechanism at very small pull-out lengths, up to a few micrometres [Dupont 2003]. Since the material at the interface zone is less hard than the surrounding bulk material due to higher porosity, very fine cracks spread at a small distance (20-50 μm) from the fibre in the de-bonding phase [Markovic 2006]. At larger pull-out lengths the second mechanism, friction, takes over. Since the displacements in the first stage are ignorable compared to the second stage, the general cohesive interface models are based on a perfectly bonded – de-bonded behaviour. With this assumption, the pull-out force can reach a critical value without any pull-out displacement taking place. Beyond this critical force, the frictional pull-out in the de-bonded phase takes over. With deformed fibres a third mechanism is introduced:

3) Mechanical anchorage creating localised load transfer points between the fibre and matrix [Robins et al 2002].

For hooked fibres the pull-out behaviour is dominated by the mechanical anchorage. Through the pull-out process, the hooked end has to be deformed into a straight end, provided that concrete spalling or fibre fracture is prevented [Figure 2.12]. Since hooked end steel fibres are used in all experiments carried out and discussed in this thesis, the effect of mechanical anchorage is emphasized in the test methods and models described in this chapter.

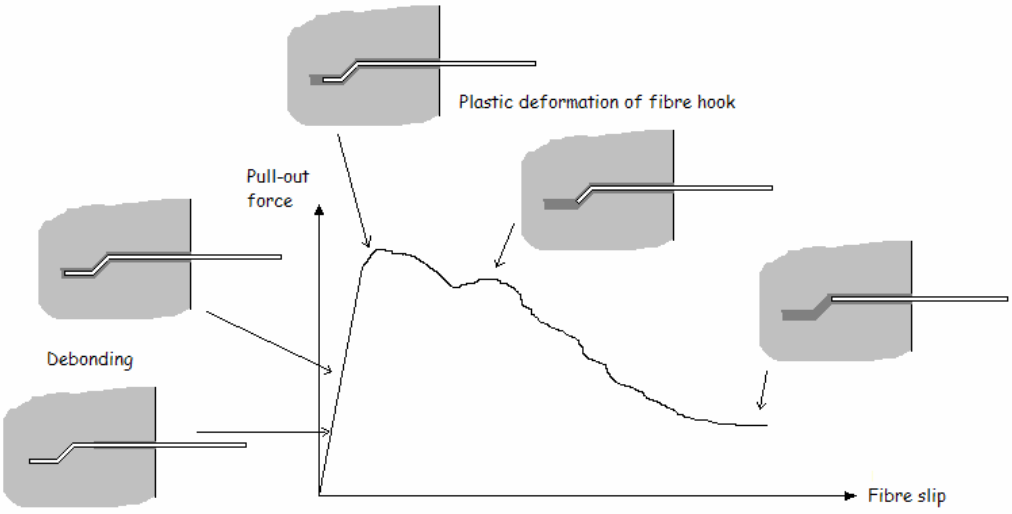

Figure 2.12: Typical pull-out response for hooked-end steel fibres, debonding and pull-out phases

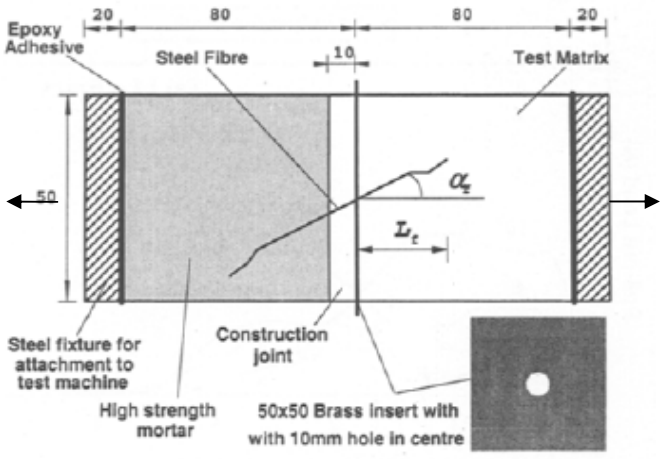

Figure 2.13: Double side specimen for pull-out test [Robins et al 2002]. First, a fibre is cast in a high strength mortar. Thereafter the test matrix is cast to embed the protruding fibre. The two concrete specimens, connected by the fibre, are then pulled from each other.

Pull-out tests can either be preformed on a group of fibres or on single fibres, and several models and test setups are in use. The pull-out test can

be preformed both on double- and single side specimens. Different test methods for fibre pull-out are described by Patrik Groth [Groth 2002a]. An example of a pull-out test well suited for hooked-end steel fibres is illustrated in Figure 2.13 [Robins et al 2002]. The test is adapted to different embedment lengths and angles. For inclined fibres, it is a major advantage to use a double side specimen, since force is directed in a way that is more true to the real pull-out behaviour in cracked concrete.

Constitutive relation – modelling the pull-out behaviour

Extensive studies have been carried out in order to model the pull-out behaviour of fibres. Two fundamentally different approaches were developed in the 80's to identify the bond parameters, the stress approach [Nammur and Naaman (1989)] and the fracture mechanical approach [Stang and Shah (1986); Gao (1987); Morrison et al (1988)]. Both approaches describe the pull-out behaviour of a single straight fibre embedded perpendicular to the crack surface.

In the first approach, a general stress-based equation is developed for a perfectly bonded – de-bonded material, where the criterion for growth of the de-bonded fibre/matrix interface is expressed in terms of interfacial stress. At a certain de-bonded length, the shear stress has a maximal value where the de-bonded zone ends. By combining an equation for the maximal shear stress and an expression for the displacement the total fibre displacement versus pull-out load can be determined numerically. A detailed calculation can be found in [Stang, Li, Shah (1990)]. The model gives a good approximation of the material behaviour, but it is rather complex, primarily because some of the input parameters have to be determined from complicated fibre pull-out tests. [Dupont 2003].

In the fracture mechanical approach, the criterion for interfacial de-bonding is expressed in terms of energy equilibrium [Stang, Li, Shah 1990]. As opposed to the stress based model, an analytical solution is possible with the fracture mechanical approach, but also here the extensive input parameters put a limit on the practical use of the model.

The average tension over a crack in a structure can be estimated from single fibre pull-out tests. The individual stresses carried by each fibre with different embedment lengths and angles are then summed and divided by the area of the crack plane. [Dupont 2003]. Models developed for averaging are developed by Balaguru and Shah (1992), Van Gysel (2000) and Stang and Li (2005) among others. The fibre bridging stress versus crack-opening relation $\sigma_f(\delta)$ can generally be expressed:

$$\sigma_f(\delta) = \frac{V_f}{A_f} \int_{\phi_0}^{\phi_1} \int_{\tilde{L}_e=0}^{1} P(\delta, \tilde{L}_e) g(\phi) \cos\phi \, p(\phi) \, \tilde{dL}_e \, d\phi$$ [Stang and Li 2005]

where

V_f and A_f is the volume and cross-section area of the fibres,

ϕ is the inclination angle,

$P(\delta, L_e)$ is the single fibre bridging force [Lin, Kanda and Li (1999)],

$g(\phi)$ is a function for the normalized load and inclination angle, which may be obtained analytically or from data fit to experiments and

$p(\phi)$ is a probability density function.

Fiber pull-out behaviour – conclusions from experiments carried out

Several factors have to be considered when transforming the stress-crack width relation from a single pull-out test to an average stress for a group of fibres with different orientation and embedment lengths crossing a crack. In addition to fibre and matrix properties, the following parameters affect the pull-out behaviour:

- Matrix spalling: If the embedment length is too short, the hook, together with the surrounding matrix is pulled out. To incorporate this into the calculation, the stress in the fibre should be put equal to zero if the initial embedment length becomes smaller than a certain fraction of the fibre length.
- Ineffective anchorage: Even when matrix spalling is avoided, a fibre with end hook will not be fully effective unless the hook is straightened, and it will not be straightened if the embedment length is too short.

- Inclined fibres: The toughness of hooked end and straight fibres has been shown to maximise at a non-zero inclination angle, typically between 15-40 degrees [Robins et al 2002]. This is mainly due to the snubbing effect which results in a higher pull-out force [Dupont 2003]. Snubbing effect causes the fibre segments bridging a crack to remain essentially normal to the crack plane as the crack opens [Stang and Li 2005], but at a certain limit other mechanisms are introduced; the concrete will get a local spalling and the fibre bends. Spalling often follows snubbing because of the high concentrated load where the fibre is forced to bend [Dupont 2003], illustrated in Figure 2.14. Another observation with regard to inclined fibres is that the pull-out response becomes increasingly less influenced by matrix strength and increasingly more influenced by the mechanical properties of the fibre as the inclination to the concrete crack surface increases [Robins et al 2002]. This is due to the snubbing effect; the fibre attempts to straighten in line with the direction of loading, and so inclined pull-out is often associated with yielding of the fibres. Hence, the snubbing effect also leads to higher probability for fibre-rupture. The behaviour of synthetic fibres in pull-out is similar. The pull-out resistance increases with increasing angle due to snubbing, but unlike steel fibre, the additional force due to fibre bending is negligible for synthetic fibres as a result of their low bending stiffness. As for steel fibres, the probability for matrix spalling increases with increasing inclination, and so the strength of the cement matrix influences the pull-out resistance at high angles. Another observation from experiments carried out is that the scatter in the data increases at inclination angles. [Li Wang and Backer 2006]
- Spacing between fibres: When the fibres are very close to each other in a group it can happen that a part of the concrete breaks off, especially with hooked end fibres [Dupont 2003]. This reduces the efficiency of the fibres considerably. The risk of concrete pieces breaking off increases with increasing fibre content.
- Fibre pre-stressing: Shrinkage of the test specimens before loading leads to pre-stressing in the fibres. The pre-stressing magnitude is gradually relaxed and diminishes to zero when the fibre is fully de-bondend. It

decreases rapidly with increasing crack-width and becomes negligible beyond 100µm. [Stang and Li 2005]

- Cook-Gordon effect: When a crack propagates normally towards a fibre, de-bonding occurs between the fibre and matrix. This happens before the crack actually reaches the fibre since the maximum tensile stress is located at a distance ahead of the matrix crack. The so called Cook-Gordon effect creates an additional crack-opening that should be accounted for. [Stang and Li 2005]

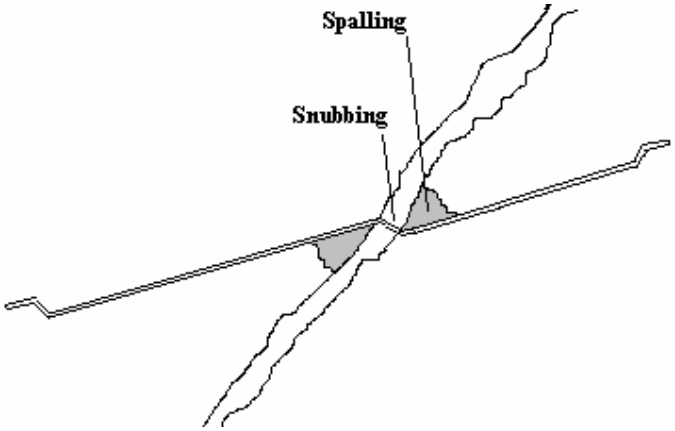

Figure 2.14: Spalling often follows snubbing because of high concentrated load where the fibre is forced to bend.

To be able to adopt a good fibre-matrix combination, it is important to be aware of all the above mentioned basic mechanisms of fibre pull-out. But for practical applications, it appears to be too time- and cost consuming to determine all of the parameters needed to calculate a comprehensive constitutive relation, like the approaches developed by Stang, Li & Shah (1990), [Balaguru & Shah 1992, Stang & Li 2001, Van Gysel 2000]. And even if these preliminary tests and calculations are carried out, the natural variations in the material may still result in an inaccurate estimate of the behaviour during failure in the actual structure. Since practical use of FRC is emphasized in this thesis, a more simple approach is presented in the next section.

Test method: Pull-out tests on single fibres [Thorenfeldt et al 2006]

The test method presented here is part of the Norwegian design rule draft for steel fibre reinforced concrete [Thorenfeldt et al. 2006]. Through this procedure, the anchorage capacity of single steel fibres in concrete is determined, dependent on the type of fibre, anchor-length and concrete strength. The load-deformation relation through pull-out is used to establish the characteristic maximal stress and expected average stress in the steel fibres after crack formation.

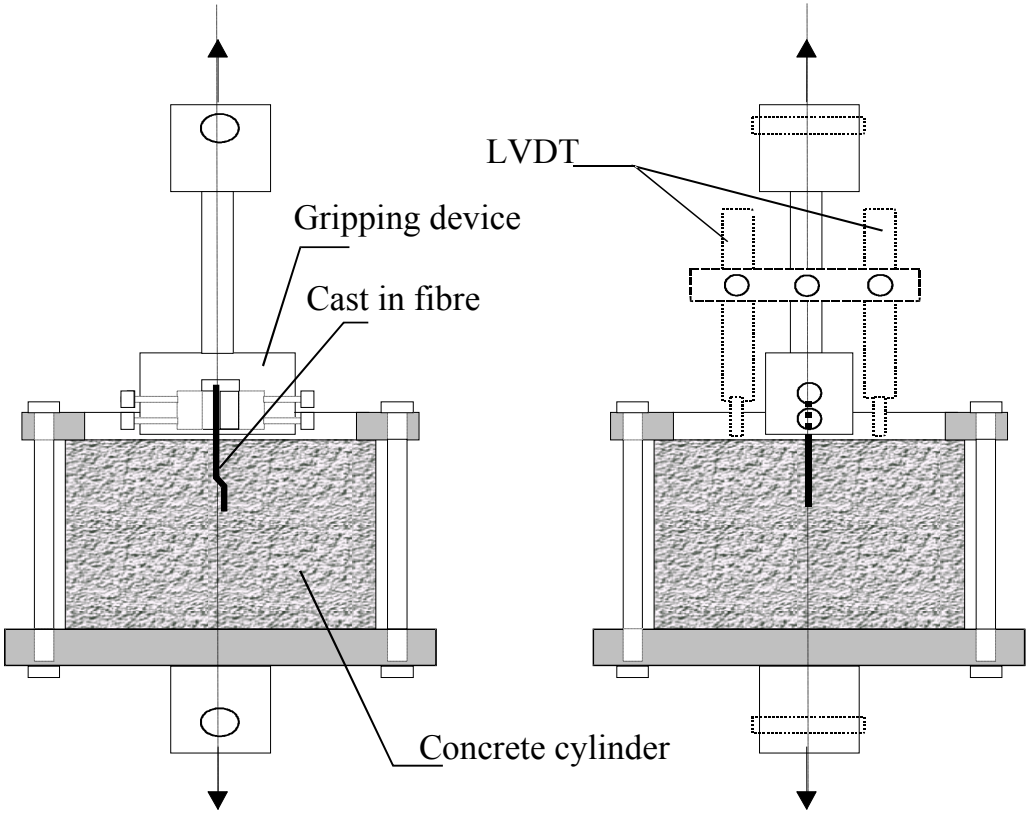

Figure 2.15: Test setup

Cylindrical concrete specimens (diameter = 100 mm and height = 60 mm) with one single fibre partly cast in perpendicular and centric to the concrete surface are placed in a test rig, as shown in figure Figure 2.15. A gripping device is fixed to the protruding fibre, and the fibre is pulled out of the concrete with a constant deformation of 0.2 mm/min up to a deformation of

3 mm. The load and deformation is logged every sixth second. The pull-out is defined as the summation of fibre slip and fibre elongation.

The reference cube compressive strength $f_{c,ref}$ for the concrete is calculated as the average of the measured strengths on minimum three cubes taken the same day as the pull-out tests. The corresponding tensile strength is calculated:

$f_{ct,ref} = 0{,}3\ (f_{c,ref})^{0,6}$ [NS 3473 (2003)]

The pull-out load versus displacement is plotted for each test, and the anchorage capacity is taken as the average load between pull-out displacements in the interval of 0.5-2.0mm (minimum three specimens):
F_{1m} : Average anchorage capacity for tests specimens with anchorage length $l_{b1} = l_f/2$.
F_{2m} : Average anchorage capacity for tests specimens with anchorage length $l_{b2} = l_f/6$.

The corresponding characteristic values (with index "k") are determined from:

$F_{1k} = F_{1m} - k_n s_{n1}$ $F_{2k} = F_{2m} - k_n s_{n2}$

where s_n is the standard deviation, and k_n is a factor depending on the number of tests [Table 2.2].

N	3	4	5	6	8	10	20	30	∞
k_n (s known)	1.89	1.83	1.80	1.77	1.74	1.72	1.68	1.67	1.64
k_n (s un-known)	3.37	2.63	2.33	2.18	2.00	1.92	1.76	1.73	1.64

Table 2.2: Standard deviation s_n and factor k_n.

The characteristic maximum tension in the fibre and corresponding average bonding strength:

$\sigma_{fk,max} = F_{1k}/A_f$

$f_{bfk} = F_{1k}/(\pi d_f l_{b1}) = 2F_{1k}/(\pi d_f l_f)$

where A_f is the cross-section area of the fibre, d_f is the fibre diameter and l_f the length of the fibre. For fibres with hooks or other anchoring, the bonding strength for the straight part of the fibre is calculated as:

$$f_{bfl} = (F_{1k} - F_{2k})/(\pi d_f (l_f/2 - l_{b2})) = (F_{1k} - F_{2k})/(\pi d_f l_f/3)$$

The anchorage capacity is $F_a = F_{1k} - 0{,}5 \cdot f_{bfl} \cdot \pi \cdot d_f \cdot l_f$, and the corresponding expected characteristic average stress for FRC in tension can be taken as:

$$\sigma_{fk,average} = (f_{tk} / f_{ct,ref})\ 0{,}5\ \sigma_{fk,max}$$

for straight fibres, and for fibres with hooks/anchoring:

$$\sigma_{fk,average} = (f_{tk} / f_{ct,ref}) \cdot (0{,}25\, f_{bfl} \pi d_f\, l_f + 0{,}7\, F_a)/A_f$$

where f_{tk} = characteristic tensile strength.

All embedment lengths are included in this expression, therefore $\sigma_{fk,max}$ has to be multiplied with a factor 0.5 (corresponding to an average embedment length of $l_f/4$). The anchorage capacity in the second term for the fibres with hooks is multiplied with a factor 0.7. This is done to account for the short embedment lengths where the hook is not fully straightened. The effect of increased capacity for fibres with inclination 15^o-40^o is not regarded, as it is assumed that the reduced capacity at higher inclination angle due to spalling neutralizes the former advantage.

In the end, the characteristic average stress can be used to determine the residual post cracking strength of the concrete: $f_{tk,res} = \eta \cdot v_f \cdot \sigma_{fk,average}$.

2.6 Orientation and distribution of fibres

2.6.1 Introduction

The post-crack tensile strength of fibre reinforced concrete is very much dependent on the distribution and orientation of fibres, which again is governed by the casting process, the concrete mix, the size and geometry of

the specimen and potential obstacles like reinforcement bars. In this section the factors affecting the orientation and distribution of fibres will be discussed, and a theoretical model for fibre orientation is described. Moreover, a method for estimating the fibre orientation based on fibre counting on sawn sections is introduced.

2.6.2 Factors influencing the orientation and distribution

The composition and workability of the concrete affects the orientation and distribution of fibres. The fibre orientation in self-compacting concrete (SCC) depends strongly on the flow of the concrete during casting, whereas the vibration is the main influence factor with vibrator compacted concrete (VCC). Since factors influencing the orientation are different for VCC and SCC, they are treated separately in this section.

VCC:

It is widely accepted that compaction by vibration of SFRC generally results in an anisotropic material [Kooiman 2000]. When the concrete is compacted on a vibration table, it is likely that a planar-random orientation occur perpendicular to the direction of the vibration [Kooiman 2000, Barrigan 2002]. Yet, if the specimen is only vibrated for a short time, vibration will not have a significant effect on the orientation [Dupont 2003]. Obviously the vibration time depends on the workability of the fresh concrete; if the workability is too high a short vibration time will result in poor compaction.

The use of to use immersion vibrator for compaction is not recommended since the fibres disperse where the vibrator is placed into the concrete. This can cause weakness zones where almost no fibres are present, or where the main orientation of fibres is pronounced differently from the average orientation in the element. However, immersion vibrator may often be the only possible compaction method for practical use in full scale structures.

Several studies have shown that the main orientation of fibres is perpendicular to the direction of casting [Bonzel and Schmidt 1986, Lin 1996, Barragan 2002, Rosenbusch 2003]. This is based on tests performed on cylinders drilled from beams [Bonzel and Schmidt 1986, Barragan 2002] and slabs [Lin 1996] taken parallel and perpendicular to the direction of casting. The compaction of concrete in these tests was done either by tamping or by shortly using a vibration table (15-40 sec), and the vibration was not considered to have any noticeable influence on the orientation.

SCC:

The SCC has to be very stable to avoid an uneven distribution of fibres. If the concrete tends to separate, a higher steel-fibre concentration in the lower part of the structure can be expected. For synthetic fibres, the opposite will occur.

Nemegeer (1999) found a pronounced orientation of long steel fibres in a direction parallel to the flow. In his study slices taken from hardened SCFRC from an L-box were analyzed. It has to be noted that general conclusions from these tests are undermined by the strong wall-effect during casting which might cause a deviating orientation. [Grünewald 2003]

Grünewald (2003) found the opposite; several cylinders were drilled from a series of tunnel segments to determine the orientation, and the results indicated that the main orientation of the fibres were perpendicular to the flow [Grünewald 2003]. However, it is likely that the funnel used during casing pre-orientated the fibres, which subsequently affected the orientation through the segment. Hence, no categorical conclusions can be drawn from the test series.

The flow of SCC is strongly dependent on casting procedure. For instance; a more uniform flow will occur along a beam if it is cast from one end of the formwork than when the concrete is poured from the middle of the beam. The same is observed for slabs. The flow direction through a wall is complex and hard to predict. In a study by Nyholm Thrane (2005), a series of SCC-walls were cast with tube fixed near one bottom corner of the wall.

Plexiglas formwork made it possible to observe the flow during casting, and colour was added to the concrete. The main flow direction is illustrated in Figure 2.16. The observations show that the flow is mainly vertical closest and furthest away from the casting point and mainly horizontal in the middle of the wall. Moreover, it was shown that a single fluid simulation of a Bingham fluid captured the observations of the flow patterns observed in the form filling experiments.

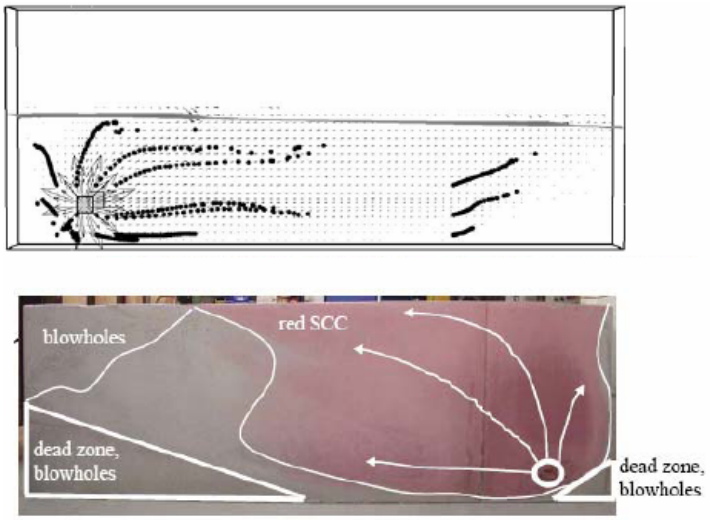

Figure 2.16: Flow during casting and the wall after demoulding, side of inlet [Thrane 2005]. During casting the new concrete removes the already placed concrete first longitudinally and then upwards further away from the casting point.

Uneven fibre distribution due to obstacles

Obstacles like reinforcement bars and cut-outs influence the orientation and distribution of fibres. It should be taken into consideration that the minimum distance between the bars is related to the fibre length and fibre volume, otherwise blocking may occur. This is especially important for structures with SCC, since the flow of the fibre concrete easily get hindered. Groth (2000) studied the passing ability of FRSCC and recommended the bar spacing to be at least three times the fibre length. In a study by Grünewald (2004) the CBI-approach 'risk of blocking' was extended for

the effect of the steel fibres. The content and the distribution of the aggregates, the type and the content of the steel fibres was considered to calculate the bar spacing for non-blocking. Grünewald defined the blocking factor:

$$BF = ROB_{(BS)} * v_f * BD$$

where $ROB_{(BS)}$ is the risk of blocking dependent on bar spacing, v_f is the fibre content (vol%) and BD is the blocking diameter $BD=0.553d_f^{-1.51}$ (d_f=fibre diameter).

By curve-fitting a series of experiments, a model for the blocking factor was defined:

$$BF = 0.607 * c/L_f - 0.857$$

where c is the clear spacing between the reinforcement bars [mm] and L_f is the fibre length [mm].

To calculate the bar spacing required for non-blocking, the blocking factor is determined from the mixture composition. To calculate the ROB, the actual bar spacing has to be estimated. A comparison between the estimated and calculated bar spacing is required to control the assumed bar spacing. [Grünewald 2004]

The fibre orientation in a structural member is also influenced by its boundaries since the fibres tend to orientate themselves parallel to the wall of the formwork. Especially for small specimens with long fibres, the wall-effect affects the orientation. Calculation models to estimate the wall-effect are developed, and will be presented in the next section.

2.6.3 Theoretical model for orientation

Various analytical and semi-empirical expressions for the combined effect of fibres on the mechanical properties of FRC can be found in literature. As a basis for modelling in this thesis, the influence of fibres after cracking is considered according to [Thorenfeldt 2003]. Compared to the

comprehensive work by Li et al. (1991), several simplifications related to the modelling of single fibres are made.

The most important factor in tension modelling is the force resultant in the fibres crossing a crack. However, the relative amount of fibres crossing a section, i.e. the section ratio, is also of interest because the theoretical value can be related to results from fibre counting and used to describe for instance systematic anisotropic fibre orientation. [Kanstad & Døssland 2004]

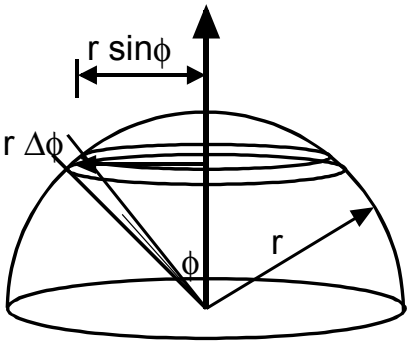

Figure 2.17: Determination of force resultant in the fibres crossing a crack. [Thorenfeldt 2003]

The horizontal plane in Figure 2.17 represents an area of the crack plane while the hemisphere represents the directions in which the fibres will be evenly distributed if isotropic conditions are assumed. The fibre fraction with the angle ($\phi \pm \Delta\phi/2$) is given as the relation between the area of the ring on the surface shown in Figure 2.17 and the area of the hemisphere $2\pi r^2$ [Thorenfeldt 2003]:

$$\rho_{f\,\Delta\phi} = (2\pi r \sin\phi \; r\Delta\phi)/2\pi r^2 = \sin\phi \; \Delta\phi \qquad (1)$$

The corresponding volume ratio for this fraction is:

$$v_{f\,\Delta\phi} = v_f \sin\phi \; \Delta\phi \qquad (2)$$

where v_f is the fibre volume. The section ratio ρ_x is defined as the area of fibres per unit concrete area. Integration of Equation (2) multiplied by $\cos\phi$ for all fibres with direction angle ϕ between 0 and $\pi/2$ gives the section ratio for all fibres crossing the crack plane:

$$\rho_x = v_f \int \sin\phi \cos\phi \, d\phi = v_f [(1/2) \sin^2\phi] = v_f /2 \qquad (3)$$

The result demonstrates that 50% of all the fibres present in a unit volume will cross a plane in any direction. If it is assumed that all the fibres are evenly distributed in a plane, the section ratio normal to this plane will be $0.637v_f$. Furthermore if the orientation is unidirectional the section ratio will be equal to v_f. [Thorenfeldt 2003, Kanstad & Døssland 2004]

Returning to the isotropic conditions, and assuming that the fibres behave in accordance with the theory of plasticity, the corresponding normal force resultant per unit concrete area can be determined as [Thorenfeldt 2003]:

$$f_{xp} = v_f \sigma_{average} \int \sin\phi \cos^2\phi \, d\phi = -v_f \sigma_{average}[\cos^3\phi/(2+1)] = v_f \sigma_{average}/3 \quad (4)$$

where $\sigma_{average}$ is the average stress in the fibres crossing the crack at relevant crack width. This stress is mainly determined by the adhesion of the fibres to the concrete, including anchorage capacity for fibres with end hooks, and it is limited by the tensile strength of the fibres.

As basis for this equation it is also assumed that the fibres keep their original direction after cracking. The normal force per unit concrete area will hereafter be called the residual stress of the concrete, $f_{t,res}$. For an arbitrary orientation, the normal force can be expressed as:

$$f_{t,res} = \eta \, v_f \, \sigma_{average}$$

where η is a capacity factor which indicates how much of the fibre forces that are effective normal to the crack plane. The capacity factor is $^1/_3$ for

isotropic orientation, ½ when the fibres are plane orientated and equal to 1 if all of the fibres are directed normal to the crack plane. Simplified the capacity factor η for a given fibre orientation can be taken as [Thorenfeldt et al. 2006]:

$\eta = 2/3\ \alpha$ when $0.3<\alpha<0.5$

$\eta = 4/3\ \alpha - 1/3$ when $0.5<\alpha<0.8$

In which the orientation factor is defined as $\alpha = \rho/v_f = n_f \cdot A_f/(v_f \cdot A_c)$ and n_f is the number of fibres. The upper and lower limit of 0.3 and 0.8 is set because an orientation that exceeds these limits is highly unlikely in practical applications.

Some advantages of the present model, compared to other approaches, is that it is linearly related to the fibre content, and that anisotropic fibre orientation relatively easily can be accounted for.

Estimating the fibre orientation in a specimen

According to the test method proposed in the preliminary Norwegian design method for FRC [Thorenfeldt et al. 2006] described in section 2.5.2 the orientation factor can be estimated by counting fibres on a sawn block taken near the cracked section of a beam exposed to 4-point bending. In this method, the volume of fibres may be determined by crushing the prism and extract and weigh the fibres. Another approach suggested here is to count the fibres on three sections perpendicular to each other to estimate the fibre volume. The latter approach is based on the theory of Thorenfeldt (2003). It is assumed that all orientations can be described as a combination between three ideal orientation situations as illustrated in Figure 2.18. If the orientation is isotropic, the section ratio of each direction is $\rho_1 = \rho_2 = \rho_3 = v_f/2$. If fibres are horizontally orientated in plane 1-2, the section ratio in the two directions will be $\rho_1 = \rho_2 = 2/\pi * v_v = 0.64\ v$ ($\rho_3 = 0$). If all fibres are uni-directed, the share of fibres in this direction would be $\rho_1 = v_v$ ($\rho_2 = \rho_3 = 0$). It is proposed that the share of fibres in each direction for a prism with an arbitrary fibre orientation can be described by combining the three ideal

orientation situations [Figure 2.18]. This gives the number of fibres in each plane as a function of ν, ω og β ($N_1>N_2>N_3$):

$$N_1 = \frac{A_c}{A_f} v_f \cdot (0,5 + 0,14\omega + 0,5\beta)$$

$$N_2 = \frac{A_c}{A_f} v_f \cdot (0,5 + 0,14\omega - 0,5\beta)$$

$$N_3 = \frac{A_c}{A_f} v_f \cdot 0,5(1 - \omega - \beta)$$

where β is the share of uni-directed fibres and ω the share of plane orientated fibres. Combining these equations leads to an expression for the fibre volume:

$$v_f = \left(N_1 + \frac{9}{16} N_2 + \frac{7}{16} N_3 \right) \frac{A_f}{A_c}$$

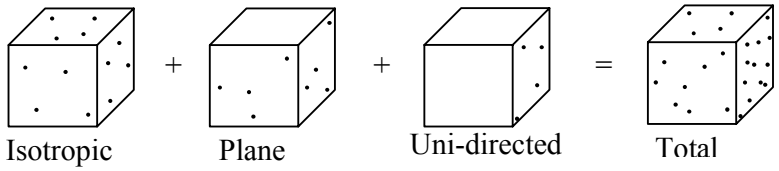

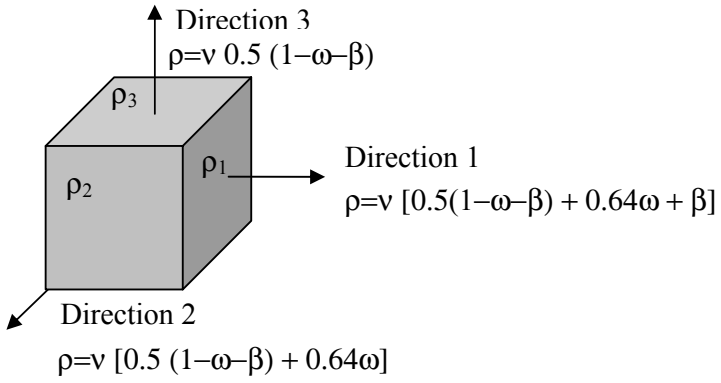

Figure 2.18: Share of fibres in each direction ρ, under the assumption that every orientation situation can be described by a combination of uni-directed fibres (β), plane orientated (ω) and isotropic orientated fibres (1−ω−β). The number of fibres in the three directions $N_1>N_2>N_3$.

Hence, the fibre volume can always be estimated by counting fibres on three cross-sections perpendicular to each other. This method requires less work then the previous mentioned, where the concrete is crushed and the fibres are extracted in order measure the fibre volume in the specimen. Another advantage is that the orientation in all three directions can be estimates. On the other hand it is more uncertain, since it is based on an idealized even distribution of fibres in the prism.

Bounderies – wall effect

Fibres tend to orientate parallel to the boundaries, inducing an orientation which is increasingly two-dimensional with decreasing thickness of the element. To account for this, Rosenbush (1996) made use of the following function proposed by Lin (1996):

$$\alpha=0.382e^{-0.0033h}+0.37$$

where h is the thickness of the structural element.

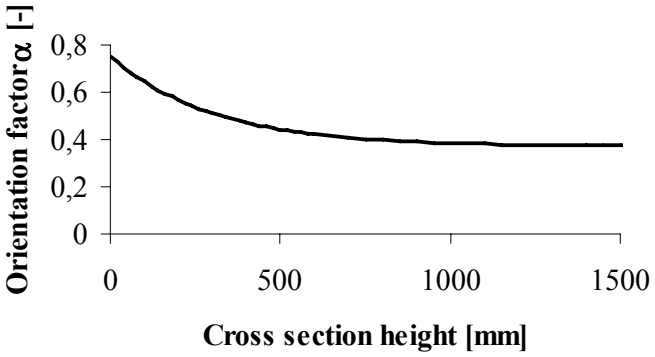

Figure 2.19: Effect of boundaries - Fibre orientation factor as a function of cross-section height according to Lin (1996) [Rosenbusch 2003].

Dupont (2003) divided the cross-section of a beam into three different zones as illustrated in Figure 2.20. In the middle of the cross section (1), the fibres are assumed to rotate freely in all directions, which results in an isotropic orientation and an orientation factor $\alpha_1=0.5$. Secondly one boundary condition is considered (2), where the orientation factor is

determined as α_2=0.6. Finally, a second boundary is added perpendicular to the first boundary for the corners (3), resulting in an orientation factor α_3=0.84. Combining the orientation factors for the three zones results in the following expression for the overall orientation:

$$\alpha = \frac{\alpha_1 \cdot (b - l_f)(h - l_f) + \alpha_2 \cdot [(b - l_f)l_f + (h - l_f)l_f] + \alpha_3 \cdot l_f^2}{b \cdot h}$$

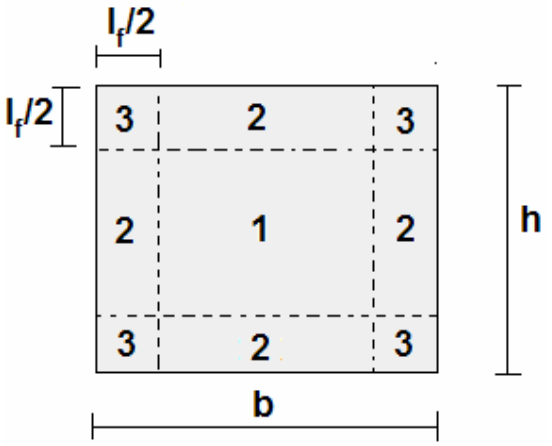

Figure 2.20: Wall effect according to Dupont (2003). l_f is the fibre length.

3 Structural analysis

3.1 Introduction

A number of different analysis approaches are available for structural analysis of fibre reinforced concrete. The approaches are either analytical, primarily developed for cross-sectional analysis, or based on the finite element method. The latter can be used both for cross-sectional and structural analysis and several different methods and constitutive models are available. [Löfgren 2005] This chapter gives an overview over different design methods which are available for calculating the response of FRC structures, focusing on the flexural and shear loading.

3.2 Tensile response: σ–ε and σ–w relations

Basically there are two non-linear approaches of describing the behaviour of SFRC under tension: the stress-strain relation (σ–ε) and the stress-crack opening relation (σ–w). [Schnütgen and Vandewalle 2003]

3.2.1 σ-w relation

A crack can be modelled using the fictitious crack model which originally was developed by Hillerborg (1980) for cracking in plain concrete, with the objective to use the model in combination with finite element modelling (FEM). In the fictitious crack model, a crack propagating in concrete is modelled by a zone of diffuse micro-cracking, called the process zone, and a localized crack. For plain concrete, the tension drops to zero when the aggregate interlock ends. For fibre reinforced concrete, the fibres crossing the crack will resist further crack opening and impose crack bridging effect on the

crack surface. The fictitious crack model for fibre reinforced concrete is illustrated in Figure 3.1. The stresses carried by fibres across a tensile crack are described as a function of the crack opening, where the tensile stress at the top of the crack is assumed to be equal to the concrete tensile strength. To determine the σ-w relation, material testing based on fracture mechanics has to be performed.

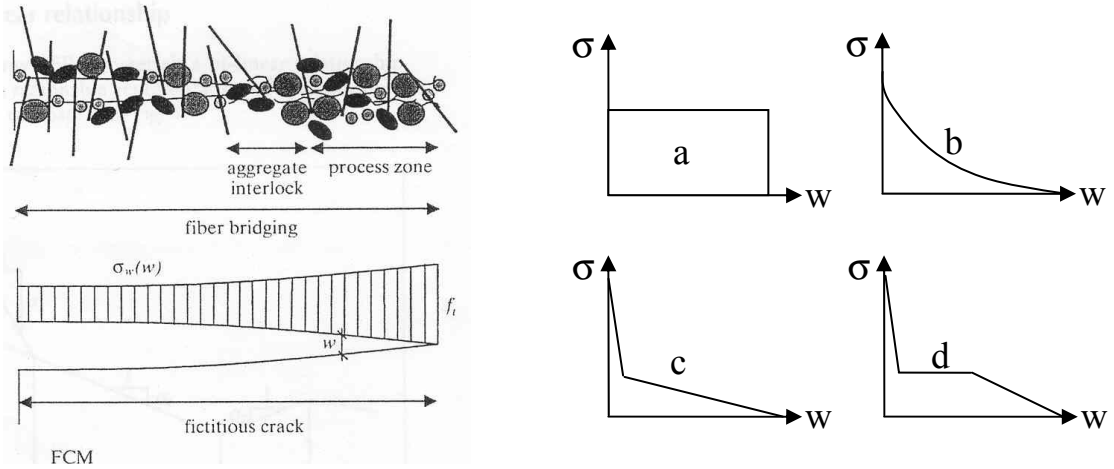

Figure 3.1: A crack in steel fibre reinforced concrete [Vanderwalle 2002] and examples of simplified σ-w relations: a) Drop-constant b) Three degrees of freedom with shape parameter c) Bi-linear d) Multi-linear.

Several models for determining the σ-w relation exists. Based on micro-mechanical modelling, Li et al. (1993) developed a semi-analytical modelling procedure. They derived an equation for the stress-crack width relation by analysing the fracture processes in FRCC under uni-axial tension. Although the model provides a basic understanding of the influence of the micro-mechanical parameters on the shape of the stress-crack width curve, it is relatively comprehensive. In addition, some input parameters are difficult to determine. A simplified approach can be achieved by inverse modelling. In an inverse modelling procedure, an idealised strain softening σ-w diagram is assumed, and the deviation between the computational and experimental

results is calculated. The softening diagram is then modified until the deviation is within an acceptable limit. [Kooiman 2000]. Examples of idealised σ-w relations are shown in Figure 3.1.

3.2.2 σ–ε relation

Different methods are available for determining simplified stress-strain diagrams based on bending tests on prisms. Three approaches are presented here developed by Bekaert [Nemegeer 1997], RILEM [RILEM TC 162-TDF 2003] and a Norwegian design rule draft [Thorenfeldt et. al 2006].

σ–ε by Bekaert [Nemegeer 1997]

In the design rules proposed by Bekaert the residual strength is determined on the basis of standardized beam tests. The equivalent bending strength is calculated from the load-displacement response of a beam of dimension b x h x L= 150 x 150 x 450 mm exposed to three point bending.

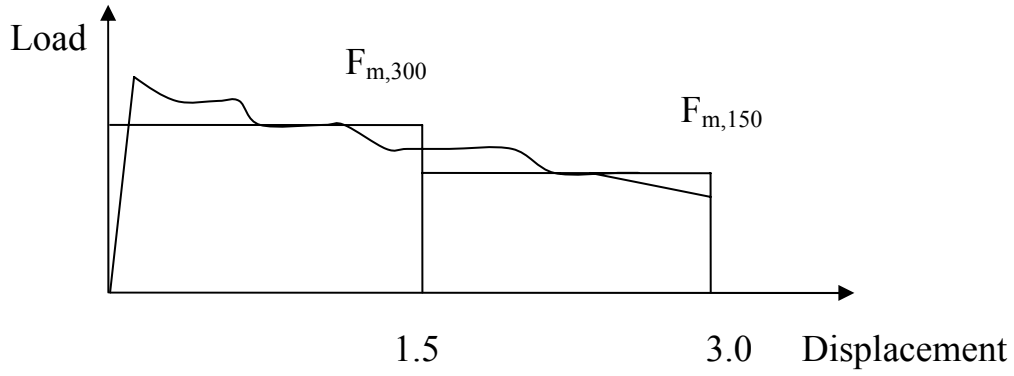

Figure 3.2: Load-deformation relation; determination of the equivalent bending strength $f_{fct,eq}$

The equivalent bending strength can be decided from the load-displacement response as illustrated in Figure 3.2, where:

$$f_{fct,eq,300} = \frac{M_{m,300}}{W_{plastisk}} = \frac{\frac{F_{m,300} \cdot l}{4}}{\frac{1}{4} bh^2} = \frac{F_{m,300} \cdot l}{bh^2} \quad \text{and} \quad f_{fct,eq,150} = \frac{F_{m,150} \cdot l}{bh^2}$$

From the equivalent bending strength the residual strength is taken as $f_{res}=0,37f_{fct,eq}$. In the stress-strain diagram, the residual strength decreases linearly from $f_{res}=0,37f_{fct,eq,300}$ to $f_{res}=0,37f_{fct,eq,150}$.

When it is not practical to perform this test, the residual strength can conservatively be taken as $f_{res}= 0,37f_{fct,eq,150}$, where $f_{fct,eq,150}$ is taken as:

$$f_{fctm,eq,150} = \frac{R_{em,150} \cdot f_{ctm,fl}}{100} \quad \text{where } R_{em} = \frac{180 W_f \lambda_f d_f^{1/3}}{180C + W_f \lambda_f d_f^{1/3}} \quad , \; f_{ctm,fl} = \frac{0,3 f_{ck}^{2/3}}{0,6}$$

and the characteristic equivalent bending strength $f_{fctk,eq,150} = 0.7\ f_{ctm,eq}$. Here W_f is the fibre content [kg/m^3], λ_f is the ratio between fibre length and diameter ratio l_f/d_f and C=20 for Dramix fibres with end hookes.

These formulas are based on experiments with maximum cube strength of f_{ck}=40N/mm^2. For higher concrete strengths additional test are recommended.

RILEM TC 162-TDF (2003)

The design parameters in the σ–ε relation are determined by means of displacement controlled bending tests on notched prisms, as described in section 2.5.2.

The stress-strain diagram adopted by RILEM is illustrated in Figure 3.3, where the stresses σ_2 and σ_3 are defined in terms of the residual flexural tensile stresses f_1 and f_3, which corresponds to crack mouth opening displacement (CMOD) of 0.5 and 3.5 mm in the RILEM TC 162 beam tests.

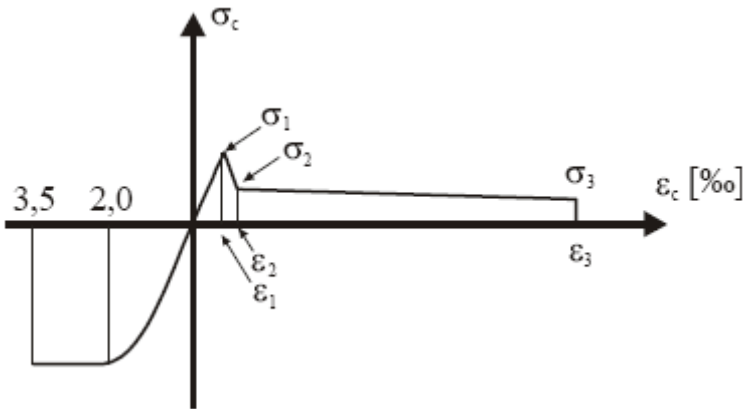

Figure 3.3: Stress-strain diagram in the σ–ε design method by RILEM [Vandewalle 2003].

Norwegian design rule draft [Thorenfeldt et. al 2006]

The residual strength is determined from the tension resultant per unit area for fibres crossing a crack going through the concrete with deflections in the range of 0.5 to 2.5 mm. It is taken as a constant value over a completely cracked section. The method is solely based on the fibre contribution, and the residual strength, $f_{residual}$, can be expressed as a function of the fibre content:

$$f_{residual} = \eta_0 \times v_f \times \sigma_{f,average}$$

where v_f is the fibre content [volume percent] and $\sigma_{f,\ average}$ is the average stress in all steel fibres with a random orientation. $\sigma_{f,\ average}$ primarily dependent on fibre properties and concrete quality and can be determined from pull-out tests or inverse analysis. η_0 is a direction orientation factor which indicates how much of the fibre forces that acts in one direction. Theoretically, the direction orientation factor is 1/3 when the fibres are isotropic orientated, ½ for plane orientated fibres and 1 when all of the fibres are uni-directed.

The residual strength can also be determined from 4point bending tests as $f_{residual}=0.37f_{teq}$, where $f_{t,eq}$ is the average equivalent bending strength recorded between 0.5 and 2.5 mm deflection as described in section 2.5.2.

3.3 Analytical approaches – design for flexure

Various methods have been proposed for calculating the moment of resistance for FRC sections. The available analytical models for cross-sectional analysis are based on different assumptions regarding cinematic and constitutive conditions [Löfgren 2005].

In the simplified calculations given in the Norwegian Design rule draft [Thorenfeldt et. al 2006] the moment of resistance of a beam with rectangular cross-section is taken as $M=0.4 \cdot f_{residual} \cdot b \cdot h^2 \cdot p_e$ where b is the width and h the depth of the beam. p_e is a size factor $p_e=1.1-0.7h>0.75$, where h is given in metres. These calculations are based on the assumption that a constant residual strength (given in the previous section) acts over 80% of the cross-section height.

3.3.1 Multi-layer force equilibrium

The equilibrium based multi layer beam model used by Hordijk (1991) is well suited to reproduce the experimental results of bending tests. Kooiman (2000) showed that the model can be used for modelling the flexural response of fibre reinforced concrete beams, and Grünewald (2004) applied the model for self compacting concrete. Further, Lappa (2007) found that the model, with some modifications, was also applicable for high-strength concrete with strain hardening in tension.

In the model, the cross section is divided in a defined number of layers connected by springs, and a linear distribution of displacement across the height is assumed. The response of the beam is then the sum of the behaviour of all springs. Based on a flow chart for SFRC, the average stress of each layer can be calculated for any iteration step (i.e. a given strain) until equilibrium is

achieved by solving the equations for the normal force and the bending moment:

$$N = \sum_{i=1}^{n} \sigma_i \cdot h_i \cdot t = 0$$

$$M = \sum_{i=1}^{n} y_i \cdot \sigma_i \cdot h_i \cdot t$$

where t is the width of the beam and y_i, h_i and σ_i is illustrated in Figure 3.4. A spreadsheet solver might be applied to determine the equilibrium for each iteration step.

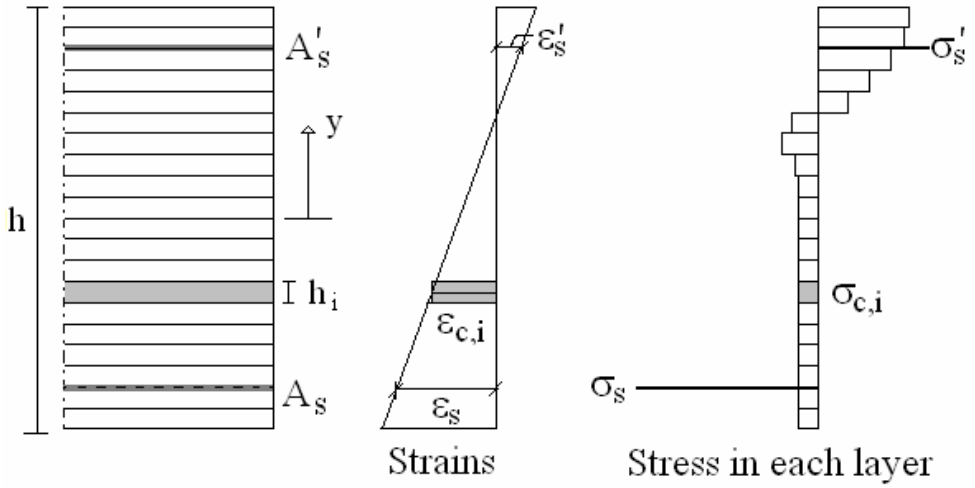

Figure 3.4: Multi layer model.

3.3.2 Non-linear hinge model: σ-w method

The σ-w method based on a non-linear hinge model [Rilem 2002] is a simplified method for modelling the hinge rotation at a crack in FRC. The non-linear hinge model is based on non-linear fracture mechanics, and a stress-crack opening approach is used to describe the tensile behaviour of the concrete. Structural calculations of beams and pipes can be done by introducing a non-linear hinge in the structure to describe a cracked section, and the non-linear response is assumed to be concentrated within the cracked

hinge. Hence, the moment capacity of the hinge is related to the hinge rotation, which again is related to the crack width [Clarke et al. 2007]. The procedure can shortly be described as follows: By prescribing the angular deformation on the non-linear hinge, the non-linear hinge solution can be used to solve the generalized stresses. The linear elastic solution for the structure is then established given the generalized stresses at the non-linear hinge and finally the structural response can be found by solving for the applied load and the total deformations [Rilem 2002]. It is important to note that the length of the hinge has to be assumed. However, it has been shown that the length of the hinge is approximately half the depth of the beam [Ulfkjær et al 1995].

To apply the non-linear hinge model in a structural analysis, the deflections are described in three terms; the elastic deflection of the beam without a crack/notch, the elastic deflection due to the presence of a crack/notch (if such exists) and the deflection due to the crack band. [Löfgren 2005].

When the crack surfaces remain plane, the overall angular deformation of the hinge is equal to the crack opening angle. According to Löfgren (2005) the sectional forces can be written as:

$$\frac{N}{b} = \int_0^{h-a} \sigma_c(\varepsilon, y)dy + \int_0^{h-a} \sigma_f(w, y)dy + \sigma_s \cdot A_s$$

$$\frac{M}{b} = \int_0^{h-a} \sigma_s(\varepsilon, y) \cdot \left(y - \frac{h}{2} \right) dy + \int_0^{h-a} \sigma_f(w, y) \cdot \left(y - \frac{h}{2} \right) dy + \sigma_s \cdot A_s \cdot \left(d_1 - \frac{h}{2} \right)$$

where the different parameters are illustrated in Figure 3.5.

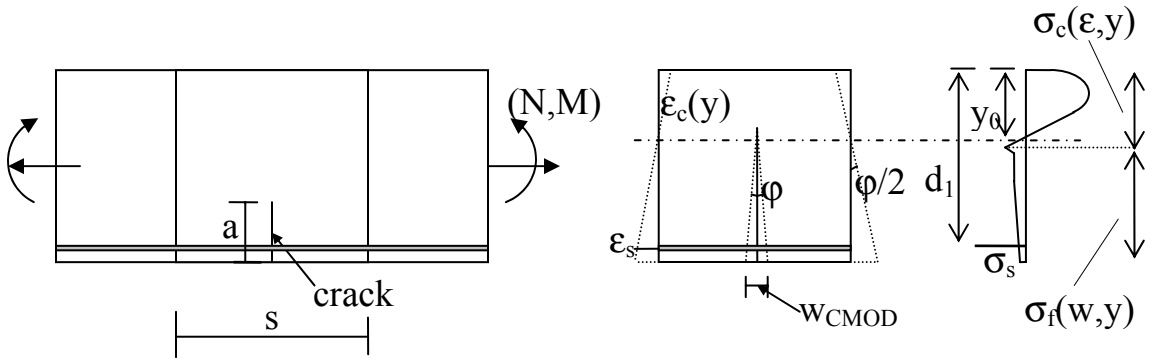

Figure 3.5: Non-linear hinge, or "crack-band" concept for a beam with reinforcement [Löfgren 2005] and [Rilem 2002].

Further information and details about the non-linear hinge model can be found in Rilem (2002), Olesen (2001), Casanova and Rossi (1997), Pedersen 1996) and (Löfgren 2005).

3.3.3 Yield line design

Yield line theory is widely used for the design of FRC ground bearing slabs and is commonly used to design pile supported ground floor slabs made from FRC. The method is relatively simple to apply and is suitable for calculating collapse loads in flexure. [Clarke et al. 2007].

Yield line theory is an ultimate load analysis that establishes either the moments in a structural element at the point of failure or the load at which an element will fail. The theory is based on the principle that the work done in rotating yield lines equals the work done in loads moving. According to Kennedy and Goodchild (2004) a yield line is defined as crack in a reinforced concrete slab across which the reinforcing bars have yielded and along which plastic rotation occurs.

Although yield line theory results in a quick and versatile design tool which generates economic concrete slabs, it also has some limitations. Firstly, no information is given on support reactions or deflections. Secondly, the method is only valid if the slabs have adequate ductility for the assumed yield lines to develop. Since yield line design concerns itself with the ultimate limit state, it does not purport to deal with serviceability issues such as deflection. Hence, it is difficult to verify that the ductility is sufficient. Another limitation is that yield line design demands familiarity with failure patterns, i.e. knowledge of how slabs might fail [Kennedy and Goodchild 2004]. There is however considerably experimental evidence to support the use of yield line analysis in the design of SFRC [Clarke et al. 2007].

There is no generally accepted way of calculating the plastic moment of resistance to be used in yield line analysis for FRC. In a semi-empirical design method for circular FRC slab tests Destree (2004) assumes that the plastic moment M_L is associated with a rectangular compressive stress block in compression over 10% of the cross section height and a constant tensile stress f_{tu} over the remaining 90% of the cross section height. f_{tu} is then given by: $f_{tu}=M_L/0.45h^2$. The method was developed based on the fact that beams made of strain softening SFRC do not, as opposed to slabs, develop multiple cracking and hence should be considered inappropriate for determining the structural response. However, the number of yield lines and the size of the loaded area are not considered by Destree (2002). These factors are taken into account in the circular slab test method used by Marti et al. (1999), which derived the following equation for the moment per unite length along the yield lines:

$$M_L=F\cdot[b\cos(\pi/n)-1]/[2n(b+2c)\sin(\pi/n)]$$

where F is the load, a, b and c are the dimensions defined in Figure 3.6 and n is the number of cracks.

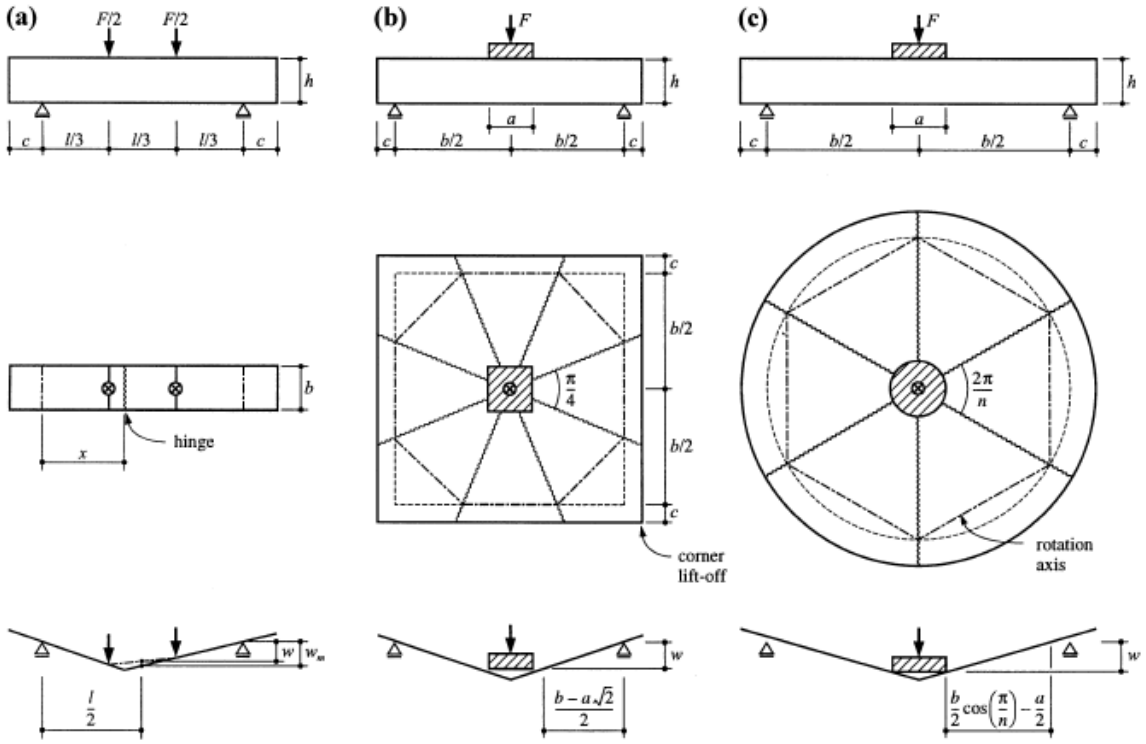

Figure 3.6: Test principles and failure mechanisms: a) modulus of rapture test, b) square slab test and c) circular slab test according to Marti et. al 1999.

In plastic analysis in general, it is important to note that when fibres are used in a combination with conventional reinforcement the moment of resistance provided by the fibres reduces with increasing reinforcement ratio due to the increase in depth to the neutral axis. [Clarke et al. 2007]

3.4 Shear capacity

Various models are available for calculating the strength of fibre reinforced concrete beams in shear. Yen Lei Voo and Stephen J. Foster (2006) did an extensive study on shear strength of steel fibre reinforced concrete. In their work, they compared the results of various models available for calculating

the strength of fibre reinforced concrete beams in shear without stirrups. The strengths calculated from the models were compared with data from 220 prestressed and non-prestressed beams reported in the published literature from 27 researchers. In these experiments, the cylinder compressive strengths varied from 20MPa to 170MPa, the shear span to effective depth ratios were in the range of 0.46 to 5.2, the total depths of 100mm to 800mm, the volume of steel fibres of 0.2 to 3.0% and the longitudinal steel ratio from 0.8 to 9.6%. When compared with the test results, a large scatter was observed for most of the models, e.g the models proposed by Narayanan & Darwish (1987) and Al-Ta'an & Al-Feel (1989) resulting in covariances of 46 % and 41 % respectively [Table 3.1]. In addition, most models did not induce a safe design as the ratios between theoretical and measured values were larger than one for a large share of the data pool. The models for shear capacity proposed by Nemegeer (1996) and Khuntia et al. (1999) performed satisfactorily. Moreover, Voo & Foster (2006) introduced a plastic shear model that reduced the covariance to 20.9% when compared to the results from the beam experiments.

It is, however, complicated to make a complete comparison between all models proposed in literature due to the variety of data required for each model. The input parameters in some models are e.g. based on information about the equivalent strength related to the crack tip opening displacement, which rarely are available for published experiments [Voo & Foster 2006]. Another example is the model by Li et al. (1992) which is based on standardized tests on beam and cylinder specimens in order to determine the flexural and splitting strength. Due to lack of data, these models are not included in the study done by Voo and Foster (2006). Moreover, some models are developed based on semi-empirical design equations where the test programs place emphasis on certain parameters like prestress or shear-span. Obviously, a good curve fitting for a given test program does not ensure correspondingly accuracy when the model is compared with a data pool where

other parameters are treated. This may be one main reason for the large scatter found by Voo and Foster (2006).

The models referred to above are presented in Table 3.1. The fibres are either considered by an additive method, i.e the shear supplement due to the fibres are added to conventional equations for plain reinforced concrete [Nemegeer 1996, RILEM 2003] or interaction is considered [Narayanan & Darwish 1987, Li et al. 1992]. The latter two models were not included in the study by Voo and Foster (2006).

Design equations for shear strength [MPa]	Authors
$\tau_u = e(0.24 f_{sp} + 80\rho d/a) + 0.41\tau \cdot F$; where $F = (l_f/d_f) v_f \beta$ and $\tau = 4.15$MPa $e = 1$ for $a/d > 2.8$; else $e = 2.8d/a$ $\beta = 0.5$, 0.75 or 1.0 for plain, crimped or hooked fibres respectively. $f_{sp} = f_{cu}/(20 - F^{0.5}) + 0.7 + F^{0.5}$	Narayanan & Darwish 1987
$\tau_u = [(1.6 f_c^{0.5} + 960\rho \cdot e \cdot d/a) + 8.5 K v_f (l_f/d_f)]/9$; where $e = 1$ for $a/d > 2.5$; else $e = 2.5d/a$ $K = 1.0$, 1.3 or 1.2 for plain, crimped or hooked fibres respectively.	Al-Ta'an & Al-Feel 1989
$\tau_u = (0.167\alpha + 0.25 F_1) f_c^{0.5}$; where $\alpha = 1$ for $a/d \geq 2.5$; else $\alpha = 2.5d/a \leq 3$ for $a/d < 2.5$; $F_1 = \beta \cdot v_f \cdot (l_f/d_f)$ $\beta = 0.67$ for plain concrete, $\beta = 1.0$ for hooked/ crimped fibre (normal concrete) or $\beta = 0.75$ for hooked/crimped fibre (lightweight concrete)	Khuntia et al. 1999
$\tau_u = \tau_{cd} + \tau_f$; where $\tau_{cd} = [0.12k(100\rho \cdot f_{ck})^{1/3} + 0.15\sigma_{cp}]$;	Nemegeer 1996 (Dramix Design Method)

$\rho=A_s/b_w d\leq 2\%$; $k=1+\sqrt{(200/d)}$ $\sigma_{cp}=P_e/A_c$ where P_e=longitudinal force $\tau_f=k_f\tau_{fd}=k_f \cdot 0.54 f_{ctk,ax}(R_t/1.5)$; $f_{ctk,ax}=0.21 f_{ck}^{2/3}$; $R_t=1.1W_f\lambda_f/(360+W_f\lambda_f)$; $k_f=1+n(h_f/b_w)(h_f/d)$ for $k_f\leq 1.5$; $n=(b_f-b_w)/h_f\leq 3$ or $n\geq 3b_w/h_f$	
$\tau_u=\tau_{cd}+\tau_f$; where τ_{cd} as for Nemegeer (1996) $\tau_f=0.7k\cdot k_1+\tau_{df}$; where τ_{df};$=0.12 f_{Rk,4}$ and $f_{Rk,4}$ is determined from standardized beam tests. k_f includes contribution of flanges in T-sections.	RILEM 2003
$\tau_u=1.25+4.68[(f_{cf}\cdot f_{sp})^{3/4}(\rho d/a)d^{-1/3}]$ for $a/d\geq 2.5$ $\tau_u=9.16[f_{cf}^{2/3}\rho^{1/3} d/a]$ for $a/d<2.5$ f_{cf} = flexural strength, f_{sp}=splitting strength	Li et al. 1992

Table 3.1: Shear strength models for FRC beams without stirrups. Here d=effective depth, a=shear span, v_f is the volume fraction of fibres, W_f is the fibre content [kg/m^3], λ_f is the fibre length to diameter ratio l_f/d_f, b_w=minimum width of section, A_s=tensile reinforcement, f_{ck} the compression strength.

In Norwegian Standard Code NS3473 the shear contribution from stirrups is given as:

$$V_{sd}=\frac{f_{sd}\cdot A_{sv}}{s}\cdot z\cdot(\cot\theta+\cot\alpha)\cdot\sin\alpha$$

for an arbitrary crack angle θ as illustrated in Figure 3.7. z can be taken as 0.9d, where d is the effective depth of the cross section.

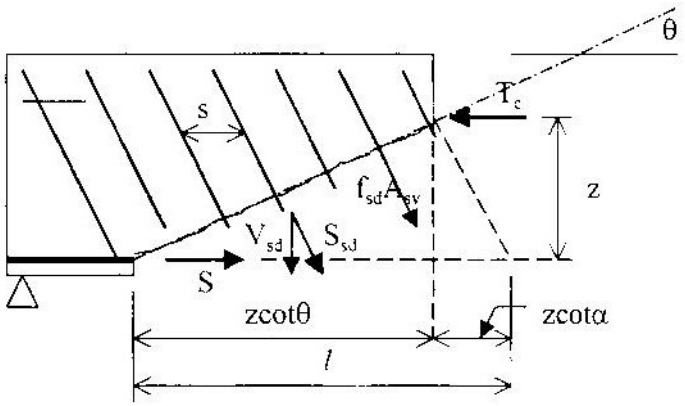

Figure 3.7: Beam with stirrups.

If the fibres are isotropic orientated the force component normal to any section will be $1/3\nu_f\sigma_{average}$ due to fibres [Thorenfeldt 2003]. By replacing the reinforcement bars in V_{sd} with steel fibres, the analogous expression will become:

$$V_f = \frac{1}{3}\nu_f \cdot \sigma_{average} \cdot b \cdot \frac{z}{\sin\theta} \cdot \sin(\frac{\pi}{2} - \theta) = \frac{1}{3}\nu_f \cdot \sigma_{average} \cdot b \cdot z \cdot \cot\theta$$

provided that the fibres are continuously and isotropic orientated. It is here chosen a section parallel to the crack, which gives $\alpha=\pi/2-\theta$. It is also assumed that all fibres have a stress $\sigma_{average}$, which equals the average stress in all fibres at failure. With a cracking angle of 45^o and assuming z=0.9d, the shear resistance due to fibres can be written:

$$\tau_f = 0.9 \cdot 1/3 \cdot v_f \cdot \sigma_{average}.$$

3.5 Finite Element Method

3.5.1 Finite element modelling

The Finite Element Method (FEM) accounts for the redistribution of stresses that takes place in reinforced concrete structures upon cracking. The accuracy of the results is dependent of the choice of mesh, the type of element, the

constitutive modelling and the numerical iteration techniques [Noghabai 2000]. Two main approaches exist for modelling cracking in concrete, namely discrete and smeared crack models. In the discrete approach, cracking is assumed to occur as soon as the nodal force in an element exceeds the tensile strength for the concrete. A geometrical discontinuity develops between the node and a newly created node. For the smeared crack model the cracking process is lumped into the integration points within the elements. The stress-strain relation is modified to account for the stiffness and strength degradation that accompanies cracking and the original mesh is kept through the cracking process [de Borst 1999].

3.5.2 Discrete crack approach

For discrete crack modelling, interface elements are used as predefined cracks. These elements have a dual set of nodes, which have the same coordinates in the initial state, and the traction is expressed as a function of the displacements between the nodes. The design principle for the discrete approach is based on the fictitious crack model, which is modelled by a stress-crack opening relationship $\sigma_w(w)$ as described in 3.2.1.

The discrete model is attractive physically, as it reflects the localized nature of cracking. The advantage with the discrete approach is to get a simple representation of tension softening. The behaviour of the discontinuity is not connected to the concrete, and due to this the main material is assumed to behave in a linear elastic fashion, while the discontinuity captures the non-linear effects.

The main disadvantage is that the solution depends on a correct estimate of the crack propagation path. It can be very difficult, or even impossible, to predict where the cracks will occur. In addition, the cracks have to follow the element

boundaries; thereby the modelling requires an introduction of additional nodal points, or a rearrangement of the original mesh [Dahlblom and Ottesen 1990].

3.5.3 Smeared crack approach

In the smeared crack model, the cracked solid is imagined to be a continuum where the notions of stress and strain remain valid. An orthotropic stress-strain relation can describe the behaviour of cracked concrete after cracking. The topology of the original mesh remains preserved, and this is a major computational advantage [de Borst 1999].

Fixed crack model

Two models for the smeared crack concept have been developed, namely the fixed and the rotating crack model. In the first model, the normal to the crack is fixed after initiation of the crack. Before cracking it is reasonable to model the concrete as an isotropic linear elastic material. For plain stress, the stress-strain relation can be expressed as

$$\boldsymbol{\sigma} = \begin{bmatrix} \sigma_x \\ \sigma_y \\ \tau_{xy} \end{bmatrix} = \frac{E}{1-\upsilon^2} \begin{bmatrix} 1 & \upsilon & 0 \\ \upsilon & 1 & 0 \\ 0 & 0 & \frac{1-\upsilon^2}{2} \end{bmatrix} \begin{bmatrix} \varepsilon_x \\ \varepsilon_y \\ \gamma_{xy} \end{bmatrix} = \mathbf{C}\boldsymbol{\varepsilon}$$

and the same relation is valid in the principal system (1-2 system):

$$\boldsymbol{\sigma} = \begin{bmatrix} \sigma_1 \\ \sigma_2 \\ \tau_{12} \end{bmatrix} = \frac{E}{1-\upsilon^2} \begin{bmatrix} 1 & \upsilon & 0 \\ \upsilon & 1 & 0 \\ 0 & 0 & \frac{1-\upsilon^2}{2} \end{bmatrix} \begin{bmatrix} \varepsilon_1 \\ \varepsilon_2 \\ \gamma_{12} \end{bmatrix} = \mathbf{C}\boldsymbol{\varepsilon}$$

After cracking, an orthotropic law replaces this model, i.e. the stress-strain relation is only valid in the principal system. For uni-axial stress, the stress-strain relation can be expressed as

$$\boldsymbol{\sigma}_e = \begin{bmatrix} \sigma_1 \\ \sigma_2 \\ \tau_{12} \end{bmatrix} = \begin{bmatrix} 0 & 0 & 0 \\ 0 & E & 0 \\ 0 & 0 & 0 \end{bmatrix} \begin{bmatrix} \varepsilon_1 \\ \varepsilon_2 \\ \gamma_{12} \end{bmatrix} = \mathbf{C}_e \boldsymbol{\varepsilon}_e$$

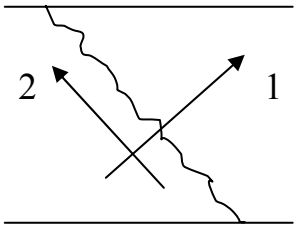

Figure 3.8: Defined local principal directions at cracking.

If the crack width is small, there will be some shear resistance in the crack. This resistance can be accounted for by assuming a reduced shear modulus βG, with β as the shear retention factor; $0<\beta<1$. In addition, numerical problems in the simulations are avoided, or at least reduced, with the introduction of β. In the same manner, a normal reduction factor μ is introduced to avoid a sudden drop of stress from f_{ct} to zero upon crack formation; a problem that arises because the stiffness normal to the crack is set equal to zero [de Borst 1999]. The principle expression can now be written:

$$\boldsymbol{\sigma}_e = \begin{bmatrix} \sigma_1 \\ \sigma_2 \\ \tau_{12} \end{bmatrix} = \begin{bmatrix} \mu E & 0 & 0 \\ 0 & E & 0 \\ 0 & 0 & \beta G \end{bmatrix} \begin{bmatrix} \varepsilon_1 \\ \varepsilon_2 \\ \gamma_{12} \end{bmatrix} = \mathbf{C}_e \boldsymbol{\varepsilon}_e$$

After cracking, this relation $\boldsymbol{\sigma}_e = \mathbf{C}_e \boldsymbol{\varepsilon}_e$ is only valid in the local 1-2 system. The stiffness relation can now be transformed to the global x-y system using a transformation matrix $\mathbf{T}(\theta_0)$, where θ is the angle between local and global coordinate system. This angle is constant for the fixed crack model ($\theta = \theta_0$).

$$\boldsymbol{\sigma}_{xy} = \mathbf{T}(\theta_0)^T \mathbf{C}_e \mathbf{T}(\theta_0) \boldsymbol{\varepsilon}_{xy}$$

The main disadvantage when using the fixed crack model is that cracks can occur in other directions than normal to the crack, due to the shear stresses that develops in the fixed crack plane. Another problem is the introduction of the shear retention factor, which has to be specified by the user.

Rotating crack model:

In the rotating crack model, the angle in $\boldsymbol{\sigma}_{xy} = \mathbf{T}(\theta)^T \mathbf{C}_e \mathbf{T}(\theta)\boldsymbol{\varepsilon}_{xy}$ may change. The stress-strain relation is consequently evaluated in the principle directions, which are rotating. By introduction of a tangential shear stiffness $(\sigma_1-\sigma_2)/2(\varepsilon_1-\varepsilon_2)$, which automatically arise from the rotation of the principle axes, the expression can be written:

$$\begin{bmatrix} \sigma_1 \\ \sigma_2 \\ \tau_{12} \end{bmatrix} = \begin{bmatrix} \mu E & 0 & 0 \\ 0 & E & 0 \\ 0 & 0 & \dfrac{\sigma_1 - \sigma_2}{2 \cdot (\varepsilon_1 - \varepsilon_2)} \end{bmatrix} \begin{bmatrix} \varepsilon_1 \\ \varepsilon_2 \\ \gamma_{12} \end{bmatrix}$$

The advantage with this model is that there is no need to assume a shear factor and that new cracks only can occur in a direction normal to the crack. A disadvantage is that the crack pattern will be complex; it is hard to see the connection with experimental results.

3.5.4 Choice of crack model in finite element analyses of FRC.

The smeared crack approach is much more user-friendly than the discrete crack approach and for concrete with fibres in addition to reinforcement bars the smeared crack method is the most practical approach. However, for concrete reinforced with fibres only, the smeared crack approach does not provide a representative picture of the non-linear behaviour, at least not at moderate fibre concentrations. Since the failure in these structural elements is

concentrated in one or a few cracks, the cracks should not be distributed over large areas as the smeared crack approach requires. If too many elements are cracked in the model, the consequence is that the ductility and load resistance will be overestimated. Therefore, cracks ought to be pre-defined in analysis of structures reinforced with fibres only, for instance by use of interface elements. Still, it is possible to use a smeared crack approach if non-linear material properties are applied only to the elements which the cracks are assumed to cross.

3.6 FRC in the serviceability limit state

Fibre reinforcement can be used to control crack widths if the fibre volume is sufficiently high. A lower fibre volume is adequate if crack control partly is maintained by the structural system itself, if external parameters related to prestressing are present, or if fibres are combined with conventional reinforcement [RILEM 2003]. Most current models for calculating crack spacing and width are empirical based and does not consider the material properties that influences the crack spacing, i.e. the post cracking or residual tensile strength. Moreover, almost no models consider cracking caused by restraint stresses, only cracking caused by external load [Löfgren 2007].

In the proposed design method for SFRC by RILEM (2003), the calculation of average crack spacing is based on the design rules in Eurocode ENV 1992-1-1, and the formula is slightly modified to account for the beneficial effect of the fibres [RILEM 2003]:

$$s_{rm} = \left(50 + 0.25 k_1 k_2 \frac{\phi_b}{\rho_r}\right)\left(\frac{50}{L/\phi}\right)$$

where:

$50/(L/\phi) \leq 1$

ϕ_b: the bar size in mm;

k_1: a coefficient which takes account of the bond properties of the bars;
k_2: a coefficient which takes account of the form of the strain distribution;
ρ_r: the effective reinforcement ratio $A_s/A_{c,eff}$ where A_s is the area of the reinforcement contained within the effective tension area $A_{c,eff}$.
L: length of steel fibre in mm;
ϕ: diameter of steel fibre in mm

The design crack width w_k can then be calculated from the following expression: $w_k=\beta s_{rm}\varepsilon_{sm}$, where β is a coefficient relating the average crack width to the design value. When calculating the mean steel strain ε_{sm} it as has to be taken into account that the tensile stress in the SFRC after cracking is not equal to zero but equal to $\sigma_F=0.45f_{Rm,1}$, where $f_{Rm,1}$ is determined from four-point bending of standardized beam tests.

When cracking is caused by an external applied force, the crack width depends on the applied force. However, if cracking is caused by an imposed deformation the force in the member depends on the actual stiffness and the crack width on the number of cracks formed. Most codes do not distinguish between these two cases [Löfgren 2007].

Löfgren (2007) proposes two different methods for calculating crack spacing and crack width when cracking is caused by an external applied force. The first method is based on EC2, were the fibres are considered by an additional factor $k_5=(1-\sigma_{fb}/f_{ct})$ leading to a modified expression for the average crack spacing $s_{r,m}=(k_3\cdot c+k_1\cdot k_2\cdot k_4\cdot k_5\cdot\phi/\rho_{s,eff})$. The second method is developed from the non-linear hinge model as described in Löfgren (2003).

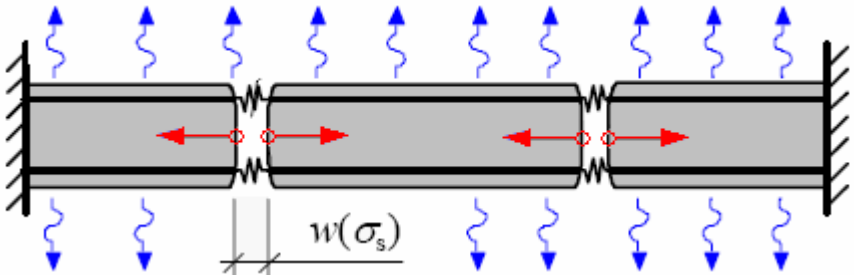

Figure 3.9: Imposed deformation on member of length l. [Löfgren 2007]

To account for restraint induced cracking, Engström (2006) proposes to model the crack by non-linear springs. By expressing the crack widths as a function of the steel stress the response during the cracking process can be described with the following deformation criteria:

$$\frac{N(\sigma_s, f_{ft,res}) \cdot l}{E_s A_s}(1-\varphi_{ef}) + n \cdot w(\sigma_s) = R \cdot \varepsilon_s \cdot l$$

where $N(\sigma_s,f_{ft.res})$ is the force acting on un-cracked parts, n is the number of cracks and R is the degree of restraint. $N(\sigma_s,f_{ft.res})$ can be taken as $N(\sigma_s,f_{ft,res})=\sigma_s \cdot A_s+f_{ft,res} \cdot (A_c-A_s)$. If $N(\sigma_s,f_{ft.res})$ is larger than the force required to initiate a new crack, N_1, more cracks will be formed. However, if $N(\sigma_s,f_{ft.res})$ is smaller than N_1 only one crack will be formed. The force required to initiate a new crack, N_1, can be calculated as:

$$N_1 = f_{ctm} \cdot \left(A_{ef} + (\frac{E_c}{E_s} - 1) \cdot A_s \right)$$

With fibres only, the number of cracks n=1 provided that the material exhibit a strain softening behaviour. The deformation criteria lead to the following expression for the crack width:

$$w = \left(R \cdot \varepsilon_{cs} - \frac{f_{ft,res}}{E_c}(1+\varphi_{ef}) \right) \cdot s_r$$

To induce more than one crack, a strain hardening FRC is necessary, or alternatively a high friction and/or adhesion to sub-base [Löfgren 2007].

More research is needed to determine the influence of fibre reinforcement in the serviceability limit state. Ongoing work is done to establish the combined effect of reinforcement and fibre bridging on the crack spacing and crack width. Another objective is to include cracking caused by restraint stresses in the design models [Löfgren 2007]. Other aspects like shrinkage and creep in FRC structures are also not yet fully understood.

4 Pull-out tests

4.1 Introduction

The pull-out behaviour of fibres in concrete is mainly influenced by four parameters: Fibre embedment length, fibre orientation, matrix strength and type of fibre; the latter including fibre geometry, strength and Youngs modulus. In this research, single fibre pull-out tests were carried out to evaluate the effect of the following parameters:

- Concrete strength
- Fibre type
- Embedment length

Furthermore, the objective was to estimate the expected average stress in the fibres over a crack in FRC, based on the data from the pull-out tests.

The tests were carried out according to the method proposed by Thorenfeldt (2006), described in section 2.5.4, where single fibres orientated perpendicular to the concrete surface are fastened in a gripping device and pulled out of the concrete at a constant rate.

Inclined fibres are not tested in this experimental series even though it is evident that the pull-out load is strongly influenced by the inclination of the fibre.

There are two reasons why inclined fibres are not included:

1) Inclined fibres demand a more complex test set-up. In a real structure, an inclined fibre in a crack is never pulled out with an initial force normal to the crack surface; the fibre will have a corresponding angle through the opposite concrete surface in the crack. To model this, the fibre has to go through two parallel concrete surfaces pulled from each other as done by Robins et al. (2002). [Figure 2.13]
2) Extensive work by others [Balaguru & Shah 1992, Stang & Li 2001, Van Gysel 2000] has shown the connection between fibre

embedment length, fibre orientation and matrix strength. It is assumed that the influence of orientation on the fibre-concrete combination is similar in the experiments described in this chapter. The scope of the pull-out experiments carried out here is to include the fibre dimensions and concrete qualities which are relevant in this thesis.

4.2 Concrete specimens – materials and casting procedure

Two self-compacting concrete mixes were used, both with a maximum aggregate diameter size of 16 mm. The concrete strengths were 62.4 and 93.7 N/mm^2, henceforth referred to as normal- and high-strength concrete. Details about the mix design, mixing procedure, fresh concrete properties and compression strength are shown in Table 4.1 and Table 4.2.

Material	Normal-strength SCC [kg/m^3]	High-strength SCC [kg/m^3]
Mass ratio*	0,6	0,45
Cement Norcem St FA	306	380
Elkem Microsilica	46	30
Water	211	185
Absorbed water	12	12
0-8mm	819	895
0-2mm	327	265
8-11mm	246	249
11-16mm	246	249
Glenium Sky 550**	4.5 (1.46 % of C)	10.1 (2.65% of C)
Silica air entrancement	1.53 (0.5 % of C)	2.73 (0.72% of C)

*Table 4.1: Mix design. Remarks: * Mass ratio = water/[cement + powder and pozzolans] ** Glenium Sky 550 is a polycarboxylate based superplasticizer (water reducer)*

The following mixing procedure was used:

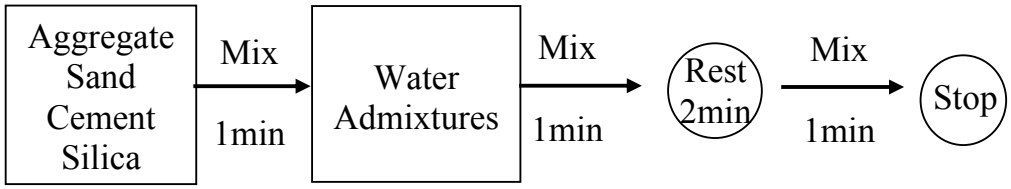

Fresh concrete properties	Normal-strength SCC	High-strength SCC
Density [kg/m^3]	2267	2380
Air [%]	6.3	1.4
Slump flow [mm]	590	790

Compression strength	Normal-strength SCC	High-strength SCC
$f_{ck,28days}$ [N/mm^2]	44.9	82.9
$f_{ck,test\ day}$ [N/mm^2]	62.4	93.7

Table 4.2: Fresh concrete quality and compression strength after 28days and at the date of testing.

Two types of fibres were used, Dramix 65/60 steel fibre and Barchip Kyodo synthetic fibre. The product data is given in Table 4.3:

Name	Dramix 65/60	BarChip Kyodo
Material	Steel	Polyolefin
Length L [mm]	60	48
Eq. diameter, d [mm]	0.9	0.9*
L/d	65	53
Densit [kg/m^3]	7850	910
Weight pr fibre [g]	0.30	0.028*
E-modulus [N/mm^2]	200.000	6000
Tensil strength [N/mm^2]	1000	550

Table 4.3: Product data for the two fibre types. The cross-section area of the synthetic fibres was determined by the average weight of 400 fibres, where the density and fibre length was given in the product data sheet from the producer.

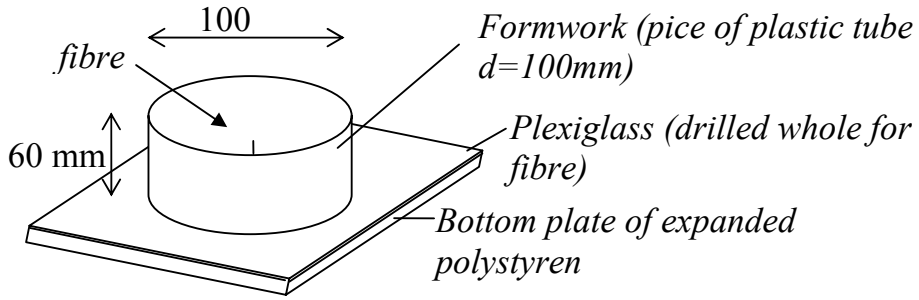

Figure 4.1: Formwork test specimens. The fibre was fixed in the bottom plate. Then the SCC was poured carefully around the fibre.

4.3 Test setup

The tests were carried out according to the method proposed by Thorenfeldt (2006) as described in section 2.5.4. The pull-out load was deformation controlled, and set to 0.2mm/min and 0.6mm/min for specimens with steel and synthetic fibres, respectively. An overview of the test specimens is given in Table 4.4.

Series	Fibre	Concrete	Embedment length	Number of tests
Hbar2	Barchip Kyodo	HSCC	$L_f/2=24$	7 (+4*)
Nbar2	Barchip Kyodo	NSCC	$L_f/2=24$	8 (+1*)
Hdr6	Dramix 65/60	HSCC	$L_f/6=10$	8 (+1*)
Ndr6	Dramix 65/60	NSCC	$L_f/6=10$	9 (+1*)
N2dr6	Dramix 65/60	N_2SCC	$L_f/6=10$	4
N2dr2	Dramix 65/60	N_2SCC	$L_f/2=30$	5

Table 4.4: Overview of test specimens
**) Some of the fibres were cut off in the gripping device during pull-out. These results are not reported.*

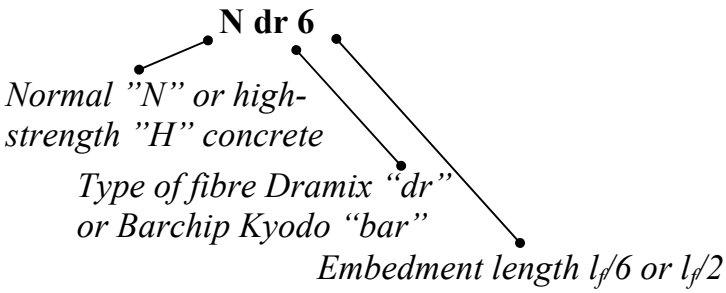

The main objective of the four first pull-out series, Hbar2, Nbar2, Hdr6 and Ndr6, was to investigate the influence of the concrete strength on synthetic and steel fibre. Later, two additional series were cast to include the effect of embedment length on Dramix fibres, or more specific to estimate the contribution of the end-hook to the total pull-out response of the fibre. In the latter two series, Nbar2 and Ndr6, the mix design for the normal-strength concrete was used to achieve comparable results [Table 4.4].

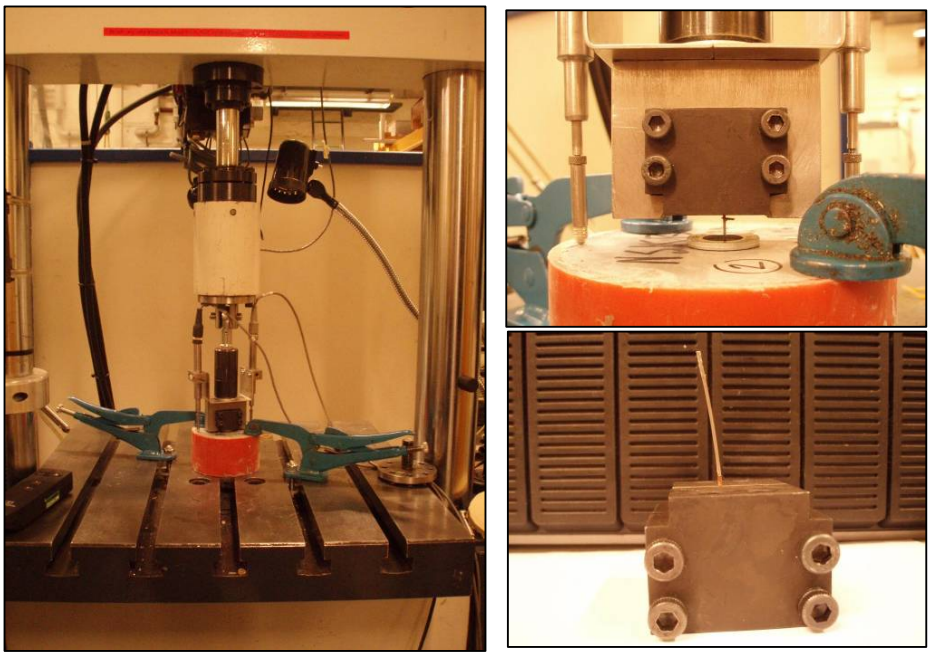

Figure 4.2: Rig. The fibre is fastened in a gripping device and pulled out. The third picture shows how the end-hook is completely straightened after pull-out.

4.4 Results

Table 4.5 shows the average maximum pull-out load for each series, with corresponding pull-out displacement. In general, it can be seen that the steel fibres have a high exploitation ratio, as the steel fibres reach a stress during pull-out which in average for all tests is 69% of the tensile strength of the fibre. More accurate, the steel fibres in the normal-strength concrete reach stresses between 49% and 78% of the tensile strength while the exploitation ratios are found to be between 67% and 97% for the fibres cast in high-strength concrete. In the case of high-strength concrete, the exploitation ratio is too high, considering that inclined fibres may reach higher pull-out loads then fibres orientated normal to a crack surface. Consequently, it is likely that fibre fracture occurs with the latter fibre-concrete combination.

For synthetic fibres, the stress during pull-out is close to the tensile strength of the fibres. In average the fibres reach 84% of the tensile strength, and in one of the tests with high-strength concrete the stress approaches 94% of the tensile strength. Here, the difference between the two concrete qualities is not so evident; the average maximum pull-out load is only 5.5% higher for the high-strength concrete than for the normal-strength concrete.

Series	Number of tests	Maximum pull-out load	Corresponding displacement
Hbar2	7	303 N	2.648 mm
Nbar2	8	287 N	2.573 mm
Hdr6	8	506 N	0.620 mm
Ndr6	9	379 N	0.850 mm
N2dr6	4	439 N	0.552 mm
N2dr2	5	425 N	0.888 mm

Table 4.5: Average maximum pull-out load and displacement for all specimens in each series.

One of the main objectives of performing these tests was to provide a basis for subsequent experiments and to make use of the results in further calculations. As described in section 2.5.4, the response of single fibre pull-out tests can be used to estimate the expected average stress in the fibres over a crack, which in the design phase is used to find the residual strength of cracked concrete. For this application, the average pull-out load over a relevant displacement interval is more interesting than the maximum pull-out load. The pull-out load versus displacement is shown in Figure 4.3 to Figure 4.5. In Figure 4.6 the average pull-out load between 0.5 and 2mm displacement is illustrated.

The difference in pull-out response for steel fibres in normal- and high-strength concrete is more pronounced at small crack-widths. The *maximum* pull-out load is in average 33.5% higher for series Hdr6 than for series Ndr6, while the difference is 23.7% for the *average* pull-out loads between 0.5 and 2mm displacement. Hence, the positive effect of higher matrix strength seems to diminish as the pull-out increases; at 3mm pull-out the difference between Hdr6 and Ndr6 is only 3.2%. For synthetic fibres, the distinction between the two concrete qualities is not that evident; the average pull-out load in the displacement interval 0.5 to 2mm is only 2.6% higher for series Hbar2 than series Nbar2.

Figure 5.3 to 5.5 shows that the pull-out response of synthetic fibres is very different from the response of steel fibres. Due to the low modulus of elasticity, the synthetic fibres reach their maximum load at a larger deformation. Hence, it is not adequate to compare the response of steel and synthetic fibres directly. As illustrated Figure 4.6, the average pull-out load between 2 and 3 mm crack width is around 30% higher than between 0.5 and 2mm crack width for synthetic fibres. Moreover, the difference in pull-out response between the two concrete qualities increases from 2.6 % at the lower displacement interval to 7.1% at the upper interval. The pull-out tests reflect one of the drawbacks of synthetic fibres; the crack widths needed to make the fibres efficient are relatively large, something that has to be accounted for in the serviceability limit state. On the other hand, the

maximum pull-out loads of the synthetic fibres are quite high; 60% of the average maximum pull-out load of steel fibres in high-strength concrete and 76% in case of normal-strength concrete. Further, the pull-out resistance remains at the same level after the initial peak, even at large pull-out lengths, which will lead to a very ductile FRC. Moreover, with embedment length $l_f/2$ the pull-out length of the synthetic fibres is shorter than that of steel fibres. Consequently, the relative difference between maximum pull-out loads of steel and synthetic fibres is even lower than the test-results displays. The synthetic fibres have clear advantages when it comes to cost-saving. They are also easier to handle. So from this point of view, synthetic fibres may compete with steel fibres. Another benefit is the low scatter of the synthetic fibre pull-out tests, illustrated in Figure 4.6. Nevertheless, the high deformations put restrictions on the use of synthetic fibres.

Regarding the effect of different embedment lengths of Dramix 65/60 steel fibre, the average pull-out load of the specimens in series N2dr6 ($l_f/6$) and N2dr2 ($l_f/2$) is similar; $F_{1m,N2dr2}$=0.402kN and $F_{2m,N2dr6}$=0.397kN between 0.5mm and 2.0mm deformation. With the relatively high scatter for the four specimens in series N2dr6 [Figure 4.5] it is perhaps more appropriate to use the average pull-out load for all specimens in series Ndr6 and N2dr6, owing to the fact that the compression strength $f_{c,N2dr6} \approx f_{c,Ndr6}$. With $F_{2m(N2dr6+Ndr6)}$=0,37kN, the average pull-out load for the fibres with embedment lengths $l_f/2$ is 9.7% higher than for the fibres with embedment lengths $l_f/6$. Accordingly, a rough estimate from these tests is that the end-hook contributes to around 90% of the total pull-out response at a crack width between 0.5 and 2mm for a fibre orientated perpendicular to the crack.

Average stress in fibres after cracking

As described in section 2.5.4, an estimate for the average stress in fibres over a crack can be found from the average pull-out load taken between 0.5 and 2.0mm displacement. The intention is to control if the estimated

average stresses correspond to the results of other experiments carried out in this thesis. Therefore, average values and not characteristic values are used (no safety factor). For hook-end fibres the average stress can be determined as:

$$\sigma_{f,average} = (0{,}25\ f_{bf1}\pi d_f\ l_f + 0{,}7\ F_a)/A_f$$

where

f_{bf1} is the bonding strength from the straight part of the fibre;

$f_{bf1} = (F_{1m} - F_{2m})/(\pi d_f\ l_f\ /3)$

F_a is the anchorage capacity; $F_a = F_{1m} - 0.5\ f_{bf1}\pi d_f\ l_f$

F_m is the average pull-out load between 0.5 and 2mm displacement for tests specimens; F_{1m} with anchorage length $l_{b1} = l_f\ /2$ and F_{2m} with anchorage length $l_{b2} = l_f\ /6$.

For the steel fibres in the normal-strength concrete, $F_{1m(N2dr2)} = 402$N and $F_{2m(Ndr6+N2dr6)} = 367$N, which gives a average stress $\sigma_{f,average} = 426$ N/mm^2.

No steel fibre specimens with embedment length $l_f/2$ were cast with high-strength concrete. Therefore, the average stress cannot be calculated directly. Yet, since the average pull-out load with $l_f/6$ was 23.7% higher for the high-strength concrete compared to the normal-strength concrete, the average stress can be estimated indirectly. A correspondingly increase from normal to high-strength concrete leads to a average stress $\sigma_{f,average,Hdr} = 527$ N/mm^2, provided that no fibre-rupture occurs. As discussed earlier, the risk of fibre-rupture in the high-strength concrete is present. Hence, the average stress calculated here might be overestimated.

An analogous evaluation of the synthetic fibres would not be adequate. The method for estimating the average stress presented in 2.5 is intended for steel fibres. As pointed out earlier, the load-deformation progress is very different for synthetic fibres. While the steel fibres reaches an approximately constant plateau at a crack width around 0.5mm, the synthetic fibres needs crack widths larger then 2.5mm to fully come into effect, and when the maximum load is reached, it does not remain constant. The reason for the wave-shaped pullout response that occurs after

maximum pullout load [Figure 4.3] is the embossed surface of the synthetic fibres, which are made to maximise the bonding to the matrix. During pull-out the embossed surface probably deforms gradually along the fibre, which causes the pull-out load to increase and decrease several times.

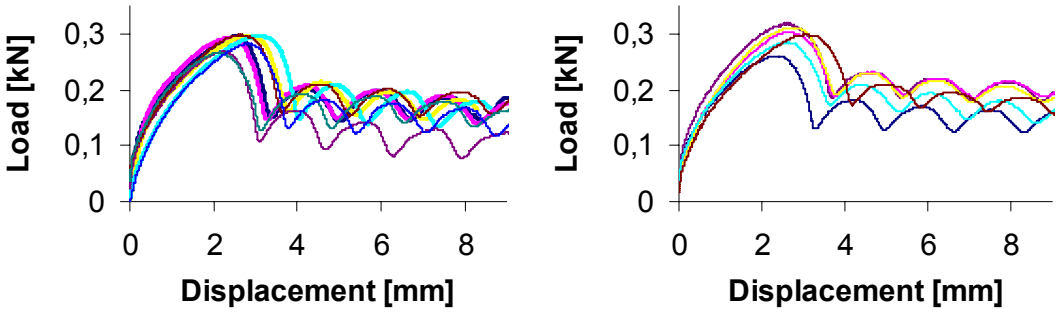

*Figure 4.3: Barchip Kyodo with embedment length $L_f/2$ a) "*Nbar2*" Normal-strength $f_{c,N}$=62.4 N/mm^2 b) "*Hbar2*" High-strength $f_{c,H}$=93.7 N/mm^2.*

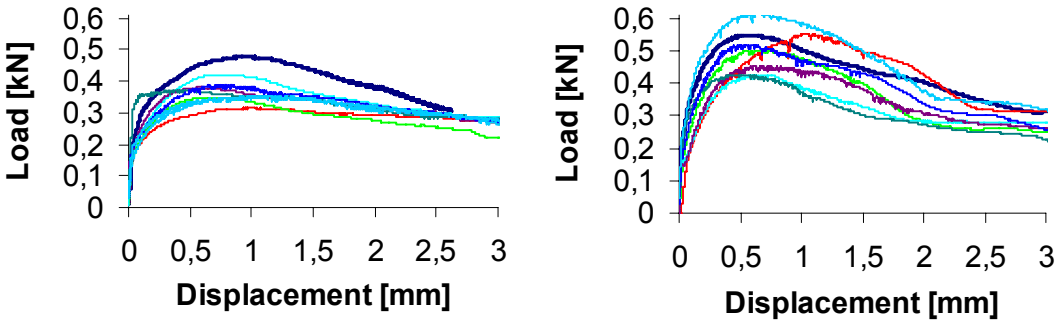

Figure 4.4: Dramix 65/60 with embedment length $L_f/6$ a) "Ndr6" Normal-strength $f_{c,N}$=62.4 N/mm^2 b) "Hdr6" High-strength $f_{c,H}$=93.7 N/mm^2.

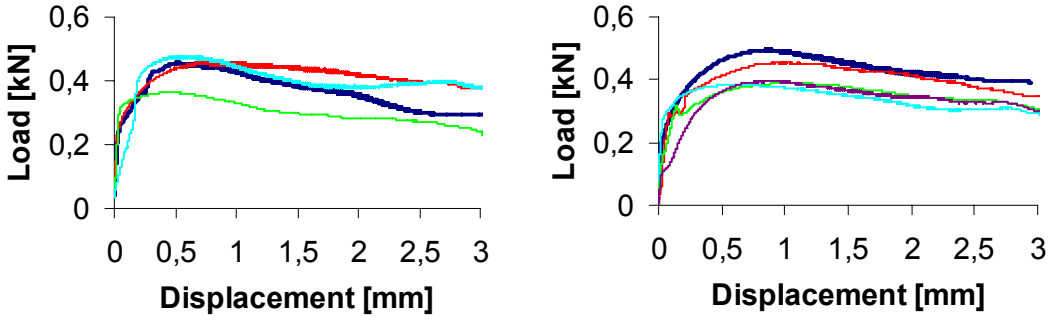

Figure 4.5: Dramix 65/60 with compressive strength $f_{c,N2}$=63.9 N/mm^2 a) "N2dr6" Embedment length $L_f/6$, b) "N2dr2" Embedment length $L_f/2$

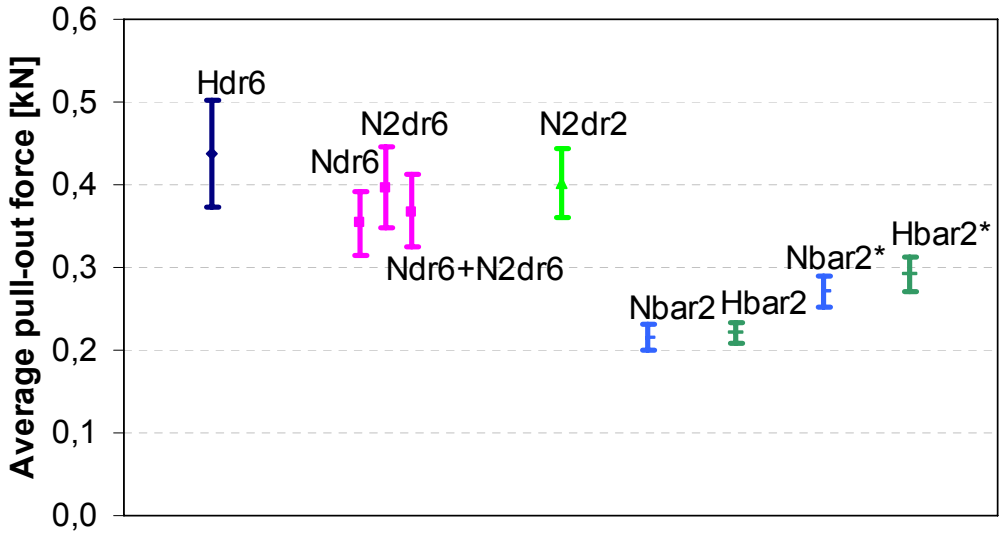

Figure 4.6: Average pull-out load [kN] and standard deviation between 0.5 and 2mm deformation. (Nbar2 and Hbar2* between 2 and 3mm deflection)*

Remark – drawback of the test method

It should be stressed that the test method used in this chapter was intended for steel fibres. A possible problem using the same test-setup for synthetic fibres is the elastic deformations in the area from the concrete surface to the point in the gripping device where the fibres can be expected to be completely fixed. This is illustrated in Figure 4.7.

The distance from the concrete surface to the fastening point in the gripping device is $L_x = h_{ring} + l_{x,\text{fastening point}}$. Over this length, the fibre will deform, and this deformation is not related to pull-out. Therefore it gives a false contribution to the measured pull-out deformation.
The height of the ring is h_{ring}=2.43mm. If the total free length of the fibre for instance is assumed to be L_x=5mm, the false contribution to the pull-out deformation at the average maximum load would be ΔL=0.39mm:

$\Delta L = \varepsilon_x \cdot L_x = P_{max,average} / (A_f \cdot E_{Barchip}) \cdot L_x = 295/(\pi \cdot 0.45^2 \cdot 6000)$ mm = 0.39 mm, which in average is 15% of the measured pull-out deformation at maximum load.

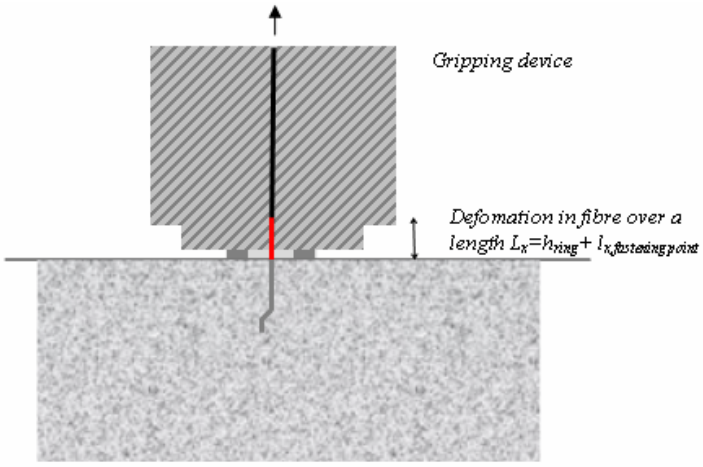

Figure 4.7: Distance from the concrete surface to the fastening point in the gripping device.

Since the Young's modulus is so much higher for steel fibres, the deformation in the part of the fibre not embedded gives a much lower contribution to the measured pull-out. An analogous estimation would give a contribution at the maximum load ΔL=0.017mm, which is 2% of the measured pull-out deformation at the maximum load.

4.5 Conclusions

Although more comprehensive methods for determining the pull-out behaviour exists, the method applied here seems be more suitable for practical applications.

The following observations were done from the pull-out tests:

- The pull-out load increased with increasing concrete strength. The difference between the two concrete strengths was most distinguished in the steel fibre pull-out tests, but there was also a noticeable difference in the pull-out tests with synthetic fibres.

Moreover, the difference in pull-out load between high- and low strength concrete diminished with increasing pull-out length.

- The utilization of the fibres were high; the maximum pullout loads were close to the tensile strength of the fibres, especially in case of high-strength concrete
- The pull-out response for the synthetic fibres was very different from the steel fibres. In the first place, the deformation is much larger when the maximum pull-out force is reached. This is due to the relatively low Young's modulus; only 3% of the Young's modulus of steel. In average, the steel fibres reached the maximum load at 0.72mm pull-out length, whereas the average pull-out length at maximum load was 2.6mm for the synthetic fibres. Secondly, after the maximum pullout load was reached, the pullout force for the synthetic fibres decreases and increases in waves as a result of the embossed surface of the fibre. For a steel fibre pull-out, the force stays more or less constant for a while, and then it diminishes gradually. The high deformations put a restriction on the use of synthetic fibres.
- The scatter of the results is relatively low, especially in case of synthetic fibres.
- The pull-out behaviour of steel fibres is dominated by the contribution from the end-hooks. In tests carried out here the end-hook, roughly estimated, contributes to around 90% of the pull-out resistance.
- The post cracking tensile strength of the steel fibre in the normal-strength concrete was estimated from the pull-out tests to be 426 N/mm^2, taken between 0.5 and 2.0mm pullout length. Assuming that no fibre fracture occurs, the estimated post cracking tensile strength is 527 N/mm^2 for the high-strength concrete. An analogous evaluation of the synthetic fibres is not adequate.

5 Steel fibre reinforced self compacting concrete

5.1 Advantages and drawbacks with FRSCC compared to FRVCC

The positive effects of FRC regarding increased productivity and better HSE conditions can be further improved by using self compacting concrete. With SCC the heavy and boisterous vibration work is avoided. Furthermore SCC improves the quality and appearance of the concrete. The major drawback with SCC instead of VCC is the material costs. In addition, more work has to be put into the concrete design phase to achieve self-compacting properties for FRC as discussed in chapter 2.3.

In FRVCC the orientation and distribution of fibres is dependent on the vibration. If the concrete is compacted by using a vibration table, it is likely that a planar-random orientation occur perpendicular to the direction of the vibration. It is not recommendable to use immersion vibrator for compaction, since the fibres disperses where the vibrator is put into the concrete. Still, in full scale constructions immersion vibrator may often be the only possible compaction method. In FRSCC the orientation is dependent on the flow of the concrete, which again is governed by the casting method. It is important to be aware of the impact of the casting method on the concrete flow in order to ensure a favourable orientation of fibres through a construction element.

5.2 36 beams sawn from wall and slab elements with SCC and VCC.

5.2.1 Introduction

Two wall and two slab elements were cast to investigate the orientation and distribution of fibres in structures of realistic dimensions. One wall and one slab element were made with vibrator compacted concrete (VCC), one wall and one slab element with self compacting concrete (SCC). Afterwards, 36 small beams (150 x 150 x 600 mm) were sawn from the elements and tested in a deformation controlled rig, exposed to four point bending [Døssland (2003) and Grimheden (2003)].

5.2.2 Concrete and casting

Both concretes had a water/cement ratio of 0.59 and a fibre content of 0.7% (56kg/m^3) Dramix 65/60. The matrix volume was 339kg/m^3 and 367 kg/m^3 in the VCC and SCC respectively. The concrete composition of the VCC and SCC is shown in Table 5.1.

VCC	
Material	[kg/m^3]
Cement standard FA	302.3
Silica	6.2
0-2 sand	186.0
0-8 sand	864.7
8-16 aggregate	357.2
16-24 aggregate	525.4
Added water	179.8
Admixtures:	
P-stoff	1.542
AD 18	1.540
Dramix 65/60	56

SCC	
Material	[kg/m^3]
Cement standard FA	321.6
Silica	15.1
0-10 sand	910.6
0-4 sand	250.3
8-16 aggregate	348.7
16-25 aggregate	402.0
Added water	191.0
Admixtures	
SP: VC140	5.39
Dramix 65/60	56

Table 5.1: Concrete composition, VCC and SCC. The VCC was delivered by the supplier NorBetong, the SCC by Unicon.

The fibres were added to the concrete lorry and mixed a couple of minutes. Further the concrete was mixed additionally on the drive to the construction site some kilometres from the mixing plant.

One wall (4 x 2.4 x 0.15m) and one slab element (2.65 x 2.65 x 0.15) was cast with VCC, the other wall and slab element was cast with SCC. The concrete was poured through a concrete scip from one side of the formwork. One week after casting, elements were sawn from the walls and slabs as illustrated in Figure 5.1, and finally three beams were sawn from each element.

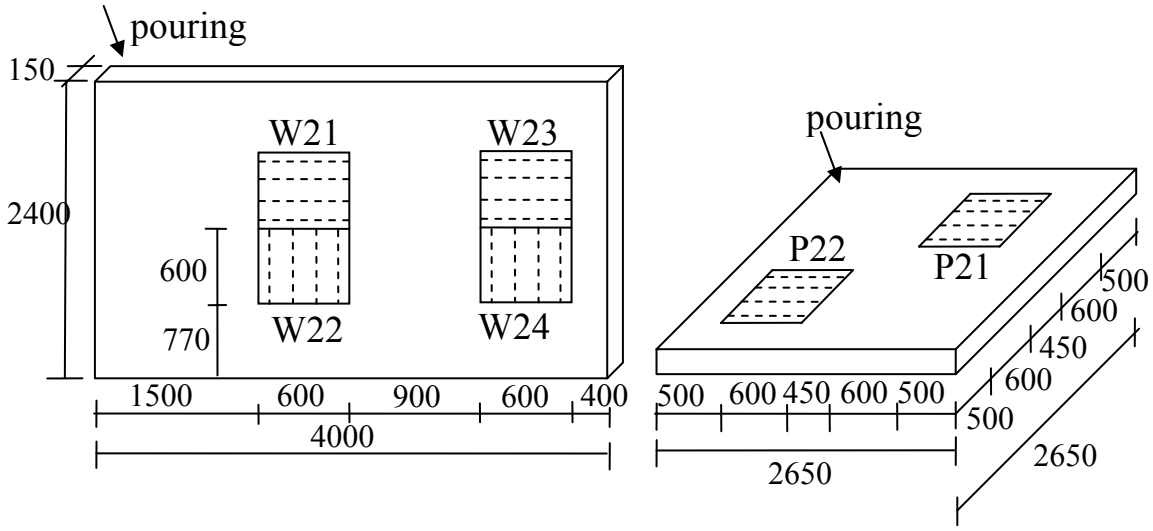

Figure 5.1: Elements sawn from wall W2 and slab P2 with SCC. W2 and P2 were cast from a concrete scip which were held still in one corner, illustrated by the arrows. Analogous elements were sawn from wall W1 (W11, W12, W13, W14) and slab P1 (P11, P12) with VCC. From each element three beams were sawn as indicated by the dashed lines.

The compression strength of the VCC after 28 days was $f_{ck28,VCC}$=60.7. The compression strength of the SCC was estimated based on the measured values after 7 days to $f_{c28,SCC}$=59.0 N/mm^2. Half of the beams were tested at age 28 days, the remaining were tested later. An overview of the hardened concrete properties is given in Table 5.2.

Element	Concrete	Age [days]	f_c** [N/mm^2]	f_t* [N/mm^2]
V11 V12 P11	VCC	28	60.7	2.4
V13 V14 P12	VCC	34	62.9	2.5
V21 V22 P21	SCC	28	59.0	2.4
V23 V24 P22	SCC	41	63.0	2.5

Table 5.2: Hardened concrete properties

**) Design tensile strength interpolated from table 5, NS3473*

The time development of the cube strength was estimated according to CEB-FIP 1990 Model Code:

$$f_c(t_e) = f_{c28} \cdot e^{s(1-\sqrt{\frac{28}{t_e}})}$$

where t_e is the maturity (or equivalent time) which is affected by the concrete composition and the temperature. Here $t_e \approx t$, where t= time from casting until testing, because the temperature in the specimen is approximately 20°C during hardening. The parameter s=0.38 for standard cement.

5.2.3 Experiments

The flexural beam tests (four-point bending) were performed according to the recommendations Norwegian Design Rules for SFRC [Thorenfeldt E et al (2006)] which are based on the guidelines by ASTM C1018 (see section 2.5.2). The load was applied with a constant deformation rate of 1mm/min. The deflections were measured by LVDT's at both sides of the beams and the tests were ended when the deflections exceeded 8mm. Afterwards, the residual strength was determined from the average equivalent bending strength recorded at 0.5 and 2.5mm deflection as $f_{residual}=0.37f_{eq,average}$.

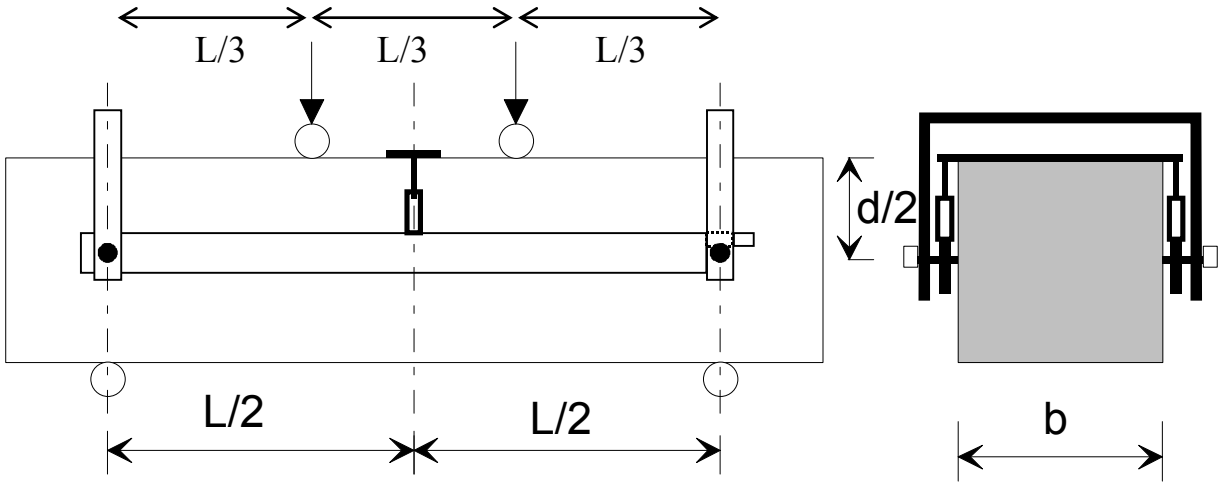

Figure 5.2: Rig, deflection measurement.

5.2.4 Orientation and distribution of fibres

To determine the actual fibre content in the failure zone, a block from each beam was sawn, about 9cm ($1.5 \cdot l_{f,fibre}$) from the failure zone [Ch 2.5.2]. First, the fibres over the cross-section were counted, thereafter, the sawn block was crushed, and finally all fibres were pulled out.
The fibre orientation-factor is previously [Chapter 2.6.3] defined as:

$$\alpha = n \cdot A_f/(A_c \cdot v_f)$$

where n is the number of fibres crossing the cross-section, A_f is the cross-section area of one fibre, A_c is the area of concrete in the current part of the cross-section, and v_f is the fibre-volume in percentage. Theoretically, the residual strength can be determined as:

$$f_{ftk,res} = \eta_0 \, v_f \, \sigma_{average}$$

where v_f is the volume of fibres and $\sigma_{average}$ is the average tension in all fibres which intersects the crack with arbitrary orientation and anchor length. η is a capacity factor which describes the relation between the normal force resultant of fibres of current distributed orientation and the resultant force in uni-directed fibres with the same stress. For uni-directed fibres $\eta=1$, for plane orientated fibres $\eta=1/2$ and for isotropic orientated fibres $\eta=1/3$.

The result of fibre-counting is shown in Table 5.3. The volume of fibres in the block that was crushed was close to the added fibre volume for all beams, which implies an even distribution of fibres through the structural elements. The volume was only controlled in one of the three beams for element P11, P21, W11, W12, W21 and W22. For the remaining elements, the volume in all three beams was controlled.

Even though the fibre volume in element P12 with VCC is close to the added fibre content, the capacity factor is very low, indicating that the main part of the fibres is orientated parallel to the cross-section. The average orientation

factor for element P11 is more than twice the size as for element P12. Hence, the fibre orientation through the slab is far from isotropic. The average orientation factors in the four elements from the VCC wall were higher for the horizontally sawn beams than the vertically sawn beams. For the SCC wall, the orientation factor is also higher for the horizontally sawn beams near the casting point, but highest for the vertically saw beams on the other end of the formwork.

		v_f [%]	ρ [-]	α [-]	η [-]
P11	VCC	0.67* / *0.62	0.0049	0.79	0.72
P12	"	0.68	0.0025	0.37	0.25
P21	SCC	0.71 */ 0.72**	0.0040	0.56	0.42
P22	"	0.71	0.0056	0.78	0.71
W11	VCC	0.74 / *0.81	0.0041	0.56	0.44
W12	"	0.75 / *0.85	0.0035	0.47	0.33
W13	"	0.77	0.0052	0.68	0.58
W14	"	0.79	0.0038	0.48	0.34
W21	SCC	0.71 / *0.74	0.0040	0.57	0.43
W22	"	0.68 / *0.63	0.0025	0.37	0.24
W23	"	0.70	0.0023	0.33	0.22
W24	"	0.72	0.0044	0.62	0.49

*Table 5.3: Result of fibre-counting for each element. For more details see Appendix A. *) The fibre content was only controlled in one of three beams (showed after the slash). To estimate the average value, the fibre content in the two remaining beams is assumed to be equal to the added volume.*

5.2.5 Results

The load-defection curves of the 12 beams sawn from the VCC wall is shown in Figure 5.3. The relation between the residual strength from the measured

response and the orientation factor from fibre-counting is similar for all beams. It is clear that the fibres are not isotropic orientated. This is partly due to the wall effect. According to Dupont (2003), the orientation factor can be determined by:

$$\alpha = \frac{\alpha_1 \cdot (h - l_f) + \alpha_2 \cdot l_f}{h}, \qquad \text{where } \alpha_1=0.5 \text{ and } \alpha_2=0,6. \qquad \text{[Ch 2.6]}$$

With a wall thickness h=150 and Dramix 65/60 steel fibres, the theoretical orientation factor $\alpha_{Dramix65/60}$=0.54. The average orientation factor for all beams in the VCC wall is 0.55, which is close to the theoretical factor. The scatter is probably partly caused by vibration. Figure 5.3 also illustrates that the post-cracking strength of the concrete first of all is dependent of the share of fibres over the cross-section, here quantified by α. The residual strength is determined from the equivalent bending strength recorded at 0.5 and 2.5mm deflection, as described in section 2.5.2. Moreover, the average residual strengths for the four elements from the VCC wall were higher for the horizontally sawn beams than the vertically sawn beams.

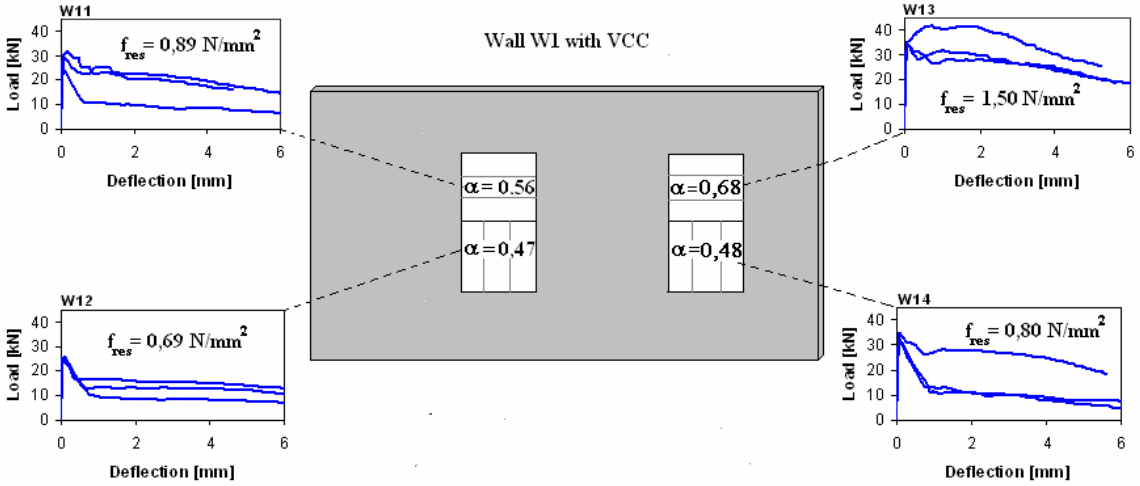

Figure 5.3: Wall with vibrator compacted concrete, result from beam tests. The residual strengths f_{res} are determined from the average equivalent bending strength (average of three beams). α is the average fibre orientation factor determined from fibre counting.

The fibre-orientation for the SCC-wall was mainly horizontal in the elements near the side of casting, while the fibres were more vertically orientated in the elements on the other end of the wall. This is also verified by the residual strength which is largest for the horizontally sawn beams near the casting point, and largest for the vertically saw beams on the other end of the formwork. The orientation of the fibres in SCC is dependent on the flow during casting. If the fibres mainly are orientated parallel to the flow, a hypothesis is that the direction of the flow could have been as illustrated in Figure 5.4.

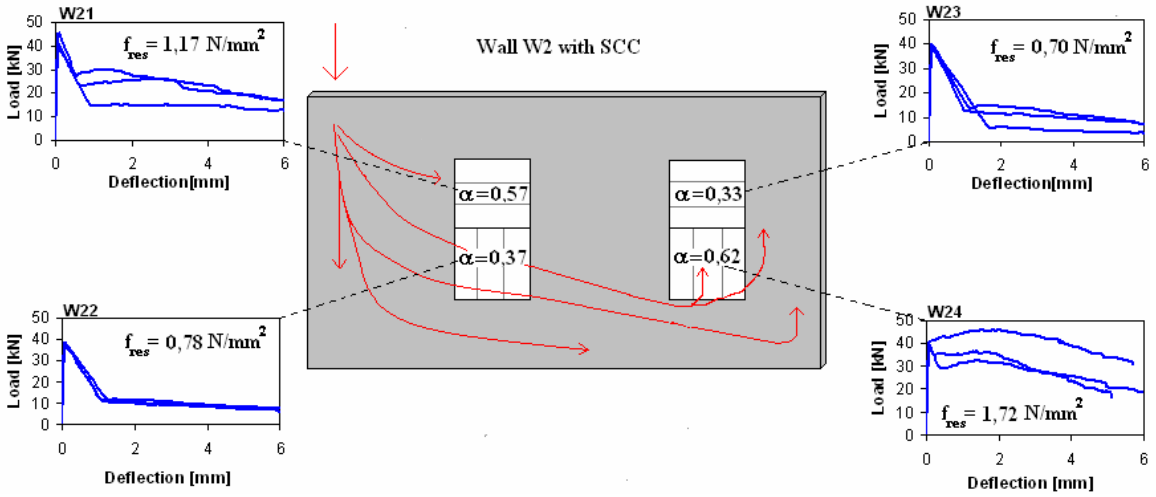

Figure 5.4: Wall with SCC, result from beam tests with the average residual stress and the average orientation factor for each element. If the fibres are assumed to orientate parallel to the flow, the direction of the flow would be as indicated by the arrows.

An important observation is that the fibre orientation factors and the concentrations in the two elements sawn from the VCC slab were very different from each other, with average orientation factors 0.70 and 0.37 for element P_{11} and P_{12}, respectively. As already stressed, the fibre content in the controlled blocks from element P12 was close to the added fibre volume, which implies that an unfavourable fibre orientation causes the low post-

cracking strength, not an absence of fibres. The uneven fibre orientation must have originated from the vibration and casting work. The residual strengths for the two elements sawn from the SCC slabs, on the other hand, were quite similar. [Figure 5.5]

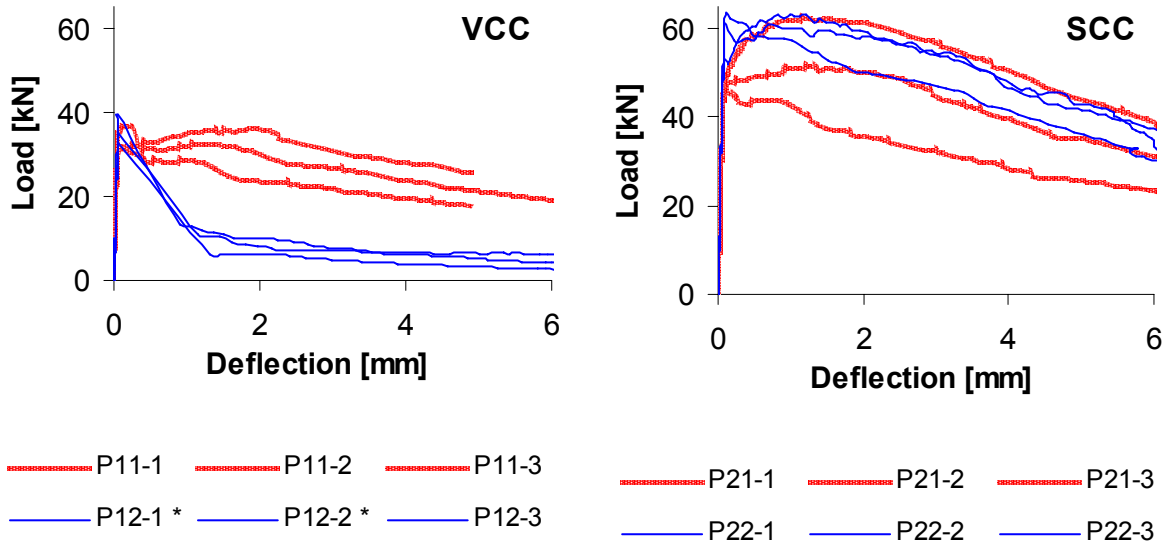

*Figure 5.5. Load-deflection curves for the 12 beams taken from the two plates. The residual strengths determined from the average equivalent bending strength are: $f_{res,P11}$=1.28, $f_{res,P12}$=0.46, $f_{res,P21}$=2.01, $f_{res,P22}$=2.55 N/mm^2. *) Two beams were tested upside down.*

The results for VCC slab illustrate a common problem for FRC; immersion vibrators can cause an uneven fibre distribution and orientation which leads to weakness zones, and should therefore be avoided. Still, in full-scale constructions, it is often impossible ensure a sufficient compaction without a immersion vibrator.

Residual strength from fibre counting

The residual strength determined from the average equivalent bending strength can be compared with the theoretically determined residual strength

$f_{ftk,res} = \eta_0 \; v_f \; \sigma_{average}$, where the capacity factor η_0 is estimated from fibre counting. The theoretically determined residual strengths illustrated in Figure 5.6 are based on an average post cracking stress in the fibres of $\sigma_{average}$ = 400MPa. Even though the average values for the experimental and theoretical determined residual strengths are similar, the scatter is large. When the crack is initiated, only the fibres in the lower part of the beam are active. As the crack expands, more fibres are activated. In Figure 5.6 the theoretically determined residual strengths are shown, both when the section ratio of fibres in the lower part of the cross section is accounted for, and when the number of fibres at the whole cross section is considered. The difference is small, and illustrates that the distribution of fibres is even.

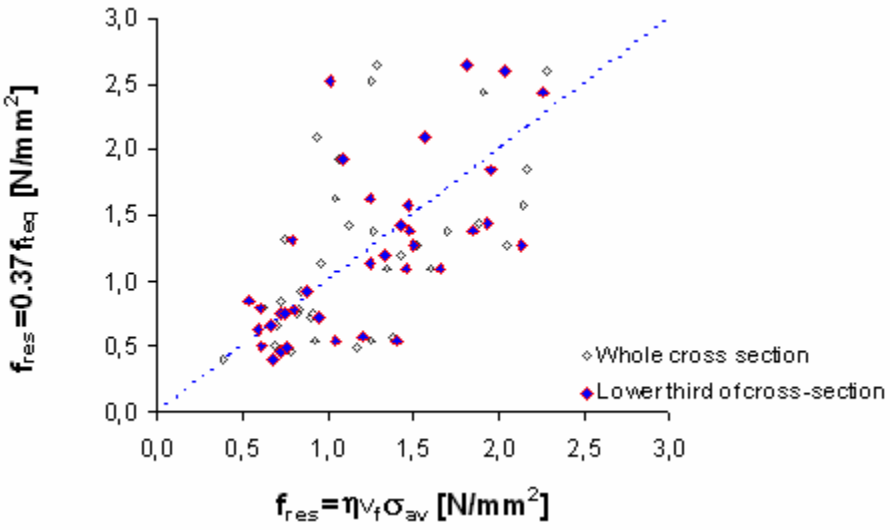

Figure 5.6: Theoretical residual strength from fibre-counting vs. experimental, $\sigma_{average}$=400 N/mm^2.

Average post-cracking stresses

The post-cracking stress is dependent on the concrete strength, as confirmed in Chapter 5. However, the compression strength for the two concrete types used

here are similar. It is still clear that the average post-cracking stress for the VCC is much lower than for the SCC. By comparing the average theoretical residual strength with the average residual strength found from the measured data for each of the concrete types, the average post-cracking stress $\sigma_{av,VCC}$=300 N/mm^2 for the VCC while it is $\sigma_{av,VCC}$=500 N/mm^2 for the SCC. The result is illustrated in figure 6.7. One reason for the difference in post-cracking strength between the VCC and SCC might be the amount of added micro silica which is 6kg/m^3 in the VCC and 15kg/m^3 in the SCC. It has been found that micro silica has beneficial effects on the bond between concrete and fibres due to [Löfgren 2005]:

- Microfiller effect: Micro silica increases the packing density around the fibre [Löfgren 2005]
- Pozzolan effect: The particles consist of amorphous silica and have a large surface area, causing a reaction with ions in the alkaline pore fluid. The reaction product resembles the hydration products of hardened cement pasta, and stabilizes and enhances the separation into finer pores. [Hjort 1982] The refined capillary pores and improved pore distribution leads to a more dense and homogenous microstructure.
- Internal bleeding is reduced due to a higher coherence of the fresh paste. [Löfgren 2005]

The results from experimental research on the effect of improved packing and fibre-matrix bonding is ambiguous. In a study by Glavind (1992) on the optimization of matrix packing density, steel fibre pullout tests with various cement matrixes were carried out. No increase in interfacial bond strengths for the matrices containing silica fume and clay were found, which indicates no correlation between packing density and interface bond strength. These findings are supported in the work by Chan and Li (1997). They found that a densification of the transition zone between fibre and concrete had little effect on the adhesive bond failure that occurred for steel and polyethylene cement systems. Yet, if the densification of the transition zone results in an enhancement of contact surface area between fibre and transition zone

material, the adhesion must improve. Most experimental results imply that an improved bond capacity will be achieved by increased packing density due to silica, e.g. [Guerro and Naaman 2000], [Robins et al 2002], [Stroeven and Stroeven 2003], [Lappa 2007], [Cunha, Barros and Sena-Cruz 2007].

Another factor that may improve the porosity further is that the matrix volume for the SCC (367kg/m^3) is larger than the matrix volume of the VCC (339 kg/m^3). The effects of matrix volume and micro silica might not be sufficient to explain the large difference between the average post-cracking stresses found in these experiments; further investigation is needed to establish the influence of porosity. However, this is not made allowances for within the scope of this thesis.

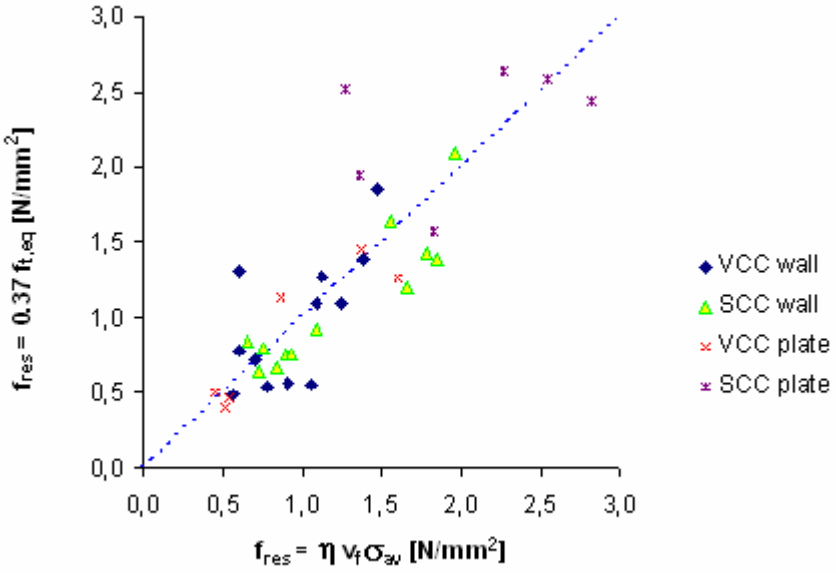

Figure 5.7: Theoretical residual strength from fibre-counting vs. experimental. Here $\sigma_{average,VCC}$*=300 N/mm*^{2} *and* $\sigma_{average,SCC}$*=500 N/mm*^{2}*.*

One main reason for the scatter between the theoretical and experimental residual strength is that the fibre-counting of the block taken 5-10cm away from the crack differs from the fibre orientation and fibre concentration in the

actual failure zone. Another reason is the chosen representative cross-section for the theoretical residual strength included in η. In Figure 5.7 the whole cross-section is included. Yet, as illustrated in Figure 5.6, considering only the lower third of the cross-section does not reduce the scatter. Obviously, the number of activated fibres increases as the crack develops. Hence the cross-section area of fibres contributing is not constant, and therefore it is difficult to choose a representative cross section area of activated fibres between 0.5 and 2.5 mm deflection, corresponding to the residual strength determined from the equivalent bending strength.

5.2.6 Finite element analysis

Finite element analyses were carried out to find a simplified stress-crack width relation which assures correspondence between the analyses and the experimental results. Further, this stress-crack width relation will be used as a basis for stress-strain relations in the total strain rotating crack model used in chapter 7, 9, 10 and 11.

For all beams, one crack developed near the middle as shown in figure 6.8. A simple model of the beams is made in FEMGEN DIANA 9.1, using a discrete crack approach with interface elements to define the crack. The traction is expressed as a function of the displacements between the nodes in the interface elements; three different multi-linear approaches are used, FEM1, FEM2 and FEM3, as illustrated in Figure 5.10. The main material is assumed to behave in a linear elastic fashion, while the discontinuity captures the non-linear effect. By comparing the analyses with the experimental results, the objective is to find a simplified stress- crack width relation which describes the material behaviour.

Figure 5.8: One crack developed in the midsection for all beams, here beam W14-1.

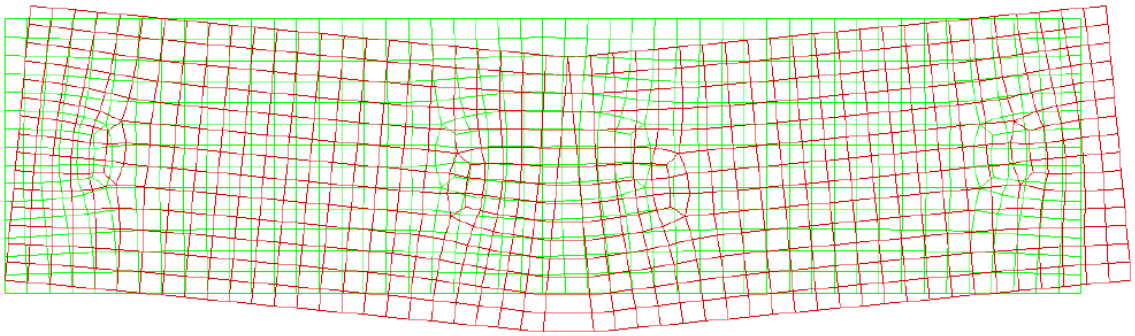

Figure 5.9: Element mesh and deflection shape of the beam in DIANA. Six-node interface elements define the crack in the middle of the beam.

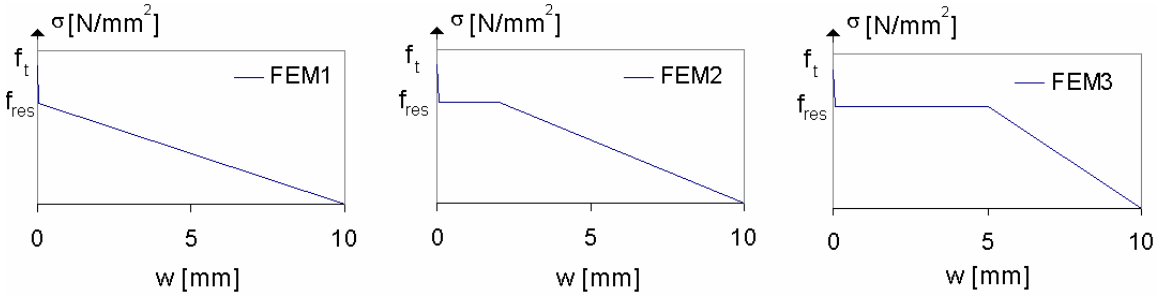

Figure 5.10: Three multi-linear stress-crack width relations in tension. The residual strength is reached at a crack width of 0.05mm, and the stress is zero at 10mm. In model FEM1, the stress decreases linearly after reaching the residual strength, while it is constant until 2mm and 5mm for model FEM2 and FEM3 respectively.

The three multi-linear stress-crack width relations are applied in the finite element analysis of nine beams. The residual strengths are calculated from the equivalent bending strength as described earlier. Figure 5.11 to Figure 5.13 illustrates the results of the beams sawn from element W13, W14 and W24. It is clear that the second approach, FEM2, is closest to the registered load-deflection relation, which is not unexpected since the residual strength is determined from the average load response between 0.5 and 2.5mm deflection. Yet, at larger deformations the first model, FEM1 is in best agreement for three of the beams: W13-3 and W14-2 and W24-2.

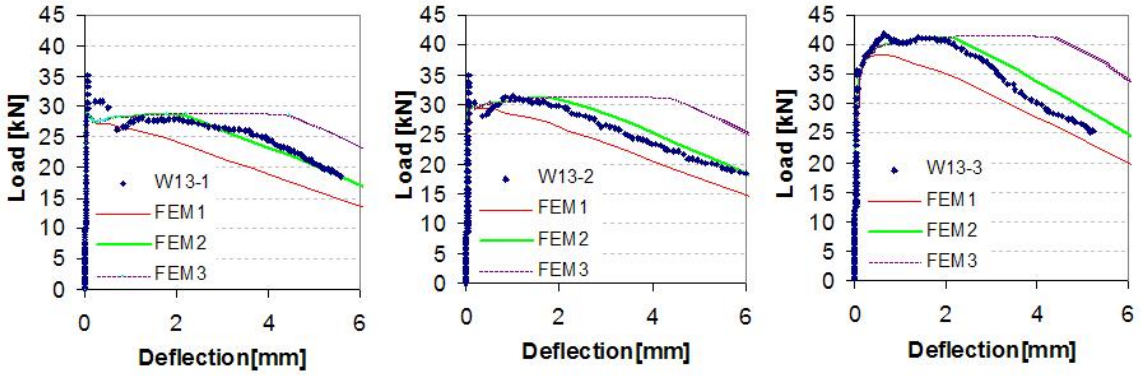

Figure 5.11: Measured load-deflection relation compared with FEA results for the three beams sawn from element W13 with VCC.

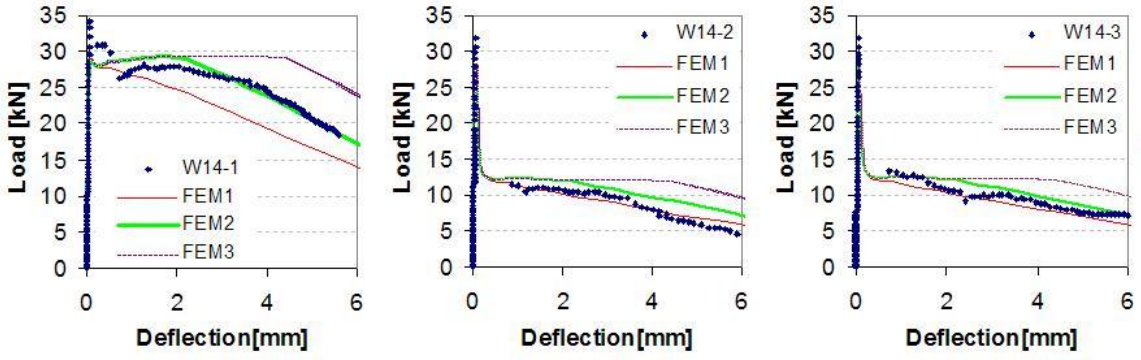

Figure 5.12: Measured and calculated load-deflection relation for the three beams from element W14 with VCC.

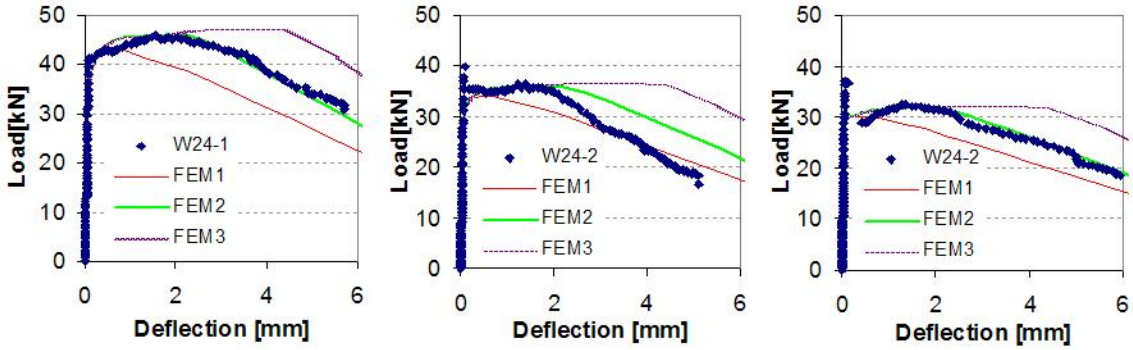

Figure 5.13: Measured and calculated load-deflection relation for the three beams from element W24 with SCC.

5.2.7 Conclusions

From the experiments, the following observations and conclusions are made:

- The relation between the fibre orientation and the residual strength is clear, although the scatter is relatively large.

- The volume distribution of fibres through the structural elements is approximately constant, both with VCC and with SCC. For the VCC-wall the average residual strength is 38 % higher for the horizontally sawn beams than the vertically sawn beams. Moreover, the average orientation factor for all 12 beams in the VCC wall is 0.55, which is close to the theoretical factor of 0.54 when the wall-effect is considered. For the VCC slab, the main orientation of the fibres is varying, and is far from isotropic for the six sawn-out beams. From these tests, it is difficult to make general conclusions on the fibre orientation in construction elements of VCC when an immersion vibrator is used, since the vibrator causes zones with uneven orientation and distribution of fibres. Therefore, when compaction has to be done with an immersion vibrator, it is important to avoid the zones which are most critical or exposed to tension in the construction. For the SCC slab the residual strength is higher

then in the VCC slab, at the same time as the scatter is relatively low. Based on these tests, FRSCC seems more suited in slab elements, assuming that the casting method provides a propitious concrete flow. The fibre-orientation in the SCC wall is mainly horizontal near the casting point, while it was more vertical in the other end of the formwork. The result of the beams taken from the SCC wall underlines the dependence of the flow, which with the current casting method causes a complex and non-uniform flow direction.

- The post cracking strength is higher for the SCC beams than for the VCC beams. By comparing the average theoretical residual strength with the average residual strength found from the measured data for each of the concrete types, the average post-cracking stress $\sigma_{av,VCC}$=300 N/mm^2 for the VCC while it is $\sigma_{av,VCC}$=500 N/mm^2 for the SCC, even though the compressive strength of the two concretes was similar. One possible reason for the difference in post cracking strength is that the pore structure is more refined in the SCC due to higher content of silica, which again might lead to improved bonding between matrix and fibres. Moreover the matrix content is higher in the SCC, which may influence the porosity in a favourable manner. Still, the difference in post-cracking stress is higher than expected.

- Using a discrete crack approach with interface element, FEA shows that a good approximation to the material behaviour in tension for the 60mm long hooked end steel fibres is a multi-linear relation where the tension is kept constant to a crack width of 2mm after reaching the residual stress. In the applied material model the tension then decreases linearly to zero at a crack width of 10mm.

6 Concrete beams reinforced with steel fibres and bars

6.1 Fibres as additional reinforcement

Use of FRC as replacement for ordinary reinforcement bars is limited to structures of short spans and can only be recommended for relatively low reliability classes. FRC combined with reinforcement bars has however a much wider range of application. As discussed introductorily, the fibres can be used to reduce the amount of reinforcement bars, primarily in order to improve the productivity and to reduce the heavy reinforcement work.

Earlier experiments show that beams with fibres as additional reinforcement exposed to bending have similar behaviour as traditional reinforced beams, although, at failure, all inelastic deformations concentrate in one single cracked section for FRC. [Espion et al (1993), Schumacher (2006)].

Moreover, as discussed in section 2.5.3, fibres can with advantage be used as shear reinforcement. This chapter presents the effect of fibres in experiments with beams designed for moment failure as for shear failure. It also emphasises the influence of concrete type and casting process.

6.2 Experiments: SFRC beams with VCC and SCC designed for moment and shear failure

6.2.1 Introduction

Two series of concrete beams were tested, the first with fibre reinforced vibrator compacted concrete (FRVCC), the second with fibre reinforced self-

compacting concrete (FRSCC). In total 7 beams were designed for moment failure ("moment beams") and 9 for shear failure ("shear beams"). An overview of the two series is given here:

Series A [Vabo 2001]:

- Four beams designed for moment failure and five beams for shear failure.
- The dimensions of the beams were b x h x L = 150 x 250 x 2850mm.
- The compression cube strength was $f_{ck} \cong 50$ N/mm^2 (VCC)
- A minimum of reinforcement bars was used in the moment beams, 2ϕ6mm, resulting in a reinforcement ratio of $\rho_s = A_s/A_c = 0.00166$. The shear beams were reinforced with 3ϕ16 ($\rho_s = 0.018$).
- Dramix steel fibres with a length/diameter ratio of 65 were added. The fibre lengths were 35mm and 65mm, and the fibre volumes 0 %, 0.5 % and 1.0 %.

Series B [Døssland 2002]:

- Three beams were designed for moment failure, five for shear failure.
- The beams were made with SCC with compression cube strength $f_{ck} \cong 60$ N/mm^2.
- Same dimensions and reinforcement as Series A.

The objective with the experiments was to investigate the effect of different fibre types and fibre volumes on beams in shear and bending, and to compare the test results with different available design methods. Moreover, the effect of concrete type (VCC/SCC) and casting procedure examined, focusing mainly on the orientation and distribution of fibres through the beams. Finally, finite element analyses were performed on all beams.

6.2.2 Reinforcement

The beams designed for shear failure were made without stirrups in the shear zone, except for one VCC reference beam without fibres. The shear beams had a higher reinforcement ratio than the beams designed for moment failure. Table 6.1 shows the tensile properties of the three reinforcement diameters.

Bar	Modulus Aut Young [MPa]	Stress at offset Yield 1 [MPa]	Stress at Max. Load [MPa]	Strain at Max Load [%]
ϕ6 Series A	227754	606	690	4.95
ϕ6 Series B	218653	651	717	3.98
ϕ8	207196	516	618	11.8
ϕ16	211809	505	603	13.1

Table 6.1: Average values of three samples from each reinforcement

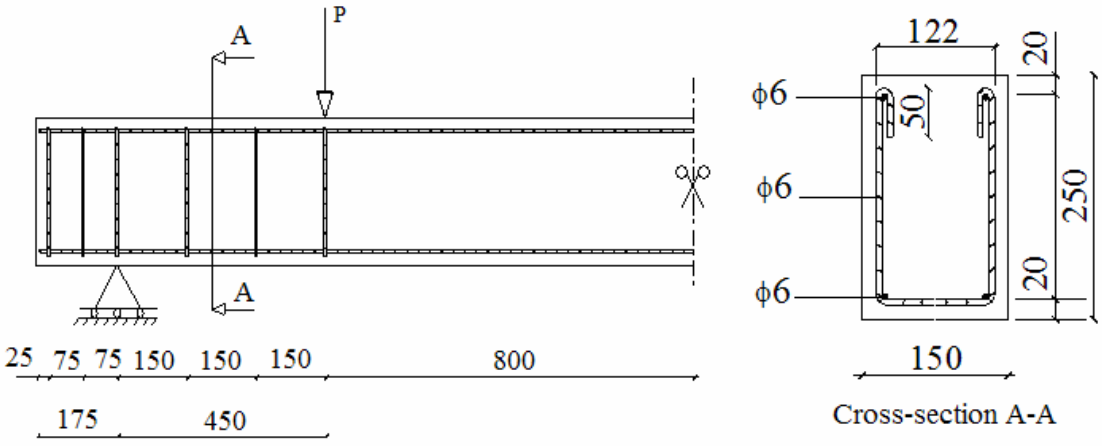

Figure 6.1: Geometry and reinforcement layout of beams designed for moment failure.

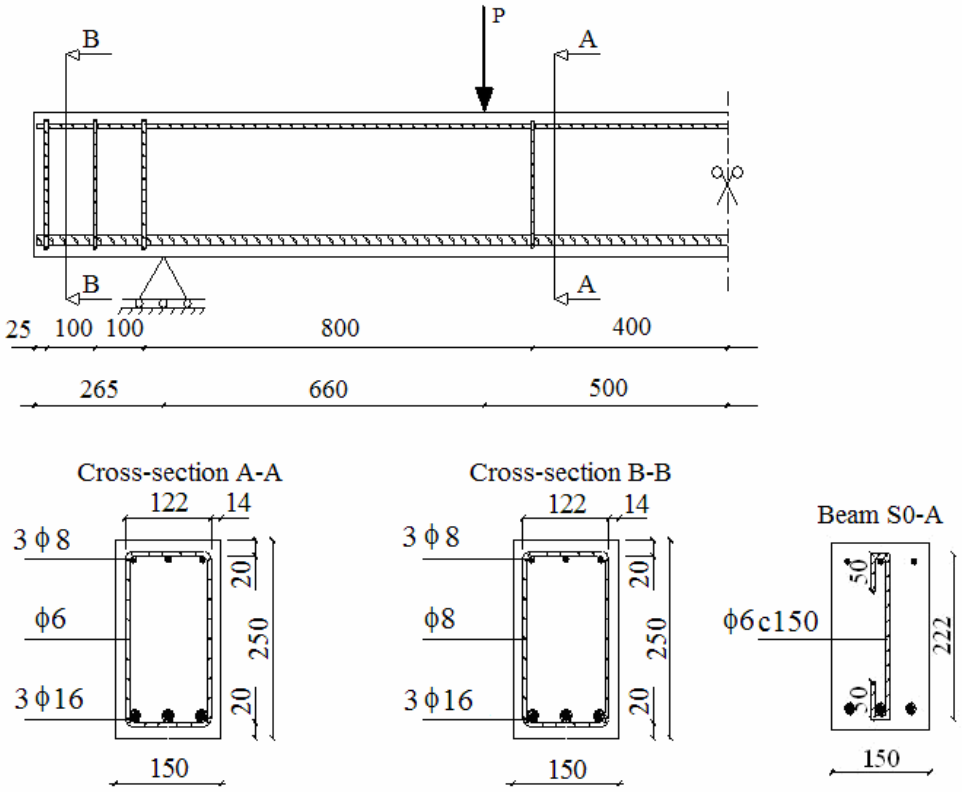

Figure 6.2: Geometry and reinforcement layout of beams designed shear failure. Beam S0-A had additional stirrups in the shear zone, as illustrated.

6.2.3 Concrete and casting

An overview of the beams with appurtenant concrete properties in the fresh and hardened state is given in Table 6.3.

Material	VCC	SCC
Cement “Norcem Standard FA”	320.0	335.1
Silica “Elkem Mikrosilika”	8.0	26.8
Fine aggregate 0-8 mm, river sand	912.4	981.9
Fine aggregate 0-2 mm, river sand	182.5	292.6
Aggregate 8-11 mm	365.0	263.0
Aggregate 11-16 mm	365.0	263.0
Water	186.2	153.6
Admixture		
Scancem P	2.300	1.34
Mighty 150	0.259	-
Scanflux SSP2000	-	3.35
Dramix 65/60	38.5	38.5

Table 6.2: Concrete composition, VCC and SCC with 0,5% fibres. The other mixtures in the two series were similar, but the content of admixtures (Mighty 150 / Scanflux SSP2000) was increased with increasing fibre content.

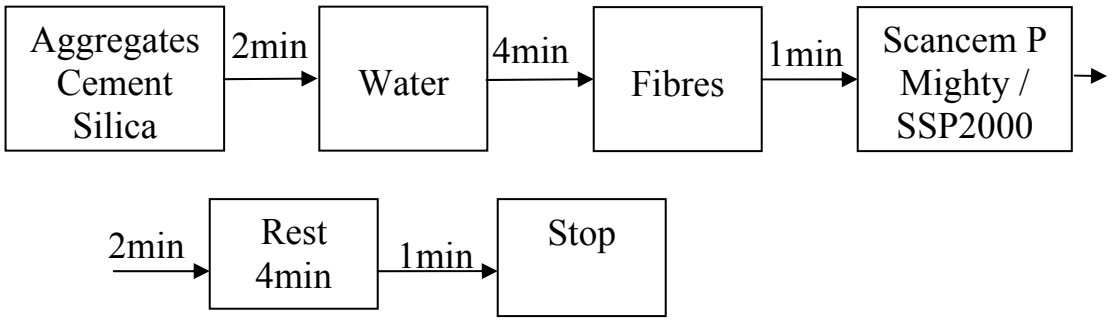

Figure 6.3: Mixing procedure.

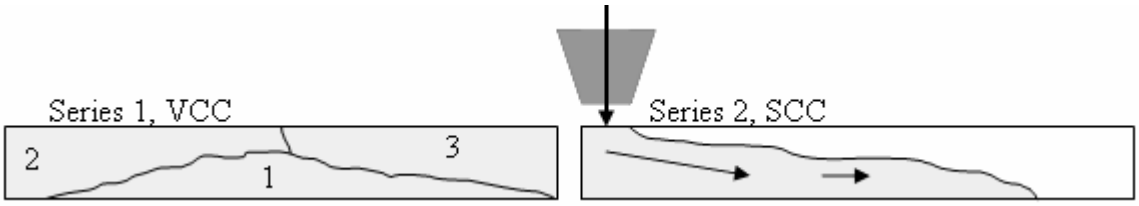

Figure 6.4: Casting. In series 1, the concrete was filled and vibrated in three layers as sketched. In series 2 the concrete was poured through a funnel from one side until the formwork was filled.

In series A, the concrete was poured from a concrete scip in 2-3 layers and vibrated until the formwork was filled. For the SCC beams, the concrete was poured from the scip through a funnel from one side of the formwork. In both series, the fibres tended to cluster when opening and closing the concrete scip. The scip therefore had to be opened fast and nearly wide open to ensure an even distribution of fibres. Some problems did occur while casting the SCC shear beams, where the flow was hindered by fibre blocking in front of the stirrups. This problem was especially pronounced for beam S4-B, were complete blockade occurred. The reason for this was that some additional stirrups were placed in the middle of beam S4-B and S5-B in an attempt to force the fibres in to a more uni-directed orientation (6ϕ6 c160, shape as additional stirrups S0-A, Figure 6.2). Due to the difficulty that occurred while casting beam S4-B, shorter fibres were used for beam S5-B. After demoulding, all beams were stored for 28 days in moistened burlap sacks at room temperature. The following test specimens were taken from each mixture:

- 6 cubes 100 x 100 x100 to measure the compressive strength.
- 3 cylinders 145 x 300 to measure the splitting tensile strength.

The E-modulus (2 cylinders 145 x 200) was measured only on the reference mixtures without fibres (M1-A and M1-B) as $E_{c,VCC}$=34620 N/mm^2 and $E_{c,SCC}$=31550 N/mm^2.

Beam test	**Name**	**Fibre volume [%]**	**Slump/ Slump flow [mm]**	**Air [%]**	**Density [kg/m^3]**	**Cube strength [N/mm^2]**	**Splitting tensile strength [N/mm^2]**	**Tensile str.** [N/mm^2]**
Series A VCC	M1-A	0	90	2.4	2.40	51.6	3.06	2.17
	M2-A	0.5	120	2.2	2.42	48.9	3.59	2.10
	M3-A	1.0	110	2.4	2.45	54.1	4.42	2.33
	M4-A	1.0*	120	3.8	2.40	43.3	4.44	2.05
	S0-A	0	*Equal to M1-A*					
	S1-A	0	*Equal to M1-A*					
	S2-A	0,5	*Equal to M2-A*					
	S3-A	1,0	*Equal to M3-A*					
	S4-A	1.0*	*Equal to M4-A*					
Series B SCC	M1-B	0	610	1.0	2.36	60.3	4.3	2.46
	M2-B	0.5	700	1.2	2.38	60.7	4.1	2.47
	M3-B	1.0	700	0.8	2.36	59.2	4.8	2.43
	S1-B	0	*Equal to M1-B*					
	S2-B	0.5	*Equal to M2-B*					
	S3-B	1.0	*Equal to M3-B*					
	S4-B	0.5	*Equal to M2-B*					
	S5-B	0.5*	625	-	-	62.3	4.7	2.52

*Table 6.3: Concrete properties in the fresh and the hardened state for Series A (VCC) and Series B (SCC). "M" denotes the beams designed for moment failure and "S" the beams designed for shear failure. The beam S0-A was made with stirrups in the shear zone, the other shear beams without. *) Dramix 65/35. Dramix 65/60 is used for all other beams. **) interpolated from NS3473*

6.2.4 Instrumentation and test setup

The strains were measured by extensometer and by strain gauges. The measuring points for the extensometer are shown in Figure 6.5. The beams designed for moment failure had two strain gauges fastened on the reinforcement bars in the middle of the beam to measure the tensile strain.

One PL-60 strain gauge were glued on top of the beam to capture the compressive strain [Figure 6.5]

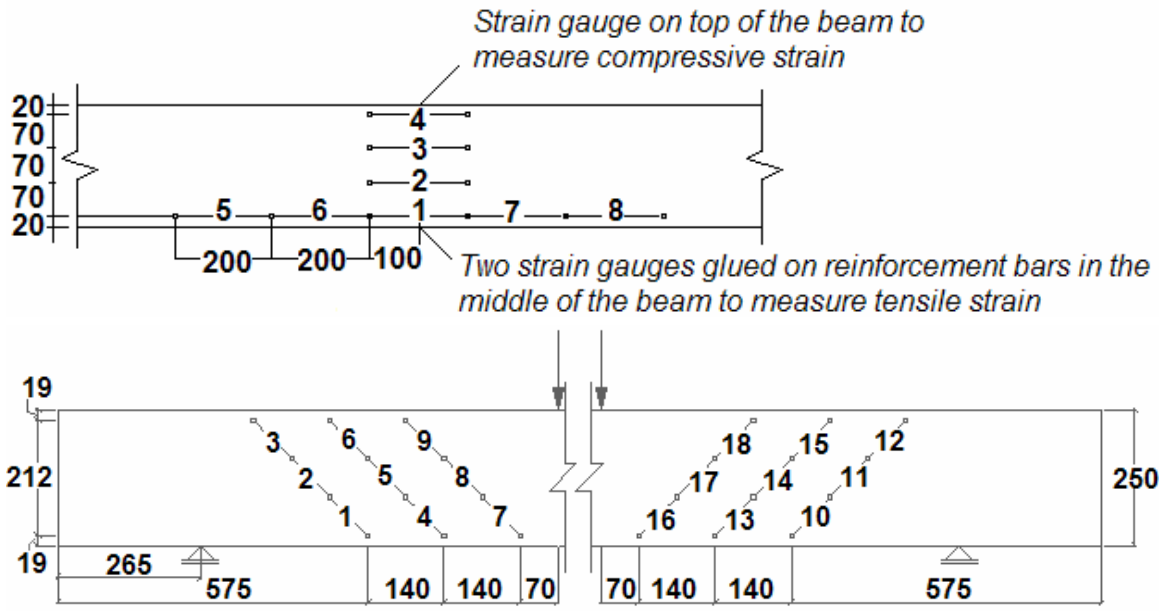

Figure 6.5: Brazen patches were glued on the concrete surface as measuring points for the extensometer. The figure illustrates the location of the patches on the moment- and shear beams respectively.

The deflections were measured over the supports, at the loads and in the middle of the beams. Dial gauges were used in series A, while LVDTs were used in series B with SCC.

All beams were simply supported and loaded with two equal point loads. The moment beams had a/d ratio 2.00 while the a/d ratio for the shear beams were 2.97 (a= horizontal distance from support to load, d = effective beam height). The load was applied by hydraulic jacks and held constant for about five minutes at each load step while the extensometer were read and the crack patterns were drawn.

6.2.5 Results - beams designed for moment failure.

An overview of the loads at first crack and at failure is given in Table 6.4. The load at the first visually observed crack varied with 18% for Series A and 38% in Series B. Roughly, these observations corresponds to the measured load-deflection ratios [Figure 6.8].

Beam	**Fibrevolume [%]**	**P_{cr} [kN]**	**M_{cr} [kNm]**	**P_u [kN]**	**M_u [kNm]**
M1-A	0	16.2	7.3	21.7	9.8
M2-A	0.5	18.6	8.4	27.1	12.2
M3-A	1.0	17.7	8.0	31.4	14.1
M4-A	1.0	15.7	7.1	29.9	13.5
M1-B	0	15.7	7.1	22.1	9.9
M2-B	0.5	15.7	7.1	34.3	15.5
M3-B	1	21.6	9.7	43.7	19.6

Table 6.4: Load at first crack and maximum load with appurtenant moments. Here:

P_{cr} *- Load as the first crack is observed*
M_{cr} *- Moment at first observed crack*
P_u *- Failure load/maximum load*
M_u *- Moment at maximum load*
$f_{ft,res}$ *- Residual strenght*

Compared to the reference beam without fibres, M1-A, the increase in moment capacity was 25%, 45% and 38% for M2-A, M3-A and M4-A, respectively. For Series B, the increase in capacity from the reference beam was 57% for M2-B and 98% for M3-B. The effect of fibres was accordingly more than twice as high for the beams with SCC compared to VCC. It is

important to stress the fact that the relative effect of the fibres would have been considerably smaller with a higher reinforcement ratio.

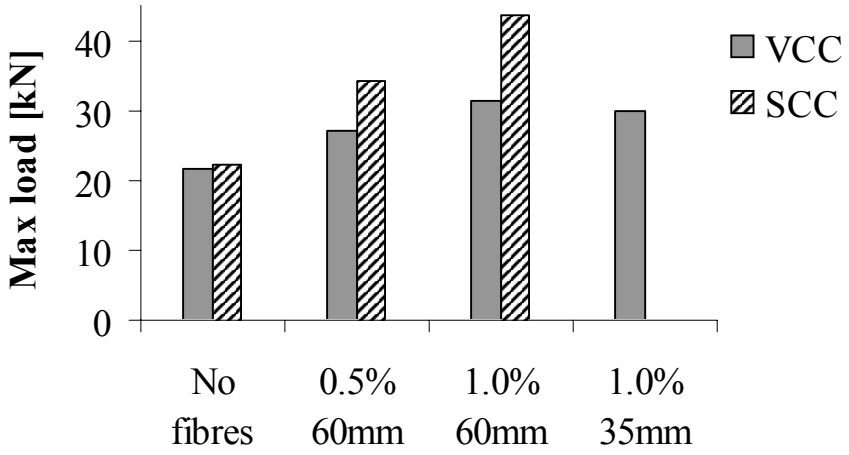

Figure 6.6: Ultimate loads for the beams designed for moment failure.

As illustrated in Figure 6.8 the moment capacity increases with increasing fibre content, at the same time as the ductility decreases. Beam M4-A with 1% 35mm long fibres reaches almost the same level as Beam M3-A with 1% 60mm long fibres, and the ductility is, surprisingly, larger. Nevertheless, it is difficult to get an accurate picture of the ductility, because the experiments are load controlled, not deformation controlled, which makes it hard to capture the descending branch of the load-deflection relation.

The measurements show that the strains increase considerable for all beams after reaching a tensile strain of around 0.1‰ [Figure 6.7], implying that the concrete starts cracking.

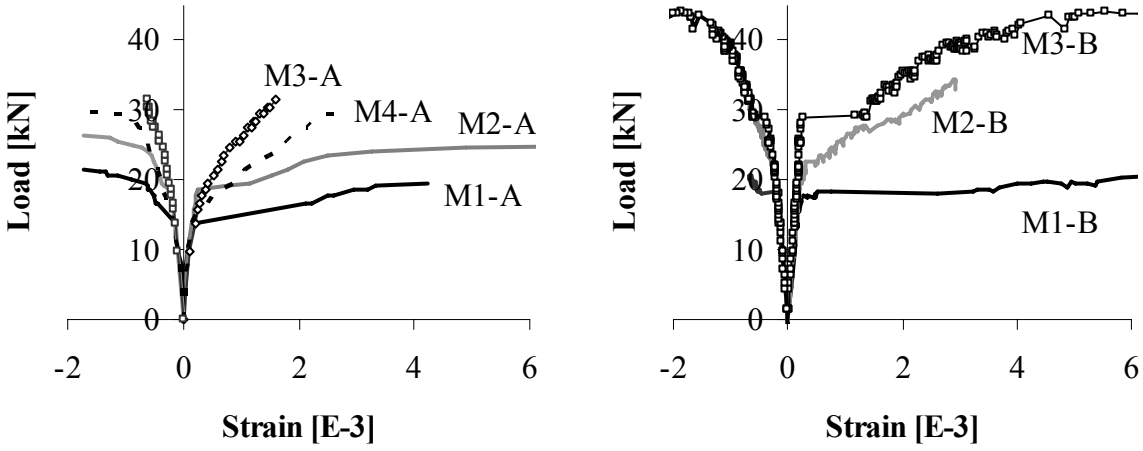

Figure 6.7: Strains in the middle of the beams. The strain was measured by strain gauges on top of the beam (compressive strains in concrete) and on the reinforcement bars (tensile strains).

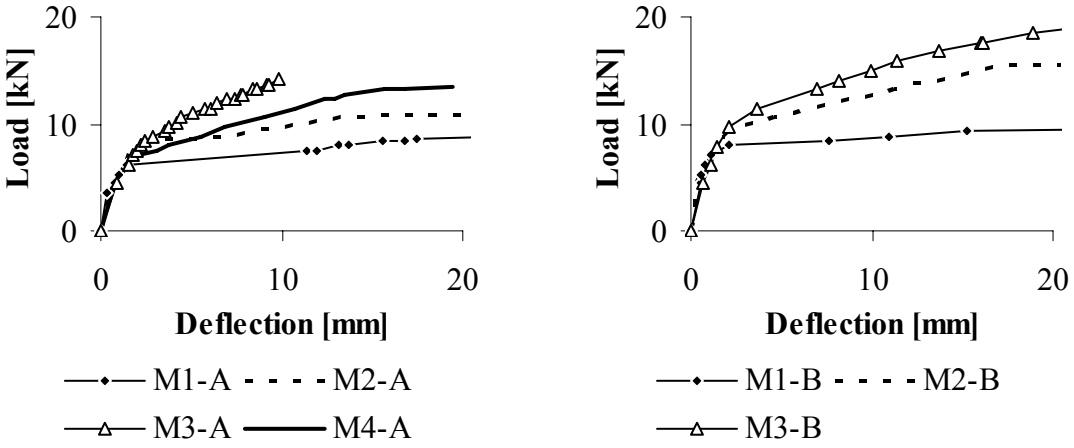

Figure 6.8: Load-deflection ratio in the middle of the beams designed for moment failure

The cracks were more or less evenly distributed between the two loads with average crack distances as shown in Table 6.5. It is clear that the number of cracks increased with increasing fibre content.

M1-A	200
M2-A	123
M3-A	80
M4-A	107

M1-B	200
M2-B	80
M3-B	64

S1-A	91
S2-A	63
S3-A	45
S4-A	71

S1-B	77
S2-B	63
S3-B	63
S4-B	71
S5-B	67

Table 6.5: Average crack distance between the two loads [mm].

Figure 6.9: Cracks in beam M2-A; average crack distance 123mm. The cracks were traced with a marker for each load-step.

As the beams reached their peak load, the deformations localized in one large crack, and failure followed as the concrete crushed in the compression zone.

6.2.6 Design load - beams designed for moment failure

Similar to RILEM's σ-ε method [RILEM 2003] the behaviour of SFRC under tension can be described by a flow chart for uni-axial stress. The flow chart used in this research [Figure 6.10] to estimate the capacity of the beams is somewhat simpler than the recommendations of RILEM.

Especially two parameters are important to establish the post-cracking behaviour; the residual strength $f_{ct,residual}$ and the appurtenant strain limit ε_{ult}.

The post-cracking strains are dependent on several factors; mainly the crack widths in the interval where the residual strength is approximately constant, the distance between the cracks and the fibre length. For the subsequent calculations, it is sufficient to use constant values for the ultimate strain and the negative slope after cracking; here taken as ε_{ult}=10‰ and $E_{c,neg}$=10000N/mm^2.

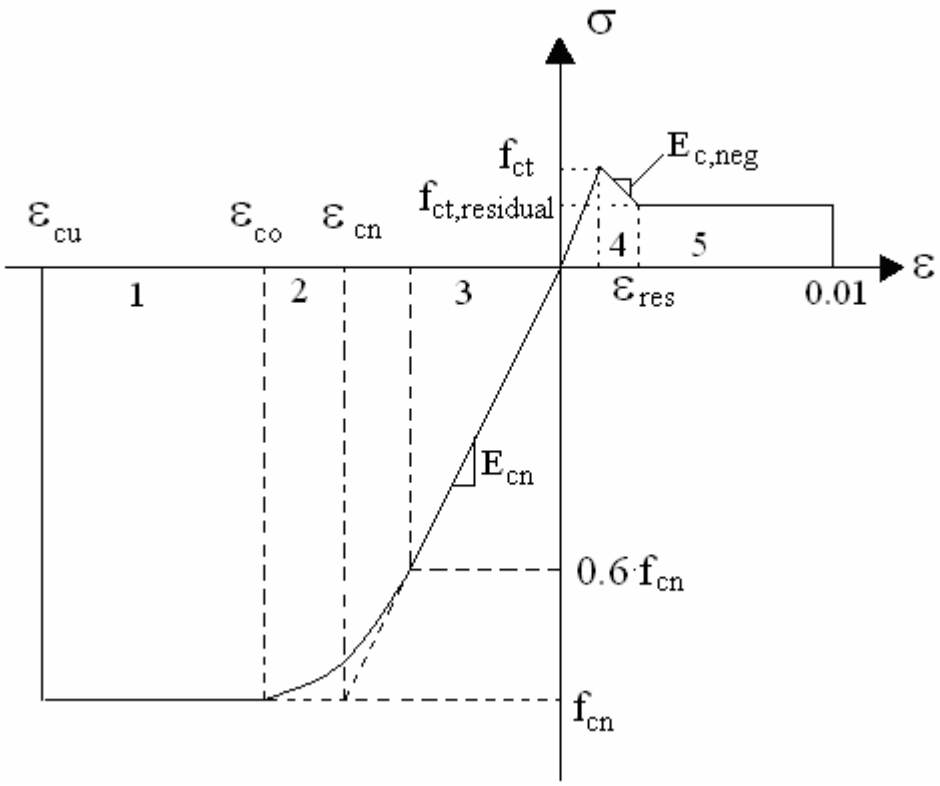

Figure 6.10: Flow chart for SFRC [Døssland, 2002]

Here:

$\varepsilon_{cu}=(2{,}5\varepsilon_{c0}/\varepsilon_{cn} - 1{,}5)/\varepsilon_{cn}$

$\varepsilon_{cn}=-f_{cn}/E_{cn}$,

$\varepsilon_{c0}=-0{,}0019-0{,}004f_{cn}$

$\varepsilon_{res}= f_{ct}/E_{cn} +(f_{ct}-f_{ct,res})/E_{c,neg}$

The stress in the different strain intervals marked 1-5 in the figure can be found from the following expressions, where the compressive behaviour is taken from NS3473 (2003):

1 $\sigma_c = -f_{cn}$

2 $\sigma_c = E_{cn} \cdot \varepsilon_c + (m-1) f_{cn} \left(\frac{\varepsilon_c \cdot E_{cn} + 0{,}6 f_{cn}}{(0{,}6-m) \cdot f_{cn}} \right)^{\frac{m-0{,}6}{m-1}}$

3 $\sigma_c = E_{cn} \cdot \varepsilon_c$

4 $\sigma_c = f_t - \left(\varepsilon_c - \frac{f_t}{E_c} \right) \cdot E_{c,neg}$

5 $\sigma_c = f_{ct,residual}$

Two methods for estimating the residual stress $f_{ct,residual}$ are considered; The method proposed in the Norwegian SFRC design rule draft, and the procedure suggested in the Dramix guidelines.

In the Norwegian Design rule draft, the residual strength can be taken as [Chapter 4.1.2]:

$f_{ct,residual} = \eta_0 \cdot v_f \cdot \sigma_{f,average}$

where :

η_0 is a factor dependent of the fibre orientation

v_f the fibre content

$\sigma_{f,average}$ is the average post-cracking stress

In the Dramix guidelines, the residual strength is determined based on three point bending tests on beams of dimension 150 x 150 x 450mm. The method is described in chapter 4.1.1. When it is not practical to perform beam

experiments, the residual strength can be taken as $f_{res}=0,37f_{fct,eq,150}$, where $f_{fct,eq,150}$ is determined from the following expressions:

$$f_{fctm,eq,150} = \frac{R_{em,150} \cdot f_{ctm,fl}}{100}$$

where $R_{em} = \frac{180 W_f \lambda_f d_f^{1/3}}{180C + W_f \lambda_f d_f^{1/3}}$, $f_{ctm,fl} = \frac{0,3 f_{ck}^{2/3}}{0,6}$

and the characteristic equivalent bending strength $f_{fctk,eq,150} = 0.7\ f_{ctm,eq}$. Here W_f is the fibre content [kg/m^3], λ_f the ratio fibre length l_f to diameter d_f and C=20 for Dramix fibres with end hooks. These expressions are based on experiments where the concrete cube strength f_c<40N/mm^2. For higher concrete qualities it is recommended to substantiate the calculated residual strength with experimental results.

The reinforcement bars are assumed to follow an idealized stress-strain relation with a maximal strain of 10‰.

Calculation and evaluation of the test results – multi-layer model

The multi-layer model for the flexural response of beams was developed by Hordijk (1991). Later on, Kooiman (2000) showed that the model was applicable for FRC, and further, Grünewald (2004) used the multi-layer model for FRSCC.

The beams evaluated in this chapter are calculated by dividing the beam cross-section into 20 layers as shown in Figure 6.11.

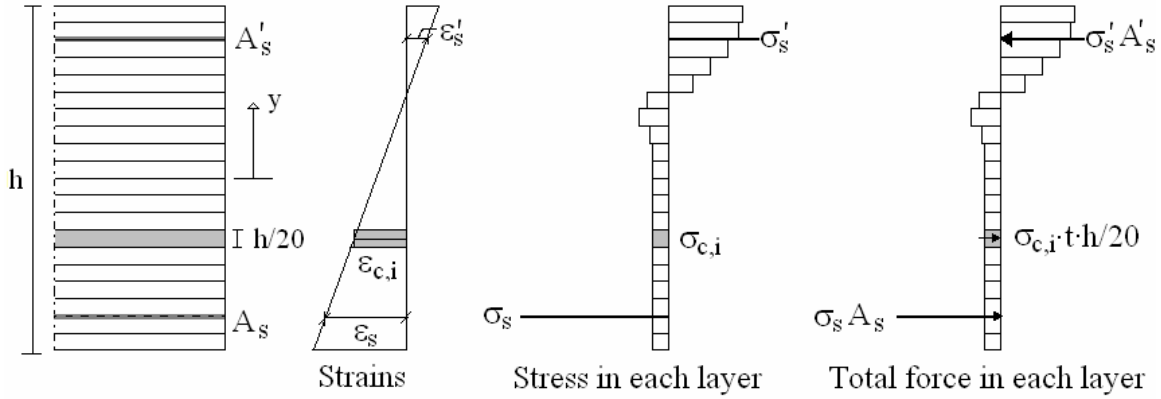

Figure 6.11*: Multi-layer model with the beam divided into 20 layers*

Axial force and moment can approximately be taken as:

$$N \approx \sum_{i=1}^{20} \sigma_{c,i} \cdot t \cdot \frac{h}{20} + \sigma_s A_s + \sigma_s' A_s' \approx 0$$

$$M \approx \sum_{i=1}^{20} \sigma_{c,i} \cdot t \cdot \frac{h}{20} y_i + \sigma_s A_s y + \sigma_s' A_s' y$$

With a linear strain distribution over the cross section height, a chosen strain (for example in top of the beam) gives the stress in each layer by the formulas 1-5 in Figure 6.10. The strain is also used to determine the resulting stresses in the compressive and tensile reinforcement bars. For each strain that is chosen, a simple spreadsheet is used to calculate the strains and stresses over the whole cross-section by solving the equation for the moment and fulfil the criteria N=0. Subsequently the moment-curvature relation for the beam can be determined.

Comparing the calculated moment-curvature relation to the moment-curvature ratio deduced from the recorded deflection data indicates that the residual strength for the experiments were higher than the calculated strengths based on Dramix Guideline. The values determined by Sintef's method correspond slightly better to the test results, but for the SCC beams, the capacity is

considerably underestimated. The occurring residual strength in the beams is determined by adjusting the theoretical moment-curvature relation to the registered one by changing the residual strength in the multi-layer model until the curves are similar. One example of this is shown in Figure 6.12. The calculated values for the moment beams are presented in Table 6.6.

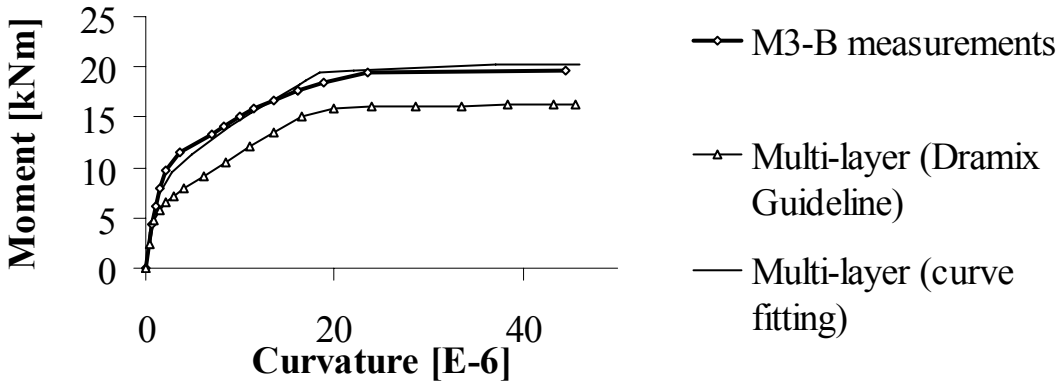

Figure 6.12: Moment-curvature ratio for beam M3-B compared with the results of the multi-layer model with $f_{res,Dramix\ \ Guideline}=1.78N/mm^2$. The appearing residual strength is determined by curve-fitting to the curvature determined from the deflection data (here $f_{res,curve\ fitting}=2.83N/mm^2$).

Beam	$f_{res,Dramix}=0,37f_{fct,eq,150}$	$f_{res}=\eta_0 \cdot v_f \cdot \sigma_{f,mean}$	f_{res} curve fitting
M2-A	1.07	0.83	0.85
M3-A	1.66	1.67	1.65
M4-A	1.35	1.67	1.50
M2-B	1.29	0.83	1.70
M3-B	1.78	1.67	2.83

Table 6.6: Residual strength determined from three different methods; Dramix Guidelines (1997), Sintef's method and experimentally by curve fitting.

Table 6.6 shows that the occurring residual strengths determined by curve fitting are in good accordance both with Dramix and Sintef's method for the

VCC beams. The residual strengths for M2-B and M3-B, on the other hand, are much higher than the calculated residual strengths. For M3-B the residual strength estimated from curve fitting is even higher than the tensile strength of the concrete.

6.2.7 Distribution and orientation of fibres – moment beams

After the experiments had been carried out, fibres were counted on blocks sawn from the moment beams in series B with SCC. The fibres were counted on three planes perpendicular to each other.

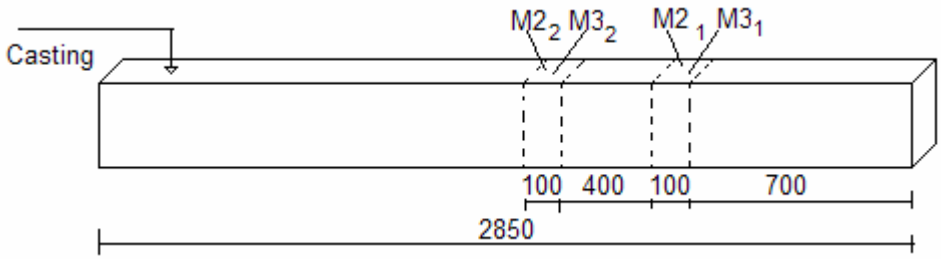

Figure 6.13: Sawn out blocks for fibre counting, beam M2B and M3B.

In the lower part of the cross-section, the fibres clearly had a preferred orientation in the longitudinal direction of the beam. By considering the fibres partly as isotropic, partly plan-orientated and partly uni-directed, the fibre counting showed that between 16% and 27% of the fibres had an isotropic orientation [Figure 6.15]. This is quite far from the typical orientation in vibrator compacted concrete, where it often is considered sufficiently accurate to assume an ideal situation with 100% isotropic orientation.

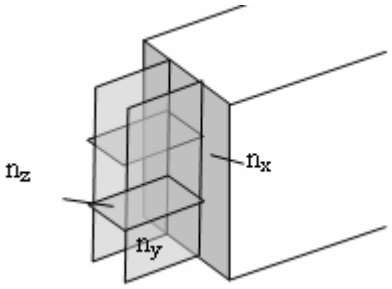

Figure 6.14: The fibres were counted on sawn-out planes perpendicular to each other as illustrated.

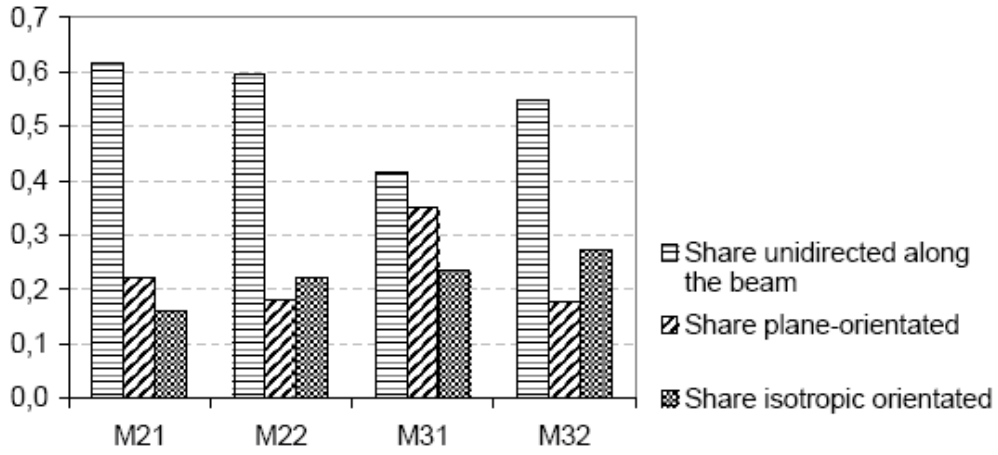

Figure 6.15: Fibre orientation in the lower half of the beam; two blocks from beam M2 with 0.5% fibres and two from beam M3 with 1% fibres.

As described in chapter 2.6.3, the fibre volume can be estimated from fibre counting on three planes perpendicular to each other:

$$v_f = (N_1 + 9/16 \cdot N_2 + 7/16 \cdot N_3) \cdot A_f / A_c,$$

where the number of fibres is denoted according to the following assumptions: $N_1 > N_2 > N_3$. Using this equation on the four sawn-out sections leads to fibre volumes of $v_{f,M21}=0.55\%$, $v_{f,M22}=0.59\%$, $v_{f,M31}=1.34\%$ and $v_{f,M32}=1.24\%$, which are higher than the added volumes of $v_{f,M2}=0.5\%$ and $v_{f,M3}=1.0\%$. This shows on one hand that the volume of fibres is not entirely constant through the beam. On the other hand, it indicates that the segregation resistance of the concrete is large, since the fibre volume does not decrease with increasing distance to the casting zone. This is also supported by fibre counting in the upper and lower half of the beam, which showed that in average 53% of the fibres were located in the lower half of the beam. Hence, the fibres did not sink much in the concrete.

X-rays were taken on two blocks with dimensions 400x250x54mm [Figure 6.16]. Although the pictures show that the fibres have a preferred orientation in the longitudinal direction of the beam, it is evident that the scatter is quite high. Still, the x-rays do not give a clear picture of the orientation, since a 3D

orientation situation is projected into a 2D photo. In order to use x-rays to establish the fibre orientation in a plane, thinner slices should be sawn from the concrete.

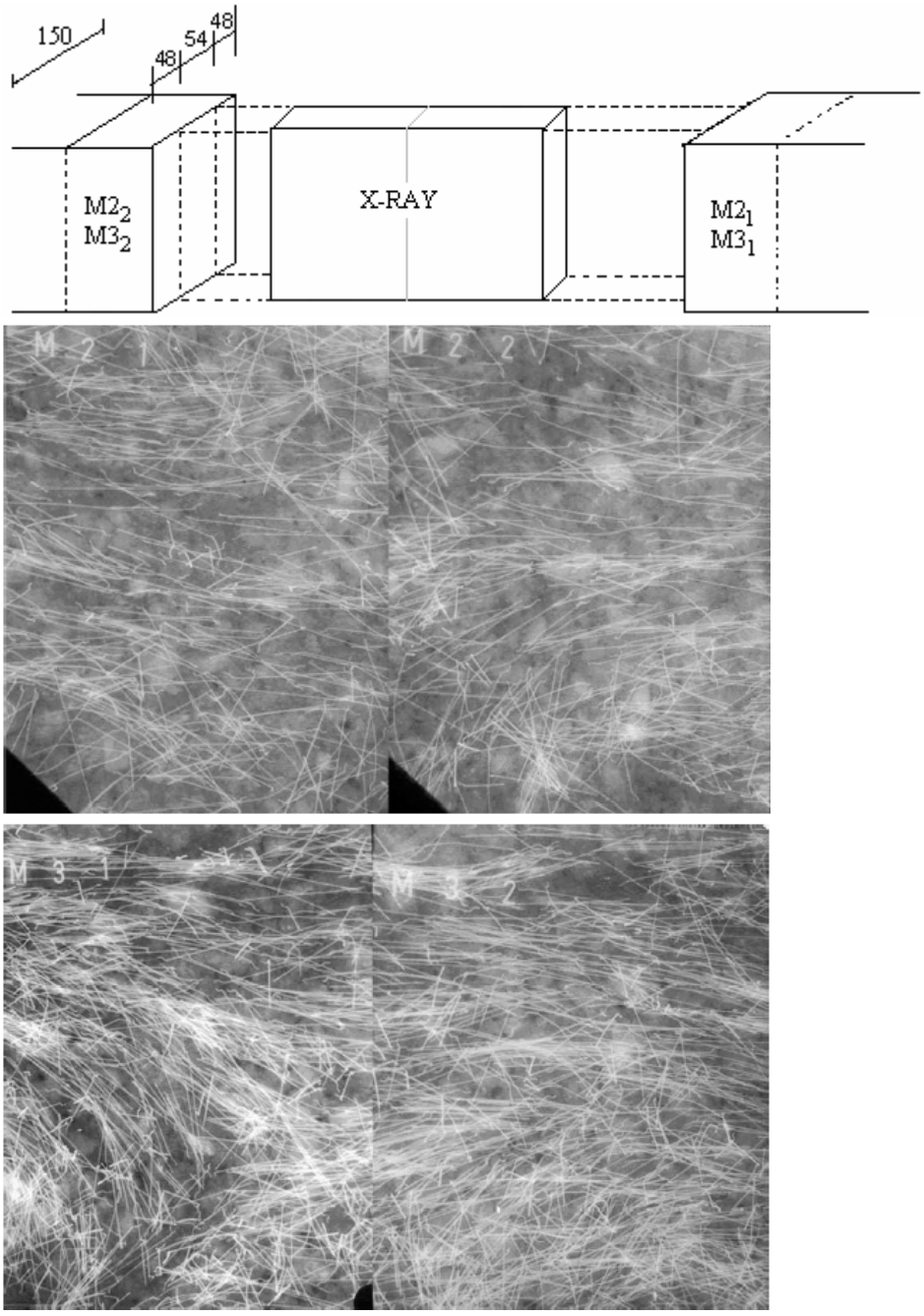

Figure 6.16: X-ray photo through 54mm thick blocks taken from beam M2-B and M3-B with SCC

The large difference in moment capacity between the VCC and SCC beams can primarily be explained by a favourable fibre orientation. The number of fibres counted in the longitudinal direction of the beams is in average 77% higher than the number of fibres in an ideal situation with evenly distributed isotropic orientated fibres. Yet, the capacity increase due to fibres for the SCC beams compared to the VCC beams is even larger than 77%; as illustrated in Figure 6.6 the increase due to fibres was more than twice as high for the SCC beams. Another factor that enhances the difference between the VCC and SCC beams is the increased post-cracking stress due to improved fibre-matrix bonding in the SCC. The reason for this improved fibre-matrix bonding is related both to the matrix strength and the concrete composition. Since the SCC has higher matrix content and contains more silica, it is likely that the pore structure is more refined, something that improves the fibre-matrix bonding. This is further discussed in section 5.2.5.

From the fibre counting it can be concluded that:

- In the lower half of the beam the fibres had a main orientation in the longitudinal direction, which indicates that the fibres had a preferred orientation parallel to the flow. The large share of uni-directed fibres can not be explained by wall-effect only.
- The volume of fibre did not decrease with increasing flow distance, nor was any considerable volume increase with increasing specimen depth observed. This indicates that the segregation resistance of the concrete was large.
- The large difference in moment capacity between the VCC and the SCC beams can primarily be explained by the favourable fibre orientation. Most likely the fibre-matrix bonding was higher in the SCC than in the VCC which enchanted the difference in moment capacity.

6.2.8 Results - beams designed for shear failure.

An overview of the loads at cracking and failure for the nine shear beams is given in Table 6.7

Series	Beam	Fibre volume [%]	P_{cr} [kN]	P_s [kN]	P_u [kN]
Series1	S0-A*	0	34.4	53.0	68.7
	S1-A	0	46.8	49.1	54.0
VCC	S2-A	0.5	35.3	69.7	79.5
	S3-A	1.0	37.3	53.0	110.9
	S4-A	1.0**	49.1	68.7	103.0
Series2	S1-B	0	0.0	58.9	58.9
	S2-B	0.5	27.0	63.8	81.4
SCC	S3-B	1.0	27.0	73.6	103.0
	S4-B	0.5	19.6	65.2	67.7
	S5-B	0.5**	19.6	73.6	83.4

*Table 6.7: Loads at first crack, first cross-crack and ultimate load. Here P_{cr} is the load at the first observed crack, P_s the load at first observed shear crack and P_u the ultimate load *) Beam S0-A were made with stirrups in the shear zone [Figure 6.2], the other beams were made without any shear reinforcement. **) Shorter fibres, Dramix 65/35*

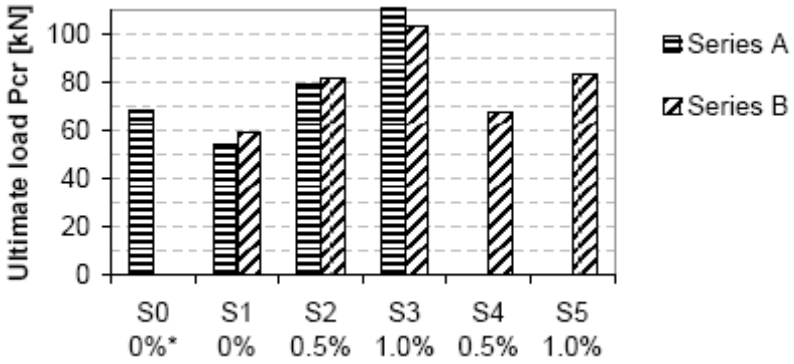

*Figure 6.17: Ultimate loads for the beams designed for shear failure. Beam S2 and S3 with Dramix 65/60, S4 and S5 with Dramix 65/35. *) S0-A were made with ϕ6c150 stirrups in the shear zone.*

Figure 6.17 illustrates how the shear capacity increases with increasing fibre content. The effect of fibres on the shear capacity is, in average, similar in the two series. As described in the previous section, fibre counting on the moment beams in series B indicates that the main share of fibres is orientated horizontally through the beam. It is therefore likely that there is an analogous reduction of the amount of fibres available to take up shear force in the five shear beams in the SCC beams. Yet, the differences between the two series are negligible. This may imply that no pronounced uni-directed orientation did occur in the shear-zone of the shear beams. But it is perhaps more likely that the post-cracking strength of the FRSCC is higher than in the VCC due to better fibre-concrete bonding, as the results in chapter 6 indicates. If so, a lower number of fibres are needed to achieve the same ultimate load as in series A.

S2-B and S4-B were originally expected to behave similar, since the only difference between them is the extra stirrups in the middle of S4-B, set up in an attempt to influence the fibre orientation. As already explained, this attempt failed as fibre blocking occurred. Therefore beam S4-B had a weakness zone

almost without fibres, which reduced the capacity noticeably. Beam S5-B with 0.5% Dramix 65/35 fibres reached approximately the same ultimate load as beam S2-B with longer fibres.

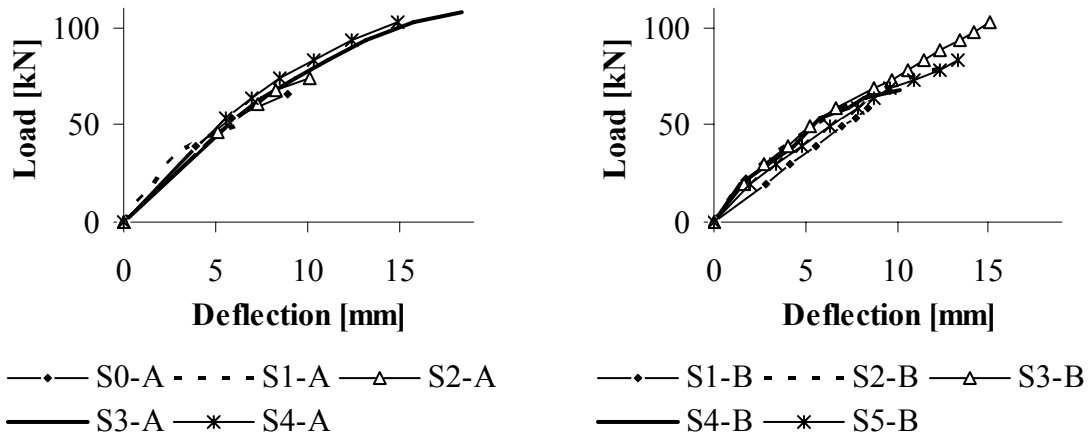

Figure 6.18: Load-deformation relation for the beams designed for shear failure; a) Series A with VCC b) Series B with SCC.

The deformation behaviour is approximately similar for all shear beams, although the beams with higher fibre content exhibit a somewhat more ductile behaviour. This especially holds for the VCC beams. Figure 6.18a shows that the deformation per load step is larger for the beams with most fibres. In addition, the figure shows that the behaviour of S0-A with stirrups in the shear zone is almost the same as S2-A with 0.5% fibres. Compared to the beam without fibres and stirrups (S1-A), 0.126% stirrups gives an increase in shear capacity of 27%, while 0.5% fibres gives 47% increase. This is reasonable since it is expected that 1/3 of the fibres are active in each direction. The behaviour of the SCC beams is more brittle than for the VCC beams, and it can also be seen from the figure that the E-modulus for the SCC beams is lower, which corresponds to the E-modulus measured on the test specimens.

6.2.9 Design load – beams designed for shear failure

Various models exist for calculating the shear capacity of FRC, of which some are reviewed in section 3.4. The ultimate loads measured for the beams designed for shear failure are compared with three of the models given in Table 3.1, here denoted A, B and C. The fourth model, D, used for comparison is deduced based on the contribution of stirrups to the shear capacity according the Norwegian Design rules NS3473 (2003) as described in section 3.4. Figure 6.19 present the relations between the test results and calculated shear capacities with the four alternative methods:

A: $\tau_u=(0.167\alpha+0.25F_1)f_c^{0.5}$ [Khunta et al.1999]
B: $\tau_u=[0.12k(100\rho\cdot f_{ck})^{1/3}+0.15\sigma_{cp}] + k_f\cdot 0.54f_{ctk,ax}(R_t/1.5)$; [Nemegeer 1996]
C: $\tau_u=e(0.24f_{sp}+80\rho d/a)+0.41\tau\cdot F$; [Narayanan & Darwish 1987]
D: $\tau_u=\tau_{cd}+ 0.9\cdot 1/3 v_f\sigma_{average}$.
where τ_{cd} is calculated from the Norwegian standard code NS3473.

For method D, an average stress in all fibres is taken as $\sigma_F=500N/mm^2$, and it is assumed that the distance to the pressure zone z=0,9d=200mm. The angle of the shear crack is taken as 45^0. Further details on the input-date are given in Appendix A.

In both series, the ultimate loads from the beam tests were higher than the calculated shear capacities, as illustrated in Figure 6.19. In average the ratios between the ultimate loads and the calculated capacities P_{max}/V_{calc} for all beams without stirrups were 1.32, 1.45, 1.23 and 1.05 for series A, B, C and D respectively. It is clear that method D based on the shear design load with traditional shear reinforcement corresponds best with the test results.

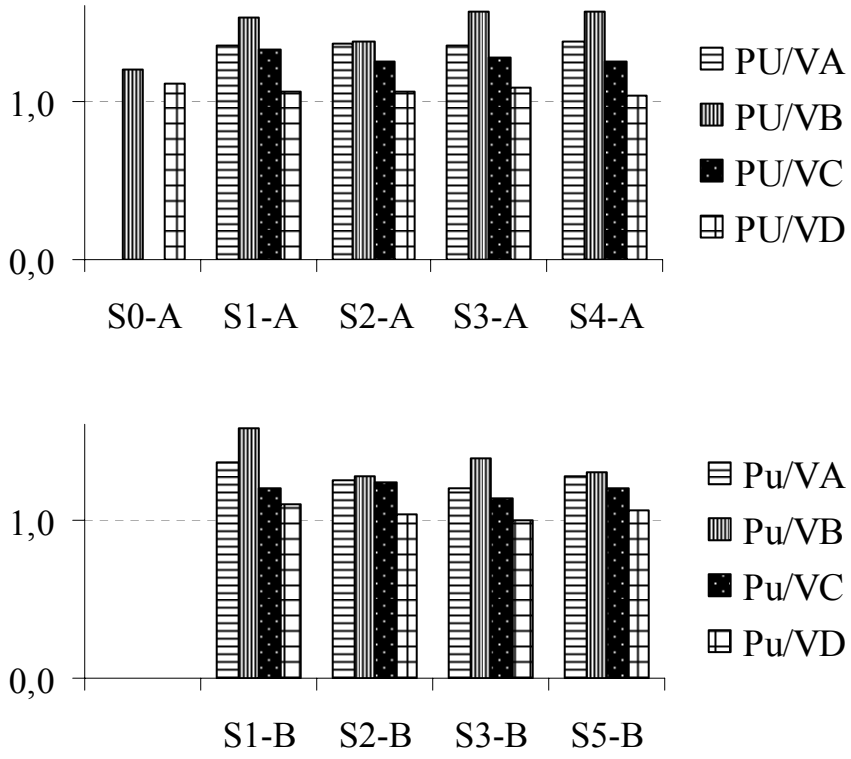

Figure 6.19: Relation between test results and calculated capacity, series A and B. Input data for calculations are listed in Appendix B.

6.2.10 Finite Element Analysis

Modelling the material behaviour

A smeared crack approach is used in the finite element modelling, assuming a homogenous isotropic material. For the beams reinforced with bars only the tensile behaviour of the concrete is modelled by a linear stress-strain relation, limited by tensile strength. Thereafter the stress decreases in an exponential strain-softening part. The strain-softening branch is determined by the fracture energy G_f and the numerical crack band width h_{cr}, where:

$G_f = \sigma_F \cdot (f_{cm}/10)^{0.7}$

Here f_{cm} is the mean cylinder strength in MPa and σ_f is a factor dependent on the maximum grain size d_{max} [CEB-FIP Model code, 1991]. Here σ_F=0.03 Nmm/mm^2 for d_{max}=16mm.

The crack band width (or the equivalent length) is dependent on the element size and shape and on the crack direction. Dahlblom and Ottesen (1990) introduced the crack band width to obtain a realistic modelling of crack sharing. This was essential for the objectivity of the smeared constitutive relations so that it was possible to establish a smeared version of the fictitious crack model. For higher order 2D elements, the value is normally taken as $h_{cr} = \sqrt{A}$ where A is the total area of the element [de Witte, 2002].

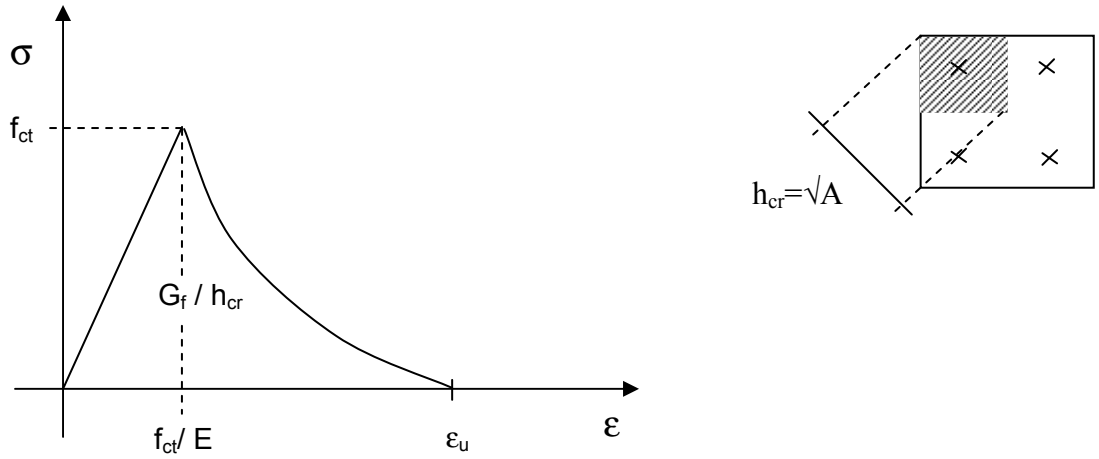

Figure 6.20: Strain softening curve used for the beams without fibres. Here f_{ct} is the tensile strength, E is the Youngs Modulus, G_f the fracture energy and h_{cr} the crack band width.

For the beams with fibres the tensile behaviour is modelled by a multi-linear relation, as shown in Figure 6.21. The stress-strain relation is based on the stress-crack width relation found in Chapter 6, and the plastic strains are found

by dividing the crack width with the average distance between the occurring cracks for each beam [Table 6.5]

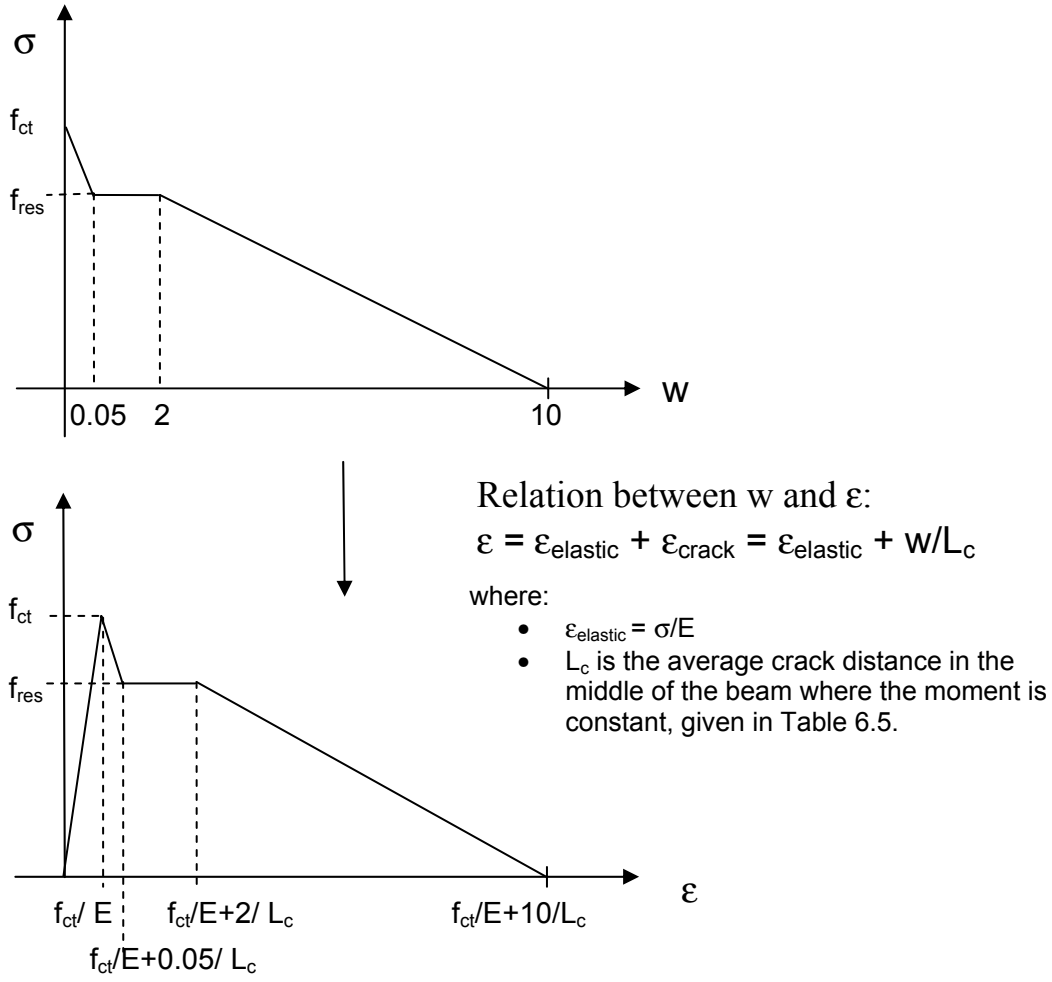

Figure 6.21: Multi-linear stress-strain relation based on a simple stress-crack width relation taken from earlier experiments with similar concrete and steel fibres.

The tensile strength is estimated from the compressive strength according to Table 5 in NS3473 (2003) [see Table 6.3], and the residual strength is taken as $f_{res}=\eta_0 \cdot v_f \cdot \sigma_{f,mean}$. It is assumed that the fibres are isotropic orientated with an average post-cracking stress of 500MPa. The values are given in Table 6.6.

The E-modulus was measured for the reference mixtures without fibres, and in both series assumed to be similar for the mixtures with fibres. The Poisson's ratio is taken as 0.2, assumed not to be affected by the fibre addition.

The compressive behaviour of the concrete is described by the extended Compressive Damage Zone (CDZ) model introduced in Chapter 2.5.1 with stress-strain relation determined from the expressions given in Figure 2.6. The following input parameters were used [Schumacher 2006]:

Filling degree	α_{fd} = 0.8/0.9 with VCC/SCC
Nominal compression strength	$f_c^* = 0.8 f_{c,cube}$ ($\approx f_{cc,cylinder}$)
Youngs modulus	$E_c = 0.9 \cdot 9500 f_c^{*(1/3)}$
Strain at maximum stress	$\varepsilon_0 = 0.7 f_c^{0.31} \cdot 0.8$
Proportionality factor	$k = 3.5 + 10 V_f l_f/d_f + 60e/h$, where e/h=1/6
Localized deformation	$w_c = 0.7$
Damage zone /total length	$L_d/L = 0.8 - 0.2 V_f l_f/d_f - e/h$
Total length	L = distance between supports

The compressive strength is taken as 80% of the measured cube strength, corresponding to the estimated cylinder strength. Due to the strain gradient in the compressive zone of the beams, an eccentricity of e/h=1/6 was used to estimate the proportionality factor k in the CDZ model, according to Schumacher (2006). To account for the confining action of the loading platen, an additional strain was introduced in the region under the load and further the compressive strength was increased by 10%.

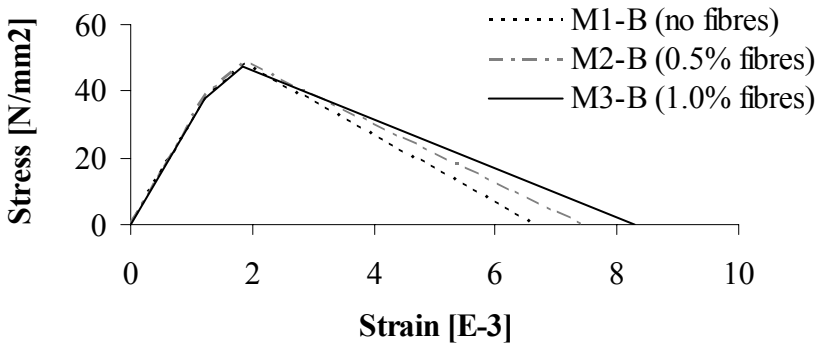

Figure 6.22: Compressive stress-strain relation for the three moment beams in series B.

The tensile material properties presented in Table 6.1 was used to model the hardening behaviour of the reinforcement.

Finite Element Model

An eight-node quadrilateral isoparametric plane stress element is used, based on quadratic interpolation and Gauss integration.

Figure 6.23: Plane stress element CQ16M in DIANA [De Witte et al. 2002]

The reinforcement is modelled with embedded reinforcement bars; any slip between the concrete and the reinforcement bars is not taken into consideration.

Due to symmetry, only half of the beams are modelled, as illustrated in Figure 6.24. The load was applied as a nodal force in deformation controlled steps.

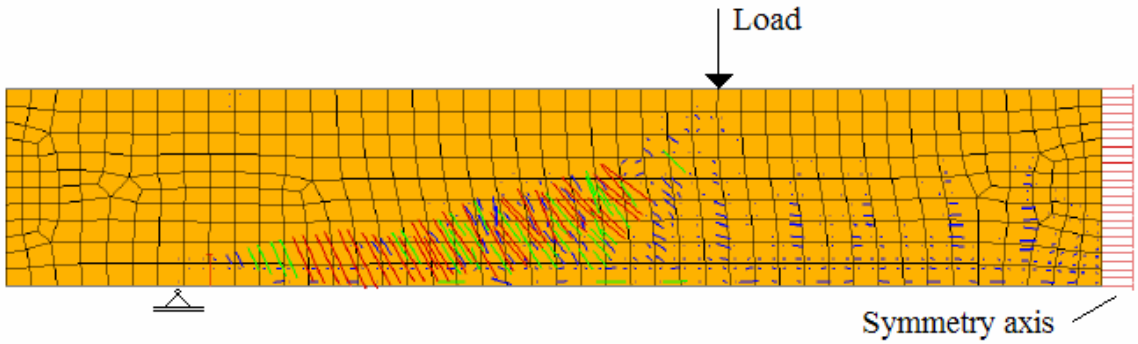

Figure 6.24: Element mesh for the shear beams. The figure also illustrates the crack pattern by vectors according to cracking strain size for beam S1-A when the shear crack is initiated (Green crack strain).

The results of the finite element analyses are compared with the test results in Figure 6.25 and Figure 6.26. In general, the agreement is good. However, for beam M2-B and M3-B the analyses underestimate the capacity. This is reasonable since the residual strengths in the analyses were based on isotropic orientated fibres, even though fibre counting showed that the fibres had a favourable distribution and orientation in the SCC beams. When the residual strengths, which were estimated by curve fitting between the experimental data and the multi-layer model are applied, the results of the analyses correspond with the experiments.

The capacity of beam M4-A is slightly overestimated by the analysis. Since the multi-linear stress-strain relation shown in Figure 6.21 is based on experiments with 60mm long fibres [5.2.6], it may not be appropriate use the same relation for beam M4-A with 35 mm long fibres. Still, due to lack of data, the same ε(w) ratio is used for beam M4-A. No fibre counting was done on the beams with VCC, but if the orientation through beam M3-A and M4-A is similar, the results imply that it is not sufficient to apply the current multi-linear stress diagram FRC with Dramix 65/35.

After cracking, the response of the test results appears to be stiffer than the analysis results. This can primarily be explained by the simplifications made in the material model [Figure 6.21]. The average crack width is determined from the total number of cracks after cracking in the zone with constant moment [Table 6.5]. In the experiments, the average crack widths decrease with increasing deflections, as more cracks develop. Thus, the constant crack width used in the FE-model results in too high cracking strains at an early stage.

For the shear beams, the response of the analysis also corresponds relatively well with the experiments, although the capacity of beam S2-B with 0.5% fibres is somewhat underestimated by the analysis. Moreover, the FE analyses seem to slightly overestimate the ductility of the beams with 1% fibres. As for the moment beams, the average crack width for the shear beams is taken as a constant value, determined from the total number of cracks that developed between the loads. In the experiments, the deformations localize in one shear crack. Hence, the simplification based on the total number of cracks may no longer be sufficient after initiation of the shear crack. Yet, altogether it seems like the FEA are able to capture the effect of fibres on the shear capacity of beams exposed to bending.

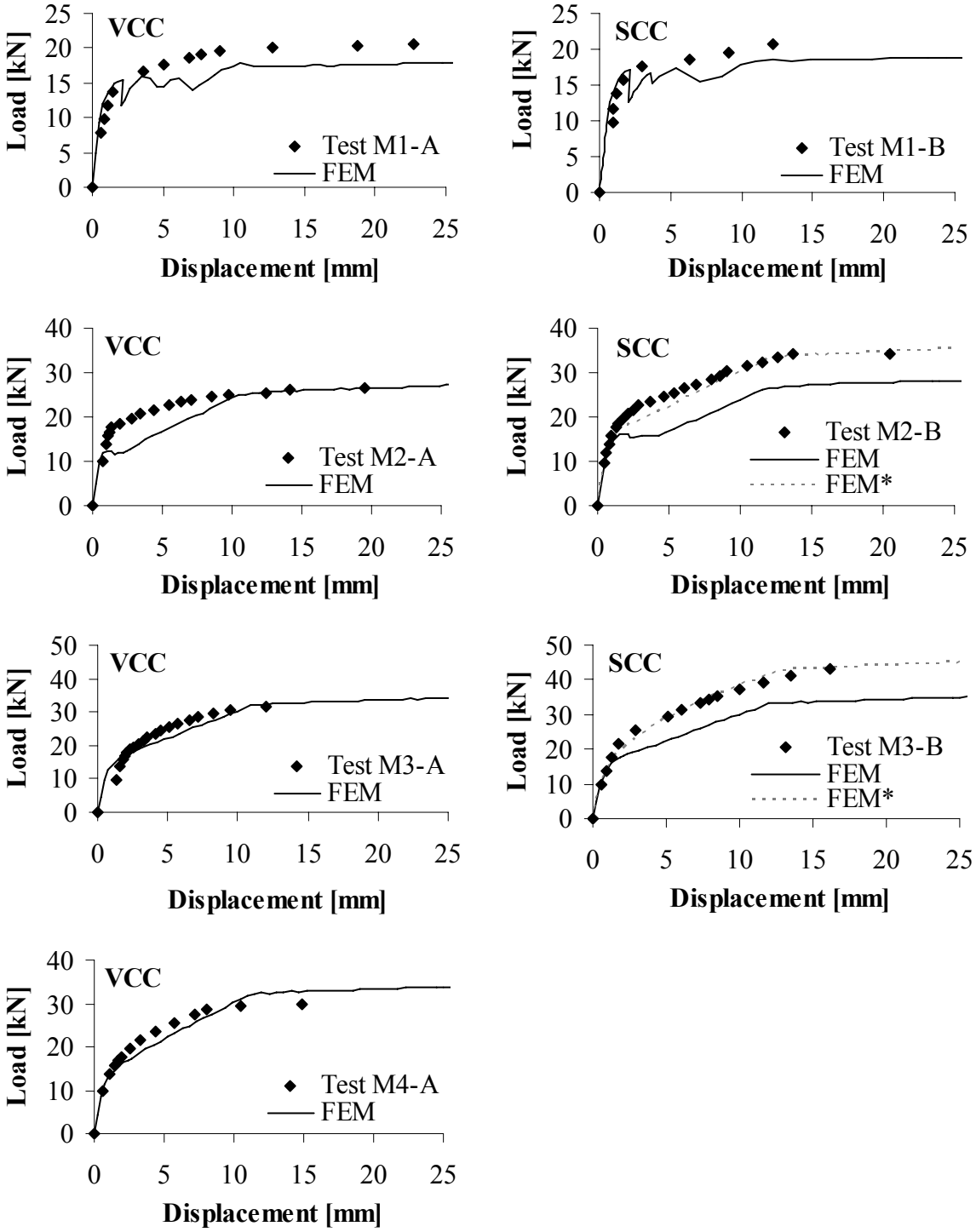

Figure 6.25: Load-deflection curves for the beams designed for moment failure compared with the result of the FEA.

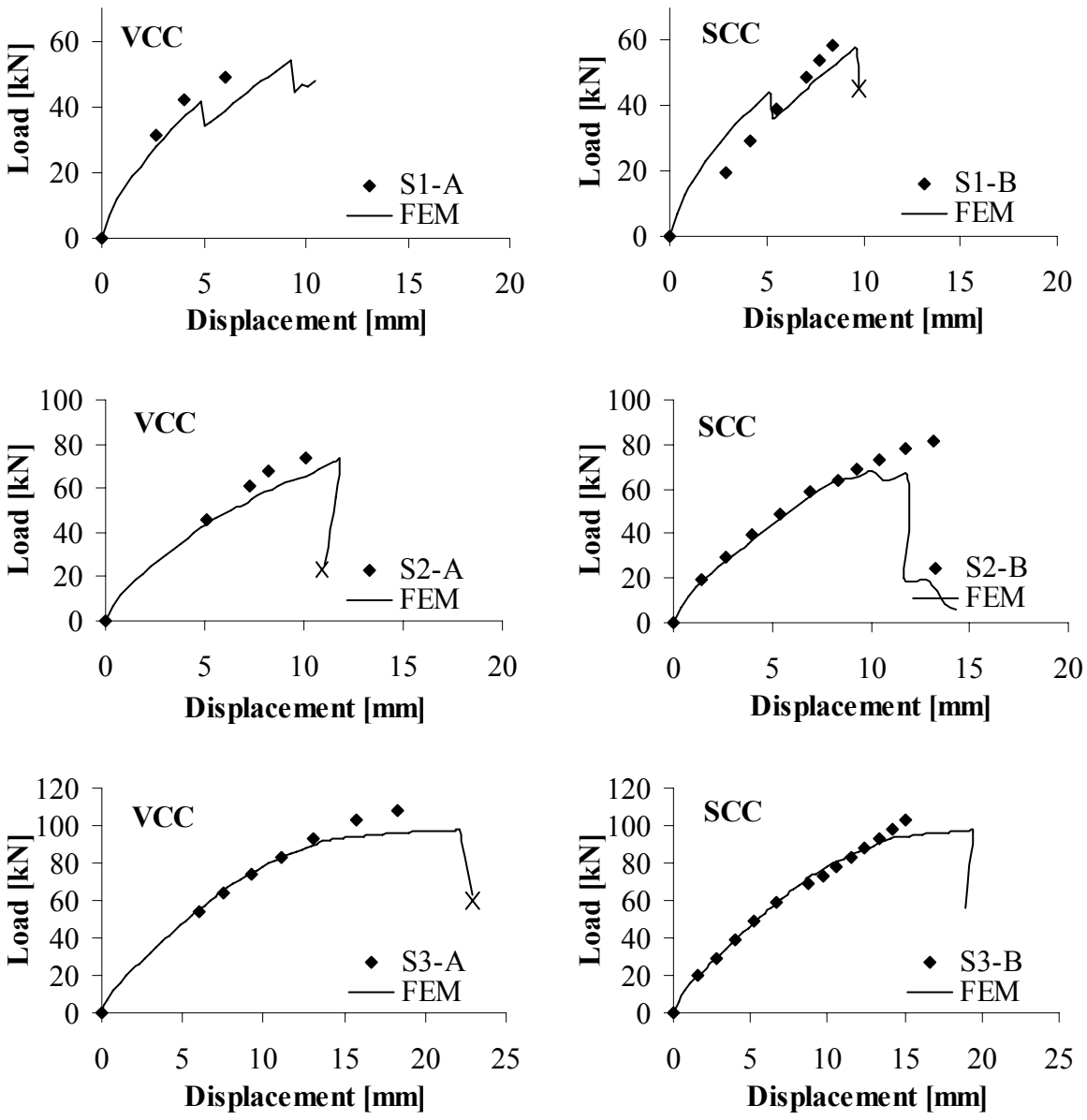

Figure 6.26: Load-deflection curves for the beams designed for shear failure compared with the result of the FEA.

6.3 Conclusions

The effect of the steel fibre content on the deformational properties and the failure capacities was significant. For the beams with VCC designed for moment failure, the moment capacity increase caused by addition of 0.5% and 1% Dramix 65/60 fibres were 24.5% and 43.5%. With SCC the corresponding capacity increases were as large as 55% and 98%. The main reason was a favourable orientation of fibres through the SCC beams. In addition, the effect of the fibres was probably better in the SCC due to a higher fibre-matrix bonding.

The moment-curvature relation of the beams designed for moment failure was estimated by a multi layer model based on a flow chart where the post cracking strength was taken as a constant residual stress. By comparing the estimated moment curvature relation with the measured data, an approximate value of the residual strength was found. This value was compared with the residual strength determined from available guidelines, based on isotropic orientated evenly distributed fibres. A good correspondence was achieved for the VCC beams. For the SCC beams the residual strengths estimated from the experiments were considerably higher, which is reasonable since fibre counting proved that a large share of the fibres were orientated in the longitudinal direction of the beams.

The shear capacity increase due to fibres was similar in the two series with VCC and SCC. However, the SCC beams designed for shear failure had a somewhat more brittle behaviour than the beams with VCC. Compared to the VCC reference beam, 0.126% stirrups gave an increase in shear capacity of 27%, while 0.5% fibres increased the shear capacity with 47%. The design loads of the beams were calculated from different guidelines, and the overall agreement was good. Especially an expression developed from the Norwegian

design rules for plain concrete (NS3473) corresponded well with the experimental results.

Based on the observed average crack distance, the beams were analysed in a FEM program with a smeared crack approach. A multi linear relation was used to model the tensile behaviour. In general, the results of the FEA were in good agreement with the test results. An exception was the two beams with 0.5% 60mm long fibres designed for shear failure, where the ultimate load was overestimated by the FE analyses.

7 Synthetic macro fibres

7.1 Advantages and limitations of synthetic fibres in load carrying structures

7.1.1 Background and range of application

Lately, the interest for synthetic macro fibres for industrial applications has increased, and some research has been done to establish the impact of these fibres. Synthetic macro fibres have many advantages compared to steel fibres:

- Lower costs (per volume)
- Synthetic fibres are easier to handle in the production; they are light and without sharp tips, which makes it possible to add them manually without gloves as protection.
- The fibres are not corroding and therefore fulfil higher requirements for endurance in constructions in aggressive environment
- Aesthetic advantages; the synthetic fibres does not corrode when the surface is left unprotected.

The use of synthetic macro fibres is still limited, partly due to lack of documentation. Some research has been carried out to determine the contribution of synthetic fibres to the ductility and the residual strength after cracking, but not to the same extent as steel fibres. When it comes to creep and fire resistance, very little documentation can be found. The latter one, fire resistance, causes a major drawback for macro synthetic fibres because of their low melting temperature. The contribution of fibres will therefore disappear in a fire. The micro synthetic fibres, on the other hand, are used to prevent damage during a course of fire. These fibres will melt

and create room for the evaporating water in the concrete, so that cracking is reduced.

Because of these limitations, the manufacturers of synthetic macro fibres primarily recommend to use them as temporary supports, for instance in mining. There are several other applications for the synthetic fibres, but most often they are used in addition to reinforcing bars. Examples are floors, staircases, walls and shotcrete applications.

While the steel fibres has an E-modulus at around 210 000 N/mm^2, the E-modulus for the macro synthetic fibres is in the region of 3-6000 N/mm^2. With hooked end steel fibres, a crack opening at around 0.05mm is required to achieve the maximum fibre stress. For the synthetic fibres, the crack opening will naturally be larger when the fibres reach their maximum stress. This puts a limitation on use of synthetic fibres in structures in aggressive environment where the allowance for maximum crack with is low. The large strains in the synthetic fibres also make it difficult to compare them directly with steel fibres based on the post-cracking strength of the FRC.

7.2 Experiments - Beams sawn from wall and slab elements of FRSCC

7.2.1 Introduction

Two series of experiments with synthetic macro fibres were carried out at NTNU in 2005:

- Series 1: 12 beams sawn from 4 slab elements. Three of the slabs were reinforced with Barchip Kyodo macro synthetic fibres. The fibre content in these three slabs was 0.55%, 1.10% and 1.65%. 0.7% Dramix 65/60 steel fibres were used in the fourth slab.

- Series 2: 24 beams sawn from 6 wall elements. Four of the wall elements were reinforced with macro synthetic fibres; 0.77% Barchip Kyodo, 1.10% Barchip Kyodo, 0.77% Synmix and 1.10% Synmix. Two of the wall elements were cast with steel fibres, and the fibre volumes in these were 0.5% and 0.7% Dramix 65/60.

All slabs were reinforced with fibres only, and the concrete was self compacting. Three beams (150x150x600mm) were sawn from each slab and tested in a deformation controlled rig. The experiments are also reported by Fjerdingstad [2005] (Series 1) and Gjestemoen [2005] (Series 2).

The objective for the experiments was to compare the post-cracking tensile strength of synthetic and steel fibre reinforced concrete.

7.2.2 Concrete and casting

The product data of the three fibre types are given in Table 7.1.

Name	Dramix 65/60	BarChip Kyodo	Synmix
Material	Steel	Polyolefin	Polyolefin
Length L [mm]	60	48	55
Eq. diameter. d [mm]	0.9	0.9*	0.82
L/d	65	53	70
Density [kg/m^3]	7850	910	910
Weight pr fibre [g]	0.30	0.028*	0.026
E-modulus [N/mm^2]	200 000	6000	6000
Tensile strength [N/mm^2]	1000	480-550	350

Table 7.1: Fibre properties specified from producer.) The equivalent diameter for the BarChip fibres are found by weighing 400 fibres, using the specified density and fibre length.*

The two concrete mixtures are compared in Table 7.2. A lower quality concrete was used in Series 2 than in Series 1. The reason for this was to obtain a more economical concrete, and also to investigate the effect of a lower concrete strength with the current fibre types. It is an advantage to reduce the difference between the tensile and post-cracking tensile strength in strain softening materials, and so it might seem favourable to use a lower concrete quality for a given fibre content. On the other hand lower matrix strength also reduces the pull-out resistance of the fibres, as shown in chapter 5. It is therefore interesting to investigate whether the relative difference between tensile and post-crack tensile strength changes with the concrete strength or not.

Materials	Series 1 [kg/m^3]	Series 2 [kg/m^3]
Cement Norcem Standard FA	369	297
Elkem Microsilica	29.5	44.6
Water	222	217
Aggregate 0-2mm	250	327
Aggregate 0-8 mm	850	819
Aggregate 8-11mm	236	246
Aggregate 11-16 mm	236	246
Scanflux SSP2000	4,3	-
Glenium 151	-	4.5
Air entrainment, concentrate	0,1	0,1
Scancem P	1,77	-
PP-fibre	10	10

Table 7.2: Concrete mixtures for the two series with 10 kg/m^3 synthetic fibres (Barchip). The concrete mixes with different fibre types and content were similar, although the admixtures were adjusted slightly to achieve the desired consistency.

The slump flow of the concrete mixes was in average 533mm. Although the concrete here is characterized as a self-compacting (no vibration was

done), it is strictly spoken not within the definition of a SCC. A common rule of thumb is that a concrete is self-compacting when the slump flow is beyond 600mm. The following definition of a SCC was used by Grunewald (2004): "a slump flow larger then 600mm, a round shape of the outflow and a homogenous distribution". Still, since the flow distance in these elements was short, the slump flow of the concrete was considered to be sufficient.

	Name	Fibre type	Fibre volume [%]	Fresh concrete properties			Compr. strength, f_c[1] [N/mm^2]
				Slump flow [mm]	Air [%]	Densit [kg/m^3]	
S1	0.55Bar	Barchip K	0.55	550	1.5	2310	67.0
	1.10Bar	Barchip K	1.10	545	1.6	2310	70.3
	1.65Bar	Barchip K	1.65	530	2.4	2300	63.2
	0.7Dra	Dramix 65/60	0.7	540	3.7	2340	71.7
S2	0.77Bar	Barchip K	0.77	510	3.3	2246	54.1
	1.10Bar	Barchip K	1.10	470	5.1	2236	45.1
	0.77Syn	Synmix	0.77	560	>15	2131	31.0
	1.10Syn	Synmix	1.10	530	>15	2038	31.3
	0.5Dra	Dramix 65/60	0.5	560	5.1	2253	43.6
	0.7Dra	Dramix 65/60	0.7	530	6.0	2240	45.6

Table 7.3: Concrete properties, fresh and hardened state.

The air content in the two concrete mixes with Synmix synthetic fibres was very high, and exceeded the maximum limit of the measuring device. The reason is probably that the content of air entrainment concentrate was increased from 0.10kg/m^3 to 0.17kg/m^3 for three of the mixes: 0.77Syn, 1.1Syn and 0.5Dra. The content of super-plasticizer, on the other hand, was reduced. The motive for adding more air entrainment concentrate was to increase the stability of the concrete, since signs of mortar separation were

[1] f_c is the characteristic compressive strength from NS3420 L5 [xx]: $f_c=f_{cm}$-w·s where f_{cm} is the average compressive stress from 100x100x100mm cubes, w=2.5 when the number of tests is three, and s is the standard deviation. The cube strength is measured the same day as the beam tests were performed.

observed for the two first mixes. Based on the concrete mixes in Series 2 it seems like the Synmix synthetic fibres entraps more air when mixed into the concrete than the Dramix-steel fibres, which seemed insensitive to the variation in air entrainment concentrate; 0.17kg/m^3 air entrainment concentrate was added in mixture "0.5Dra", 0.10kg/m^3 was added in mixture "0.7Dra". It is not so likely that the high air-content is caused by the Synmix fibre in particular, since the two synthetic fibres that were used were similar and they both had embossed surfaces [Table 7.1]. It rather indicates that synthetic macro fibres are more sensitive to air entrainment than steel fibres. Due to the high air-content, the compressive strengths of the two mixes with Synmix are much lower than the remaining mixes. The test series illustrates a common problem with FRSCC: The variation of air content in the fresh concrete after adding fibres is large and can be hard to predict as it is dependent on the mixing procedure, the concrete consistence, the fibre type and the fibre volume.

The concrete was pored carefully from one point at the element, illustrated in Figure 7.1. In Series 2 a funnel was placed on one end of the wall, and the concrete was poured very slowly from a bucket to reduce whirling motion.

After demoulding, moistened sacks were packed around the elements, and finally they were wrapped in plastic to keep the humidity high. After two months, three beams were sawn from each element as illustrated in Figure 7.1. The end pieces were cut off to reduce the wall-effect on the fibre orientation in the beams. Then, flexural beam tests were carried out as described in chapter 5.2.3, and the results were logged accordingly.

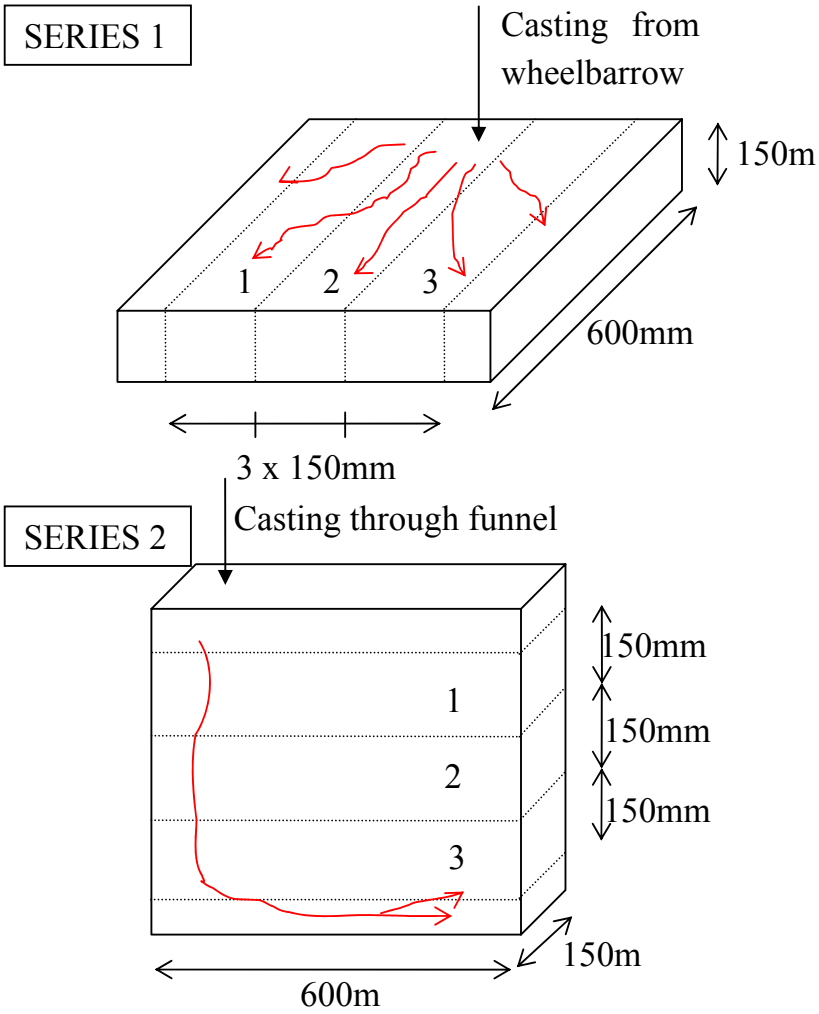

Figure 7.1: Plate and wall elements in Series 1 and Series 2. Both elements were cast from one point, which led to a main direction of the flow as indicated by the arrows. The beams were sawn and numbered as illustrated.

7.2.3 Results

Series 1

The load-deflection response of the beams in Series 1 is illustrated in Figure 7.2. The results are very promising, and show that synthetic macro fiber reinforcement is able to transfer tensile stresses across cracks in a similar way as SFR. In average the beams with 1.65% synthetic fibres

reach a maximum load $P_{max,1.65Bar}$=58kN, which is close to the maximum load of the beams with 0.7% steel fibres $P_{max,0.7Dra}$=66kN. The scatter is also lower for the synthetic fibres compared to the steel fibres. Still, the maximum load is achieved at higher strains with synthetic fibres, which demonstrates that the synthetic fibres need larger crack widths to utilize the capacity of the fibres. This is expected due to the low E-modulus of the synthetic fibres, and is in accordance with the results of the pull-out tests in Chapter 4.

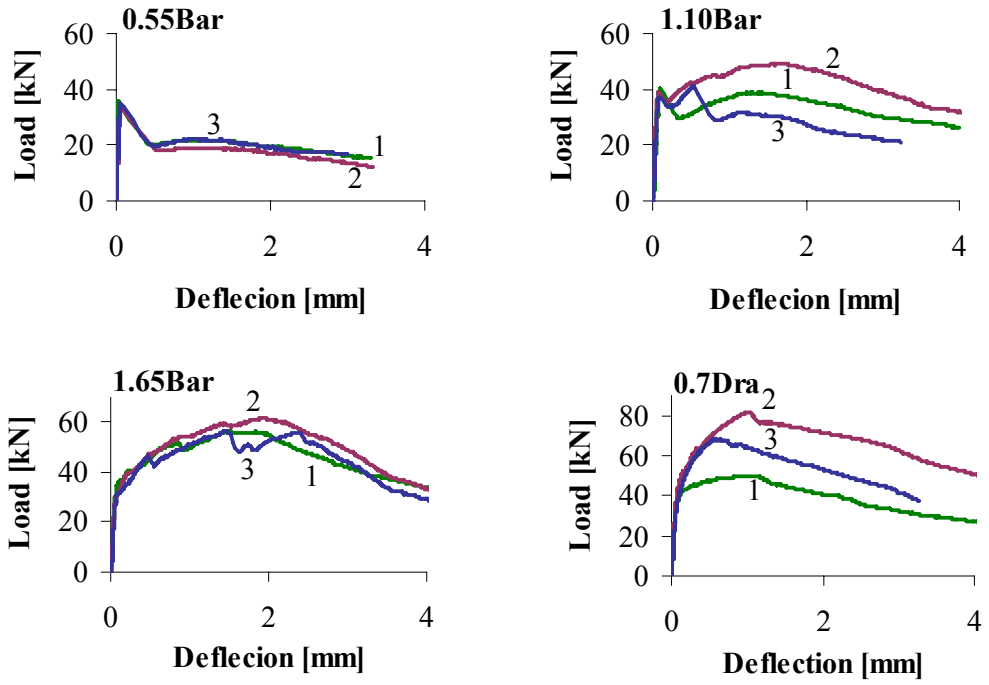

Figure 7.2: Series 1; Load deflection relation of the twelve beams sawn from four plate elements with different fibre content, the three first with synthetic macro fibres, the last one with steel fibres.

In average the load at first crack is 35, 39, 32 and 41 kN for element 0.55Bar, 1.1Bar, 1.65Bar and 0.7Dra respectively. The variation in the load at first crack seems to be in proportion to the compressive strengths of the four mixes, showed in Table 7.3.

For plate element 0.55Bar, the post-cracking strengths of the three beams are similar. For the three other series, beam number two in the middle has a

higher post-cracking strength. This indicates that the fibres to some extent was orientated parallel to the flow since the plate was cast from one point in the middle one side as illustrated in Figure 7.1.

The residual strength was determined as 0.37 times the average equivalent bending strength recorded between 0.5 and 2.5mm deflection. In average, the residual strength for the four elements were $f_{res,0.55Bar}$=0.91N/mm^2, $f_{res,1.10Bar}$=1.73N/mm^2, $f_{res,1.65Bar}$=2.37N/mm^2 and $f_{res,0.7Dra}$=2.71N/mm^2 [Table 7.4]

	Name	Fibre type	f_{res} Beam1 [N/mm^2]	Beam2 [N/mm^2]	Beam3 [N/mm^2]	Average [N/mm^2]
S1	0.55Bar	Barchip Kyodo	0.97	0.81	0.95	0.91
	1.10Bar	Barchip Kyodo	1.69	2.22	1.28	1.73
	1.65Bar	Barchip Kyodo	2.32	2.47	2.33	2.37
	0.7Dra	Dramix 65/60	2.04	3.48	2.63	2.71
S2	0.77Bar	Barchip Kyodo	1.13	1.54	1.50	1.39
	1.10Bar	Barchip Kyodo	1.37	1.59	1.44	1.47
	0.77Syn	Synmix	0.93	0.93	0.46	0.77
	1.10Syn	Synmix	1.20	1.16	0.90	1.09
	0.5Dra	Dramix 65/60	1.20	1.34	1.41	1.32
	0.7Dra	Dramix 65/60	2.31	2.02	1.37	1.90

Table 7.4: Experimental residual strength taken between 0.5 and 2.5 mm deflection.

Remark: In both series, inserts were placed between the load and the beam to ensure an even force transfer to the beam surface. As cracking occurs and the load drops, the inserts leads to some resistance due to expansion, which makes it hard to catch the decreasing branch of the load-deflection relation right after cracking. Therefore, the load-drop actually happens more abruptly in the concrete structure then what the load-deflection curve indicates. This error is accounted for when estimating the equivalent

bending strength after cracking, which are used to determine the residual strength.

Series 2

Figure 7.3 shows the load-deflection curves for all beams in Series 2. The average residual strength for each element was $f_{res,0.77Bar}$=1.39N/mm^2, $f_{res,1.10Bar}$=1.47N/mm^2, $f_{res,0.77Syn}$=0.77N/mm^2, $f_{res,1.10Syn}$=1.09N/mm^2, $f_{res,0.5Dra}$=1.32N/mm^2 and $f_{res,0.7Dra}$=1.90N/mm^2 [Table 7.4]

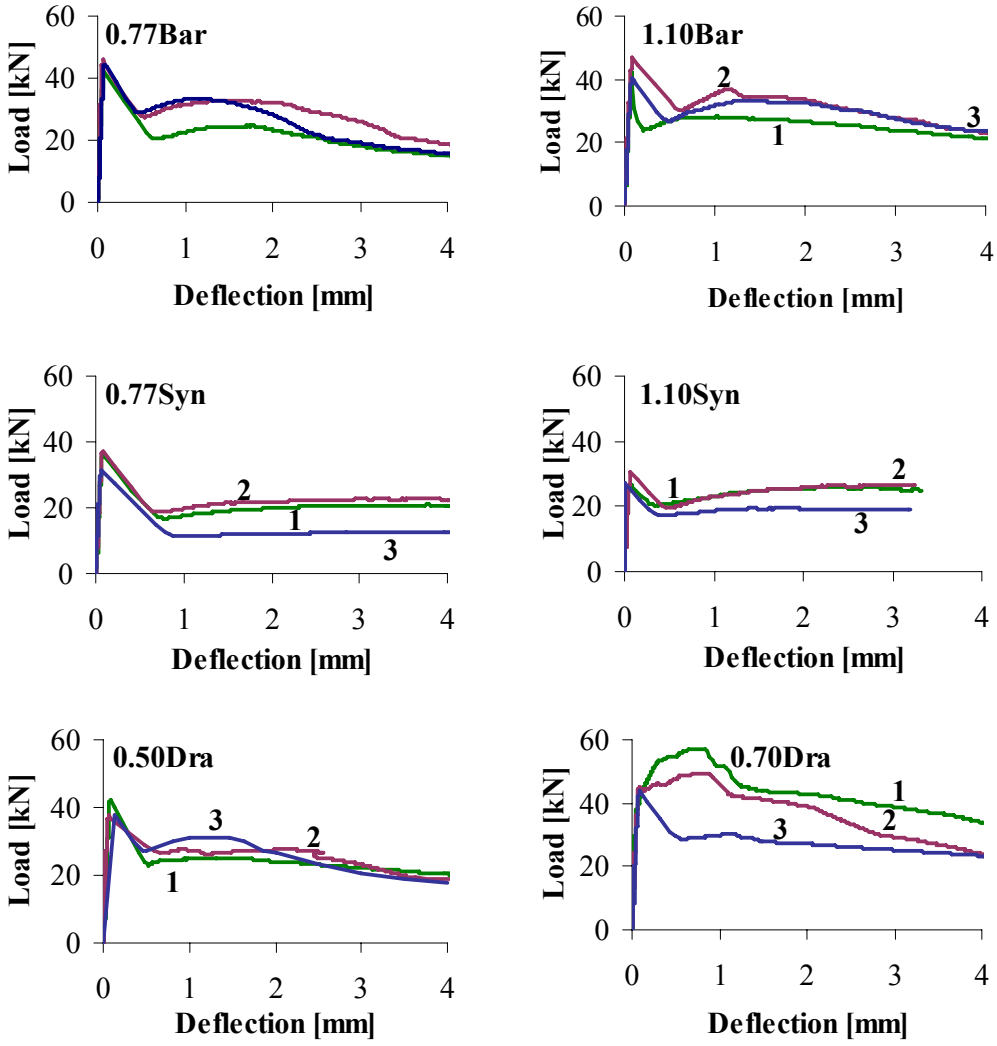

Figure 7.3: Series 2; Load deflection relation of the 18 beams sawn from six wall elements with different fibre types and content.

There is not a systematic difference between the three beams sawn from the wall elements. For the two series with Barchip synthetic fibres the upper beam, beam 1, has the lowest post-cracking strength, whereas the opposite is the case for the two series with Synmix synthetic fibres. For the two series with Dramix steel fibres, the post-cracking strength is lowest for beam 1 with 0.5% steel fibres and highest with 0.7% steel fibres. The reason for the relatively large scatter for the three beams from element "0.7Dra" is most likely that some pasta separation did occur during casting, which led to a higher concentration in the last buckets poured through the tract. The average value of the residual strength should still be representative for the added fibre concentration.

For design purposes it is desirable to avoid a sudden drop in the load after cracking. Therefore, as mentioned introductorily, it is relevant to investigate whether the relative difference between tensile and post-crack tensile strength changes with the two concrete qualities. For Series 2 the average load at first crack is 44, 43, 28, 35, 39, and 45 kN for element 0.77Bar, 1.1Bar, 0.77Syn, 1.1Syn, 0.5Dra and 0.7Dra, respectively. Hence, the load at first crack is lower in Series 1 then in Series 2 for the elements with Dramix and Barchip fibres. This is unexpected since the measured compression strength is higher in Series 1 then in Series 2, and therefore the tensile strength and the load at first crack should both theoretically be higher in Series 1. The tensile strength of the concrete is strongly dependent on the humidity. In both series the elements were wrapped and stored in wetted sacking and plastic. Still, it is possible that the humidity during storing was not constant or similar for all elements. Nevertheless, the post-cracking strength in Series 2 was generally lower compared to the load at first crack then in Series 1, and therefore no advantages regarding the tensile behaviour were gained by using a lower quality concrete in Series 2.

Figure 7.4 gives an overview of the beam tests in Series 2. As for Series 1 it is evident that the beams with synthetic fibres reach their maximum post-cracking stress at a larger deformation than the steel fibres. Moreover, even

though the product data of the two different fibre types resembles and the Young modulus specified from the producer is similar, the Synmix fibres needs much larger crack widths before the fibres comes fully into effect. The results of the Barchip fibres are more promising; at a deflection of 0.8mm, the beams reinforced with 0.77% Barchip reaches the same level as the beams with 0.5% steel fibres.

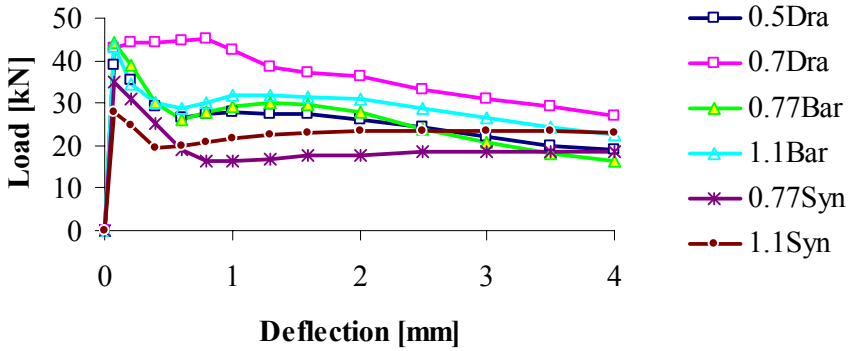

Figure 7.4: Comparison between the 6 wall elements in Series 2. The average values between the three beams in each element are taken.

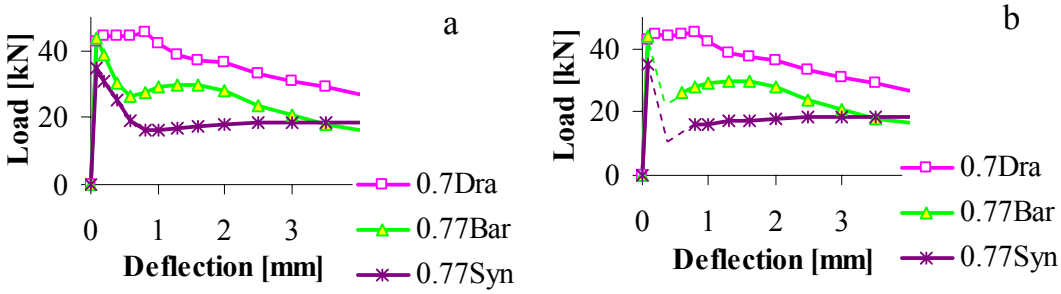

Figure 7.5: Comparison between the three different fibre types in Series 2. a) The figure shows the measured load-deflection relations for the three wall-elements with similar fibre content. b) The assumed load-deflection relations after cracking are sketched, as the inserts under the load made it impossible to capture the sudden drop in load.

The three wall-elements with resembling fibre content are compared in Figure 7.5; 0.7% Dramix steel fibres, 0.77% Barchip Kyodo fibres and 0.77% Synmix macro fibres. At small deflections, the steel fibres are much

more efficient than the synthetic fibres. At a deflection of 1mm, the average load is 42kN for the steel fibre beam, 29kN for the beam with Barchip synthetic fibres and 16kN for the beam with Synmix fibres. This implies that a fibre volume of 1.2% Barchip fibres would give the same post-cracking strength as 0.7% Dramix steel fibres at this deformation, presuming that the post-cracking strength increases linearly with the fibre content. Hence, in constructions where relatively large crack widths are tolerated, macro fibres are able to compete with steel fibres.

Comparing the efficiency of fibres in the two concrete mixes.

The results show that the post-cracking strength of fibres is higher in Series 1 than in Series 2. This was also expected due to higher concrete quality which increases the adhesion between fibre and matrix. The results for the beams with 1.1% Barchip synthetic fibres are compared in Figure 7.6, where the estimated average residual strengths are 1.73 N/mm^2 and 1.43 N/mm^2 for Series 1 and Series 2, respectively. The corresponding compression strengths are $f_{cm,S1}$=70N/mm^2 and f_{cm}=41N/mm^2.

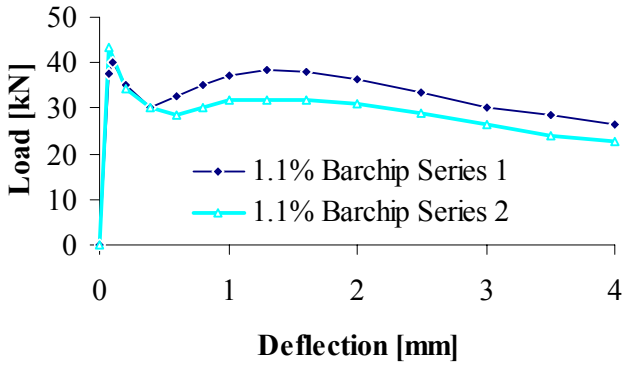

Figure 7.6: Results for the beams with 1.1% Barchip synthetic fibres in Series 1 and 2. The average values for the three beams in each element are taken.

The difference between the two series is more pronounced with steel fibres, illustrated in Figure 7.7. For 0.7% Dramix steel fibres the average residual stress is 2.71 N/mm^2 in Series 1 (f_{cm}=72N/mm^2) and 1.9 N/mm^2 in Series 2

(f_{cm}=42N/mm^2). This is reasonable, since steel fibres tend to sink in the SCC, causing a higher fibre concentration in the lower half of the beams in Series 2, which increases the post-cracking strength. The opposite effect is expected for the synthetic fibres due to their low density. Hence, the difference between the residual strengths in Series 1 and Series 2 induced by the difference in concrete strengths is most likely reduced as a result of a disadvantageous fibre distribution in the slabs with synthetic fibres, while the difference is enhanced due to a favourable fibre distribution in the slabs with steel fibres.

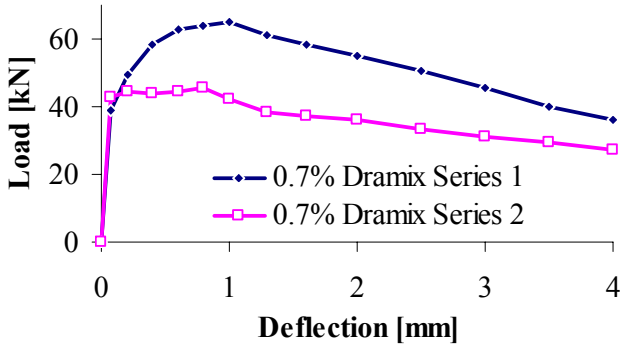

Figure 7.7: Average load-deflection relation for the tree beams from each series with 0.7% Dramix steel fibres.

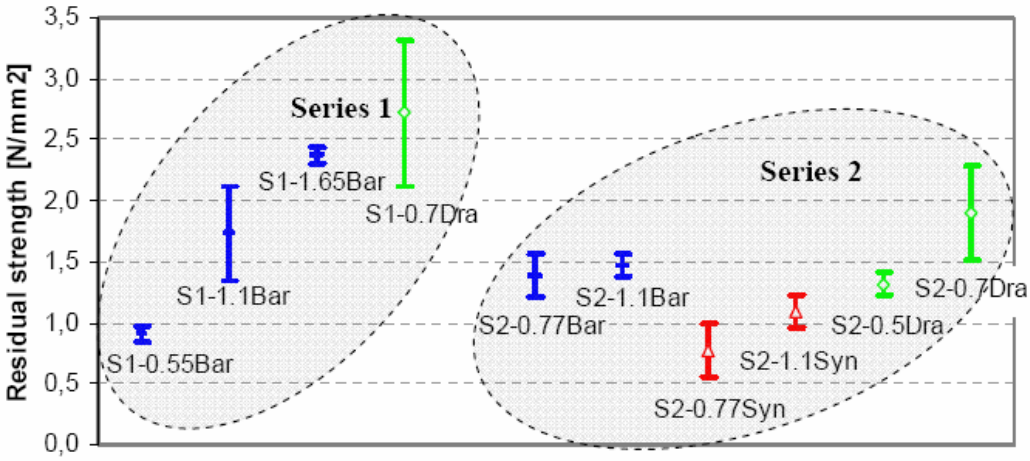

Figure 7.8: Average residual strength and standard deviation for the three beams in each element.

An overview of the residual strength and standard deviation for each element is given in Figure 7.8. The experiments imply that the pull-out load of the current steel fibres is more dependent on concrete strength than the pull-out load of the synthetic fibres. Moreover, the post-cracking strength increases approximately linearly with the fibre content, except for the two elements with Barchip synthetic fibres in Series 2, where the difference between the two fibre concentrations is less then expected. Yet, in this evaluation the orientation of the fibres is not taken into consideration.

7.2.4 Orientation and distribution of fibres

In Series 2, blocks were cut out from each beam according to the Norwegian design rule draft [Thorenfeldt, Fjeld et al 2006] to determine the fibre orientation factor. Fibre counting were performed on the beam cross-section, the average from the two planes from the block were taken. For some of the beams, fibres were also counted on planes perpendicular to each other, as illustrated in Figure 7.9, in order to estimate and control the fibre volume.

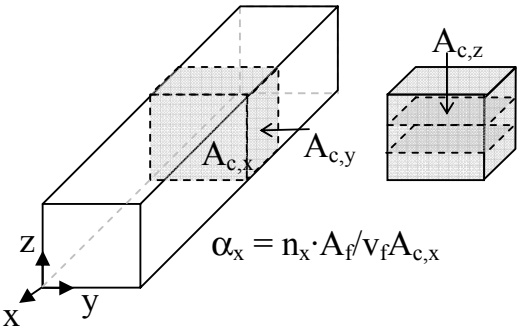

$$\nu_f = \left(N_1 + \frac{9}{16} N_2 + \frac{7}{16} N_3 \right) \frac{A_f}{A_c}$$

where

$N_1 > N_2 > N_3$

Figure 7.9: Sawn-out block from beam for fibre-counting. When fibres are counted on three planes perpendicular to each other, the fibre volume v_f can be estimated as described in Ch. 2.6.

The fibre orientation factors with corresponding capacity factors for all beams in Series 2 are shown in Table 7.5. An estimate of the average post-cracking stress in the fibres can be done by comparing the experimental residual stress with the theoretical residual stress based on the orientation

and volume of fibres. If the distribution of fibres in the entire element is constant, the experiments indicates an average stress of 254 N/mm^2 with Barchip synthetic fibres, 184 N/mm^2 with Synmix synthetic fibres and 508 N/mm^2 with Dramix steel fibres [Table 7.5]. The large scatter in the estimated stress is most likely caused by an uneven fibre distribution.

Fibre type	v_f [%]	b [mm]	h [mm]	n_x [-]	ρ_f [-]	α [%]	η [-]	$f_{res.exp}$ [N/mm^2]	$\sigma_{average}$ [N/mm^2]	$\sigma_{average}$ [N/mm^2]
Barchip	0.77	150	151	157	0.0044	0.58	0.43	1.13	336	254
		150	151	206	0.0058	0.76	0.67	1.54	296	
		150	151	214	0.0060	0.79	0.71	1.50	272	
Barchip	1.10	149	150	297	0.0085	0.77	0.70	1.37	178	
		150	150	261	0.0074	0.67	0.56	1.59	256	
		150	150	301	0.0086	0.78	0.70	1.44	186	
Synmix	0.77	151	150	205	0.0048	0.62	0.49	0.93	244	183
		151	150	233	0.0054	0.70	0.61	0.93	199	
		152	151	178	0.0041	0.53	0.37	0.46	159	
Synmix	1.1	150	150	354	0.0083	0.76	0.67	1.20	162	
		151	151	329	0.0076	0.69	0.59	1.16	179	
		152	151	314	0.0072	0.66	0.54	0.90	151	
Dramix	0.5	150	150	116	0.0033	0.65	0.54	1.20	448	508
		150	150	90	0.0025	0.51	0.35	1.34	777	
		150	150	125	0.0035	0.71	0.61	1.41	464	
Dramix	0.7	150	151	316	0.0089	0.80*	0.73	2.31	450	
		152	151	171	0.0047	0.68	0.57	2.02	507	
		151	150	154	0.0043	0.62	0.49	1.37	401	

*Table 7.5: Average stress in fibres between 0.5 and 2.5mm deflection, determined from the experimental residual strength and the section ratio of fibres. *) For 0.7Dra-1, the section ratio leads to α=1.27, demonstrating that the fibre volume is not constant. Here α is set as α_{max}=0.8.*

The fibre volume was controlled by counting fibres on three planes perpendicular to each other on sawn out blocks near the crack [Figure 7.9].

An extensive control by extracting and weighing the fibres was not done. As illustrated in Figure 7.10, the fibre volume in the sawn-out blocks is not far from the added volume. Still, the fibre counting showed that the fibre volume was not entirely even over the element. Especially for beam 0.7Dra-1, it is clear that the fibre volume must be quite high, owing to the fact that the added volume would have given an orientation factor α=1.27, which exceeds the maximum orientation factor for uni-directed fibres α=1. According to Thorenfeldt et al. (2006), α_{max}=0.8 for practical applications, therefore $\alpha_{0.7Dra-1}$=0.8 in Table 7.5. It is also possible that the orientation in the crack varies from the orientation in the sawn out prism, which would give an inaccurate estimate of the average stress. Yet, by averaging the estimated post-cracking stresses for the six beams with the current fibre type, the estimate of $\sigma_{average}$ is assumed to be applicable for this concrete mix.

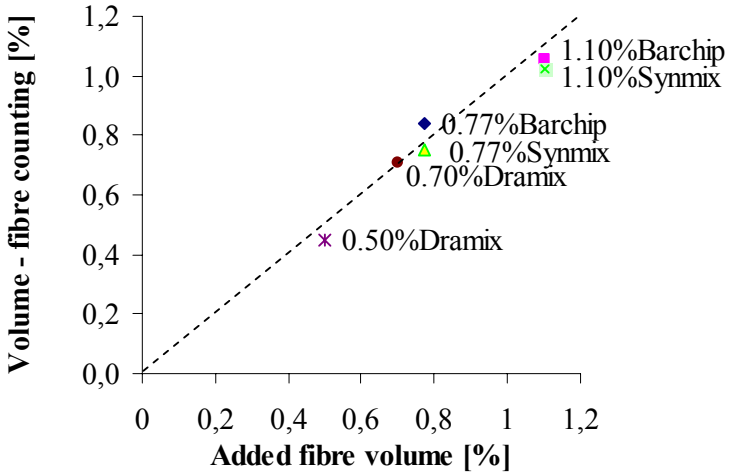

Figure 7.10: Control of fibre volume by counting fibres on three planes perpendicular to each other on sawn-out blocks near the cracks. This check is performed on beam nr 2 for all of the mixes and in addition on beam 0.77Bar-1 and 0.5Dra-3.

7.2.5 Conclusions

The results show that synthetic macro fibres are able to transfer tensile stresses across cracks in a similar way as steel fibres, but the fibres reach their maximum stress at a larger crack width than the steel fibres. The synthetic fibres can therefore only be used in an efficient way in structures with relatively high tolerance regarding maximum crack width.

Two types of synthetic fibres were tested: Barchip Kyodo and Synmix. Even though the given fibre properties resemble, the results were quite different. The Synmix fibres required larger deflections to come fully into effect, and the crack widths when the maximum post-cracking strength was reached were beyond 3mm.

The air content in the concrete with Synmix synthetic fibres were very high; it exceeded the maximum limit of the measuring device of 15%. The mix designs indicated that synthetic fibres are more sensitive to air entrainment then steel fibres.

The post-cracking strength increased with increasing concrete strength, and the difference between the two concrete qualities was most pronounced in the beams with steel fibres. This is probably due to the density of the fibres, which caused a larger concentration of steel fibres in the lower part of the slabs, while the concentration of synthetic fibres was largest in the upper part of the slabs. The post-cracking strength increased approximately linearly with fibre content, both with steel- and synthetic fibres.

The results of the beam experiments in Series 1 with average compression strength 68 N/mm^2 implies that the fibre content of Barchip synthetic fibres must be approximately 2.5 times higher than the content of Dramix 65/60 steel fibres in order to achieve the same residual strength. For Series 2 with lower compressive strength a fibre content of $v_{f,Barchip}=1.5v_{f,Dramix}$ would be required to reach the same residual strength, provided that the residual

strength increases linearly with increasing fibre content. The residual strength of the Synmix fibres were lower; a fibre volume of $v_{f,Synmix}=2.7v_{f,Dramix}$ is needed to achieve the same effect.

The post-cracking strength of the beams from plate elements implies that the fibres in some extent had a preferred orientation parallel to the flow. Still, no categorical conclusion can be made due to the short flow distance and lack of data on the fibre orientation. For the second series, no systematic difference in post-cracking strength was found between the three beams from each wall element. Fibre counting showed a main fibre orientation horizontally along the beams, parallel to the apparent flow direction during casting.

8 Size effect on beams exposed to bending

8.1 Background

The material strength of the concrete appears to decrease with increasing structural size. Several comprehensive studies have been carried out to confirm and explain this phenomenon, called size effect. For a long time the size effect was explained statistically as a consequence of the randomness of material strength, based on the fact that it is more likely for a large than a small structure to encounter a material point of lower strength. Later Bazant proposed [Bazant 1984, 1986] that the size effect should be explained by energy release caused by macrocrack growth, claiming that the randomness of strength only plays a negligible role. The latter explanation, based on strain energy release due to fracture growth, has gradually been widely accepted and has been thoroughly supported by laboratory evidence [Bazant 1994].

Another reason for size dependency is that shrinkage is dependent on the ratio between volume and drying surface area. A variation in thickness affects the shrinkage strain rate as well as other time-dependent properties of concrete, which again changes the cracking behaviour. [Groth 2000, paper E] However, size dependency due to shrinkage is not treated in this chapter.

The most extensive study done so far to investigate the size effect in SFRC structures is a Brite EuRam project reported by Erol Erdem (2003). In this project, an experimental program was carried out at several research laboratories and universities in order to explain and quantify the dependence of the size, and formulate simple rules to achieve a safe design. In addition to specimen depth, the specimen width, the span-to-depth ratio and the influence of additional compression forces was investigated. The σ–ε relationship proposed by RILEM Committee 162 [2002] was defined

as a basis. The influence of different member depths was investigated by a total amount of 36 specimens with three depths; 100, 400 and 600mm. In general, the calculated loads based on the σ–ε relation were higher than the experimental loads. The ratio of experimental to calculated loads were descending in the range of small to medium depths and maintained at a constant plateau from medium to large depths. Furthermore, when the fibre content was increased and the conventional reinforcement lowered, the size dependence increased. [Erdem 2003]. This is also in accordance with the results of a study by Sener et al. (2002), where it was concluded that the bending failure in the steel fibre reinforced beams exhibited a greater size effect than beams plain concrete.

In the same manner as for plain concrete, it is evidently practical to include a size factor in the design models for FRC. Moreover, it is useful to carry out more experiments investigating the size effect in FRC structures in order to establish more clearly the dependence of the specimen depths.

8.2 Experiments – effect of cross section height for different reinforcement conditions

8.2.1 Introduction

To investigate the size-effect of fibre reinforced concrete, nine beams of three dimensions were exposed to bending:

a) b x h x L = 150 x 150 x 900
b) b x h x L = 150 x 250 x 2850
c) b x h x L = 150 x 500 x 4000

The a/d relations were (150/130=) 1.15 for beam dimension a, (450/219=) 2.05 for b and (625/436=) 1.43 for beam dimension c, where a is the distance between the support and the load, and d is the effective depth (Figure 8.1 to Figure 8.3). Three experimental series were carried out, each series containing all three beam dimensions:

1) 1% fibres combined with reinforcement bars

2) 1% fibres only
3) 0.3% fibres only

The load was deformation controlled which made it possible to capture the descending part of the load-deflection curve.

8.2.2 Concrete and casting

The mix design of the concrete was similar to Series A in Chapter 6. Table 8.1 shows the measured compression strength on cubes and cylinders after 28 days and at date of testing. The E-modulus was not measured, but was estimated after the Norwegian design rules NS3473; $E_c=k_E \cdot f_c^{0.3}$, where k=10000 and f_c is taken as the cylinder strength at 28 days. For the beams of mix 3 with 0.3% fibres the cylinder strength at 59 days is used, according to date of testing.

	Mix 1	**Mix 2**	**Mix 3**
Density [kg/m^3]	2420	2410	2400
f_c 28 days, cube [MPa]	47.6	48.5	48.4
f_{cc} 28 days, cylinder [MPa]	38.1	38.8	38.7
f_c 59 days, cube [MPa]	-	-	57.0
f_{cc} 59 days, cylinder [MPa]	-	-	45.6
f_{tn} 28 days interpolated from NS 3473 [MPa]	2.07	2.09	2.08
f_{tn} 59 days interpolated from NS 3473 [MPa]	-	-	2.30

Table 8.1: Measured compressive strengths and tensile strengths interpolated form the Norwegian design rules NS 3473. The beams of mix 1 and 2 were tested after 28 days

Dramix 65/60 steel fibres were used in all beams. In Series 1, additional reinforcement bars were used as shown in Figure 8.1 to Figure 8.3. The content of reinforcement bars varied between 0.48 and 0.62% for the three dimensions, which is 3 to 4 times as much as the reinforcement bars used in

the experimental series in Chapter 6. The reinforcement data is shown in Table 8.2. Series 2 and 3 were cast with fibres only.

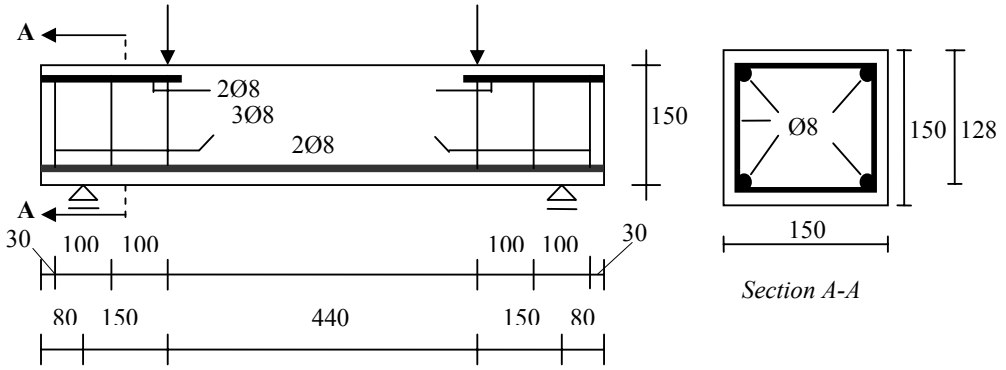

Figure 8.1: Test rig and dimensions for beam 1a, 150 x 150 x 900 mm (All numbers in mm).

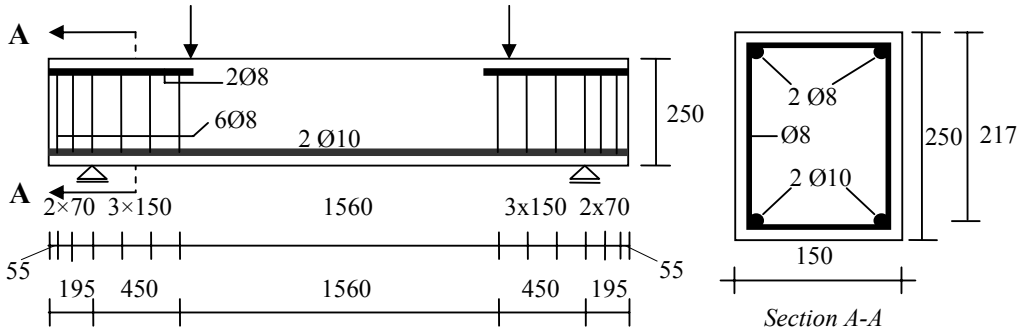

Figure 8.2: Test rig and dimensions for beam 1b, 150 x 250 x 2850 mm.

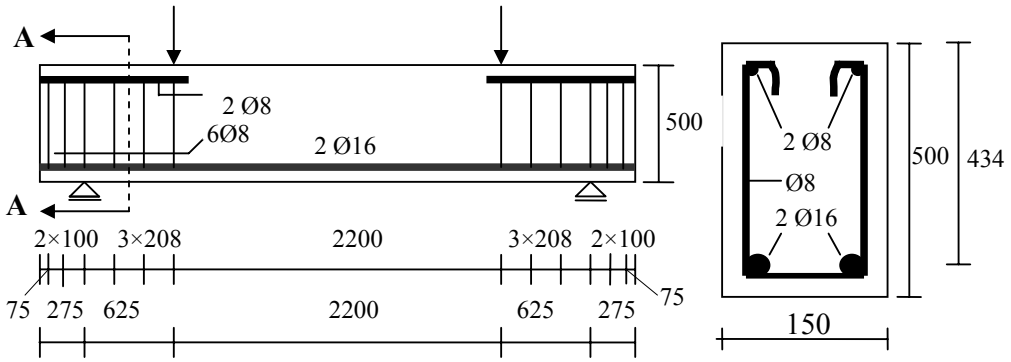

Figure 8.3: Test rig and dimensions for beam 1c, 150 x 500 x 4000 mm.

Reinfo. diameter [mm]	Reinfo. content [mm^2]	Yield stress [N/mm^2]
Beam dim. a): ϕ8	100.5 (ρ=0.515%)	530
Beam dim. b): ϕ10	157 (ρ=0.478%)	Not tested
Beam dim. c): ϕ16	402 (ρ=0.615%)	552

Table 8.2: Reinforcement data. The Youngs modulus was not tested.

8.2.3 Test setup and instrumentation

The beams were exposed to four-point bending as illustrated in Figure 8.1 to Figure 8.3. The deflections were measured by LVDTs in the middle of the beams, under the loads, and at the supports for the medium and large beams. For the smallest beams dimension, the deflection was measured at the supports and at the middle of the beams only.

The strains were measured by LVDTs and by extensometer according to Figure 8.4. In addition, the strains in Series 1 were measured with strain gauges on the tensile reinforcement bars.

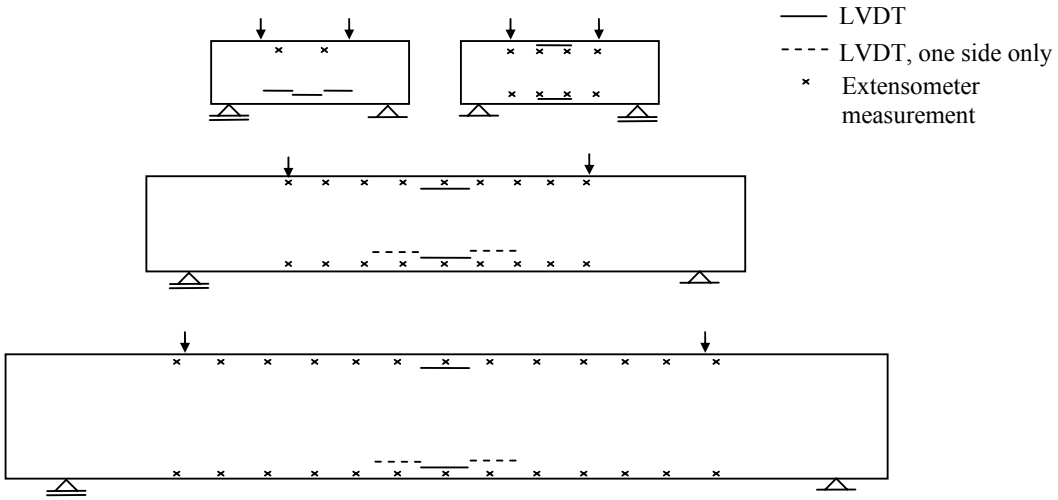

Figure 8.4: Strain measurements. Both sides are shown for the smallest dimension. For the two larger dimensions, the measurements were identical on both sides, except from the LVDTs illustrated with the dashed lines.

The load was applied in deformation controlled steps. At prescribed load steps, the load was held constant while the extensometer measurements were taken, and the crack patterns traced with a marker.

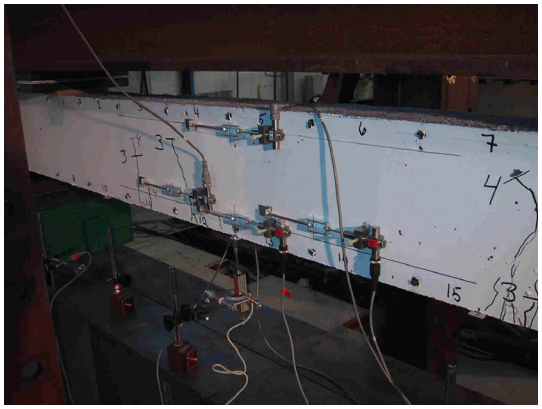

Figure 8.5: Beam of medium size during testing.

8.2.4 Results

Table 8.3 shows the observed loads at cracking and the maximum loads for all nine beams. In addition, the loads at a 2.5 mm deflection are registered in order to compare the effect of fibres after cracking in the beams reinforced with fibres only. Load-curvature and load-crack-width relations for all beams are shown in Figure 8.17 to Figure 8.19.

Bjelkenr.	P_{cr} **[kN]**	P_{u} **[kN]**	$P_{2.5mm}$ **[kN]**
1a	18.7	60.3	
1b	14.4	52.7	
1c	49.6	175.3	
2a	14	19.2	15.6
2b	12.1	16.0	14.0
2c	30	33.2	26.0
3a	13.6	13.6	4.6
3b	11.0	11.0	4.1
3c	29.9	29.9	16.5

Table 8.3: Load at first crack P_{cr} and load at failure P_{u}. T

The bending strengths at first crack are estimated from the moment-curvature relations and illustrated as a function of the cross-section height in Figure 8.6. A significant size effect on the bending tensile strength was observed. It can also be seen that the bending tensile strength is higher for the concrete with 1.0% fibres than with 0.3%. In the Norwegian design rules, NS3473, a scale factor k_v is used for plain concrete to calculate the load at first crack and the shear capacity. This scale factor k_v=1,5-h >1 (h in metre) is illustrated in the figure, and it is seen that the agreement with the experiments is rather good. The Norwegian design rule draft for SFRC suggest a scale factor p=1.1-0.7h>0.75.

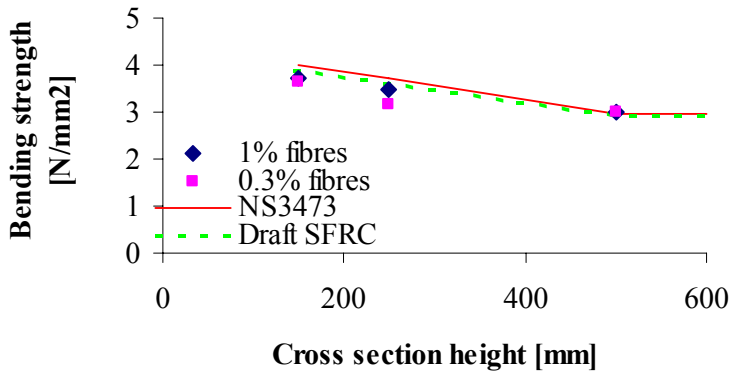

Figure 8.6: Bending strength determined from the first stiffness reduction on the load-curvature relations. The size dependence according to the two scale factors k_v and p is also illustrated in the figure.

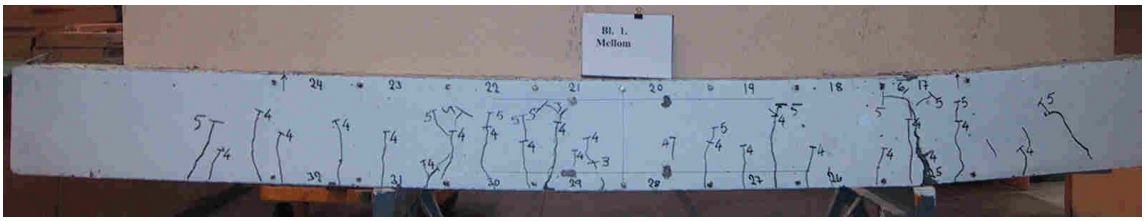

Figure 8.7: Cracks in beam 1b (medium size) marked and numbered according to load-step. The small and large beam had a similar distribution of cracks.

The three beams in Series 1 with steel fibres in addition to reinforcement bars behaved in a ductile way with cracks distributed over the whole zone

with constant moment. The tests where ended after reaching maximum crack widths over 10mm, with tensile strains around 50‰. Since the load was increasing until this point, it is concluded that the ductility is satisfactory. After reaching the peak-load, the deformations localized in one large crack, and failure followed as the concrete crushed in the compression zone. This behaviour corresponds to the observations that were done in the experimental series described in Chapter 6. The average crack distances between the twin loads were 88, 87 and 96mm for the small, medium and large beam respectively.

The behaviour of the beams with fibres only was quite different. Figure 8.8 to Figure 8.10 shows the cracks in the medium size beam with 1.0% and 0.3% fibres. For the beams in Series 2 with 1% fibres 2, 4 and 1 crack developed in the small, medium and large beam accordingly. These cracks were branched, especially the one that developed in the large beam. After cracking, the load was increasing further with 37, 32 and 11% for the small, medium and large beam.

The results of these tests indicate that both the bending strength, the maximum load and the ductility is size-dependent. One practical consequence of this is that higher fibre content is needed in large beams to maintain a corresponding capacity as a small beam.

For all beams with 0.3% fibres, only one crack developed, and the load at the first observed crack was even with the ultimate load. Table 8.4 shows how the loads dropped immediately after failure with 66, 63 and 45% for the small, medium and large beam, respectively. Hence, the size effect on these beams is the opposite of the observations done for the beams in Series 2 with 1% fibres, which makes it difficult to draw any categorical conclusions.

Beam	Increase from 1st crack to max load [%]	Drop after max load [%]
2a	37	19
2b	32	13
2c	11	22
3a	0	66
3b	0	63
3c	0	45

Table 8.4: Comparison of the beams in Series 2 and 3 with 1.0% and 0.3% fibres.

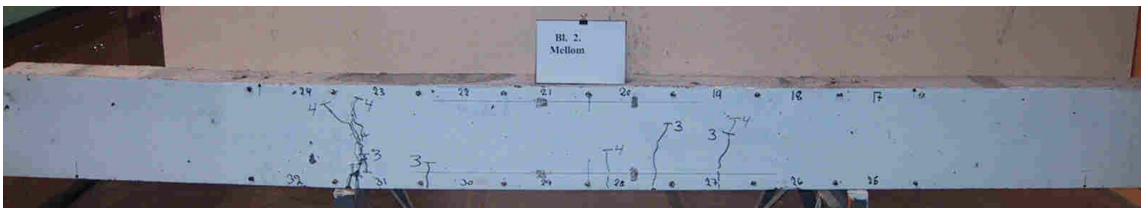

Figure 8.8: Beam 2b. The cracks are marked and numbered according to load step.

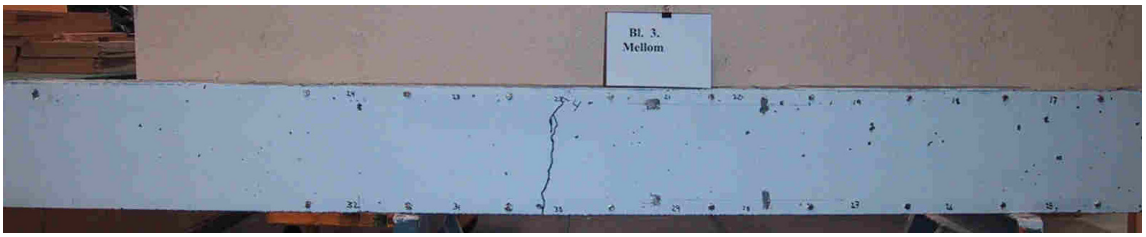

Figure 8.9: Crack in beam 3b.

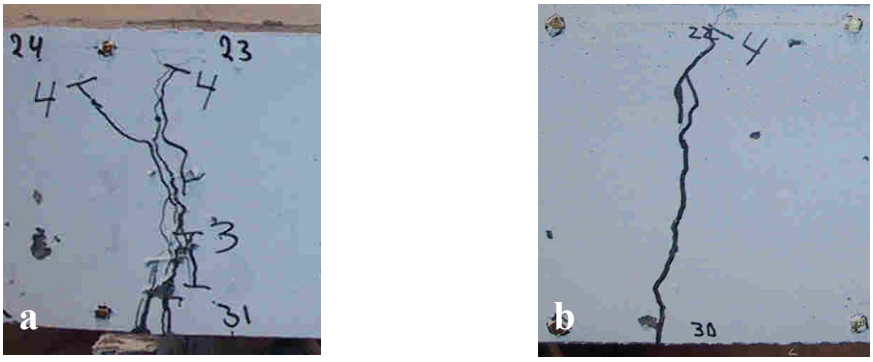

Figure 8.10: Cracks in the failure zone for beam 2b and 3b.

8.2.5 Orientation and distribution of fibres

To investigate the orientation and distribution of fibres, a 90mm thick block was sawn a short distance from the fracture zone and the number of fibres on each side of the sawn out block were determined. Figure 8.11 illustrates the ratio between the observed and theoretical number of fibres. The theoretical number of fibres is taken as $n_{theory}=\alpha \cdot vf \cdot A_c/A_f$, where the wall-effect is included in the orientation factor α according to Dupont (2003):

$$\alpha = \frac{\alpha_1 \cdot (b-l_f)(h-l_f) + \alpha_2 \cdot [(b-l_f)l_f + (h-l_f)l_f] + \alpha_3 \cdot l_f^2}{b \cdot h}$$

The relation between the observed and theoretical number of fibres was in average for all beams $n_{measured}/n_{theory}=1.00$. The scatter is relatively small for Series 1 and 2 with 1% fibres. For Series 3 with 0.3% fibres the scatter is larger, and varies between $n_{measured}/n_{theory}=0.70$ and 1.22. The measured average orientation factors are $\alpha=0.55$, 0.58 and 0.60 for the small, medium and large beam, respectively, while the corresponding theoretical orientation factors according to Dupont (2003) are $\alpha=0.60$, 0.58 and 0.56 for the three beam sizes. The theoretical orientation factor is $\alpha=0.5$ for an ideal isotropic orientation. For the largest beam size, the degree of unidireced fibres is beyond the expected value, even with the wall-effect included. The opposite is the case for the smallest beam. Still, some scatter will always occur for FRC, and the scatter observed in this experimental series is acceptable.

No systematic difference between the orientation in the upper and lower part of the cross-section is observed.

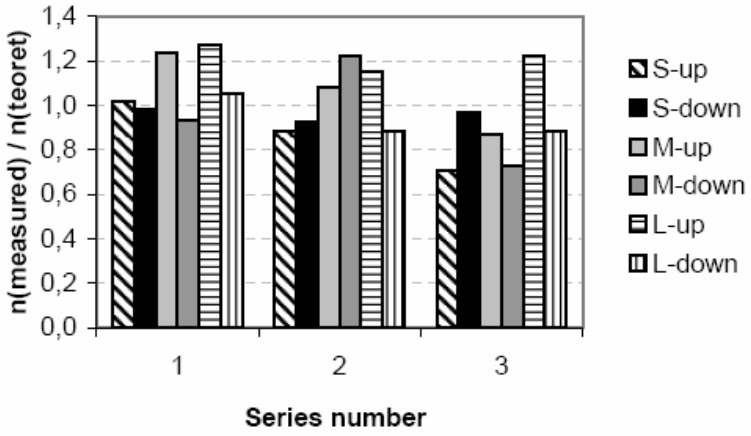

Figure 8.11: Results of fibre counting on the small (S), medium (M) and large (L) beam in Series 1, 2 and 3. The figure also shows how the number of fibres varied on the upper and lower half of the cross-section

8.2.6 Finite element analysis

Finite element analysis was performed for all nine beams. The objective was to control if the size effect in the three series were captured by the analysis, and also, for the beams with 1% fibres only, to compare the results of a discrete crack approach with a smeared crack approach.

The finite element analysis was based on the stress-crack width relation proposed in Chapter 6. For the beams with ordinary reinforcement, the smeared crack approach was used, while the discrete crack approach was used for the beams in Series 3 with 0.3% fibres only. The beams in Series 2 with 1% fibres were analyzed both with a discrete and a smeared approach.

It is assumed a plane stress state. For all beams, an eight-node quadrilateral isoparametric plane stress element is used, the CQ16M element [Figure 8.12]. For the discrete analysis, the CL12I element is used; an interface element between two lines in a two-dimensional configuration.

Figure 8.12: a) CQ16M eight-node element, b) CL12I interface element. The opposite nodes may overlap: 1 and 4, 2 and 5, 3 and 6.

In the FE analyses, the fibres are assumed to be isotropic orientated with an average post-cracking stress of 500 N/mm^2, which gives a residual strength: f_{res}= 1/3·0.01·500=1.67 N/mm^2. The σ–w relation is based on the calculations in Chapter 6, and the σ–ε relation is determined by dividing the crack width on the average crack spacing, $L_{average}$, as illustrated in Figure 8.13.

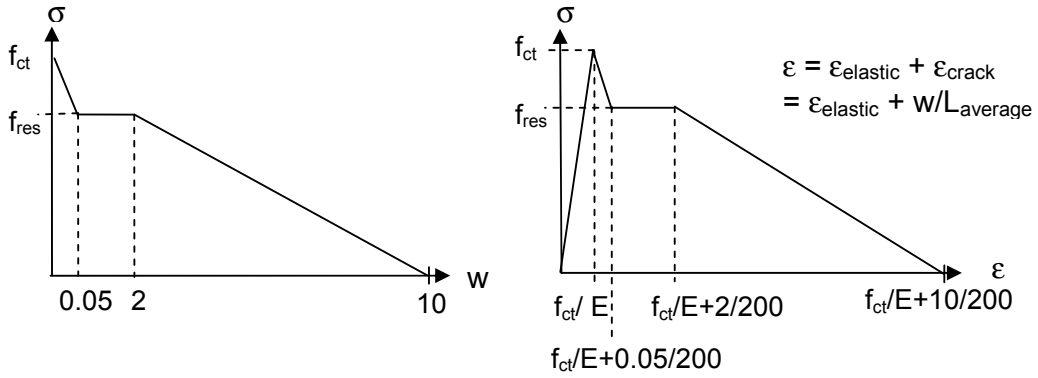

Figure 8.13: Multi-linear stress-crack width and stress-strain relation as presented in Chapter 7.

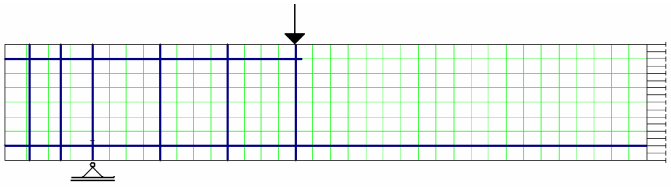

Figure 8.14: Reinforcement and element mesh, beam 1b. Only half of the beam modelled due to symmetry.

The three beams in Series 1 are modelled with a smeared crack approach with σ–ε relation as given in Figure 8.13. $L_{average}$ is taken from the experiments as 88, 87 and 96 for the small, medium and large beam respectively.

In Series 2 the beams are modelled both by the discrete and the smeared approach with two, four and two vertical cracks for the small, medium and large beam, respectively. In the smeared crack analysis, all elements except from the elements marked with A and B in Figure 8.15 have a high tensile strength to ensure that cracking only occurs in the same zone as where the interface elements were placed in the discrete analysis. For comparison, the stress-strain relation for the smeared analysis should correspond to the stress-crack width relation for the discrete analysis. In the smeared crack analyses, cracks occur in all four integration points (2x2 Gauss), i.e. *two* cracks develop for all element-columns that are modelled with lower tensile strength. This results in a relation between the strain and crack width of $\varepsilon_{crack} = w / (l_{elem.}/2)$. On the other hand, the fracture energy is best reflected if the same number of cracks develops in the smeared and discrete crack model, and that leads to the relation $\varepsilon_{crack} = w / l_{elem.}$ In the following, two smeared crack analyses for each beam have been carried out, one where one crack per element are considered ('SM1'), the other one with two cracks per element ('SM2'). It is here considered sufficient to model half of the beam, although this is a simplification since the distance from the cracks to the middle of the beam is not equal on both sides.

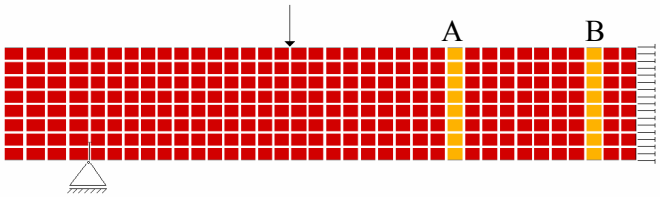

Figure 8.15: Beam 2B with 4 cracks. The elements in the prescribed cracks A and B have a tensile strength of 2.09 N/mm^2, while the tensile strength in the surrounding elements is higher.

A discrete approach was used in Series 3 with the interface elements placed in the middle of the beams. Figure 8.16 shows the element mesh and deflection for the medium beam in Series 3.

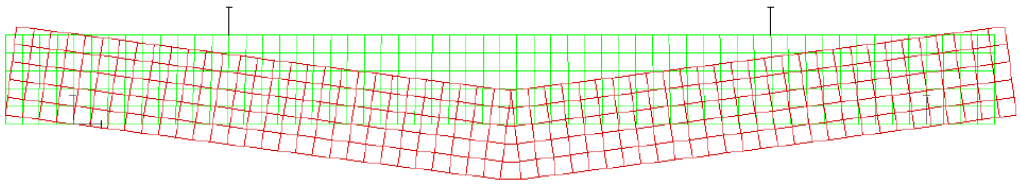

Figure 8.16: Element mesh and deflection, beam 3b with 0.3% fibres. (output DIANA 9.1)

The test results for the three beams in Series 1 with ordinary reinforcement in addition to fibres are in relatively good agreement with the results of the smeared analysis, especially for the small and medium beam [Figure 8.17]. For the large beam, the maximum load from the analysis is slightly higher than the measured maximum load. The beams reach their maximum load at a later deformation-stage in the experiments than in the analyses, indicating that the stiffness of the beams is somewhat overestimated by the analyses. This may be due to the fact that the average crack widths are based on the number of cracks that has developed by the end of each experiment. In the first part of the load-deflection curve, the number of cracks is gradually increasing until the maximum force is reached, which indicates that the tensile strains prescribed in the σ–ε relation are underestimated in this region.

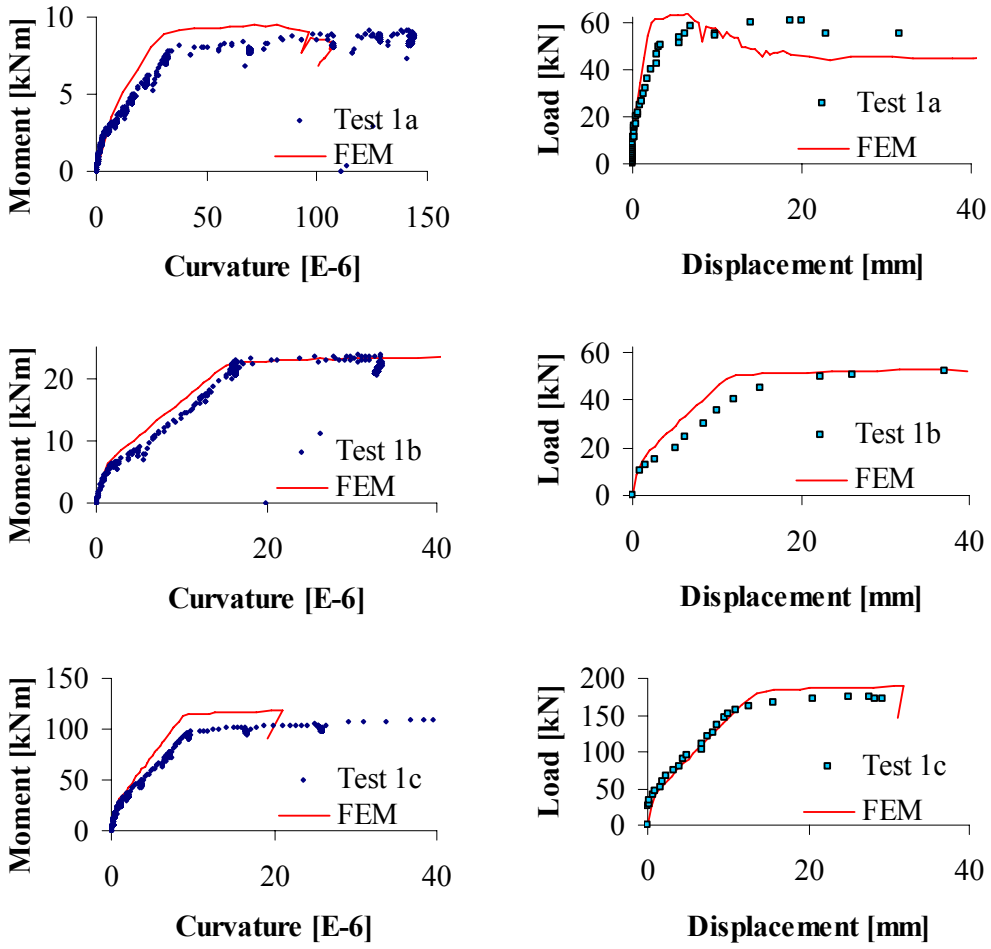

Figure 8.17: Measured and calculated moment-curvature and load-deflection ratio for the three beams in Series 1 with 1% fibres and reinforcement bars. The curvatures are determined from the LVDTs in the middle of the beams [Figure 8.4].

The load-deflection relations and the local load-crack opening relations for the three beams with 1% fibres only are shown in Figure 8.18. For the small beam, the SM1 analysis with one crack per element is closest to the discrete solution and in good agreement with the test results.

For the medium beam, the measured and analyzed load-deflection and load-crack width relations corresponds, and the difference between the two smeared crack analyses is ignorable. The load-crack width relations in Figure 8.18 illustrate the average value of the cracks. For all beams with 1% fibres, only half of the beams are modelled due to geometrical symmetry. Consequently, two and two of the cracks are forced to expand equally, which is not true to the observed behaviour, where one crack suddenly expanded rapidly and led to complete failure. The phenomenon is partly reflected in the finite element analysis with four cracks; at a certain deflection the cracks do not expand steadily anymore. The deformation is concentrated in crack A (see Figure 8.15). This is most pronounced in the discrete analysis, where crack B stops expanding at a deflection of 12mm. In the two analyses with the smeared crack approach, the cracks expand evenly until the beam reaches a deflection of 20mm. Thereafter, crack A starts to expand more rapidly. The difference between the cracks is more pronounced in the SM2 than the SM1 analysis. Even though there is a difference in crack growth between crack A and B in the three FE analyses, the average cracking behaviour and the overall load deflection ratios are in good agreement.

For the large beam, there is a great difference between the measured and calculated results. The analysis overestimates the capacity of the beam considerably. As opposed to the small beam, the result of the SM2 analysis with two cracks per element is in best agreement with the discrete analysis.

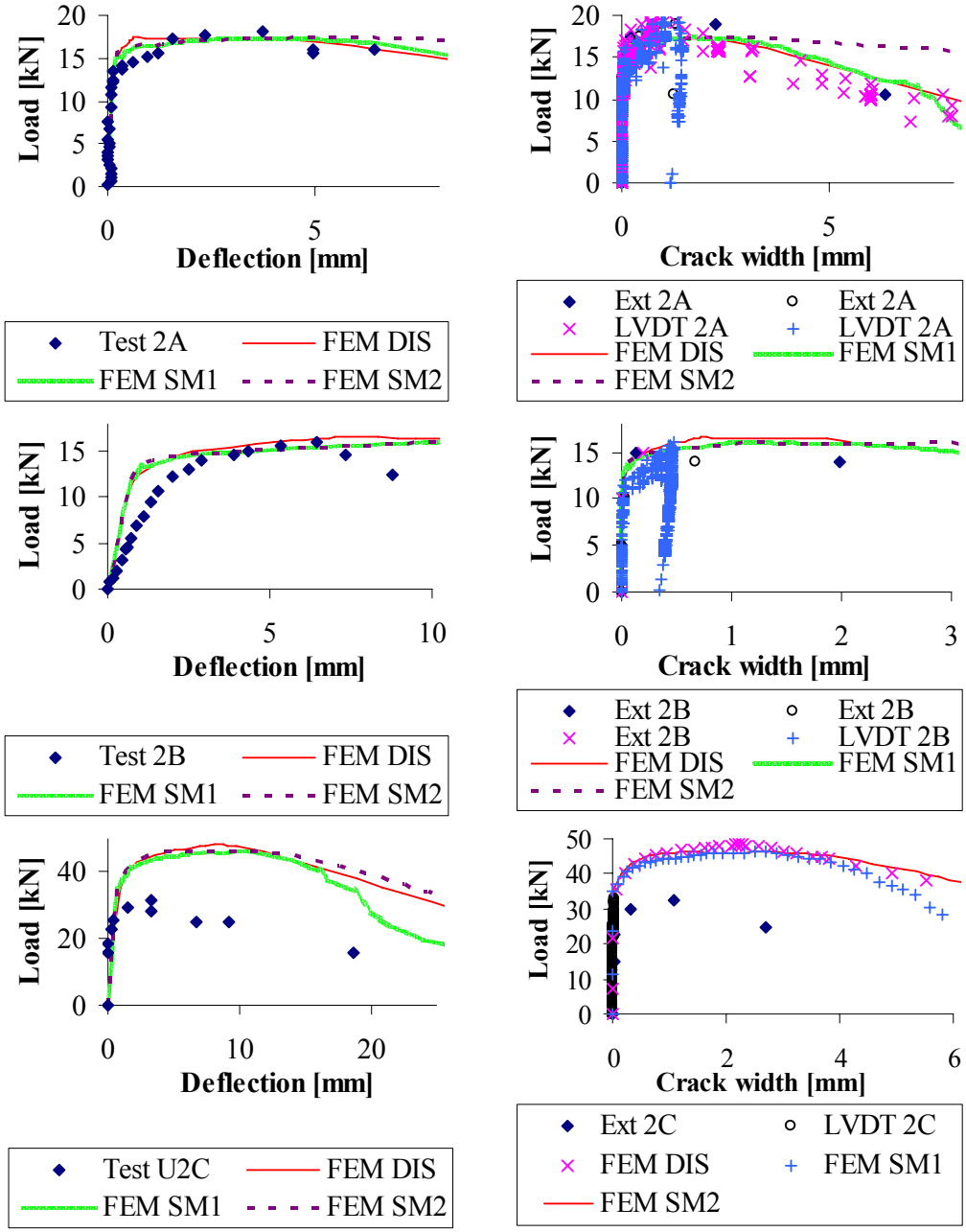

Figure 8.18: Beams with 1% fibres without reinforcement bars. The test results are compared with the FEA results where DIS=discrete crack approach, SM1 and SM2= smeared crack approach with the σ–ε relation determined from one and two cracks per element respectively. For the crack-width relation, the measurements of the extensometer ("Ext") and the LVDTs over the cracks are shown. The crack withs from the analysis is taken as the average value of the 2, 4 and 2 cracks that were modelled for the small, medium and large beam.

In Series 3 with 0.3% fibres only, the analyses and the measurements are in relatively good agreement for all three beams, although the analysis slightly underestimates the post-cracking response of the large beam. In addition, the cracking loads are underestimated by the analyses, indicating that the tensile strength of the concrete might have been larger than prescribed in the FE analyses.

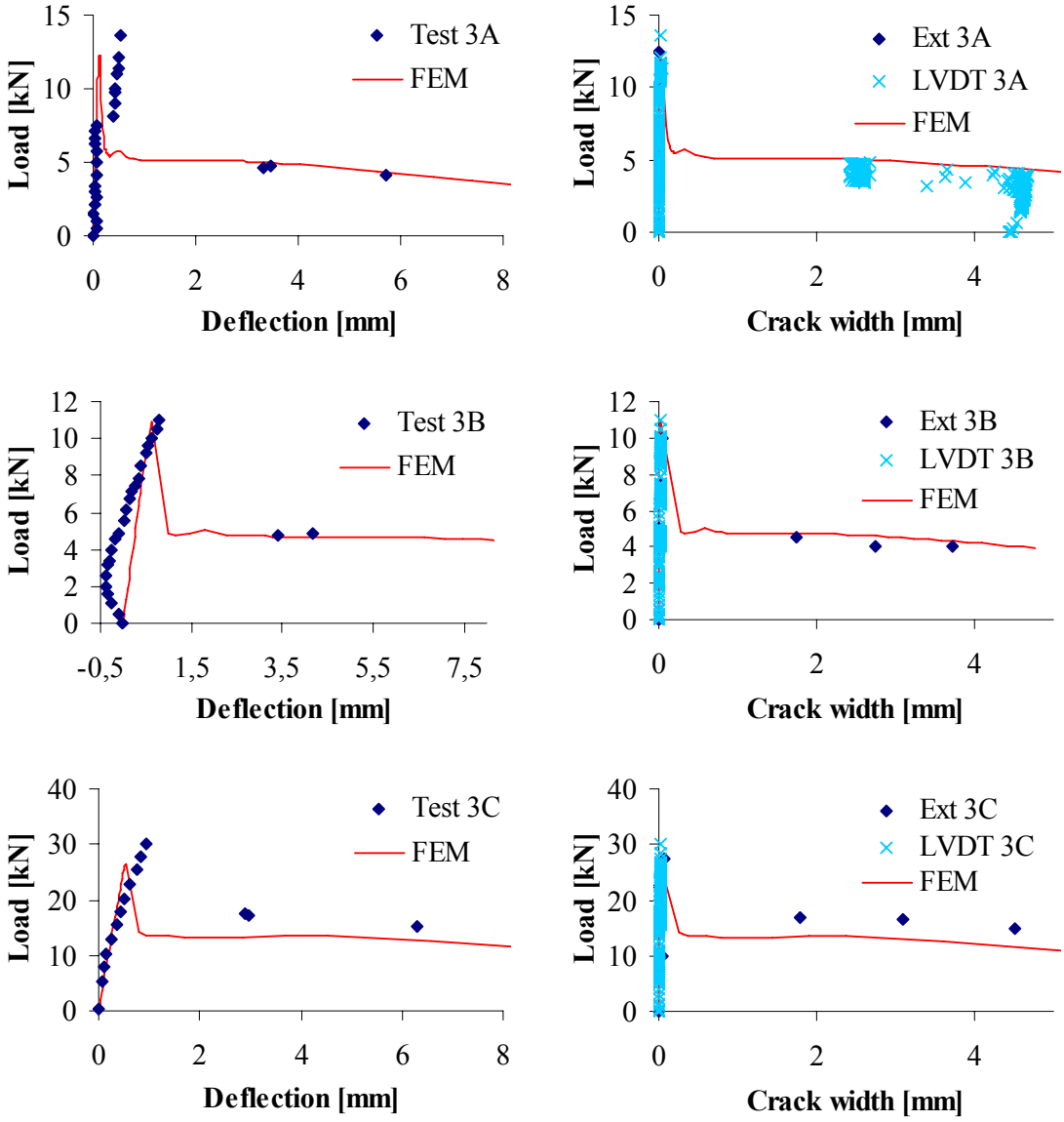

Figure 8.19: Beams with 0.3% fibres. The measured load-deflection and load-crack width data are compared with the FEA results, discrete crack approach.

8.2.7 Conclusions

Nine beams of three dimensions were exposed to bending to investigate the size-effect of FRC. The results showed that the influence of cross section height on the bending strength (1st crack) was similar to plain concrete.

For the beams with steel fibres in addition to reinforcement bars the cracks were distributed over the whole zone with constant moment, and the average crack distances between the twin loads increased slightly from the small to the largest beam.

The results of the beams with 1% fibres only indicated that both the bending strength, the maximum load and the ductility is size-dependent. After cracking, the load increased further with 37%, 32% and 11% for the small, medium and large beam, respectively. However, the opposite behaviour was observed for the beams with 0.3% fibres only. In percentages, the drop in load after cracking decreased with increasing cross section height. This makes it difficult to draw any categorical conclusions regarding the size effect.

In average, the number of fibres counted on sawn out blocks from the beams corresponded to the theoretical number of fibres when the wall-effect is included according to Dupont (2003). For the beams with 1% fibres the scatter was relatively low, while it was slightly larger for the beams with 0.3% fibres.

Finite element analyses of the beams with fibres as an addition to ordinary reinforcement underestimates the capacity slightly for the smallest beam, while it overestimates the capacity for the largest beam. This implies that the size effect probably is not fully described by the FEM.

A comparison between a smeared and a discrete crack approach was done for the beams reinforced with 1% fibres only. In the smeared approach, the material was modelled both with one and with two cracks per element. For

the small beam, the smeared analysis with one crack per element was closest to the discrete solution, while the opposite was the case for the largest beam. The analysis corresponded well for the small and medium beam, but the measured loads for the largest beams were considerably lower than the calculated loads.

For the beams with 0.3% fibres only, the FEA were in relatively good agreement with the measurements, although the post-cracking strength for the large beam was slightly underestimated.

The overall agreement between the analysis and the experiments implies that the material model that was used in the FEA is adequate to describe the behaviour of FRC structures.

9 Slabs exposed to bending

9.1 Introduction

In all standard codes, a minimum bar spacing is required to insure that the forces are distributed through the structure when cracking occurs. With fibres as an additional reinforcement, it is reasonable to assume that the minimum distance between the bars can be increased, because the fibres contribute to more distributed cracking and increase the toughness of the concrete. When a structure for instance is exposed to a concentrated load, the punching resistance will increase due to the fibres, since the fibres can take up shear stresses. Several researchers have shown that the use of FRC significantly enhance the punching shear capacity [Swarmy (1982), Harajli et al. (2006), Choi et al. (2007)]. To add further knowledge on FRC structures with a minimum of ordinary reinforcing bars, two series with slabs exposed to concentrated loads have been carried out.

9.2 Simply supported slabs with FRSCC exposed to concentrated loads

9.2.1 Experiments

13 slabs of dimension 1.2 x 0.15 x 3.6m were exposed to bending. The slabs were simply supported with a concentrated load applied in the middle of each slab, and the loading platen had an area of 50 x 50mm. All slabs were made with SCC. In the first series, Series A, the reinforcement ratio was very low, with a section ratio of ρ=0.07% and 0.15%. The fibre content was 0.7vol%. In addition one reference slab was made without fibres (ρ=0.33%). In the second series, Series B, the reinforcement ratio was higher; ρ=1.12% and 1.36%.

Both steel fibres and different types of synthetic fibres were tested, with fibre contents of 0.7% and 1%. An overview of the slabs is given in Table 9.1.

	Name	Fibre volume	Fibre type	Reinfo. bars
Series A	$S0A_{ref}$	0	-	6ϕ10
	$S1A_{0.7Dr35,2\phi8}$	0.7 %	Steel, Dramix 65/35	2ϕ8
	$S2A_{0.7Dr60,2\phi8}$	0.7 %	Steel, Dramix 65/60	2ϕ8
	$S3A_{0.7Dr35,2\phi12}$	0.7 %	Steel, Dramix 65/35	2ϕ10
	$S4A_{0.7Dr60,2\phi12}$	0.7 %	Steel, Dramix 65/60	2ϕ10
Series B	$S1B_{1Dr35,4\phi25}$	1.0 %	Steel, Dramix 65/35	4ϕ25
	$S2B_{1En,4\phi25}$	1.0 %	Synthetic, Enduro	4ϕ25
	$S3B_{0.7Dr60,4\phi25}$	0.7 %	Steel, Dramix 65/60	4ϕ25
	$S4B_{0.7Dr60,2\phi32}$	0.7 %	Steel, Dramix 65/60	2ϕ32
	$S5B_{1Dr60,4\phi25}$	1.0 %	Steel, Dramix 65/60	4ϕ25
	$S6B_{1Dr60,2\phi32}$	1.0 %	Steel, Dramix 65/60	2ϕ32
	$S7B_{1Ba,4\phi25}$	1.0 %	Synthetic, Barchip K	4ϕ25
	$S8B_{1Ba,2\phi32}$	1.0 %	Synthetic, Barchip K	2ϕ32

Table 9.1: Simply supported slabs; Name and reinforcement.

The objective was to investigate the effect of the different fibres and reinforcement ratios with respect to crack distribution, ductility and peak load, and to control if the fibres were able to transfer the loads from the middle of the slab to the reinforcement bars placed near the sides.

9.2.2 Reinforcement

The slabs were reinforced as illustrated in Figure 9.1. Reinforcement bars of quality B500C were used, which has a guaranteed minimum yield stress of 500N/mm^2. Due the difference in bar diameter, the effective height was reduced from d=130mm in Series A to d=120mm in Series B.

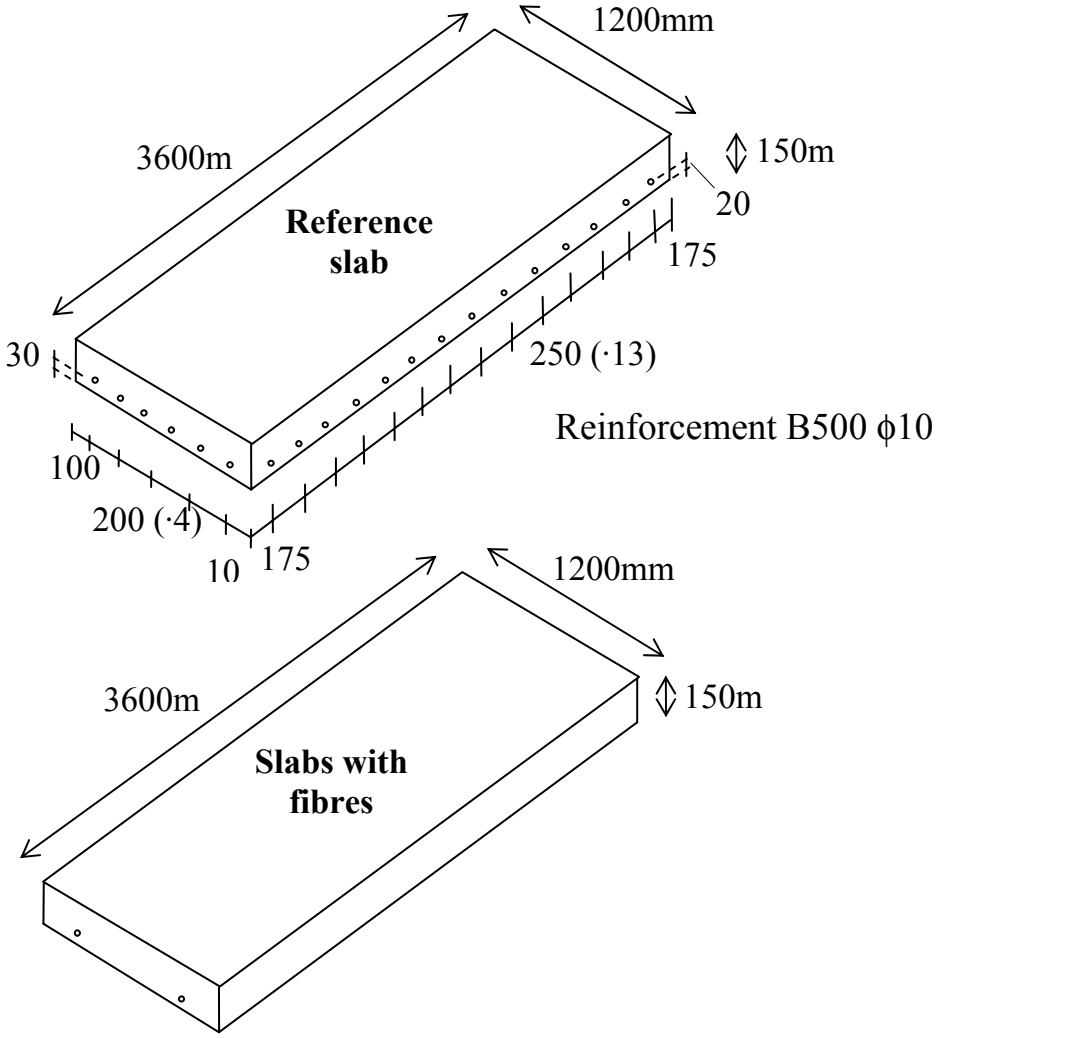

Cross-sections:

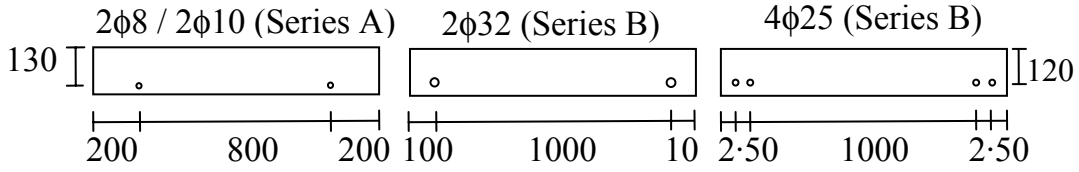

Figure 9.1: Reinforcement in the slabs. The effective height was d=130 for the FRC slabs in Series A, and d=120 for the reference slab and for the slabs in Series B

9.2.3 Concrete and casting

The fibres were added in the concrete mixer truck with a mixing time of 10 minutes. A concrete scip was used for casting, and the concrete was poured from one side of the formwork until the height of the formwork was covered as illustrated in Figure 9.2. The scip was then gradually moved towards the other end to fill the formwork completely. This casting procedure was adopted in an attempt to obtain a constant flow direction of the concrete.

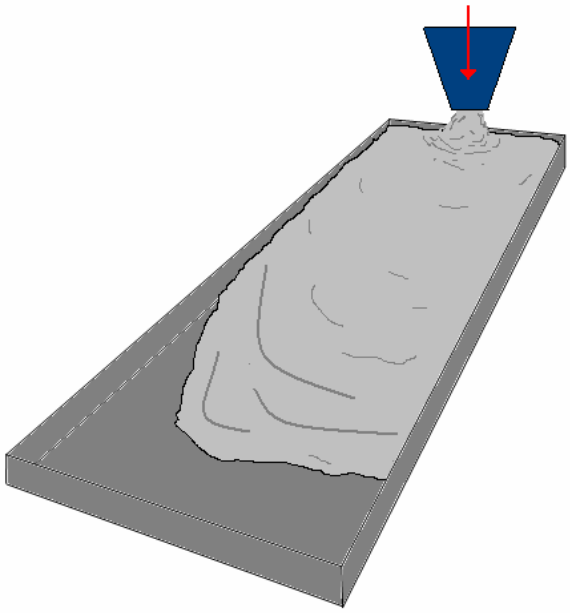

Figure 9.2: Casting

The slump flow was measured before and after casting. For all mixes, the slump flow increased after casting. The two mixes that were used for S1B and S3B/S4B were on the verge of separation, and tendencies of pasta separation were observed by the end of the casting. The change of concrete characteristics during casting indicates that the mixing time was too short. For the last mixes the mixing time with fibres was therefore increased by 5 minutes. The fresh concrete properties are given in Table 9.2. For three of the mixes in series A, the slump flow shows that the concrete is not within the

definition of a SCC, strictly speaking. Still, no vibration was needed to fill the formwork, and the concrete will henceforth be regarded as a SCC.

	Fibres	Density [kg/m^3]	Air content [%]	Slump flow after casting [mm]
S0A	-	2474	1.8	640
S1A	0.7% Dramix 65/35	2280	6.3*/9.4**	535
S2A S4A	0.7% Dramix 65/60	2411	4.2	560
S3A	0.7% Dramix 65/35	2404	2.7*/4.5**	480
S1B	1% Dramix 65/35	2459	3.4	620
S2B	1% Enduro (synthetic)	2421	0.9	600 – 650***
S3B S4B	0.7% Dramix 65/60	2511	1.0	670
S5B S6B	1% Dramix 65/60	2385	2.7	660
S7B S8B	1% Barchip (synthetic)	2421	3.4	600

*Table 9.2: Fresh concrete properties *) Measured at 0.5 Bar. **) Calculated air content (1.0Bar) ***) Lacking slump flow data for this mixture, but pictures show that the slump was in the indicated range.*

The air content for series S1A was measured according to NS EN 12350-7 (the pressure method) requiring an air pressure of 1.0Bar. For two of the mixtures, S1A and S3A, the air pressure applied was only 0.5 Bar. The air content can simplified be estimated from the density of the concrete based on the reference mixture as follows:

The mix with 0.7% long fibres (S2A S4A) had an air content of 4.2% and a density 2411kg/m^3. With 4.2% air, the expected density of mix S1A is equal to S2A/S4A. However, the measured density was only $\rho_{S1A,measured}$ = 2280kg/m^3. If 1% air corresponds to 25kg/m^3 then $\Delta\rho$ = 2411-2280 = 131kg/m^3 indicates a difference in air content between S1A and S2A of 5.2%. The air content of mix S1A should accordingly be 4.2+5.2 = 9.4%. An analogous calculation for mix S3A leads to an air content of 4.5%.

The high air content in the mix for slab S1A resulted in low compression strength; 37% lower than the compression strength of the reference slab. Moreover, it was found that the compression strengths of the two mixes with synthetic fibres were somewhat lower than the compression strength of mixes with steel fibres.

	Fibres	f_{ck} [N/mm^2]	f_t [1] [N/mm^2]	E-modulus [GPa]
S0A	-	55.5	2.3	31.43[2]
S1A	0.7% Dramix 65/35	36.8	1.8	27.74[2]
S2A S4A	0.7% Dramix 65/60	49.3	2.1	30.08[2]
S3A	0.7% Dramix 65/35	49.2	2.1	30.06[2]
S1B	1% Dramix 65/35	61.5	2.4	29.51
S2B	1% Enduro (synthetic)	58.3	2.4	27.38
S3B S4B	0,7% Dramix 65/60	62.1	2.4	31.12
S5B S6B	1% Dramix 65/60	58.4	2.4	28.66
S7B S8B	1% Barchip (synthetic)	50.8	2.1	22.70

Table 9.3: Concrete properties in hardened state. The compressive cube strength is taken as the average value of three specimens. The E-modulus was tested on three cylinders from each mixture in series B. Average values are used, not characteristic values.

9.2.4 Instrumentation and test setup

Figure 9.3 shows the instrumentation and test setup for the slabs in series B. The same setup was used for series A with the following exceptions: Only 4

[1] The tensile strength is interpolated from table 5 in NS3473 (2003)
[2] In series A, the E-modulus is taken as 10000 $f_{cck}^{0.3}$, where the cylinder strength f_{cck} is estimated from the compressive strength according to NS3473.

LVDTs were used to measure the strains, two on top of the slab under the load [Detail 2, Figure 9.3], and two on one of the sides [Detail 1, Figure 9.3]. Moreover, the distance between the supports was 3450mm in series A while it was 3360 in series B.

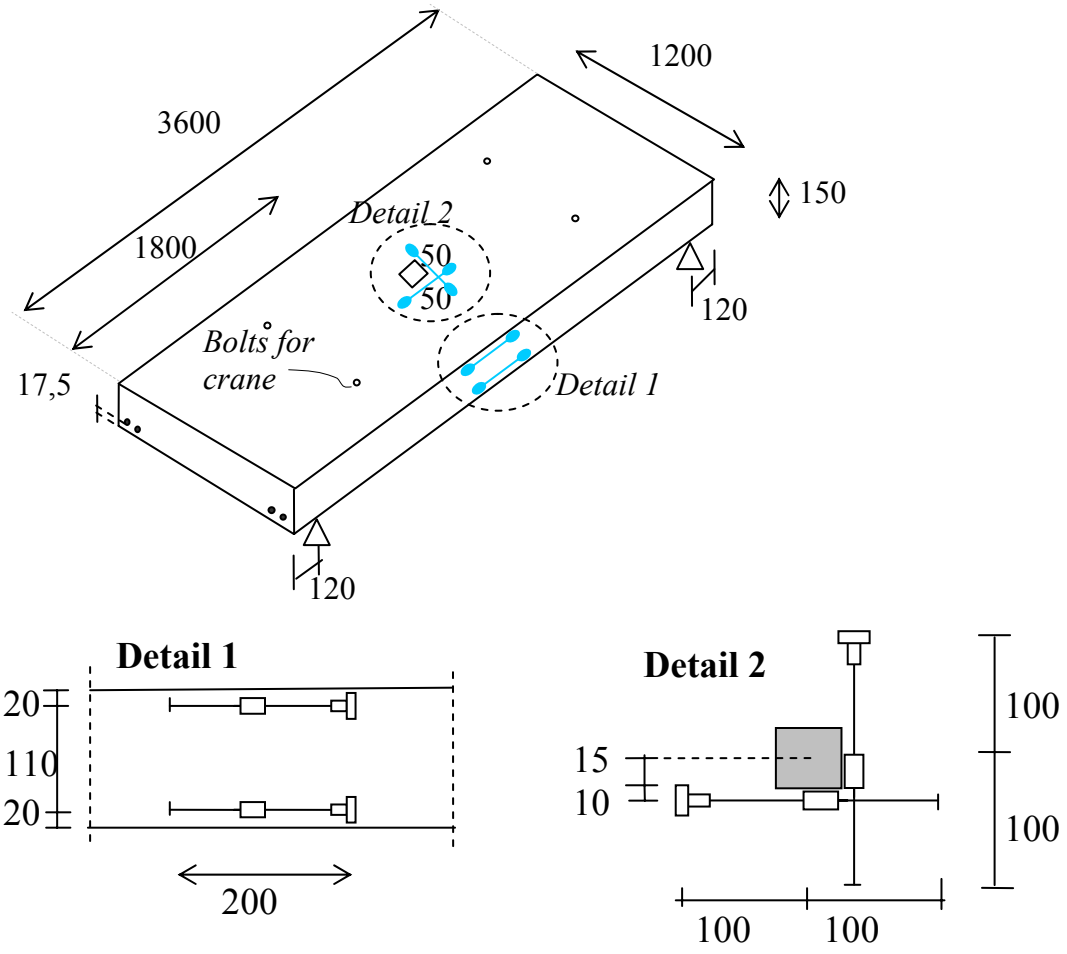

Figure 9.3: 8 LVDTs were used to measure the strains on each slab; two on each side to capture the strains over the cross-section height [Detail 1] and two over and under the slab with the same horizontal placement [Detail 2]. Also the deflections were measured by LVDTs; one at each support and one in the middle of the slab. All units in mm.

9.2.5 Results

It is clear from the two series that fibre length influences the results. The longer fibres were more effective than the shorter fibres.

In series A, the slabs with fibres reached a higher load than the reference slab for deflections up to around 30mm. However, when the deformations increased further, the load for the fibre reinforced slabs decreased, while the load for the reference slab continued to increase at large deformations. Consequently, when maximum allowed deflections in the serviceability limit states for normal structures are considered, the FRC slabs were more adequate.

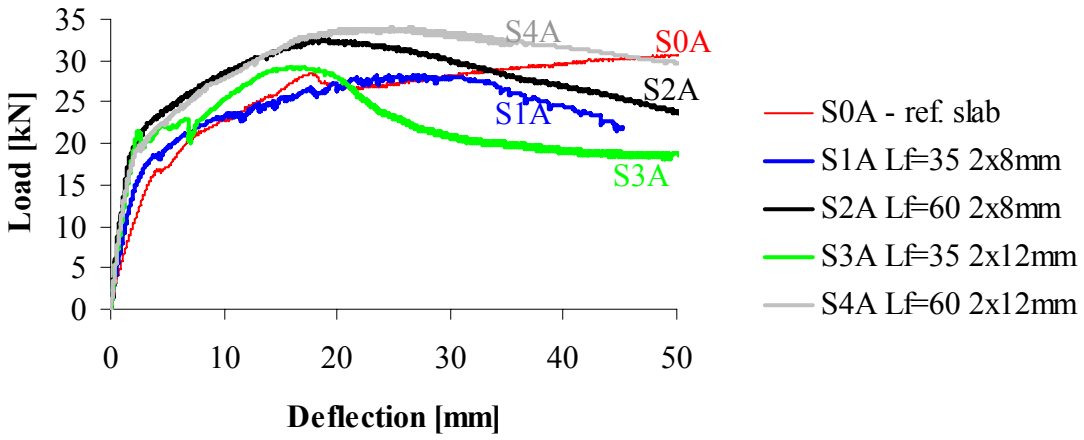

Figure 9.4: Load-deflection measured by LVDTs in the middle of the slabs for Series A.

Figure 9.4 illustrates that the longer fibres were more effective than shorter fibres. Moreover, it shows that the decrease in load for the FRC slabs at deflections over 30mm is larger with 2ϕ8mm bars than with 2ϕ12 bars, which is reasonable since the fibres are most efficient at an early deformation stage. The maximum loads for the four FRC slabs was 28.3kN (Δ=27mm), 32.6kN (Δ=18mm), 29.2kN (Δ=16mm) and 33.9kN (Δ=26mm) for slab S1A, S2A,

S3A and S4A respectively. Hence the maximum load increased, in average with 3% from 2ϕ8 to 2ϕ12, while the difference in maximum load between the shorter and longer fibres was 17%. Accordingly, the influence of the fibre length on the capacity was more important than the reinforcement ratio for the slabs in Series A.

For all slabs in series B, cracks initiated under the load gradually developed in all directions at the bottom of the slab [Figure 9.5]. Owing to the fact that the load increased considerably after crack initiation, it is clear that the fibres succeeded in transferring the tensile stresses to the reinforcement bars. However, the finale failure was dominated by an anchorage/shear failure, as the reinforcement bars were pulled out at the supports [Figure 9.6]. This was primarily due to the concrete cover and bar spacing, which was lower than what is recommended in all design rule codes.

Figure 9.5: a) Loading. b) Cracks initiated under the load. c) Cracks under the load after failure.

Figure 9.6: Slab S1B. Anchorage/shear failure.

Figure 9.7 shows the load-deflection relation for the five slabs in Series B with steel fibres. The maximum loads were 156, 151, 142, 164 and 145kN for slab S1B, S3B, S4B, S5B and S6B, respectively. The maximum load for S5B was 13% larger than for S1B, showing that the longer fibres were more effective than the shorter, which supports the observation done in Series A. An increase in fibre volume from 0.7vol% to 1.0vol% had a smaller influence on the results than the two fibre lengths; the increase from S3B to S5B with 4ϕ25 was 9%, and from S4B to S6B with 2ϕ32 the increase was 2% only. All slabs reinforced with 4ϕ25 reached higher loads than the slabs reinforced with 2ϕ32.

Figure 9.8 illustrates the load-deflection relations for Series B with synthetic fibres. The maximum loads were 126, 111, 105kN for S2B, S7B and S8B respectively, implying that the Enduro fibres were more effective than the Barchip fibres. Moreover, it was evident that the slabs reinforced with 4ϕ25 had a higher capacity than the slab with 2ϕ32.

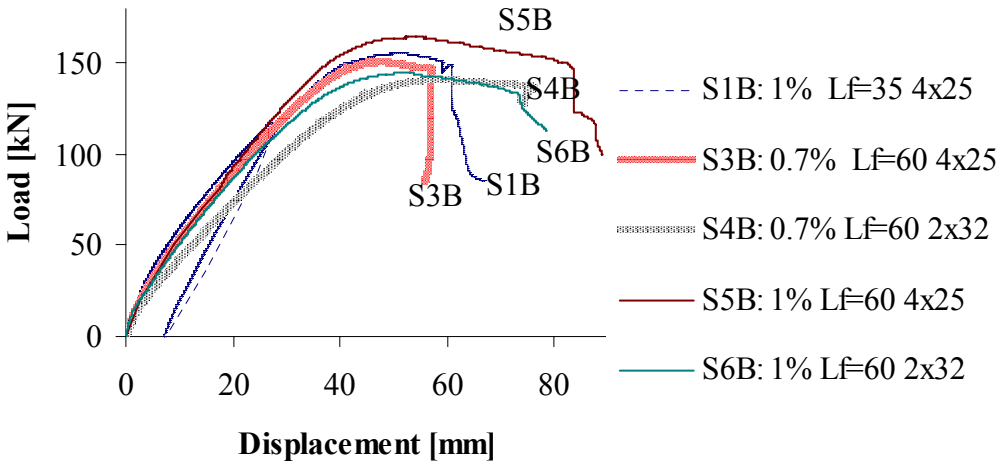

Figure 9.7: Load-deflection measured by LVDTs in the middle of the slabs for Series B with steel fibres. At 0.75P_{max}, S1B was un-and reloaded as illustrated.

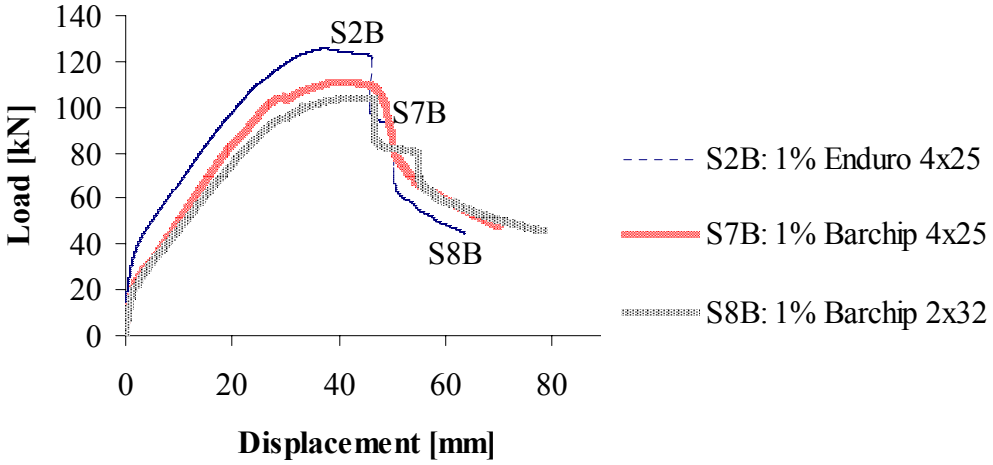

Figure 9.8: Load-deflection for Series B with synthetic fibres.

9.2.6 Orientation and distribution of fibres

Four cylinders were drilled from each slab, and fibres were counted on the surface. Afterwards the cylinders were sawn in three layers to count fibres

orientated vertically. The fibre volume and the residual strength could then be determined as $v_f = (N_1+9N_2/16+7N_3/16)A_f/A_c$ as described in section 2.6.3.

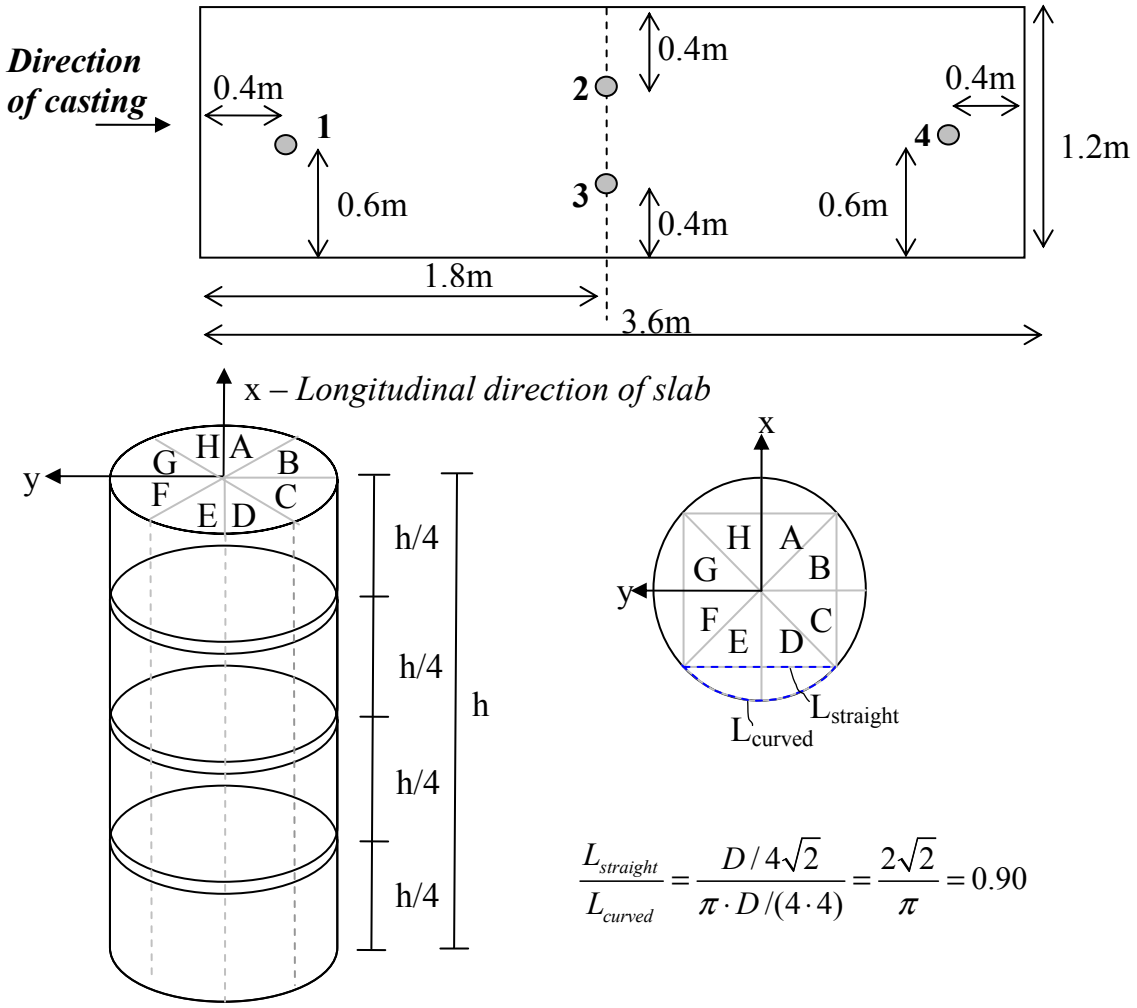

Figure 9.9: Counting of fibres on cylinder surface. The number of fibres on each curved surface (HA, BC, ED and FG) was projected to straight surfaces as illustrated in the figure. The fibres in z-direction were counted in three layers at a distance h/4.

To determine the fibres in the longitudinal and transversal direction of the slabs, the fibres counted on the cylinder surface were projected to a straight surface with length corresponding to the inscribed square [Figure 9.9]. If the

share of uni-directed fibres is equally distributed over the length of the diameter D of the cylinder, the number of uni-directed fibres will be underestimated by $(D-L_{straight})/D=29.3\%$. Thus, counting of fibres on cylinders will underestimate the difference between the longitudinal and transversal direction of the slabs due to the underestimation of uni-directed fibres. However, this will not affect the estimated fibre volume.

Name	Reinforcement	$\sigma_{average}$ [N/mm^2]	v_f [%]	$v_{f,lower}$ [%]	η_0	$f_{res,}$ [N/mm^2]
S1A	1% Dr35+2ϕ8	400	0.78	0.84	0.34	1.13
S2A	1% Dr60+2ϕ8	500	0.71	0.84	0.38	1.58
S3A	1% Dr35+2ϕ12	400	0.58	0.57	0.30	0.70
S4A	1% Dr60+2ϕ12	500	0.65	0.73	0.31	1.13
S1B	1% Dr35+4ϕ25	400	0.87	0.95[1]	0.43	1.65
S2B	1% Enduro+4ϕ25	250	0.93	0.93	0.44	1.03
S3B	0.7% Dr60+4ϕ25	500	0.74	0.81[1]	0.43	1.74
S4B	0.7% Dr60+2ϕ32	500	0.80	0.87[1]	0.44	1.92
S5B	1% Dr60+4ϕ25	500	1.28	1.39[1]	0.45	3.10
S6B	1% Dr60+2ϕ32	500	0.99	1.08[1]	0.44	2.40
S7B	1% Barchip+4ϕ25	250	0.97	0.94	0.46	1.09
S8B	1% Barchip+2ϕ32	250	1.17	1.18	0.55	1.61

Table 9.4: Results from fibre counting on cylinders. Here v_f is the fibre volume while $v_{f,lower}$ is the fibre volume on the lower half of the cylinder. For series A the capacity factor $\eta_0=\eta_{0,x}$. Due to the diagonal crack pattern, η_0 is taken as $\eta_0=(\eta_{0,x}+\eta_{0,y})/2$ in Series B.

[1] No isolated fibre counting on the lower part of the cross section was done; $v_{f,lower}$ is therefore based on Series A, where the fibre volume in the lower half was 9% larger than in the upper half.

Table 9.4 gives an overview of the results from the fibre counting. A more detailed overview can be found in Appendix C. The residual stress after cracking is calculated from $f_{res} = \eta_0 \cdot v_f \cdot \sigma_{average}$ where the fibres volume v_f is estimated from fibre counting on the cylinders and the capacity factor η_0 is determined from the orientation factor $\alpha = n \cdot A_f/(A_c \cdot v_f)$ as [Section 2.6.3]:

$\eta_0 = 2/3\alpha$ for $0.3 < \alpha < 0.5$

$\eta_0 = 4/3\alpha - 1/3$ for $0.5 < \alpha < 0.8$

The average stress is taken as $\sigma_{average} = 500$ N/mm^2 for the longer steel fibres, Dramix 65/60, in accordance with the results in Chapter 6.2.5 and 8.2.4. Since the experiments indicate that the shorter fibres, Dramix 65/35, is less effective than the longer fibres, it is here assumed that the average post cracking stress with these fibres is $\sigma_{average} = 400$ N/mm^2. In chapter 8.2.4 it was found that the average stress for the Barchip fibres was 250N/mm^2 for a SCC with compression strength 50N/mm^2. This corresponds to the concrete used in S7B and S8B. Since no suitable data exists for the Enduro synthetic fibres, the average post cracking stress is assumed to be 250N/mm^2 for all three slabs with synthetic fibres.

Figure 9.10 illustrates the horizontal orientation of fibres versus the coordinates in the longitudinal direction of the slabs, where 3.6m is the location furthest away from the casting point. In general, the estimated capacity factors η_0 are larger than the factor for isotropic orientated fibres $\eta_0 = 1/3$, indicating that the fibres mainly were horizontally orientated. In average the same amount of fibres are orientated parallel and perpendicular to the casting direction. However, the share of steel fibres orientated in the longitudinal direction increases as the concrete flows from the casting point until the middle of the slab, while the share of fibres orientated perpendicular to the flow direction decreases. As the flow distance increases further, the average orientation of steel fibres remains constant. This may be due to the velocity of the flow, which gradually decreases with increasing distance from casting point. Hence, it is reasonable to conclude that the steel fibres tend to

orientate parallel with the flow distance, provided that the flow has an adequate velocity. For the synthetic fibres, the opposite tendency is found; Figure 9.10 b/d indicates that number of fibres orientated perpendicular to the flow increases with increasing flow distance. Yet, the number of tests is not large enough to draw any certain conclusions, especially not with the large scatter that is found.

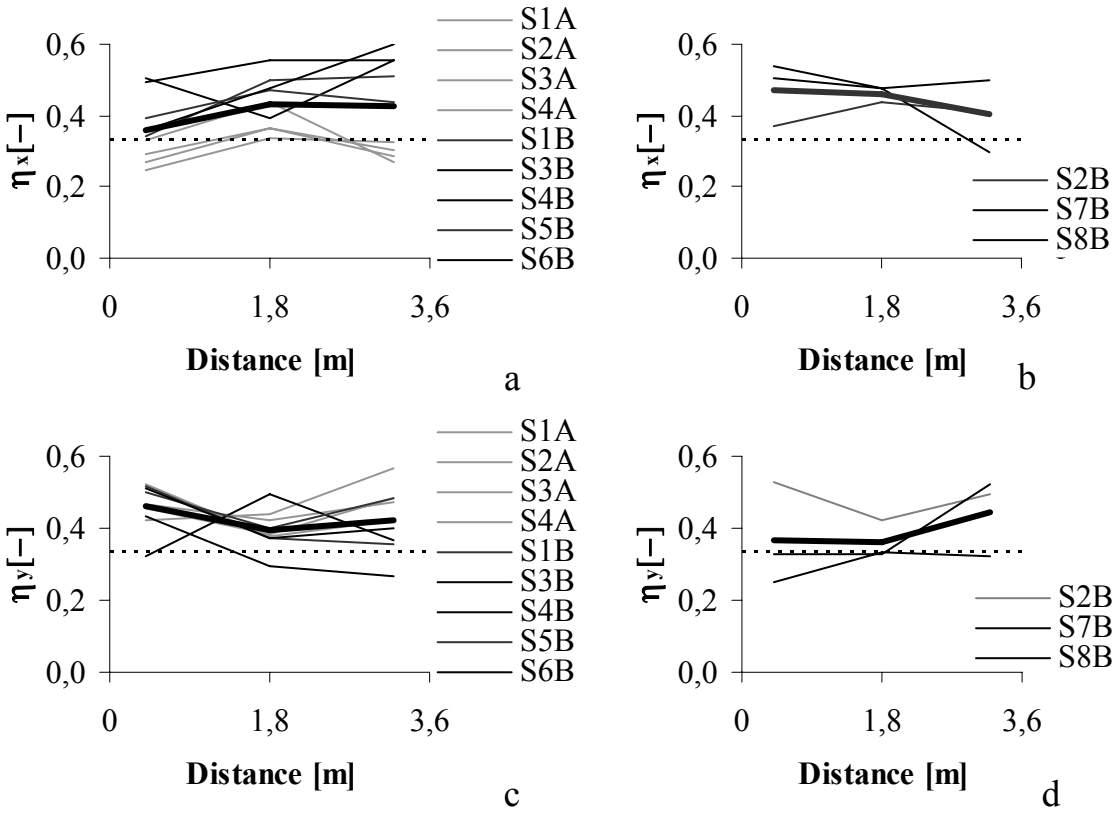

Figure 9.10: Fibre orientation versus distance from casting point, cylinders drilled from slabs. Figure a/c with steel and b/d with synthetic fibres, x: longitudinal direction of slabs, y: transverse direction. For isotropic orientated fibres, $\eta_0=1/3$, as indicated by the dashed lines in the figures. The thick lines indicate the average values.

In average, the fibre volume was 9% higher in the lower half of the slabs with steel fibres (measured in series A). Although no such beneficial volume distribution of fibres was observed for the slabs with Barchip synthetic fibres,

the orientation of fibres were favourable because more fibres were orientated horizontally in the lower half, leading to an increased residual strength of the concrete.

In general, the fibre volume is higher in cylinder 1 than cylinder 2,3 and 4, with 13 % reduction from cylinder 1 to cylinder 2/3, and 15 % from cylinder 1 to 4, implying that the fibre volume decreases as the flow distance of the SCC from the starting point of casting increases.

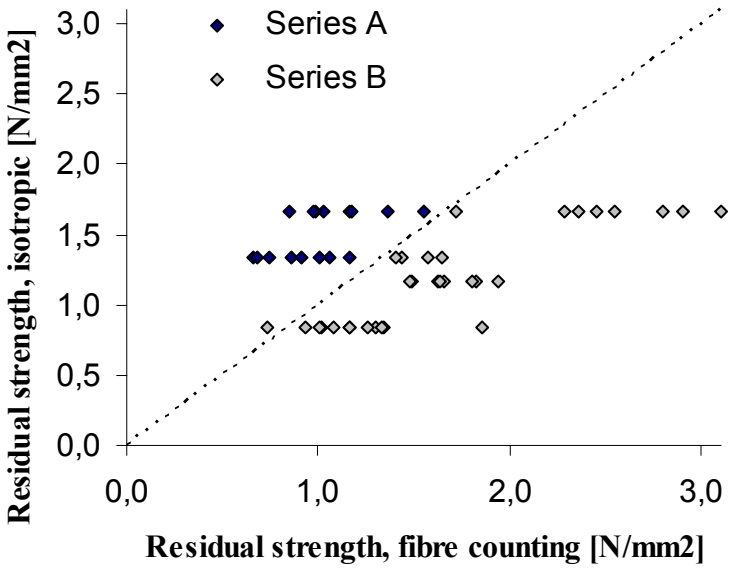

Figure 9.11: Residual strength from fibre counting on the cylinders compared with an ideal isotropic orientation.

Figure 9.11 illustrates the scatter in the residual strengths determined from fibre counting over the whole cross-section height (i.e height of cylinders). The residual strengths from fibre counting are compared with the residual strength from an ideal situation with isotropic evenly distributed fibres. The figure shows that the residual strength from fibre counting in Series B is larger than the theoretical one, which is reasonable since the fibres were mainly orientated horizontally. This favourable orientation was, however, not so

pronounced for Series A. Moreover, as shown in Table 9.4, the fibre volume determined from fibre counting in Series A was considerably lower than 1.0 %, indicating that the fibre concentration added to the mixer truck might have been too low. Yet, one of the most important conclusions from the fibre counting is related to the scatter of the results, which shows that fibre counting on small specimens is not sufficient to estimate the fibre content through the structure.

9.2.7 Finite element analysis

The slabs are modelled with Q20SH, a four-node quadrilateral isoparametric curved shell element. It is based on linear interpolation and Gauss integration over the $\xi\eta$ element area [Figure 9.12]. The number of integration points is prescribed to 2x2x6 Gauss in the ξ, η and ζ direction respectively. To avoid shear locking, which results in an excessively stiff behaviour, DIANA automatically modifies the transverse shear strain fields.

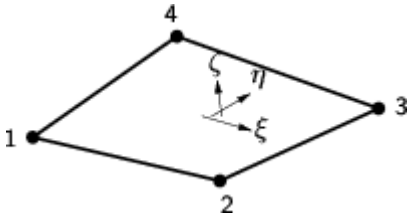

Figure 9.12: Q20SH element used in the FEA [De Witte et al. 2002].

Due to symmetry, ¼ of the plate is modelled in Series A with 512 elements.
For illustration purposes, the whole slab is modelled in Series B, with 672 elements. The load is applied as a deformation controlled load in the mid-node.

In the FEA a total strain rotating crack model was used, with a smeared crack approach and embedded reinforcement. The FRC was modelled by a multi-linear stress-strain diagram in tension, and a CDZ model in compression as described and illustrated in section 6.2.10. The confinement in the zone under

the load was accounted for by an additional strain, and the tensile and compressive strength were both increased by 10‰ in this area. The average post cracking stress of the 60mm long fibres is assumed to be $\sigma_{average}$=500MPa. The experiments described in this chapter imply that the 35mm long fibres are less effective than the 60mm long fibres. This is also supported by the beam experiments in Chapter 6. Obviously, the crack width where the stress approaches zero is reduced with the shorter fibres. Moreover, there is a larger uncertainty attached to the value of the average stress after cracking due to lack of data. In the FEA, the relation between strain and crack width is assumed to be identical with the longer fibres, and the average post cracking stress is taken as $\sigma_{average}$=400MPa. The same was done in the analyses of the slabs with synthetic fibres, but with an average stress of $\sigma_{average}$=250MPa. The latter approximation is questionable, since the post-cracking behaviour of the synthetic fibres differs so much from the steel fibres as shown in the pull-out tests in chapter 4.

For every slab, one initial analysis is run to find the deformation of the slab due to its dead weight, which is determined from the measured density. Then the slab is loaded with a deformation-controlled point load in the middle, and the dead weight is accounted for by subtracting the initial deformation with appurtenant load from the total load-deflection response. The FEA results are compared with the measured data in Figure 9.13 and Figure 9.14.

In Series A, the FEA corresponds to the measurements for the reference slab S0A, although the load at cracking is overestimated by the analysis. Also for the FRC slabs, the cracking load in the analyses is higher than the observations done in the experiments. This implies that the tensile strength used in the calculation has been too high. The analysis underestimates the capacity of the two slabs reinforced with 2ϕ8, while the opposite is the case for the two slabs with 2ϕ12.

The analysis captures the relative difference between the long and short fibres. This indicates that the choice of average post cracking stress of $\sigma(\varepsilon)=400$ for the FRC with Dramix 65/35 is acceptable.

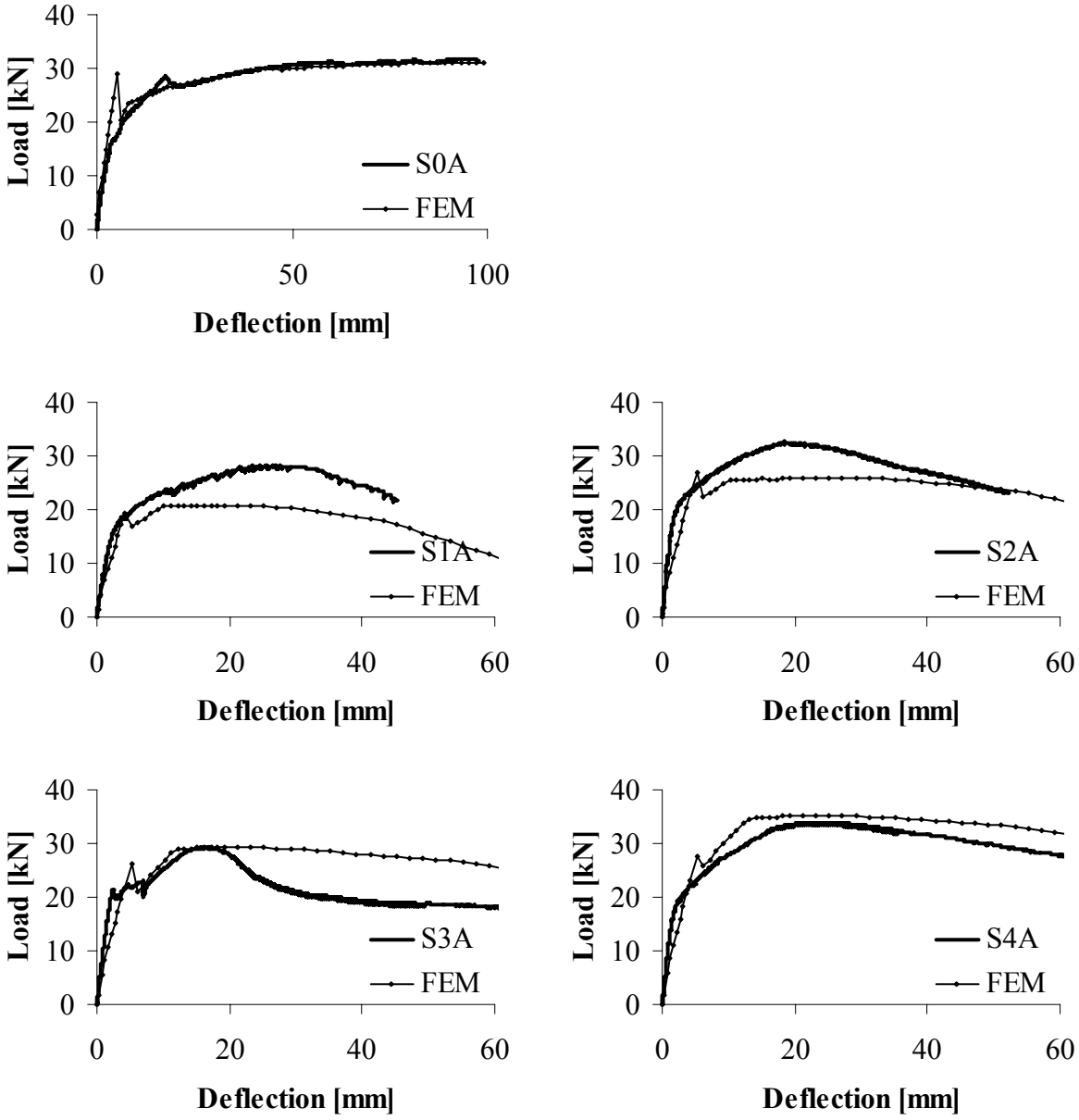

Figure 9.13: FEA results series A

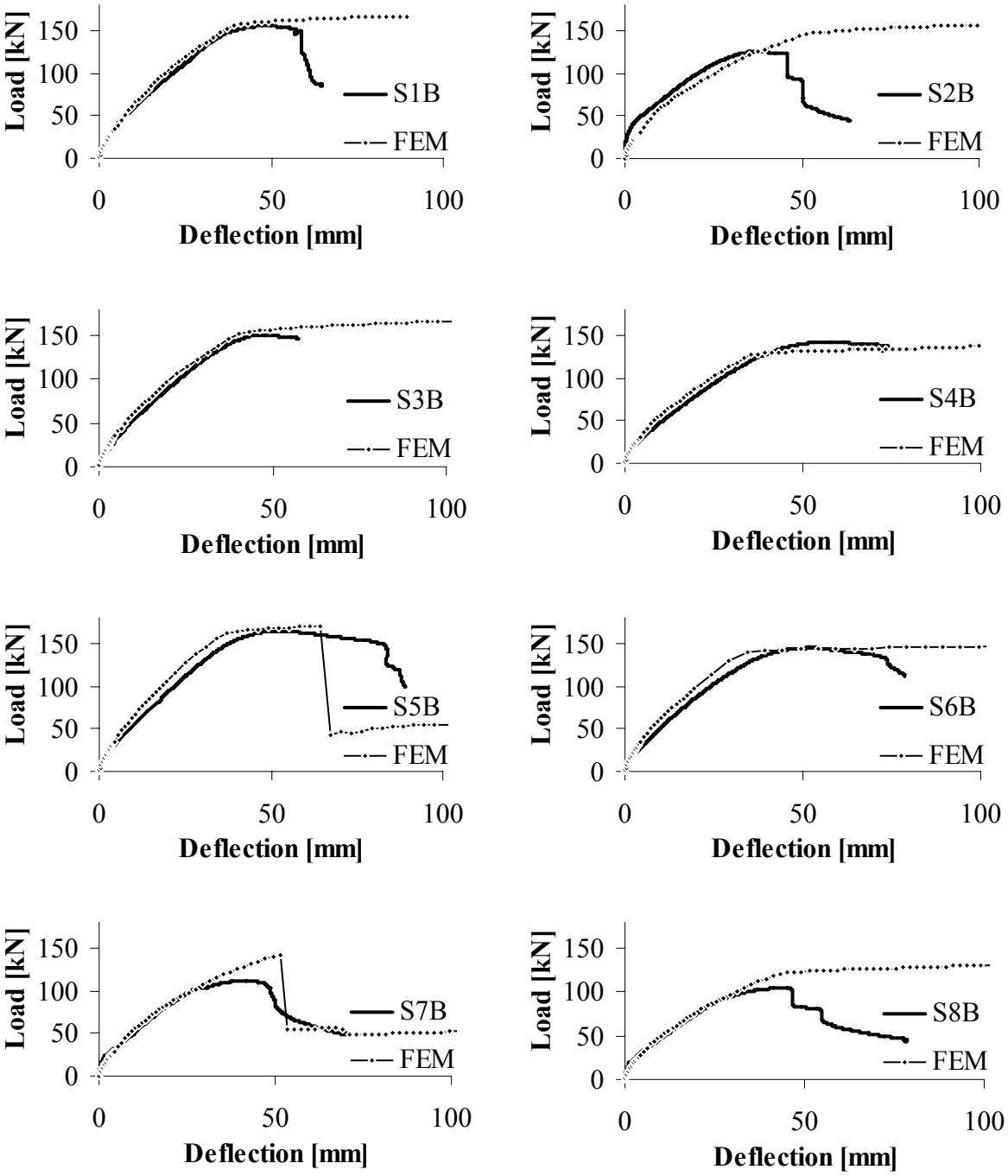

Figure 9.14:FEA Series B conmpared with the measured deflection data.

In Series B, the FEA corresponds with the measured data for the slabs reinforced with steel fibres, up to the point where anchorage/shear failure

occurs. In the FEA, slip between reinforcement and concrete is not made allowance for and, consequently, anchorage/shear failure cannot be captured by the analyses. However, since the anchorage/shear failure breaks out after the peak load is reached at large deformations this is not considered to be a principal matter in the evaluations of the experiments. Yet, it illustrates the importance of sufficient overcoverage in concrete structures.

Slab S5B had the highest capacity also in the FEA, but at a deflection of 64mm the load suddenly dropped from 170kN to 43kN as one crack expanded across the slab under the load. This is illustrated in Figure 9.15.

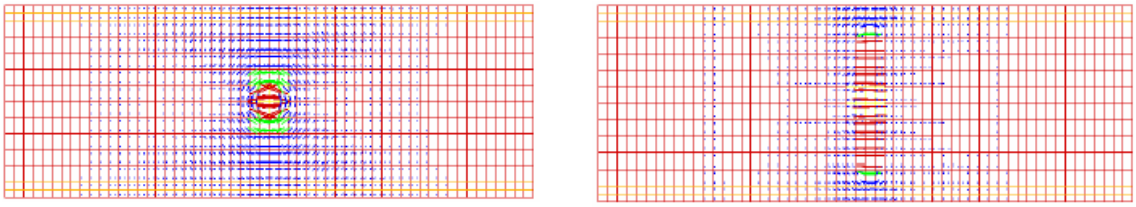

Figure 9.15: Slab S5B, output from iDIANA-9.1. The vectors illustrate the cracking strains under the slab before and after the sudden drop in load in the FEA.

The FEA overestimates the capacity of all three slabs with synthetic fibres. This is not unreasonable, since the real stress-strain relation for synthetic FRC is fundamentally different from steel fibre reinforced concrete. However, convergence problems made it difficult to apply a stress-strain ratio related to the observation done in the pull-out tests in chapter 4, which is why the $\sigma(\varepsilon)$ relation from section 6.2.10 was applied in the FEM. The analyses prove that this approximation of the material behaviour in tension is not sufficient.

9.2.8 Conclusions

The experiments with 13 slabs exposed to bending illustrated clearly that fibres are able to transfer the stresses from concentrated loads to

reinforcement bars at a large bar spacing. Hence, the maximum bar spacing requirements in the design codes can be increased if fibres are added.

It was obvious that the 60mm long steel fibres were more efficient than the 35mm long steel fibres. This was especially visible for the slabs with low reinforcement ratio (ρ=0.07% and 0.15%). It also was observed that the drop in load after the maximum load was reached was more sudden for the slabs with shorter fibres, which can be explained by a shorter pull-out length of the fibres. Moreover, the capacity increase due to synthetic fibres was much lower than with steel fibres.

Due to the low concrete cover for the eight slabs with reinforcement ratios 1.12% and 1.36%, the final failures were dominated by anchorage/shear failure. However, this failure occurred at a large deformation after the peak load had been reached, showing that the fibres were able to transfer large stresses through the structure.

Fibre counting on four cylinders drilled from each slab indicated that the fibre volume slightly decreased with the distance from the casting point. The fibres had a pronounced horizontal main orientation. Moreover, the fibre counting implied that the steel fibres tended to orientate parallel with the flow direction, while the opposite was the case for the synthetic fibres. Still, the large scatter of the results showed that fibre counting on small specimens is not a sufficiently accurate method to estimate the fibre content through a structure.

The FEA slightly underestimated the capacity of the slabs with reinforcement ratio ρ=0.07%, while it overestimated the slabs with ρ=0.15%. Yet, the overall agreement was good, especially for the steel fibre reinforced slabs with reinforcement ratio ρ=1.12% and 1.36%. The tensile behaviour of the FRC with synthetic fibres was modelled similarly as the FRC with steel fibres, although with a lower residual strength. The FEA results for the three slabs

with synthetic fibres showed that this approximation was not sufficient as the analysis overestimated the capacity considerably.

10 Field tests

10.1 Steel fibres as shear reinforcement in prestressed hollow core units

10.1.1 Shear failure in hollow core cross-sections

The conditions for use of FRC is especially good in the prefabrication industry since the production allows a closer control and better routines when it comes to casting procedures. As already underlined, one main challenge for use of FRC is associated with the production, since the distribution and orientation of fibres in a structure is governed by the concrete composition and the casting method.

Prestressed hollow core units are one of the most common products in the precast industry, mainly designed to resist bending moment and vertical shear. Due to the production techniques, there is no transverse or vertical reinforcement, which makes the hollow core units sensitive to combined shear and torsion. Practical examples in which shear forces, bending moment and torsional moment are simultaneously present in hollow core slabs are [Broo 2005]:

- Slabs supported on three edges
- Slabs carrying a trimmer beam to support interrupted units
- Floors with columns in alternating positions at the ends of units
- Slabs supported on beams with divergent inclinations
- Slabs with pronounced skew ends

When vertical shear and torsion act simultaneously, the shear stresses from these forces interact, and may cause failure. Fibres can be used to increase the shear capacity of the hollow core elements, providing that the production technique allows sufficient fibre volumes. To investigate the effect of fibres on the shear capacity, a series of hollow core elements was

tested in cooperation with Contiga, a Scandinavian supplier of prefabricated concrete. The tests were carried out in Contiga's factory in Moss.

One key parameter that has to be established when performing shear tests on hollow core sections, is the distance from the support to the load; the a/d relation (where "a" is the distance from load to support and "d" the effective cross-section height). If the distance from the support to the load is too small, a pull-out failure will occur as the adhesion between the concrete and prestressing steel is exceeded. On the other hand, if the a/d relation is too large, the final failure will be a result of bending moment. As the influence of steel fibres on the adhesion between concrete and prestressing steel is not fully established, the setup for the current experiment is based on standard shear tests done on hollow core elements at the Contiga factory, where the a/d relation is taken as 2.5. However, if the fibres cause a poor compaction of the concrete around the prestressing bars, it is expected that the failure will be dominated by pull-out rather than shear.

Earlier experiments on hollow core sections without fibres have shown that the probability for a pure shear failure is largest when [Thorenfeldt 2002]:

- The number of prestressing bars for a 1.2m wide element is 13. This is due to the adhesion between steel and concrete; if the number of bars is high, the tension is more distributed. On the other hand, if the number of prestressing bars is too high, the compaction of the concrete might be poor.
- The prestressing force is high, since this reduces the chance of moment failure.
- For different dimensions of the hollow core sections produced in Norway, the probability of shear failure with a/d=2.5 is highest for the larger elements with cross-section height 400mm.

These conclusions are based on the results of 388 experiments done on hollow core units, which are described in the report by Thorenfeldt (2002).

The cross-section heights of the elements were 200, 265, 320 and 400mm, and in total 83 of the elements failed due to pull-out.

10.1.2 Experiments

Twelve simply supported hollow core units of dimension 4 x 1.2 x 0.32m were exposed to a line load at a distance 2.5h=800mm from the support. Six different mixes were applied, with two elements from each mix:

- Mix 1: Reference mix without fibres
- Mix 2 0.37 % Dramix 65/35 steel fibres
- Mix 3: 0.74 % Dramix 65/35 steel fibres
- Mix 4: 1.1 % Dramix 65/35 steel fibres
- Mix 5 0.37 % Dramix 65/60 steel fibres
- Mix 6: 0.74 % Dramix 65/60 steel fibres

The elements were tested 9-10 days after casting. All elements were loaded first from one side and thereafter from the other as the element was rotated 180 degrees in order to repeat the testing procedure, which means that in total 24 tests were run. Even though the deflections in the second test on each element were influenced by the fact that the other end had a fracture, the influence of this on the ultimate load can be neglected. An overview is given in Table 10.1. The load was applied with a constant deformation rate. For one test from each mix the deflections were measured by LVDTs at the supports and under the load. In addition, the strains were measured on both sides of the element as illustrated in Figure 10.5, where the 200mm long LVDTs were placed to capture the cracks.

The concrete used in hollow core units is relatively dry and stiff, and fibres reduce the workability even further. As shown in Table 10.1 the fibres were taken into account by reducing the amount of aggregate compared to the reference concrete. Even with this reduction, the workability was reduced noticeably as the fibre content increased. However, the grading curve was

not optimized since it was decided to use the aggregate and sand available at the concrete factory.

Figure 10.1: Casting of hollow core sections. The concrete is filled and compressed through the machine. The cores are made by rotating cylinders. [Contiga 2007]

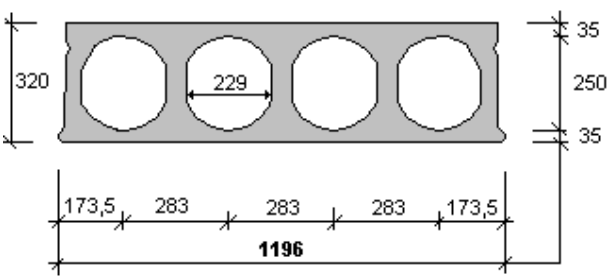

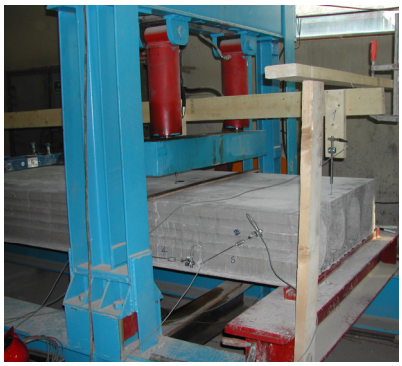

Figure 10.2: Dimensions and loading of the hollow core elements. The number of prestressing steel was 10.

Concrete mix, 1m^3	Mix 1	Mix 2 Mix 5	Mix 3 Mix 6	Mix 4
Steel fibres [%]	0.0	0.37	0.74	1.10
Cement [kg/m^3]	330	342	355	368
Water [kg/m^3]	135	140	145	150
Sand 0-8 mm [kg/m^3]	998	1055	1104	1150
Aggregate 8-16 mm [kg/m^3]	928	826	734	645
Admixture RN15 [kg/m^3]	1.72	1.78	1.84	1.91
Matrix content [kg/m^3]	252	261	271	280

Table 10.1: Concrete mix with mass ratio 0.38 developed by Johansen (2006).

Series			4	5	6	Mean
1	ρ	[kg/m^3]	2570	2570	2590	2580
	f_{cck}	[MPa]	68.1	65.7	64.5	66.1
2	ρ	[kg/m^3]	2550	2580	2550	2560
	f_{cck}	[MPa]	69.0	67.7	67.7	67.9
3	ρ	[kg/m^3]	2550	2560	2560	2560
	f_{cck}	[MPa]	65.9	67.9	69.3	67.7
4	ρ	[kg/m^3]	2530	2550	2530	2540
	f_{cck}	[MPa]	71.1	68.6	69.4	69.7
5	ρ	[kg/m^3]	2540	2540	2530	2540
	f_{cck}	[MPa]	60.6	63.0	62.8	62.1
6	ρ	[kg/m^3]	2550	2530	2550	2540
	f_{cck}	[MPa]	63.9	63.5	67.6	65.0

Table 10.2: Cylinder compression strength (f_{cck}) and density (ρ) for the six mixes.

To measure the compression strength, three cylinders (D x H = 185 x 94mm) were drilled from one of the elements from each mix as illustrated in Figure 10.6. The results are shown in Table 10.2. The scatter was relatively low, with the lowest measured compression strength of 61MPa

for cylinder 5-4, and highest compression strength of 71MPa for cylinder 4-4. In average, the three mixes with the shorter fibres, Dramix 65/35, had higher compression cylinder strength than the mixes with longer fibres, and the cylinders taken from mix 4 with 1.1 % fibres had the highest measured values. The variation in the measured density was negligible.

In addition, the cube strength was measured at the concrete factory at the day of testing, with an average value of f_{ck}=77N/mm^2.

10.1.3 Results

An overview of the test results is given in Table 10.3. The fibres did not cause a clear improvement of the shear capacity. Even though the ultimate load increased slightly with the longer fibres, the apparent difference between the two fibre types can possibly be explained by the casting technique, which improved slightly from mix 2 to mix 6. The feeding of fibres to the machine gradually became more continuous and smooth, resulting in a shorter casting time. The exception was mix 4 with 1.1 % fibres, where blocking occurred so that the concrete remained in the machine for more than one hour.

When the failure is caused by a large opening of a more or less vertical crack under the load, at the same time as an appurtenant slippage of the steel wires occur at the end of the slab, the failure is characterized as a pull-out failure, indicated with “M” in Table 10.3. With the shorter fibres, pull-out was the dominating failure mechanism, while shear failure occurred more often with the longer fibres. Moreover, in series 2 and 4 with shorter fibres, the ultimate load was even lower than in the reference mix without fibres.

v_f/L_f		Load [kN]		
0	$1a_1$	23.5	31	S
	$1a_2$	35.0		S
	$1b_1$	34.0		S
	$1b_2$	32.3		S
0.37% 35mm	$2a_1$	28.2	28	M
	$2a_2$	27.0		S
	$2b_1$	25.5		M
	$2b_2$	33.1		S
0.74% 35mm	$3a_1$	31.8	32	M
	$3a_2$	30.9		S
	$3b_1$	31.1		M
	$3b_2$	33.2		S

v_f/L_f		Load [kN]		
1.1% 35mm	$4a_1$	25.5	25	M
	$4a_2$	29.6		M
	$4b_1$	29.2		M
	$4b_2$	25.0		S
0.37% 60mm	$5a_1$	36.1	33	S
	$5a_2$	32.2		S
	$5b_1$	31.2		S
	$5b_2$	32.8		S
0.74% 60mm	$6a_1$	35.3	36	M
	$6a_2$	36.2		S
	$6b_1$	39.0		S
	$6b_2$	32.7		M

Table 10.3:Ultimate loads for the 24 tests. From each mix two elements (a and b) were tested, each of them tested on both sides denoted by the index. The average ultimate load for each mix is also shown. S and M indicates if the fracture at failure was mainly due to shear or moment (bond failure).

The main advantage with the fibres was increased ductility. While the fractures for the four elements without fibres were very brittle, the elements with fibres all behaved in a ductile manner, both for the elements where wire-slip occurred and for the elements with a more pronounced shear failure. Figure 10.5 illustrates how the strains developed for one of the elements where moment failure occurred (2a) and one element where shear failure occurred (5a).

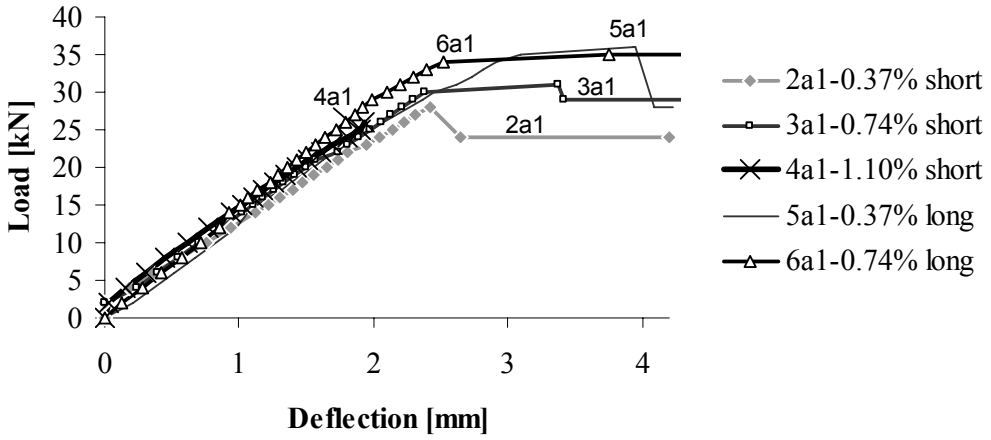

Figure 10.3: Load-deflection measured under the load. For test $1a_1$ problems occurred with the measurements, the series is therefore not included in the figure, but it was observed that the failure of this test was very brittle.

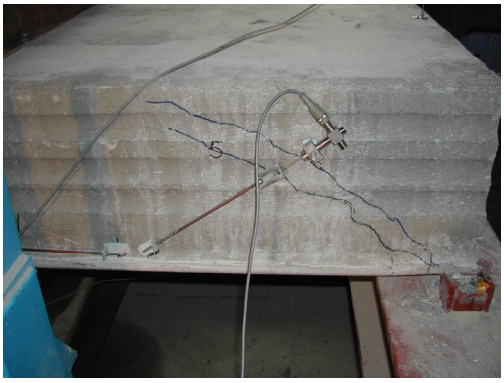

Figure 10.4: The picture shows the placement of the LVDTs (Element $5a_1$), and it illustrates the branching of the cracks caused by the fibres.

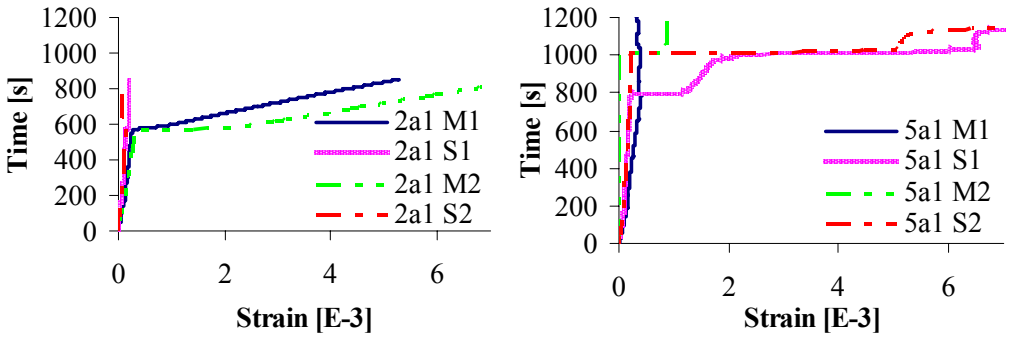

Figure 10.5: Tensile strain development vs time for test $2a_1$ and $5a_1$ (0.37 % fibres). The strains were measured by four LVDTs, two on each side for every test. M measures the vertical cracks (horizontal LVDT), S measures the shear cracks (inclined LVDT).

10.1.4 Orientation and distribution of fibres

To be able to explain the scatter in the results, fibres were counted on the following test specimens [Figure 10.6]:

I. Half of the cross-section (b/2 x h = 1196/2 x 320)
II. Cylinders drilled from the lower flange of the cross-section. Dimensions: diameter x length =100 x 220
III. Middle pieces/webs between the hollow cores chiselled out and sawn in order to count fibres in the y and z-direction [Figure 10.6]. It was not possible to count fibres in the x-direction of this specimen since the side coincided with the surface of the hollow cores. The dimensions on the specimens were l_x x l_y x l_z = 50 x 90 x 220mm.
IV. Cylinders form the upper flange (Number 5, only for mix 5 and 6). The surface of these cylinders was grinded in order to perform a standard compression test on them, which erased the marking indicating the x and y-direction. These cylinders could therefore only be used to indicate the fibre volume in the upper flange, not the fibre orientation.

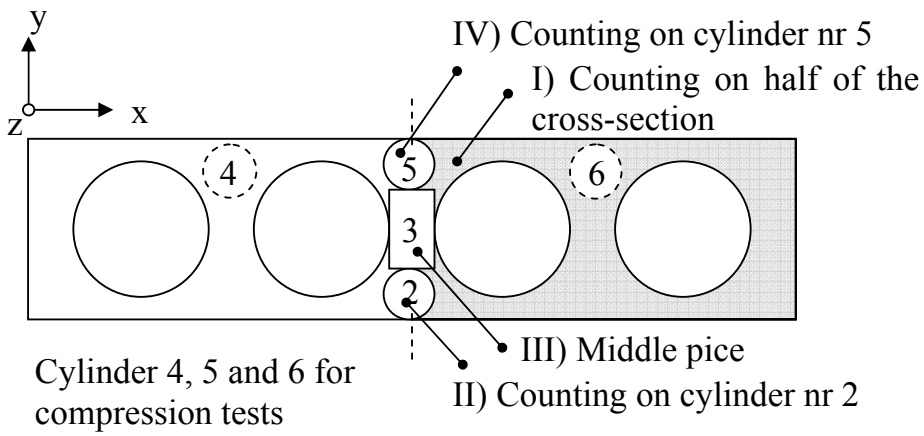

Figure 10.6: Specimens for fibre-counting. Cylindre number 4, 5 and 6 were drilled out to determine the compression strength of the concrete.

Specimen		Mix2	Mix3	Mix4	Mix5	Mix6
I	Share of fibres, lower half of the cross-section	0.42	0.39	0.40	0.50	0.46
II	ρ_x/v_f	0.32	0.28	0.41	0.32	0.35
	ρ_y/v_f	0.38	0.46	0.31	0.43	0.31
	ρ_z/v_f	0.29	0.26	0.28	0.24	0.34
	v_f	0.15	0.44	0.30	0.26	0.47
III	$n_{y,bottom}/n_{y,top}$	0.87	1.05	0.53	1.57	0.90
	n_z/n_y	0.51	0.28	0.46	0.56	0.55

Table 10.4: Results from fibre counting. I) The distribution over the cross section is indicated. If the fibre orientation and distribution of fibres were constant over the cross-section height, 50 % should be located on the lower half. II) The results of the cylinders taken from the lower half, the orientation of fibres in the three directions is shown. In an ideal isotropic situation, $\rho_x/v_f=\rho_y/v_f=\rho_z/v_f=1/3$. III) Middle section; the number of fibres per mm^2 shows the difference between the upper and lower part of the specimen, as well as the ratio between horizontally and vertically orientated fibres.

An overview of the results from fibre counting on specimen I, II and III is given in Table 10.4. The main conclusions are that:

- The number of fibres in the longitudinal direction of the slab was larger in the upper than in the lower half of the cross sections (specimen I).
- In the lower part (specimen II), the share of fibres in the longitudinal direction was somewhat lower than in the vertical direction, and the fibre volume was much lower than the added concentration, especially for the cylinder from mix 4 where the added volume was almost four times as high as the volume estimated from fibre counting.
- Fibre counting from the web in the middle showed that the number of vertically orientated fibres was decreasing in the lower part of the section, presumably mainly caused by a lower concentration of fibres. It also showed that the number of fibres in the vertical direction in average was twice as high as the number of fibres in the longitudinal direction of the hollow core element.
- The fibre volumes estimated from fibre counting on cylinder 5 in the upper half were 0.48 % and 1.0 % for mix 5 and mix 6 respectively, which was higher than the added volume of 0.37 % and 0.74 %.

Figure 10.7 shows a cylinder drilled from the hollow core unit made of mix 4 with 1.1 % fibres. The cylinder is taken from the end of the element at the support, and it illustrated how the steel wire has moved relative to the concrete, resulting in a pull-out failure. It also shows that the packing of concrete around the steel wire is poor.

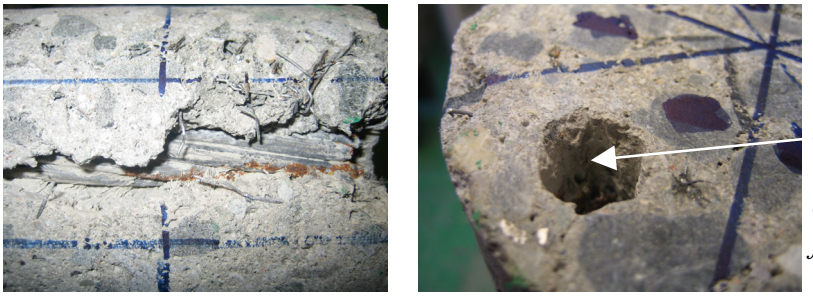

Whole where the steel wire has slipped into the concrete after pull-out failure.

Figure 10.7: Cylinder from mix 4 with 1.1 % added fibres.

10.1.5 Experience and conclusions – hollow core units

The experiments described in this section demonstrate that the ductility of the shear failure can be improved significantly with fibres. They also indicate that the shear capacity can be increased by adding fibres, provided that improvements are made with respect to concrete mix design and casting procedure. It is apparent that the pull-out failure occurred more frequently than shear failure as the fibre content increased. However, it should be stressed that pull-out failure sometimes does occur in the standardized tests for hollow core elements with plain concrete, even if the reference slabs in this series failed due to shear.

Fibre-counting on specimens taken from the hollow core units showed a larger concentration of fibres in the upper part of the cross-sections, suggesting that some fibre blocking occurred as the concrete was pressed in between the hollow cores. Moreover, visual observations of the sawn out cross-section proved that the concrete was not always sufficiently compacted around the steel-wires, which probably led to a pull-out failure before the shear capacity was reached. No categorical conclusions with respect to fibre content and fibre length should be made, as the casting procedure improved from mix1 to mix6. Yet, it can not be expected that a fibre concentration of 0.37 % (mix 2 and 5) will result in any substantial increase of the shear capacity.

To be able to utilize the potential of the fibres, it is essential to do more research on the mix design for the particular concrete that is used in hollow-core elements. It is likely that the uneven grading curve of the sand and aggregates is part of the reason for the poor compaction in experiments described in this chapter. Moreover, it is advantageous if the feeding of fibres to the machine can be automated in order to reduce the time of the casting process.

If an improvement in mix-design and casting procedure can be reached, it would also be of interest to increase the number of prestressing steels and

the prestressing force as mentioned introductorily in order to determine the influence of fibres on the shear capacity on hollow core elements.

10.2 House of SFRC, full scale testing of slabs with SFRSCC

10.2.1 Introduction

In July 2004 the Norwegian Defence Estate Agency constructed a village of concrete houses at Rena military training camp. In one of the buildings at the camp, steel fibre reinforced self compacting concrete (SFRSCC) was used in walls, slabs and in the roof. Through co-operation with the contractor, and financed by a research project group [Section 1.2], preliminary tests were carried out to control the concrete and casting procedure. After completion, full scale experiments were carried out in the building. A concentrated load was applied on three slabs with different combinations of fibres and ordinary reinforcement; one reference slab with ordinary reinforcement bars, one slab with steel fibres combined with a minimum of reinforcement bars, and one slab with steel fibres only.

10.2.2 Concrete mix and preliminary test elements

Before casting the steel fibre reinforced concrete house at the training camp, three test elements in realistic size were made: A slab, a wall and an inclined plate with a slope corresponding to the roof of the house. These elements were cast to check if it was possible to get an even distribution of fibres, and to see if the ordinary reinforcement bars in the two plates would lead to fibre blocking. Another objective was to investigate the relation between the direction of the flow during casting and the fibre orientation.

The wall was made without reinforcement bars, while the slab and inclined plate was reinforced according to the bar spacing of the roof and the slabs in the house. The fibre content was 0.8 % Dramix 65/60 steel fibres. Table 10.5 gives an overview of the concrete composition.

Concrete composition	Kg/m^3
Norcem Anlegg, CEM I 52.5 N-LA (HSC)	255
Norcem Industri, CEM I 42.5 RR (RPC)	91
Condensed silica fume from Elkem	26
Free water	206
Absorbed water	17
Fine aggregate, 0-8 mm	850
Fine crushed sand, 0-0.5 mm	147
Crushed aggregate, 8-16 mm	620
Copolymer, Glenium 27, Degussa	6.7
AEA Scanair 1:9	8.4
Bekeart RC65/60 steel fiber	62

Table 10.5: Concrete composition.

The aggregate and sand available at the mixing plant did not have an optimal grading curve, which made the FRSCC exposed to segregation. Several test mixes were therefore made to find an applicable concrete composition. To make the concrete adhesive and less prone to segregation, a blend of normal and rapid cement was used. Condensed Silica Fume (CSF) was necessary to decrease the segregation of the SCC, and test mixtures with 5.0 %, 7.5 % and 10 % CSF of cement weight were made. The mix with 7.5 % CSF was used in the delivery to the SIBO Village. The addition of a copolymerbased superplasticizing agent was normally done at the ready-mix plant, and it was observed that the slump flow measure increased by 20 to 30 mm during the transport to site. However it was sometimes necessary to add copolymer at the building site as well. Preliminary tests revealed that to make FRSCC the matrix volume had to be 40-50 l/m^3 higher than for ordinary SCC. The main reason for using an

air entraining agent was to increase the matrix-aggregate ratio. According to Hammer and Johansen (2005) the entrained air influences the flowability of the concrete in a similar way as increased matrix volume. In a series of mortar tests they showed how the flowability increased with increasing air content. Dispersed fine air bubbles made the concrete flow better without segregation. [Busterud et al. 2005]

To get a description of the flow in the test elements, colour was added to the concrete. One third of the elements were cast with grey concrete, then red colour was added to the next third, while black colour was used in the last part.

The wall element (4 x 2.5 x 0.15m) was made with fibres only, and was filled with the three coloured mixes from one end of the formwork. Plexiglass formwork made it possible to observe the flow. The main tendency was that the concrete moved towards the bottom of the wall where it was poured in and pushed the older concrete up towards the opposite side of the formwork as illustrated in Figure 10.8.

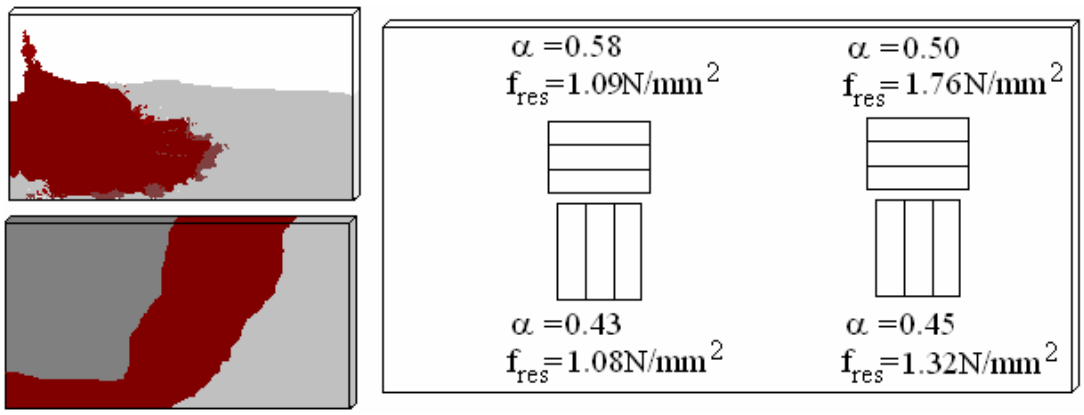

Figure 10.8: Left: Wall filled with the three coloured mixes. Right: The average residual strengths and the orientation factor for the 3x3 beams sawn horizontally and vertically.

Twelve small beams cut from the wall were tested in a deformation controlled rig to study the post-cracking behaviour, according to the test

method described in section 2.5.2 [Thorenfeldt et al. 2006]. The residual strength was determined as

$$f_{ftk,res} = 0{,}37\ f_{ftk,eq}$$

where $f_{ftk,eq}$ is the average characteristic equivalent bending strength recorded between 0.5 and 2.0mm deflection. The residual strength was in general somewhat lower for the beams closest to the casting point, although the scatter for the beam series was relatively large. No pronounced difference between the vertically and horizontally sawn beams was found from the measured load-deflection data.

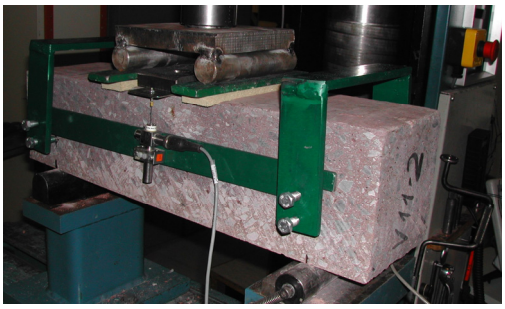

Figure 10.9: 4point bending of beams (150 x 150 x 600mm).

After testing, 90mm thick blocks were sawn from the beams near the failure zone, according to the Norwegian Design rule draft [Thorenfeldt et al. 2006]. The residual strength was then determined based on the fibre counting results:

$$f_{ftk,res} = \eta_0\, v_f\, \sigma_{fk,average}$$

The average stress is taken as 500MPa, and η_0 is determined from the fibre orientation factor as described in 2.6.3 while the fibre volume was determined as [Section 2.6.3]:

$$\nu = \left(N_1 + \frac{9}{16} N_2 + \frac{7}{16} N_3 \right) \frac{A_f}{A_c}$$

As opposed to the results of the 4 point bending tests, the orientation factors determined from fibre counting indicates that more fibres were orientated horizontally than vertically through the wall [Figure 10.8]. The results from the beam tests and the fibre counting were consequently not in agreement.

The observations done with the coloured mixes with respect to flow direction, as well as the scatter in the results of the beam tests show that the orientation of fibres through a wall is hard to predict with the applied casting method.

The slab element (2 x 3 x 0.2m) was cast from one side of the formwork [Figure 10.10]. Although some blocking did occur in front of the two transversal bars, beam tests and fibre counting indicated a relatively even fibre distribution [Figure 10.11]. The orientation of fibres was mainly horizontal.

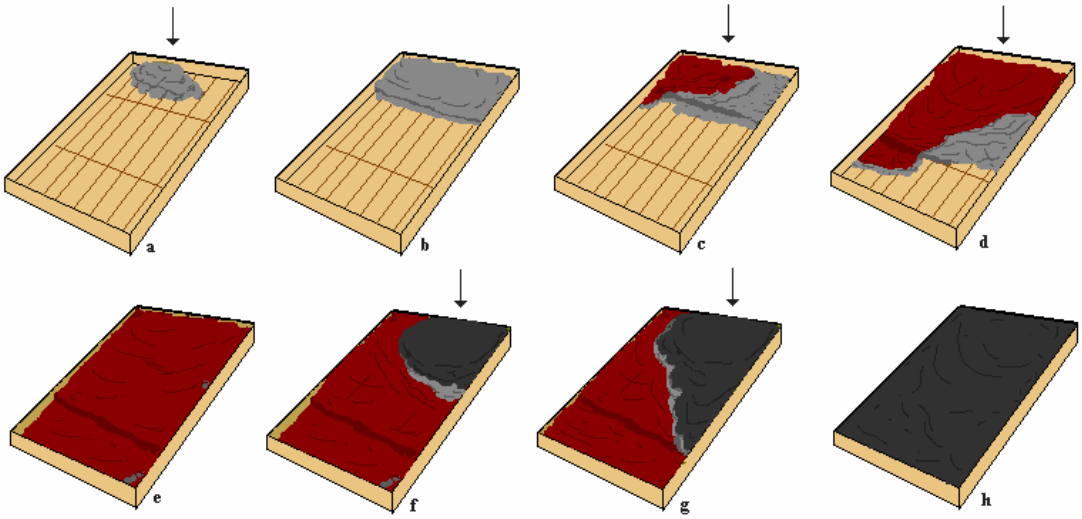

Figure 10.10: Casting of slab
a: The concrete was poured from one side of the formwork
b: First batch with grey concrete, the transversal reinforcement bar hinders the concrete flow
c-d: Second batch with red colour. The new concrete partly pushes the old concrete to the casting front and partly flows over it.
e: Before casting the last batch: the red concrete covers the whole surface.
f-g: Third batch with black colour. The first batch is again pushed forward to the casting front; eventually the black concrete starts to flow over the older concrete.
h: It is necessary to move the concrete scip along the formwork to fill it completely.

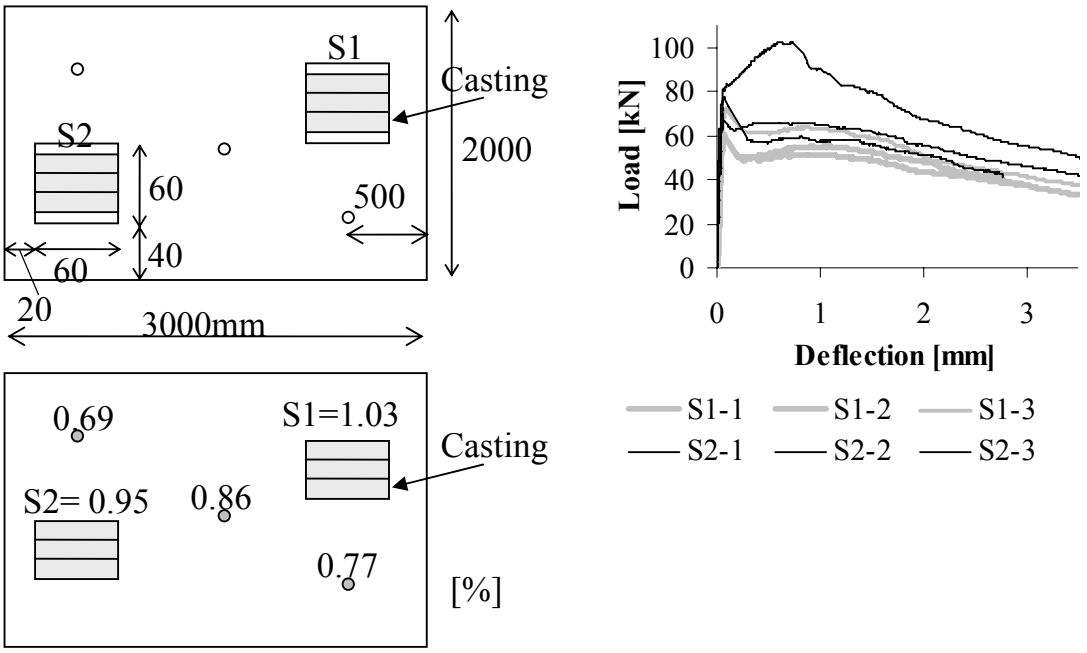

Figure 10.11: Left: 6 beams sawn from slab + 3 cylinders (d=100mm) for fibre counting. The fibre volumes estimated from fibre counting are indicated (average value of the three beams). Right: Load versus mid-deflection for the sawn beams from the slab.

There were no problems during the casting of the test plate with a slope of 22°. However, when the roof of the house was cast, blocking did occur. The reason for this was probably that the roof contained more transverse bars than the test element.

Figure 10.12 illustrates that the residual strengths determined from fibre counting on sawn blocks from the beams were higher than the residual strength from four point bending, in average 30 %. The main reason for this is most likely that several fibres at the sawn surface were without anchorage as discussed in 2.5.2. Moreover, the fibre contents were probably slightly higher in the sawn sections close to the cracks than in the actual failure zones. Further, it is possible that the assumed average stress after cracking of 500N/mm^2 is too high, although this value was suitable for other experiments with SCC described in chapter 5-10.

Since the thickness of the slabs was 200mm, the heights of the beams sawn from the slab were not within the specifications given in the Norwegian Design rule draft [Thorenfeldt 2006]. According to Bazant (1984), the span-to-beam height ratio l/h must be higher than 2.5 to prevent energy dissipation at the supports. With h=200, l/h=2.25, which is under the minimum requirement of 2.5. However, the energy dissipation at the supports will, if anything, overestimate the residual strength, and therefore the difference between the two methods can not be explained by the aberration from the prescribed dimensions. Besides, the differences between the residual strength determined from bending tests and fibre counting are approximately the same for the 150mm and the 200mm high beams, which implies that the energy dissipation at the supports can be neglected.

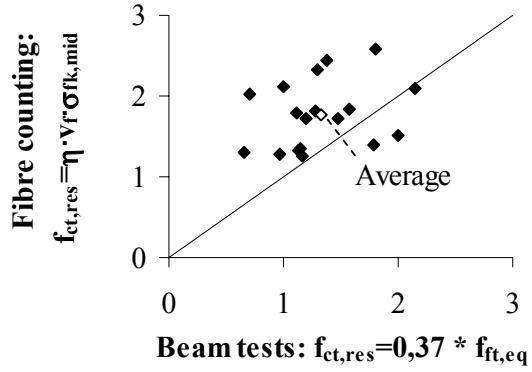

Figure 10.12: Residual strength from 4point bending test compared with residual strength from fibre counting for the 18 sawn out beams. The average value from the two methods is illustrated in the figure.

The residual strength from the beam tests were also determined according to Dramix Guidelines [Nemegeer 1997] as $f_{res}=f_{ct,eq150}$ described in section 3.2.2. The residual strengths according to the Norwegian Design rule draft [Thorenfeldt et al. 2006] were in average 19 % higher than the residual strengths determined from the Dramix Guideline. Hence, the deviation from the residual strength based on fibre counting was even larger with the latter method.

10.2.3 Full scale experiment – loading of slabs.

The concrete composition developed for the preliminary test elements was used in the full-scale experiments with FRC [Table 10.5], and a similar concrete without fibres was used in the reference slab. The fresh and hardened concrete properties for the FRC are shown in Table 10.6:

Density	Air	Temperature	Slump flow	Cube strength (28d)
2319 kg/m^3	6.0 %	25^{o}C	550 mm	45.91 N/mm^2

Table 10.6: Properties in fresh and hardened state.

Except from the slabs that were tested, the house was reinforced according to the minimum requirements of the Norwegian Design rules for plain concrete, NS3473. Hence, the distance and placing of the reinforcement bars was not adapted to the FRSCC. Even though there were no complications during casting of the preliminary elements, blocking occurred several times as the house was cast, primarily around windows and at the transversal reinforcement in the roof. Thus, the total consumption of time was higher than for the surrounding traditional reinforced houses in the SIBO village, but the final result was satisfactory.

Figure 10.13: a) Controlling the steel fibre content. b) The SFRC house.

A simple equipment was made for controlling the steel fibre content. The concrete was poured on a sieve and washed down an inclined plate with a fish-bone pattern. During this process the steel fibres were removed with a

magnet [Figure 10.13]. The amount of removed steel fibres was in good accordance with the prescribed dose.

Full-scale load experiments were performed on three slabs in the building:

I. Reference slab with ordinary reinforcement bars, ratio ρ=0.28 and dimensions 3.0 x 3.4 x 0.15m.
II. Steel fibres in combination with a minimum of reinforcement bars in the main span direction only. Dimensions 3.0 x 7 x 0.15m.
III. Fibres only (except from joint reinforcement bars between slab and basement wall [Figure 10.14]). Dimensions 3.0 x 3.4 x 0.15m.

The fibre volume and concrete was the same as for the preliminary test elements. A concentrated load was applied in the middle of the slabs, and the tests were ended when the slabs were in the ULS just before failure. An overview of the reinforcement in the slabs is given in Figure 10.14, and the test setup and measuring devices are illustrated in Figure 10.15.

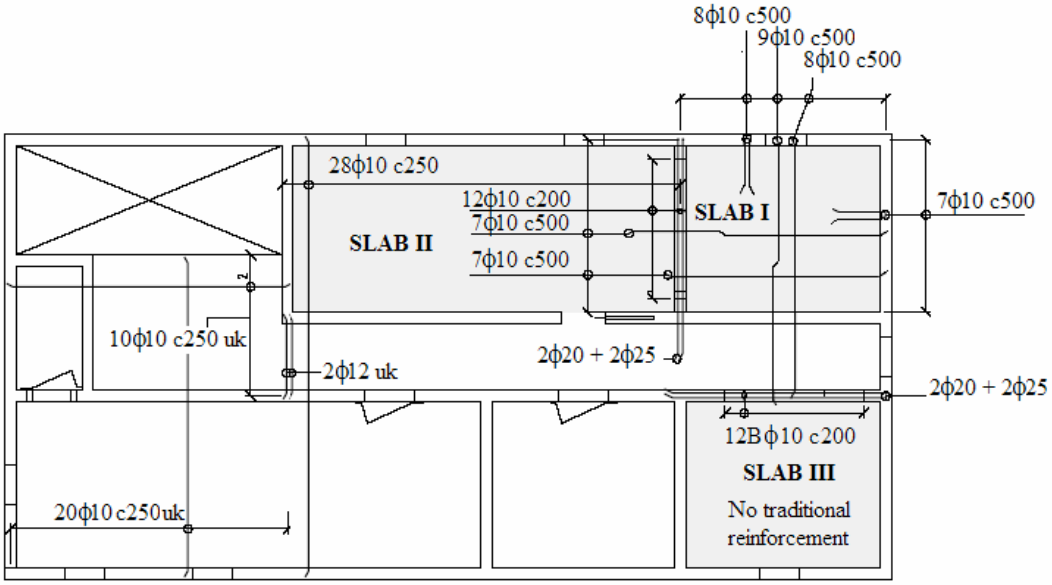

Figure 10.14: The three slabs tested on the ground floor.

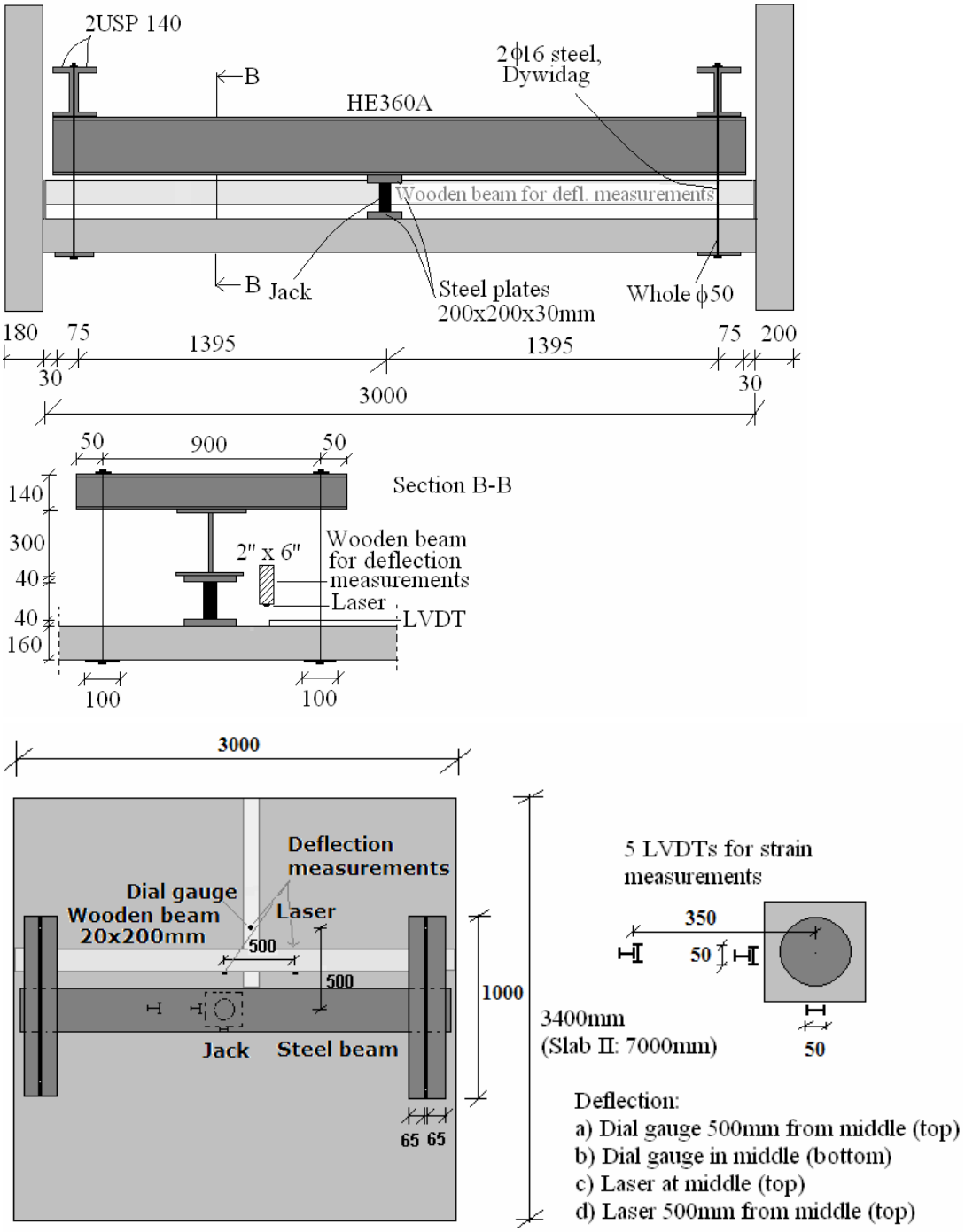

Figure 10.15: Equipment for loading and deformation measurement. The load was applied in the middle of the slab by a hydraulic jack held against a stiff steel-beam. The deflections were measured by dial gauges and lasers, while the compressive strains were measured by LVTDs on top of the slabs.

10.2.4 Finite element analysis

The three slabs were analysed in DIANA 9.1, using a smeared crack approach in a total strain rotating crack model. Due to symmetry, half of the slabs were modelled. Four-node quadrilateral isoparametric curved shell elements were used [Figure 10.10].

The material behaviour in tension and compression was modelled according to Figure 7.20-7.22, where the residual strength for FRC after cracking was taken as $f_{ftk,res} = \eta_0 \cdot v_f \cdot \sigma_{fk,mid} = 1/3 \cdot 0{,}8\% \cdot 500MPa = 1{,}3N/mm^2$. Since the crack distances in the slabs will increase with increasing distance from the load, the cracks had to be predefined in the analyses in order to have reasonable relations between crack widths and cracking strains [Figure 7.21]. A simplified crack pattern was therefore assumed as illustrated in Figure 10.16. To initiate cracks in the prescribed areas, the material strengths in tension and compression were increased by 10 % for all elements surrounding the assumed cracks. The crack distance was then taken as the diagonal length of the element. In the CDZ-model, the compression strength was presumed to be equal to the cylinder strength of the concrete, estimated from the cube strength [Figure 7.22].

The reinforcement was modelled according to von Mieses hardening criteria with yielding stress $500N/mm^2$, increasing linearly to a stress of $550N/mm^2$ at a plastic strain of 10‰.

The load was applied in deformation controlled steps in the middle of the slabs. It was assumed that the slabs had fixed boundaries due to the joint reinforcement with the basement walls. Analyses were also run with 50 % fixed boundaries (50 % restrained rotation). However, this had little effect on the capacities of the slabs. Hence, the results of these calculations are not presented here. The arc effect was included by restraining the slabs horizontally at the boundaries.

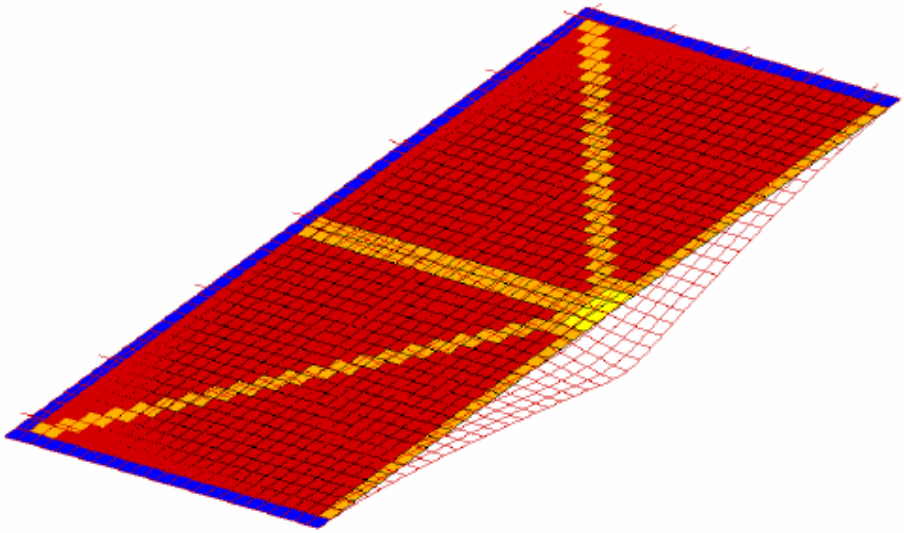

Figure 10.16: Slab III without bottom bars. Output from DIANA 9.1 illustrating the deflection of the slab and the pre-defined cracks which are given a lower strength than the surrounding elements. The elements along the boundaries are also modelled with lower tensile strength in accordance with observations done in the experiments. Half of the slab is modelled due to symmetry.

Figure 10.17: Left: Slab II after loading, seen from below. The cracks were marked by a tracer at each load step. Right: Crack below Slab III, illustrating fibre bridging. Small pieces of concrete were spalling off around the fibres near the surface.

10.2.5 Fibre counting on drilled out cores from the slabs

To check the orientation and distribution of fibres, two cylinders were drilled from each of the slabs with fibres, close to the middle. First, the fibres lying in the horizontal plane of the slab crossing the vertical cylinder surface were counted, and then the cylinders were sawn in three sections in order to count the vertically orientated fibres. The fibre volume was estimated as $v_f = (N_1 + 9/16 \cdot N_2 + 7/16 \cdot N_3) \cdot A_f/A_c$, where the number of fibres in the three directions $N_1 > N_2 > N_3$ as described in 2.6.3, leading to a fibre volume of 0.75 % and 0.82 % for Slab II and III, respectively, which is close to the added fibre content. For Slab II, the fibre counting indicated that 53 % of the fibres were located on the lower half, and that 78 % of the fibres in the lower half were horizontally orientated. In an ideal situation with isotropic orientated fibres, 66.7 % of the fibres will be orientated horizontally. Hence, the fibres had an orientation and distribution favourable with respect to the loading. For slab III, this effect was even more pronounced; 72 % of the fibres were concentrated in the lower half, and the share of horizontally orientated fibres in this part was 86 %.

10.2.6 Results

To assure that the tests did not induce any irreparable damage to the building, the experiments were terminated before the maximum loads were reached. The capacity of the slabs can therefore not be compared directly. Moreover, for the reference slab the test was interrupted at an earlier stage than for the two slabs with fibres. This was due to the loading; a 30 ton jack was used for the reference slab, while a 50 ton jack was applied on the two slabs with fibres.

The measured and calculated load-deflection relations are shown in Figure 10.18. As illustrated in Figure 10.15, the deflections were measured by two dial gauges and two lasers. For the reference slab, problems occurred for

two of the measuring devices; the dial gauge on top of the slab (“Dial gauge a”) and the laser near the middle (“Laser a”). These measurements are therefore disregarded. Since dial gauge b under the slabs was fastened in the middle, these measurements are expected to correspond best with the FEA. However, at large deformations, the cracks expanded rapidly under the slab and concrete spalling occurred. This is probably the reason why the deformations measured by dial gauge b gradually increases compared to the deformations measured on top of the slabs, as well as the FE results.

The results of the FE analyses are in relatively good agreement with the measurements until unloading. Still, the upward slope on the curves as the tests are interrupted indicates that the maximum load was not yet reached. On the other hand, the FRC slabs could probably not have been loaded much further, since the deformations after unloading were rather large. Nevertheless, the capacities of the two fibre reinforced slabs were underestimated by the analyses. This can be explained by the favourable orientation and distribution of fibres that were found from fibre counting on the cores drilled from the slabs. It is difficult to estimate whether the FEA underestimated the capacity of the reference slab, since the loading was interrupted at an earlier stage.

The responses from the FEA were slightly stiffer than the measurements, which probably is caused by deviation between the prescribed and real crack pattern.

Even though the slab without reinforcement bars was loaded further into the ULS than the reference slab, it was clear that a fibre volume of 0.8 % was sufficient to replace all traditional reinforcement. Moreover, the ductility was satisfactorily since the load was increasing for a long period after crack initiation at large deformations. In addition, observations during testing showed that a refined crack pattern occurred for all slabs.

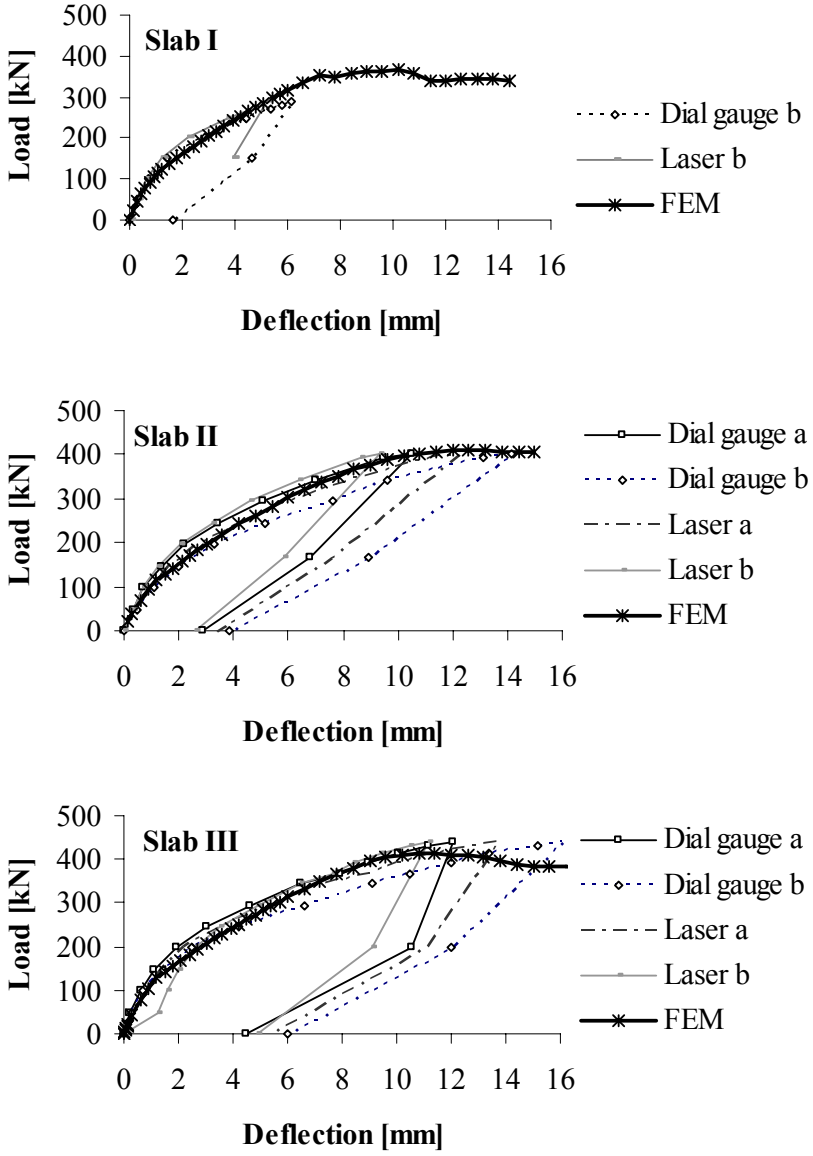

Figure 10.18: Results of FE analyses and measured load-deflection relation, where dial gauges and lasers are placed according to Figure 10.15.

10.2.7 Conclusions – house with FRSCC

The full-scale experiments gave useful information and experience both regarding the concrete composition and casting of FRSCC. A homogenous and robust FRSCC was achieved based on locally available sand and aggregate. Yet, when the concrete house was cast, blocking occurred in front of the transversal bars. This illustrates how important it is to adapt the placing of the reinforcement bars to the FRSCC, especially with respect to fibre length and fibre volume.

Due to large scatter in the results from the preliminary test elements, it is dubious whether fibre counting on small specimens taken from structural elements can be used to predict the post cracking strength through the structure. The deviation between 4point bending tests on beams sawn from the preliminary test elements and the estimations from a method based on fibre counting are considerable. Moreover, the 4point bending tests on sawn beams indicate that the casting method used for the wall was not propitious since the residual strength varied significantly through the wall. The scatter for the beams sawn from the slab was lower, implying that the casting method was more suitable for this type of structural element.

Even though some problems due to blocking was registered during the casting of the house, controls from the fresh concrete and drilled out cores after hardening indicated an even distribution of fibres through the slabs. Hence, the final result was satisfactory.

FEA corresponded relatively well with the measurements, although the ultimate load for the fibre reinforced slabs were somewhat underestimated by the analysis. This can be explained by a favourable distribution and orientation of the fibres. Further, the ductility of the FRC slabs was satisfactory. Most important, the full scale experiments proved that load carrying structures with relatively short spans can be reinforced with steel fibres only, without any traditional reinforcement.

10.3 Casting methods and fibre orientation - FRSCC walls cast with tube

10.3.1 Introduction

The fibre orientation in a structure is strongly dependent on the flow of the concrete and, thus, the casting procedure. It is beneficial to develop casting procedures that induces favourable fibre orientations with respect to the loads applied on the structural element. Especially in the prefabrication industry, necessary conditions for optimizing the casting procedure are present, since the production allows better routines with respect to casting methods.

The orientation of the fibres in SCC structures is primarily dependent on the flow direction of the concrete. However, the flow through a wall is complex, and there are several factors that have to be considered in order to simulate a form filling, for example the fresh concrete properties, the velocity of the pouring, geometry and friction of formwork as well as potential obstacles like cut outs and reinforcement bars. Moreover, the casting method has a major impact on the flow. On-site, walls are either cast with tubes or by concrete scip through funnels on top of the wall. If tubes are used, the form filling will be dependent on whether the tubes are submerged or not, and if the tube is held still at one point or moved along the wall. In precast wall elements, the concrete is often pumped from a bottom corner.

An extensive study on form filling of SCC was carried out by Thrane [2005]. In his experiments, the casting was done by pumping from the bottom corner of a wall at a filling rate of $10m^3/h$. By adding colour to the concrete, he studied the flow direction of the concrete and found the dead zones where blowholes occurred. Further, he simulated the flow based on a FEM formulation of the Navier-Stokes equations, and a Bingham model

was applied. The results corresponded well with the observed behaviour. Although it would be useful to perform a similar study on FRSCC to determine the relation between flow direction and fibre orientation more clearly, this is not included in this thesis.

The SCC walls presented in Chapter 5 and section 10.2.2 were cast from a concrete scip through a funnel on top of the wall. This casting procedure led to a main orientation of fibres that varied strongly in the different cut out sections of the walls. In the prefabricate industry, casting with tube is a more common and practical approach. Obviously, this approach induces a different fibre orientation through a wall than the orientation found for the walls cast with concrete scip.

A series of wall elements were cast at Contigas concrete plant in Moss, where the FRSCC concrete was pumped through a tube. The objectives were to:

- Test if it was possible to produce a stable SCC for pumping with sufficient fibre content by using the available aggregate at the plant.
- Control whether the fibres would cause blocking or not in the tube and in the pump while casting.
- Investigate the orientation and distribution of fibres through the walls.

10.3.2 Concrete and casting

Four fibre reinforced SCC walls of dimension 5 x 2.5 x 0.2m were cast:

- Wall 1: Dramix 65/40 galvanized steel fibres. During casting the tube was moved back and forward along the formwork [Figure 10.19].
- Wall 2: As Wall 1, but the tube was held still at one end of the formwork.
- Wall 3: Dramix 65/60 galvanized steel fibres, tube at one end.
- Wall 4: Synmix synthetic fibres (length 55mm and diameter 0.80mm), the tube was held at one end of the formwork.

All concrete had a fibre content of 0.6 %. The concrete composition and hardened concrete properties are given in Table 10.7 and Table 10.8.

	Dramix [kg/m^3]	Synmix [kg/m^3]
Cement	295	295
SH- Slite	159	159
Silica	22,7	22,7
Sand 0-8	972	972
Aggregate 8-14	698	698
Admixture SP-N	9.3	8.5
Air entrancement; Mapeair 1:9	0.7	0.7
Fibres	50	7

Table 10.7: Concrete mix [kg/m^3]. Identical mixes for the two steel fibres, Dramix 65/40 and Dramix 65/60.

	Dramix 65/40	Dramix 65/60	Synmix 55
$f_{c,7days}$	70.8	64.3	67.8
$f_{c,28days}$	89.4	87.3	85.6

Table 10.8: Cube strenght [N/mm^2]

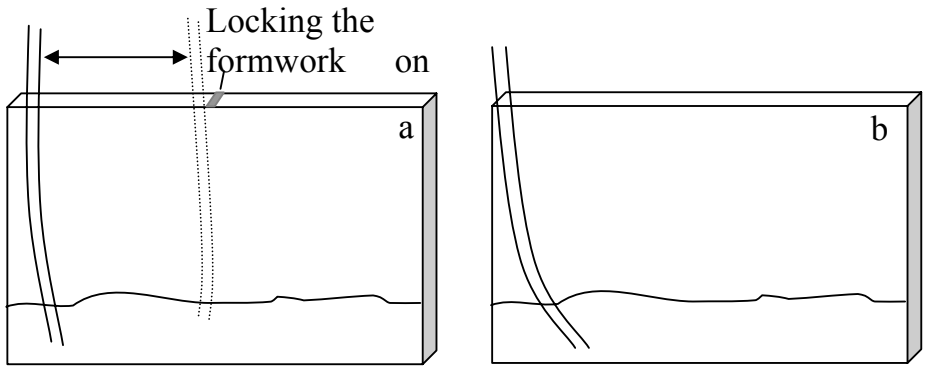

Figure 10.19: a) Casting Wall1. The tube was moved back and forward during casting as indicated. b) Casting Wall 2, 3 and 4 with the tube standing still in one end of the formwork.

It is most practical to cast the walls from one point, either through a rigidly mounted footing on the outside the wall near the bottom or manually through a tube submerged in the concrete. Yet, it may be favourable for the distribution and orientation of fibres if the tube is moved back and forwards along the formwork during casting. Hence, Wall 1 was cast to investigate if any beneficial effects were achieved by the moving the tube, while Wall 2, 3 and 4 were cast from one end of the formwork. Due to the lock on top of the formwork, and since the tube was held manually, it was not possible to move the tube along the whole length of the formwork as intended for Wall 1. Instead, the tube was moved back and forward over the length indicated in Figure 10.19.

The risk of separation increases when SCC is pumped through a tube. With fibres, it can be challenging to make the concrete robust enough, especially in this case, where the grading curve of the locally available aggregate was not optimal. Several test mixes were therefore carried out to achieve satisfactory fresh concrete properties. Yet, tendencies of pasta segregation were observed for Wall 4.

Figure 10.20: Left: The fibre concrete was poured in a pump. Right: Wall4 with synthetic fibres from the opposite side of the casting point. The picture shows that tendencies of pasta separation occurred.

10.3.3 Beam tests

In total 30 beams of dimension 200x200x800mm were sawn from the walls: 6, 6, 9 and 9 from Wall 1, Wall 2, Wall 3 and Wall 4, respectively, as illustrated in Figure 10.21. The main purpose of the beam tests was to estimate the orientation and distribution of fibres through the wall, and compare the casting method used for Wall 1 and Wall 2.

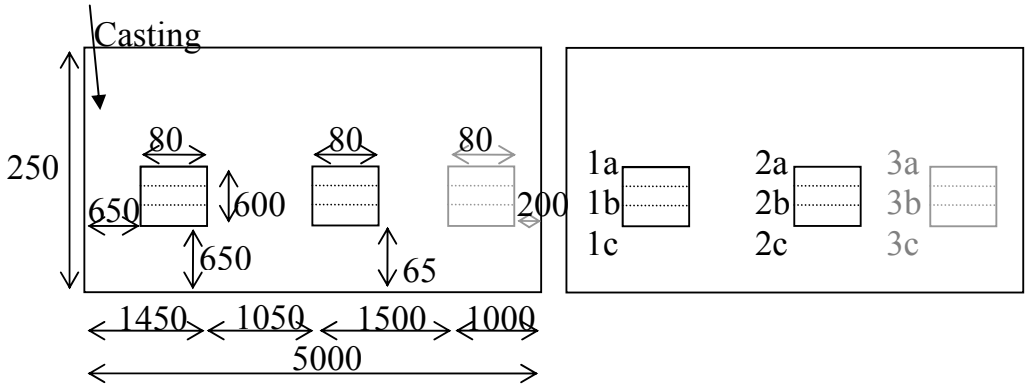

Figure 10.21: Dimensions and numbering of beams sawn from walls. Beam 3a-c were sawn from Wall 3 and Wall 4 only.

Figure 10.22: Beam 2a from Wall 3

The tests were performed according to the Norwegian design rule draft for FRC [Thorenfeldt et al. 2006]. However, since the thickness of the walls was 200mm, the beam dimensions were increased to 200x200x800 mm, and the test setup was upgraded correspondingly. The load was applied deformation controlled at a speed of 1mm/min, and the tests were ended at

a deflection of 8mm. The residual strength was taken as 0.37 times the average equivalent bending strength recorded between 0.5 and 2.5mm deflection.

10.3.4 Results

The measured load deflection relations for the 30 beam are shown in Figure 10.23. The figure also indicates the average residual strengths for the three beams (a,b,c) sawn from each section. The average residual strength decreased with the flow distance in all four walls. Moreover, the residual strength for Wall 1, where the tube was moved, was higher than for Wall 2 where the tube was held at one end of the formwork

The load at cracking was around 80kN for the beams, and for five of the beams with Dramix 65/40 fibres the load increased further after cracking. The average residual strength for all beams from the three walls with steel fibres were f_{res}=1.33N/mm^2, which is above the theoretical orientation factor for isotropic orientated fibres according to the Norwegian design rule draft; $f_{res} = \eta \cdot v_f \cdot \sigma_{average} = 1/3 \cdot 0.006 \cdot 500$ N/mm^2 = 1.00 N/mm^2. This indicates that the fibre orientation in average was favourable.

Five of the nine beams with synthetic fibres went to brittle failure. The results of these tests are not included in Figure 10.23 since no residual post cracking strength was registered. Neither was any fibres observed crossing the crack. The reason for this can either be that there was very few fibres orientated horizontally in this area, that fibre rupture occurred due to a high adhesion with the concrete, or it may be a combination of few fibres and high adhesion. For the three beams closest to the casting point, the average residual strength was $f_{res,P1}$=0.48 N/mm^2. The experiments described in chapter 7 indicates that the average post cracking strength of SCC with Synmix synthetic fibres is around 200MPa, which leads to a theoretical residual strength of $f_{res} = 1/3 \cdot 0.6 \cdot 200$ = 0.4 N/mm^2. This is not far from the residual strength estimated for the three beams closest to the casting point.

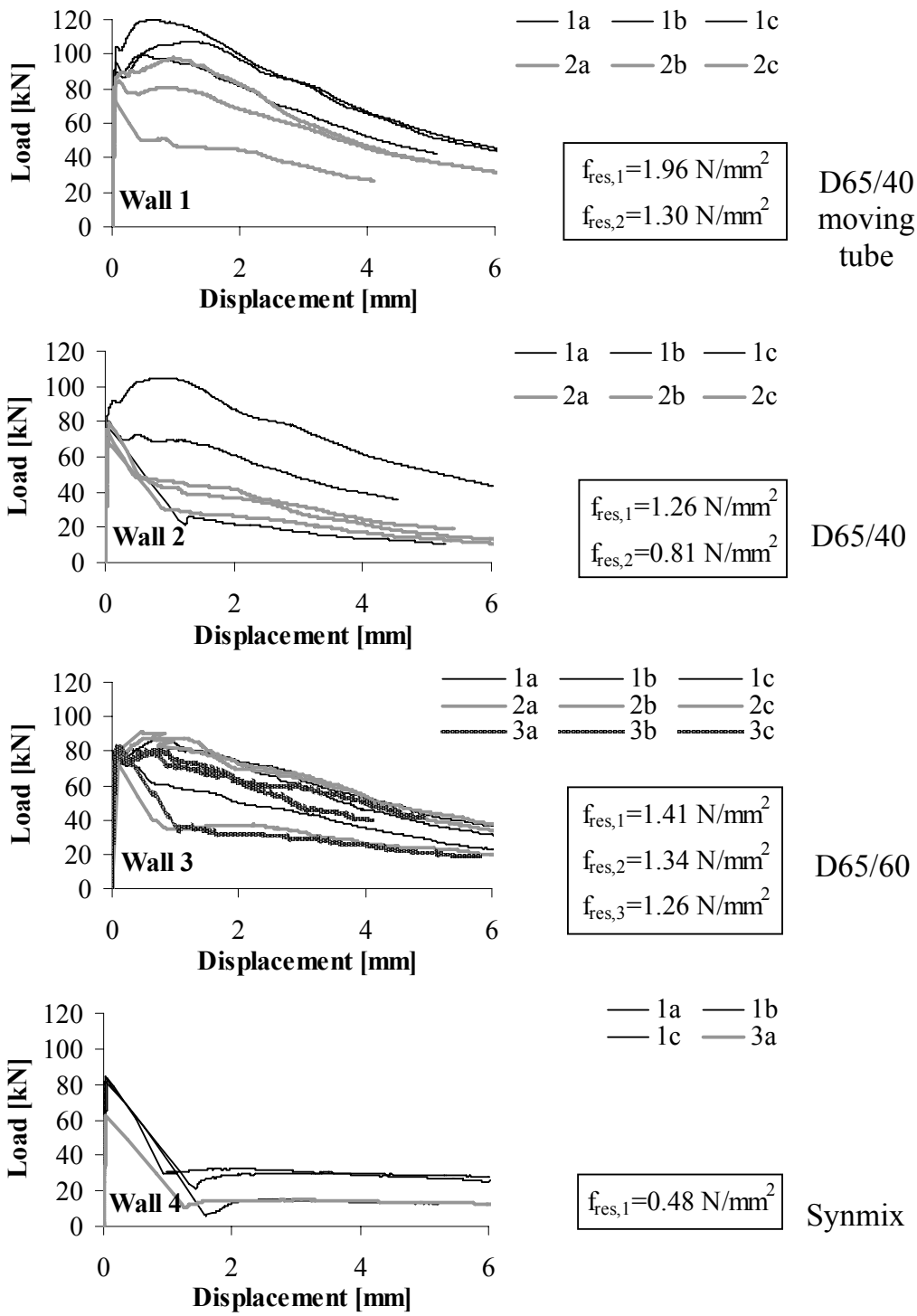

Figure 10.23: Load-deflection curves for the sawn out beams from the walls. The average residual strength for the three beams (a, b and c) taken from each of the sawn out elements are indicated

To estimate the fibre content in the beam, blocks were sawn 90mm from the failure zone, and fibres were counted on three planes perpendicular to each other. The fibre volume was than taken as:

$$\nu_f = \left(N_1 + \frac{9}{16} N_2 + \frac{7}{16} N_3 \right) \frac{A_f}{A_c}$$

where the number of fibres in the three directions $N_1 > N_2 > N_3$ as described in section 2.6.3. The fibre orientation was considered by the factors α and η, determined according to the Norwegian design rule draft [Thorenfeldt et al. 2006] as described in section 2.6.3.

Bjelkeserie	Fiber-type	v_f [%]	α [-]	η [-]	$f_{res,counting} = \eta_0 \, v_f \, \sigma_{fk,mid}$ [N/mm^2]	$f_{res,test} = 0{,}37 \, f_{ftk,eq}$ [N/mm^2]	Deviation [%]
Wall 1– 1c	Steel	0.86	0.63	0.51	2.19	1.90	15
Wall 1– 2b	Dramix	0.72	0.59	0.45	1.61	1.39	16
Wall 2– 1b	65/40	0.75	0.66	0.54	2.04	1.25	63
Wall 2– 2a		0.69	0.43	0.29	0.99	0.70	41
Wall 3– 1c	Steel	0.76	0.68	0.57	2.15	1.47	68
Wall 3– 2a	Dramix	0.77	0.61	0.48	1.83	1.58	16
Wall 3– 3b	60/60	0.63	0.65	0.53	1.68	1.39	21
Wall 4– 1b	Syntetic	0.63	0.68	0.57	0.73	0.54	35
Wall 4– 2b	Synmix	0.66	0.31	0.21	0.27	-	
Wall 4– 3a		0.50	0.22	0.15	0.15	-	

Table 10.9: Results of fibre counting on blocks from one beam (a, b or c) from each element (the beam a/b/c with residual strength closest to the average value for the three beams was chosen). Here v_f=fibre volume, α=orientation factor, η is a function of the orientation factor, $f_{res,counting}$ and $f_{res,test}$ are the residual strengths determined from fibre counting and beams tests. The last column shows the deviation between the two methods.

Table 10.9 shows that the residual strength determined from fibre counting on sawn blocks from the beams is higher than the residual strength from four point bending for all beams. This is similar to the results in 10.2.2, and

is most likely primarily caused by cut-off fibres on both sides of the beams, resulting in several fibres without anchorage. Further, the orientation factor can be higher in the sawn block than in the actual failure zone of the beam.

The fibre counting indicates that the decrease in residual strength with increasing flow distance is caused by a combination of decreasing fibre volume and an unfavourable fibre orientation, since fewer fibres are orientated in the longitudinal direction of the wall with increasing flow distance.

For Wall 4 with synthetic fibres, the fibre counting indicated that few fibres were orientated in the longitudinal direction of the wall for element 2 and 3. The fibres were mainly orientated vertically, which was not propitious for the beam tests. This explains the brittle failure that occurred for five of the beams. As mentioned, the concrete used in Wall 4 was on the verge of separation, and tendencies of separation were observed during casting. It is likely that this caused an uneven fibre distribution, since synthetic fibres due to the low density will flow to the surface whenever pasta separation occurs. Hence, it is difficult to separate the effect of flow direction and the influence of the apparent pasta separation on the distribution and orientation of fibres. Therefore, the results of the beam tests from Wall 4 cannot be placed emphasis on.

10.3.5 Conclusions – wall elements

With the available aggregate, it was difficult to achieve a stable SCC with a fibre content high enough to replace the traditional reinforcement bars required in the walls according to the Norwegian design rules NS3473. Since the concrete was pumped through a long tube, and had to flow further for 10 meters, it was essential to obtain a robust concrete with high flowability. Even though the concrete was stable before casting, the fibre counting showed that the fibre volume decreased slightly with increasing flow distance, which indicated that tendencies of separation did occur.

The flow of the concrete cast with tube appeared to be more uniform than the flow of the walls cast with scip described in 9.2.2. Fibre counting showed that the fibres mainly were orientated in the longitudinal direction of the wall, consequently parallel to the apparent direction of the concrete flow. This corresponds to the results described in 7.2.3 and 9.2.6. As the flow distance increased, the share of uni-directed steel fibres in the longitudinal direction of the walls decreased, which probably is connected to the deceleration of the flow. Moreover, the fibre orientation appeared to be more constant through the wall where the tube was moved back and forward during casting. However, more extensive studies on form filling have to be carried out to establish the connection between flow direction/velocity and fibre orientation.

For the wall with synthetic fibres, the main orientation of fibres was vertical, except for the three beams sawn near the casting point. This may indicate that synthetic fibres tend to orientate perpendicular to the flow. However, since the concrete showed tendencies of separation, no categorical conclusions regarding flow direction and orientation of synthetic fibres can be made based on these experiments. Moreover, for the SCC slabs with synthetic fibres described in chapter 7, the synthetic fibres were mainly orientated parallel to the flow. Yet, it is not unlikely that the orientation of synthetic fibres through a structure is considerably different from steel fibres due to the large difference in density.

10.4 Conclusions

The field tests emphasize the challenges that occur when experiments are performed outside the controlled conditions in the lab. The available aggregate is often not optimal, and adaptations regarding mix design and casting procedures have to be done. Yet, if the contractor is aware of the factors that influences the distribution and orientation of fibres through the structure, the production can be adapted accordingly. In spite of challenges, the results obtained through the full scale tests described in this chapter were satisfactory, although further improvements are necessary before the use of FRC is profitable for these types of applications. The potential of fibre reinforcement can only be utilized when the advantages and limitations are taken into account.

11 Conclusions

11.1 Summary and conclusions

This thesis provides further information on the use of fibre reinforcement in load carrying concrete structures. An extensive experimental study was carried out, investigating the effect of various parameters, both in the fresh and in the hardened state. The results of the study are used to evaluate existing design theories, and the measurements are compared with finite element analyses. Through the work, it has been focused on fibre reinforcement in practical applications. As a consequence, a large share of the experiments is carried out using casting procedures and aggregates available on site, but also by choosing testing methods which are not too time and cost consuming.

Interfacial bond properties

The interfacial bond properties of SFRC have been studied by single-fibre pull-out tests considering three parameters: concrete strength, fibre type and embedment length. The pull-out response of synthetic fibres was essentially different from the response of hooked-end steel fibres. Due to the relatively low E-modulus the synthetic fibres reached the maximum load at considerably larger deformations than the steel fibres, and the post-peak response decreased and increased in waves as a result of the embossed surface. For the steel fibres, on the other hand, the maximum force stayed approximately constant for a while, and then diminished gradually. The end-hook contributed to around 90% of the pull-out resistance of the steel fibres. Further, the pull-out load increased clearly with increasing concrete strength, and the increase was most distinguished in the steel fibre pull-out tests.

Structural elements of VCC and SCC – fibre orientation

Through the study it has been found that both the fibre-matrix bond and the orientation of fibres through a structure are dependent on whether vibrator compacted concrete (VCC) or self compacting concrete (SCC) is used. With SCC, the orientation of fibres is governed by the flow of the concrete which again depends on the casting method. Four point bending tests on small beams sawn from structural elements indicated an even distribution of fibres through a SCC slab and a horizontal main orientation. The results of the sawn beam from a SCC wall, on the other hand, showed an uneven fibre orientation. This underlines the dependence of the flow, which with the current casting method lead to a complex and non-uniform flow through the wall, while it was more constant for the slab. The scatter in post-cracking strengths for the cut out beams from a VCC wall was somewhat lower than with SCC, whereas the opposite was the case for a VCC slab where a weakness zone occurred with very few fibres orientated in the longitudinal direction of the beams. Hence, it is not recommendable to use immersion vibrator for fibre reinforced concrete. The VCC and SCC used in the test series had similar compression strengths. Yet, the difference in post-cracking strengths was considerable. The main reason is probably a more refined pore structure in the SCC due to higher silica content and higher matrix volume, which improves the fibre-matrix bond. To get a better picture of the post-cracking response of FRC the beams were analysed in a FEM program where the cracks were modelled by interface elements. The results showed that a multi linear stress – crack width ratio where the stress after cracking was taken as a constant value until 2mm and then linearly decrease to zero at a crack width of 10mm lead to a good correspondence with the measured load- deflection ratios.

Beams designed for moment and shear failure

Two series of beams designed for moment and shear failure, one with SFRSCC and one with SFRVCC also demonstrated the influence of concrete

type and casting procedure. The effect of steel fibres in the beams designed for moment failure was more than twice as high for the beams with SCC compared to the VCC, which can be explained by a combination of a favourable fibre orientation and a better fibre-matrix bond in the SCC. The residual strengths in the beams designed for moment failure were estimated by inverse analyses based on a multi-layer model, and for the VCC beams the estimated residual strengths corresponded well with the values determined from available guidelines based on isotropic orientated fibres. The shear capacity was similar for the VCC and SCC beams, and the results were in agreement with the design loads calculated from different guidelines. All beams were analysed in an FEM program with a smeared crack approach based on the observed average crack distance and a multi linear relation in tension and in compression, and the stress – crack width relation described above was used to develop a stress – strain relation in tension. The overall agreement was good. This indicates that the applied material model was adequate to describe the material behaviour.

Synthetic fibres

The post-cracking stress of synthetic fibre reinforced concrete has been compared with steel fibre reinforced concrete in a series of beams sawn from wall and slab elements. It was found that synthetic fibres are able to transfer relatively large stresses over the cracks. For the fibre types applied in the study the volume of synthetic fibres had to be doubled to achieve similar stresses as with steel fibre reinforced concrete. However, the maximum pull-out stress for the synthetic fibre reinforced concrete was achieved at higher crack widths, as demonstrated in the single fibre pull-out tests. Hence, synthetic fibres can only be utilized when relatively high crack widths are accepted.

Size effect

Size effect of fibre reinforced concrete was investigated in a series of beams with three different cross-section heights, of which three were reinforced with 1 % fibres, three with 0.3 % fibres and three with 1 % fibres combined with conventional reinforcement bars. It was found that the bending strength decreased with increasing cross-section height similarly to plain concrete. Moreover, for the beams with 1 % fibres the maximum load and ductility decreased relatively to the load at cracking with increasing cross-section height. Generally, the finite element analyses were in agreement with the measurements. Yet, for the beams with fibres in addition to reinforcement bars the analysis underestimated the capacity of the largest beams slightly while capacity for the largest beam was overestimated. This implies that the size effect probably is not fully described by the FEM.

Structural elements - fibres combined with conventional reinforcement

To control the fibres ability to redistribute large stresses a series of simply supported slabs were loaded with a concentrated load in the middle while the reinforcement bars were placed furthest out on the sides. The results were promising and indicated that maximum distance between reinforcement bars in accordance with common design rules can be increased when combined with fibres. Further, fibre counting on drilled out cylinders showed that the steel fibres tended to orientated parallel to the flow while the opposite was the case for the synthetic fibres. FEA was in relatively good agreement with the measurements for the slabs with steel fibre reinforced concrete, but the analyses did not reflect the results of the slabs with synthetic fibres, partly because anchorage/shear failure occurred.

Fibres as shear reinforcement in precast elements

Hollow core elements are normally produced without shear reinforcement, even though they often are subjected to large shear and torsion forces. It was therefore attempted to use steel fibres as shear reinforcement in a series of

simply supported hollow core elements. With the available aggregates and production technique it turned out to be difficult to achieve a sufficient compaction of concrete around the prestressed steel wires. As a consequence, the increase in maximum load due to fibres was ignorable because pull-out failure occurred before the shear capacity was reached. Hence, the only advantage achieved was increased ductility. Yet, if it is possible to achieve a better compaction of the concrete through improvements in mix design and casting procedure, steel fibres may be applied as shear reinforcement also in hollow core elements.

Full-scale load tests on slabs

Full scale load tests performed on three slabs in a house made of fibre reinforced concrete indicated that fibres can replace all conventional reinforcement in load carrying slabs with relatively short spans. One reference slab was made with conventional reinforcement and one was made with fibres only, both with a length-to-width ratio of 1.1. The third slab had a length-to-with ratio of 2.3 and was reinforced with a combination of fibres and conventional reinforcement. Even though the three slabs were loaded to different stages in the ULS, the load-displacement ratios implied that the capacities were similar. Moreover, the FEA were in good agreement with the measurements.

FRSCC cast with tube versus concrete scip

A series of wall elements with SCC were cast with tube to investigate if it was possible to achieve a more constant fibre orientation in the wall than in the previous SCC walls cast with concrete scip through a funnel. The results showed that the fibre volume decreased somewhat with the flow, which indicated that the SCC was on the verge of separation. Moreover, a more favourable orientation and distribution was achieved for the wall where the tube was moved back and forward along the formwork during casting. Yet, the fibre orientation in all walls cast with tube was more even than in the walls

cast with concrete scip through a funnel. Hence, it is favourable to cast walls with tube as opposed to concrete scip, although extra work might be required in the mix design phase to achieve a fibre reinforced concrete which is stable enough for pumping, especially when the locally available aggregates are not optimal as in this case.

11.2 Final conclusions and future perspectives

Most of the test series were evaluated through calculations and FEA and compared with available design rules. Generally the agreement was good, both with discrete and smeared crack approach. This shows that FEA is an appropriate tool to determine the contribution of fibres to the load bearing capacity. Moreover, the results of the test series implied that the theoretical framework that exists today describes the behaviour of fibre reinforced structures relatively well, and that the design rules which are developed is satisfactory. Even though there are still room for further improvements regarding design rules, the main challenge ahead is related documentation and execution. The main objective is to develop and describe material qualities and casting methods which ensures an even and predictable distribution and orientation through the structures.

12 References

Al-Ta'an, A.A.; Al-Feel, J.R. (1990): *Evaluation of Shear Strength of Fibre-Reinforced Concrete Beams*. Cement & Concrete Composites 12 pp 87-94.

Ashour, S.A., Ghazi, S. H., Wafa, F.F. (1992): *Shear Behaviour of High-Strength Fiber Reininforced Concrete Beams*. ACI Structural Journal, March-April 1992.

Balaguru and Shah (1992): *Fiber-reinforced cement composites*, R. R. Donnelley & Sons Company 1992, ISBN 0-07-056400-0.

Barrigan B. E. (2002): *Failure and toughness of steel fiber reinforced concrete under tension and shear*. Univesitat Politecnica De Catalunya, Doctoral Thesis, Barcelona 2002.

Bazant, Z. P. (1984): *Size effect in blunt fracture: concrete, rock, metal*. Journal of Engineering Mechanics, ASCE, 110(4), pp 518-535.

Bazant, Z. P. (1986): *Mechanics of distributed cracking*. Appl. Mech. Rev., Vol. 39, pp 675-705.

Bazant, Z. P. (1994): *Fracture Size Effect: Review of Evidence for concrete structures.* J. Structural Engineering, Volume 120, Issue 8, pp. 2377-2398.

Bonzel J., Schmidt M. (1986): *Distribution and orientation of steel fibres in concrete and their influence on the characteristics of steel fibre concrete*. Developments in fibre reinforced cement and concrete, Rilem symposium 1986.

British Standard institution, BS EN 14889-1, *Fibres for concrete, Part 1. Steel fibres – Definition,* London, 2006.

Borst, R. de (1999). *Computational methods in non-linear solid mechanics. Part 2: Physical non-linearity*. Report nr. 25-2-91-2-06, TU-Delft.

Broo, H. (2005): *Shear and torsion interaction in prestressed hollow core slabs. Department,* Thesis for the degree of licentiate of engineering, Department of civil and environmental engineering, Chalmers University of technology, Sweden.

Carlswärd, J. (2006): *Shrinkage cracking of steel fibre reinforced self compacting concrete overlays: test methods and theoretical modeling*. Doctoral thesis, Luleå university of technology; Sweden.

Casanova P., Rossi, P. (1997): *Analysis and design of steel fiber reinforced concrete beams, ACI Structural*, J. 94 (5) 595-602.

CEB-FIP 1991. *CEB-FIP Model Code 1990*. Comité Euro- International du Béton.

Chan, Y.W.; Li, V.C (1997): *Effects of Transition Zone Densification On Fiber/Cement Paste Bond Strength Improvement*. Elsevier Science Ltd, New York.

Choi K.-K., Taha, M. M. R., Park, H.-G. and Maji, A. K. (2007): *Punching shear strength of interior concrete slab-column connections reinforced with steel fibers*. Cement and Concrete Composites, Volume 29, Issue 5, May 2007, pp 409-420.

Clarke, J. L, Vollum, R. L., Swannell, N. et al. (2007). *Technical Report No. 63. Guidance for the Design of Steel-Fibre-Reinforced Concrete*. Report of a Concrete Society Working Group. UK.

Clarke, J. L, Peaston, C., Swannell, N. et al. (2007). *Technical Report No. 65. Guidance for the use of Macro-synthetic-fibre-reinforced Concrete*. Report of a Concrete Society Working Group. UK.

Contiga (2007): Picture from web site: www.contiga.no

Cunha, V.M.C.F; Joaquim A.O; Sena-Cruz.(2007): Pullout behaviour of hooked-end steel fibres in self-compacting concrete. Report, Azurem, Portugal.

Dahlblom O., Ottosen N. S. (1990): *Smeared crack analysis using generalized fictitious crack model*. Journal of Engineering Mechanics, Vol. 116, No. 1, pp 55-76.

De Borst, R. (1999): *Computational methods in non-linear solid mechanics. Part 2: Physical non-linearity*. Report nr. 25-2-91-2-06, TU-Delft.

De Witte, F. C., Wijtze, P. K. (2002): *DIANA – Finite Element Analysis User's Manual Release 8.1*. TNO Building and Construction Research, The Netherlands. First edition, September 2002.

Destrée, X. (2004): *Structural application of steel fibre as only reinforcing in free supspended elevated slabs: conditions – design – examples*, 6th RILEM Symposium, Arena, Italy, RILEM Publications.

Dupont, D. (2003): *Modelling and experimental validation of the constitutive law (σ–ε) and cracking behaviour of steel fibre reinforced concrete.* PhD thesis, Leuven.

Dupont, D.; Vandewalle, L. (2003): *Calculation of crack widths with the σ–ε method*, Test and DesignMethods for Steel Fibre Reinforced Concrete – Background and Experiences, Proceeding of RILEM TC 162-TDF Workshop, RILEM publication pp 119-144.

Dupont, D.; Vandewalle, L. (2005): *Distribution of steel fibres in rectangular sections*. Cement and Concrete Composites, Volume 27 Issue 3.

Døssland, Å L (2002): *Konstruksjonar av stålfiberarmert sjølvkomprimerande betong*. (In Norwegian) Master thesis, The Norwegian University of Science and Technology (NTNU).

EN 14488-3 (2006): *Testing of sprayed concrete – Part 3: Flexural strengths (first peak, ultimate and residual) of fibre reinforced beam specimens*. European Committee for Standardization, Brussels 27 February 2006.

EN 14488-5 (2006): *Testing of sprayed concrete – Part 5: Determination of energy absorption capacity of fibre reinforced slap specimens*. European Committee for Standardization, Brussels 27 February 2006.

Engström, B. (2006): *Restraint cracking of reinforced concrete structures*, Chalmers University of Technology.

Erdem, E. (2003): *The Flexural behaviour of SFRC beams and slabs: Bending with the σ–ε–method*. Proceedings RILEM TC 162-TDF Workshop: Test and Design Methods for Steel Fibre Reinforced Concrete – Background and Experiences.

Espion, B., Devillers J. J. and Halleux, P. (1993): *De l'utilisation de fibres métalliques comme armature complémentarie de pouters en béton armé soumises à flexion*. Materials and Structures, 1993, 26, pp 479-485 (In French).

Fjerdingstad, O. (2005): *Syntetisk fiberarmering I betongkonstruksjoner: Anvendelsesområder og virkemåte etter oppressing*. (In Norwegian). Master thesis, The Norwegian University of Science and Technology (NTNU).

Gao, Y. C. (1987): *Debonding along the interface of composites*. Mechanics research communications Vol. 14(2), pp.67-72.

Gjestemoen, A. (2005): *Syntetisk fiberarmering I selvkomprimerende betong. Utførelse og bøyeprøving av veggelementer*. (in Norwegian). Master thesis. The Norwegian University of Science and Technology (NTNU).

Groth P. (2000a): *Fibre reinforced concrete – Fracture mechanics methods applied on self-compaction concrete and energetically modified binders*. PhD Thesis, Luleå University of Technology.

Groth, P. (2000b): *Steel Fibre Reinforced SCC, Final report of task 6, Brite Euram project (BE 96-3801*. Doc. No. RT6-v1.doc.

Grimheden, David (2003a): *Orientering hos stålfibrer i betong*. Master thesis KTH, Stockholm (in Swedish).

Grimheden, David (2003b): *Results from tests on small beams sawn from walls and slabs of realistic dimensions produced by ordinary or self-compacting concrete*. In T.Kanstad (ed), Design Rules for Steel Fibre Reinforced Concrete Structures: Proc Nordic miniseminar:, Oslo, 6. October 2003, The Norwegian Concrete Association, Oslo.

Grünewald, S., Walraven, J.C., Obladen, B., Zegwaard, J.W. Langbroek, M. Nemegeer, D. (2003): *Tunnel segments on self-compacting steel fibre reinforced concrete*. 3rd international symposium on SCC, Reykjavik.

Grünewald, S., Walraven, J.C. (2003): *Maximum content of steel fibres in self-compacting concrete*. 3rd international symposium on SCC, Reykjavik.

Grünewald, S. (2004): Performance-based design of self-compacting fibre reinforced concrete. PhD-thesis, Delft University of Technology.

Grunewald, S, Walraven, J.C (2005): *Optimisation of the mixture composition of self-compacting fibre reinforced concrete*. In SP Shah (Ed.), Proceedings 2nd North American conference on the design and use of self-consolidating concrete/4th international RILEM symposium on self-compacting concrete (pp. 393-399). Addison, IL, USA: Hanley Wood. (TUD).

Guerrero P.; Naaman A.E. (2000): Effect of Mortar Fineness and Adhesive Agents on Pullout Response of steel Fibers. ACI Materials Journal, Vol 97, pp 12-20.

Gysel, A. van (2000): *Studie van het uttrekgedrag van staalvezels ingebed in een cementgebonden matrix met toepassing op staalvezelbeton onderworpen aan buiging.*, PhD Thesis, University of Gent (in Dutch).

Hammer, T. A., Johansen, K. (2005). *On the influence of entrained air on theology of paste and mortar*. Proceedings, Nordic concrete research meeting, Sandefjord, Norway.

Hauge, B.B (2003): *Stålfiberarmerte betongkonstruksjoner: Evaluering av dimensjoneringsmetoder ved hjelp av forsøksresultater og ikke-lineære beregninger med elementmetoden*. (In Norwegian) Master thesis, The Norwegian University of Science and Technology (NTNU).

Harajli, M., Hamad, B., Karam, K. (2002): *Bond-slip response of fibre reinforcing bars embedded in plain and fiber concrete*. Journal of materials in civil engineering November/December 2002, pp. 503-511.

Harajli, M. H.; Soudki, K. A.; Kudsi, T (2006): *Strengthening of Interior Slab–Column Connections Using a Combination of FRP Sheets and Steel Bolts.* J. Compos. for Constr., Volume 10, Issue 5, pp. 399-409.

Hillerborg, A. (1980): *Analysis of fracture by means of the fictitious crack model, particularly for fibre reinforced concrete*. The Int. J. Cem. Comp., 2, 177-184.

Hjorth, L. (1982): *Microsilica og betong*. Lecture notes course TKT4215 The Norwegian University of Science and Technology (NTNU) 2003, Published by Aalborg Portland (in Danish).

Johansen, K. (2006): *(personal correspondence).* SINTEF Building and Infrastructure, Trondheim.

Kennedy, G., Goodchild, C.H. (2004): *Practical Yield Line Design*, The Concrete Centre, September 2004, ISBN 1-904818-08-0.

Kanstad, T.; Døssland, Å.L. (2004): *Testing and Modelling of Steel Fibre Reinforced Concrete Beams Designed for Moment Failure*. Proceedings FraMCos-5 - Fracture Mechanics of Concrete Structures; Vail Colorado.

Khuntia, M., Stojadinovic, B., Goel, S. (1999): *Shear Strength of Normal and High-Strength Fiber Reinforced Beams without Stirrups*. ACI Structural Journal, March-April 1999, pp. 282-289.

Kooiman, A.G (2000*): Modelling Steel Fibre Reinforced Concrete for Structural Design*. PhD thesis, TU Delft.

Kwak, Y.K; Eberhard, M.O.; Kim, W.S.; Kim, J. (2002): *Shear Strength of Steel Fiber-Reinforced Concrete Beams without Stirrups.* ACI Structural Journal, Volume 99, No. 4, pp. 530-538.

Lappa, E.S. (2007): *High Strength Fibre Reinforced Concrete. Static and Fatigue Behaviour in Bending*, PhD thesis, Delft University of Technology.

Li, V.C., Wang, Y., Backer, S. (1990) *Effect of inclining angle, bundling and surface treatment on synthetic fibre pull-out from a cement matrix*. Composites, volume 21 no.2, pp. 132-140.

Li., V.C., Ward, R., Hamza, A.M. (1992): *Steel and Synthetic Fibers as Shear Reinforcement*, ACI Material Journal, V. 89, No. 5, pp. 499-508.

Li, V.C, Stang, H. And Krenchel, H. (1993) *Micro mechanics of crack bridging in fibre reinforced concrete*, Materials and Structures, Vol. 26, pp. 486-494.

Lin, Y. (1996): *Tragverhalten von Stahlfaserbeton.* Schriftenreihe des Institutes für Massivbau und Baustofftechnologie Universität Karlsruhe, Heft 28 (in German).

Lin, Z., Kanda, T. and Li, V. (1999): *On interface property characterization and performance of fiber reinforced cementitious composites*. Journal of Concrete Science and Engineering, RILEM 1, pp 173-184.

Löfgren, I. (2005): *Fibre reinforced concrete for Industrial Construction – a fracture mechanics approach to material testing and structural analysis*. PhD, Chalmers University of Technology, Göteborg.

Löfgren, I. (2007): *Calculation of crack width and crack spacing for members with combined reinforcement*, presentation, Nordic miniseminar for fibre reinforced concrete, November 2007.

Markeset, G. (1993): *Failure Of Concrete Under Compressive Strain Gradients*, PhD thesis, NTH, Trondheim.

Markovic, I. (2006): *High-performance Hybrid-Fibre Concrete, Development and Utilisation*. DUP Science, PhD-thesis, TU Delft.

Marti, P., Pfyl, T., Sigrist, V., Ulaga, T. (1999): *Harmonized Test Procedures for Steel Fiber-Reinforced Concrete*, ACI Materials Journal, Vol. 96, No. 6, November-December 1999.

Morrison, J.K.; Shah, S.P; Jenq, Y.S (1988): *Analysis of Fiber Debonding and Pullout in Composites*. Journal of Engineering Mechanics, Vol. 114, No. 2, February 1988, pp. 277-294.

Naaman A.E. (2003): *Engineered Steel Fibers with Optimal Properties for Reinforcement of Cement Composites*, Journal of Advanced Concrete Technology, Vol. 1, No. 3, 2003, pp 241-252.

Nemegeer D. (1997): *Dramix: Design guidelines for Dramix steel wire fibre reinforced concrete*, N.V. Bekaert S.A., Harelbeke, Belgium.

Narayanan, R..; Darwish, I.Y.S (1987): *Use of Steel Fibers as Shear Reinforcement*. ACI Structural Journal, May-June 1987, pp. 216-227.

Nammur, G. and Naaman, A. (1989): *Bond Stress Model for Fiber Reinforced Concrete Based on Bond Stress-Slip Relationship,* ACI Material Journal Vol. 86, pp 45-57.

Noghabai, K. (2000): *Beams of fibrous concrete in shear and bending: Experiments and model.* Journal of structural engineering, Volume 126, Issue 2, pp 243-251.

NS3473 Norges Standardiseringsråd (2003): Prosjektering av betongkonstruksjoner. Beregning og konstruksjonsregler. (In Norwegian). Norwegian Standard Instutution.

Okamura, H., Ouchi, M. (1999): "*Self-compacting concrete. Development, present use and future*", Self-Compacting Concrete, RILEM Symposium Stockholm, RILEM publications, Cachan (France), pp.3-14.

Olesen, J. F. (2001): *Fictitious crack propagation in fiber-reinforced concrete beams*, Journal of Engineering Mechanics, Vol. 127, pp 272-280.

Pedersen, C. (1996): *New production processes, materials and calculation techniques for fiber reinforced concrete pipes*, PhD thesis, Department of Structural Engineering and Materials, Technical University of Denmark, Series R, no. 14.

Petersson, Ö.(1998): *Preliminary Mix Design – Final Report of Tast 1*, Brite Euram project (BE 96-3801) – Rational production and improvemed working environment through using SCC, Document RT1-v2.doc.

RILEM TC 162-TDF (2001): *Test and design methods for steel fibre reinforced concrete. Recommendations for uni-axial tension test.* Materials and Structures 34, Jan-Feb 2001, pp.3-6.

RILEM TC 162-TDF (2002): *Test and design methods for steel fibre reinforced concrete. Design of steel fibre reinforced concrete using the s-w method: principles and applications.* . (Chairlady L. Vanderwalle) Materials and Structures, Vol 35, pp. 262-278.

RILEM TC 162-TDF (2003): *Test and design methods for steel fibre reinforced concrete: s-e- Design Method Final Recommendation.* (Chairlady L. Vanderwalle). Materials and Structures 36, pp.560-567.

Robins P., Austin S., Jones P (2002): *Pull out behaviour of hooked steel fibres.* Materials and Structures Vol. 35, pp. 434-442.

Rosenbusch, J. (2003): "*Zur Querkrafttragfähigkeit von Balken aus Stahlfaserverstärktem Stahlbeton.* PhD thesis. TU Braunschweig (in German).

Rots, J. G. (2002): *Comparative study of crack models*. Invited paper, Proceedings of the third DIANA World Conference, Tokyo, Japan ISBN 90-5809-530-4.

Schnütgen, B.; Vandewalle, L. (2003): *Test and Design methods for Steel fibre reinforced concrete – Background and Experiences*. Preface. Rilem Proceedings PRO 31, RILEM TC 162-TDF Workshop.

Schumacher, P. (2006): *Rotation Capacity of Self-Compactong Steel Fiber Reinforced Concrete. PhD thesis*, TU Delft, Netherlands.

Sener, S.; Begimgil, M.; Belgin, C. (2002): *Size Effect on Failure of Concrete Beams With and Without Steel Fibers*. Journal of Materials in Civil Engineering.

Silfwerbrand, J. et al (1998): *Stålfiberbetong – rekommentdationer för konstruktion, utförande och provning. Betongrapport nr.4*. (In Swedish) 2. edition, Swedish Concrete Association.

Stang, H., Li, V. C. (2001): *Micro: Interfaces and Pull-out*, Proceedings of the summer course "Mechanics of Fiber Reinforced Cementbased Composits DTU, Lyngby August 2001.

Stang, H., Li, V. C. (2005): *Meso: Interfaces and Pull-out*. Study material for DTU-RILEM Doctoral Course "Mechanics of fiber reinforced concrete", Lyngby June 2005 (draft text).

Stang, H., Li, Z., Shah, S. P. (1990): *Pullout Problem: Stress Versus Fracture Mechanical Approach.*, Journal of Engineering Mechanics, ASCE, Vol. 116, no 10, pp. 2136-2150.

Stang, H., Shah P. (1986): *Failure of fibre-reinforced composites by pull-out fracture*. Journal of Materials Science, Vol. 21, 1986 pp. 953-957.

Shaaban, A.M, Gesund, H. (1994): *Punching Shear Strength of Steel Fiber Reinrorced Concrete Flat Plates*, ACI Structural Journal, V.91, No. 3, July-August 1994.

Shah, S. P.; Skarendahl, Å. (1985): *Steel fiber concrete*. Preface. US-Sweden Joint seminar (NSF-STU, Stockholm Sweeden.

Swarmy, R. N., Ali, S. A. R. (1982): *Punching Shear Behavior of Reinforced Slab-Column Connections with Steel Fiber Concrete*. ACI Journal, Proceedings V. 79, No. 5, Sept.-Oct. 1982, pp. 425-432.

Sukontasukkul, P., Mindess, S., Banthia, N. and Mikami, T. (2001): *Impact resistance of laterally confined fibre reinforced concrete plates*. Materials and Structures, Vol. 34, December 2001, pp 612-618.

Takás, P.F, Høiseth, K.V, Sørensen, S.I, Kanstad, T. (2002): *Non-linear analysis of prestressed concrete beams with a total strain based model: FEM model and full-scale testing*, Proceedings of the third DIANA World Conference, Tokyo, Japan ISBN 90-5809-530-4.

Thorenfeldt E., Fjeld, S., et al (2006): *Stålfiberarmering i betong. Veiledning for prosjektering, utførelse og kontroll*. (in Norwegian) Draft.

Thorenfeldt, E. (2002a): *Hulldekkeelementer med øket bæreevne. Analyse av prøver med forankringsbrudd og kommentarer til prøvingsopplegg*. (in Norwegian), Sintef Bygg og miljø, Trondheim, February 2002.

Thorenfeldt, E. (2002b): *Fiberarmerte konstruksjonsløsninger. Effekt av stålfiber*. In Norwegian. Note, SINTEF 2002.

Thorenfeldt E. (2003): *Theoretical tensile strength after cracking, fibre orientation and average stress in fibres*. Proceedings Workshop "Design Rules for Steel Fibre Reinforced Concrete Structures", The Nordic Concrete Federation, Oslo 6 October 2003.

Thrane L N, (2005): *Simulation and Verification of Form Filling with Self-Compaction Concrete*." Proceedings Nordic concrete research meeting Sandefjord, Norway, ISBN 82-91341-91-5.

Ulfkjær, J.P., Krenk, S. and Brincker, T. (1995): *Analytical model for fictitious crack propagation in concrete beams*, ASCE, J. Eng. Mech. 121 pp 7-15.

Uomoto, T., Weeraratne, R.K., Furukoshi, H., Fujino, H. (1986): *Shear strength of reinforced concrete beams with fibre reinforcement*, Proceedings: Developments in fibre reinforced cement and concrete, Rilem symposium, Volume 2, RILEM Technical Committee 49-TFR.

Vandewalle, L. (2003): *Design with s-e method*. Proceedings RILEM TC 162-TDF Workshop: Test and Design Methods for Steel Fibre Reinforced Concrete – Background and Experiences.

Vabo, T. (2001): *Stålfiberarmerte betongkonstruksjoner: Gjennomføring av bjelkeforsøk og litteraturstudium*. Master thesis. The Norwegian University of Science and Technology (NTNU), Norway.

Van Mier, J.G.M (1997): *Fracture processes of concrete Assessment of Material Parameters for Fracture Models*, CRC Press, Boca Raton, Florida, ISBN 0 8493 9123.

Voo, J.Y.L, Foster, S.J (2006): *Shear strength of steel fibre reinforced concrete beams without stirrups – A review*. Draft. The University of New South Wales.

Publication list

Døssland, Å.L (2007): *Nye erfaringer med fiberarmerte konstruksjoner*. (In Norwegian) Norsk Betongdag, Trondheim Norway.

Døssland, Å.L. (2005) *Stålfiberarmering i betong. Fullskalaforsøk elementfabrikk*. (In Norwegian). The Norwegian University of Science and Technology (NTNU). ISBN 82-7482-071-1.

Busterud, L.; Johansen, K.; Døssland, Å. L. (2005). *Production of Fibre Reinforced SCC*. The Second North American Conference on the Design and Use of Self-Consolidating Concrete and the Fourth International RILEM Symposium on Self-Compacting Concrete.

Døssland, Å.L; Kanstad, T. (2005): *Full scale experiments with steel fibre reinforced self compacting concrete*. Proceedings, Nordic Concrete Research Meeting, Sandefjord, Norway.

Fjeld, S.; Kanstad, T.; Døssland, Å.L. (2005*): Laboratory and field tests for verification of Norwegian guidelines for structural design of steel fibre reinforced concrete.* Proceedings Nordic Concrete Research Meeting, Sandefjord, Norway.

Kanstad, T.; Døssland, Å.L. (2004): *Testing and Modelling of Steel Fibre Reinforced Concrete Beams Designed for Moment Failure*. Proceedings FraMCos-5 - Fracture Mechanics of Concrete Structures; Vail Colorado.

Kanstad, Terje; Døssland, Å.L. (2003) *Stålfiberarmerte betongkonstruksjoner: Bjelkeforsøk gjennomført ved NTNU 2001-2002. Resultater og evaluering.* (In Norwegian) Trondheim: The Norwegian University of Science and Technology (NTNU). ISBN 82-7482-065-7. 65 s.

Døssland, Å.L (2003): *Beams of ordinary and self compacting concrete reinforced with steel fibres and ordinary reinforcement tested in moment and shear.* Proceedings Workshop "Design Rules for Steel Fibre Reinforced Concrete Structures", The Nordic Concrete Federation, Oslo 6 October 2003.

Døssland, Å.L. (2003): *Results from tests on small beams (b/h = 150/150) sawn from walls and slabs of ordinary or self-compacting concrete. Part 2*. Design Rules for Steel Fibre Reinforced Concrete Structures", The Nordic Concrete Federation, Oslo 6 October 2003.

Kanstad, T.; Døssland, Å.L (2003): *Moment capacity of beams with different cross section height and steel fibre content: results from tests, simplified calculations and FE-analysis*. Design Rules for Steel Fibre Reinforced Concrete Structures", The Nordic Concrete Federation, Oslo 6 October 2003.

APPENDIX A

Overview: fibre counting on 36 specimen - Chapter 5.

					Fibre counting		Experimental data	
	v_f [-]	ρ [-]	α [-]	η [-]	f_{res}* [N/mm^2]	f_{res}** [N/mm^2]	$f_{ft.eq}$ [N/mm^2]	$f_{ft.eq.res}$ [N/mm^2]
P11-1	0.0062	0.0056	0.897	0.862	2.14	1.60	3.42	1.27
P11-2	**0.0070**	0.0052	0.740	0.653	1.83	1.37	3.91	1.45
P11-3	**0.0070**	0.0039	0.556	0.408	1.14	0.86	3.08	1.14
P12-1	0.0070	0.0025	0.362	0.241	0.68	0.51	1.09	0.40
P12-2	0.0070	0.0027	0.382	0.255	0.72	0.54	1.25	0.46
P12-3	0.0063	0.0023	0.363	0.242	0.61	0.46	1.38	0.51
P21-1	0.0072	0.0045	0.631	0.507	1.46	1.83	4.25	1.57
P21-2	**0.0070**	0.0037	0.521	0.362	1.01	1.27	6.81	2.52
P21-3	**0.0070**	0.0038	0.543	0.390	1.09	1.37	5.23	1.94
P22-1	0.0077	0.0061	0.801	0.735	2.25	2.82	6.59	2.44
P22-2	0.0069	0.0055	0.802	0.736	2.04	2.55	7.00	2.59
P22-3	0.0068	0.0051	0.747	0.663	1.82	2.27	7.12	2.63
W11-1	**0.0070**	0.0028	0.404	0.270	0.75	0.57	1.33	0.49
W11-2	**0.0070**	0.0049	0.694	0.592	1.66	1.24	2.95	1.09
W11-3	0.0081	0.0048	0.586	0.449	1.45	1.09	2.95	1.09
W11-1	**0.0070**	0.0030	0.426	0.284	0.79	0.60	2.12	0.78
W12-2	0.0085	0.0035	0.416	0.278	0.94	0.71	1.94	0.72
W12-3	**0.0070**	0.0040	0.573	0.430	1.21	0.90	1.54	0.57
W13-1	0.0081	0.0049	0.596	0.462	1.50	1.13	3.45	1.28
W13-2	0.0080	0.0054	0.683	0.578	1.84	1.38	3.75	1.39
W13-3	0.0071	0.0054	0.766	0.687	1.95	1.46	4.99	1.85
W14-1	0.0083	0.0030	0.359	0.239	0.79	0.59	3.54	1.31
W14-2	0.0077	0.0039	0.502	0.336	1.04	0.78	1.47	0.54
W14-3	0.0076	0.0045	0.594	0.458	1.40	1.05	1.49	0.55
W21-1	**0.0070**	0.0045	0.646	0.528	1.48	1.85	3.74	1.38
W21-2	0.0074	0.0043	0.586	0.449	1.33	1.66	3.22	1.19
W21-3	**0.0070**	0.0033	0.469	0.312	0.87	1.09	2.50	0.93
W22-1	0.0063	0.0020	0.314	0.210	0.53	0.66	2.29	0.85
W22-2	**0.0070**	0.0027	0.386	0.257	0.72	0.90	2.03	0.75
W22-3	**0.0070**	0.0028	0.397	0.265	0.74	0.93	2.03	0.75
W23-1	0.0072	0.0025	0.349	0.233	0.67	0.83	1.80	0.66
W23-2	0.0071	0.0022	0.310	0.206	0.58	0.73	1.72	0.64
W23-3	0.0068	0.0022	0.330	0.220	0.60	0.75	2.16	0.80
W24-1	0.0076	0.0048	0.639	0.518	1.57	1.96	5.64	2.09
W24-2	0.0072	0.0041	0.575	0.433	1.24	1.56	4.41	1.63
W24-3	0.0067	0.0043	0.646	0.528	1.42	1.78	3.86	1.43
				average:	1.22	1.21		1.21

** σ_{res}=400 N/mm^2 ** $\sigma_{res.VCC}$=300 and $\sigma_{res.SCC}$=500 N/mm^2. These stresses are determined by comparing the residual stress from experiments and fibre counting*

APPENDIX B

Shear capacity calculations – Chapter 6

A: $\tau_u=(0.167\alpha+0.25F_1)f_c^{0.5}$ [Khunta et al.1999]

B: $\tau_u=[0.12k(100\rho\cdot f_{ck})^{1/3}+0.15\sigma_{cp}] + k_f\cdot 0.54f_{ctk,ax}(R_t/1.5)$; [Nemegeer 1996]

C: $\tau_u=e(0.24f_{sp}+80\rho d/a)+0.41\tau\cdot F$; [Narayanan & Darwish 1987]

D: $\tau_u=\tau_{cd}+ 0.9\cdot 1/3 v_f\sigma_{average}$.

where τ_{cd} is calculated from the Norwegian standard code NS3473.

A: Khunta et al. 1999

$\tau_u=(0.167\alpha+0.25F_1)f_c^{0.5}$;

α=1 for a/d≥2.5; else α=2.5d/a≤3 for a/d<2.5

$F_1=\beta\cdot v_f\cdot(l_f/d_f)$

β=1.0

Here a/d= 3 hence α=1

l_f/d_f= 67 for Dramix 65/60

l_f/d_f= 65 for Dramix 65/35

	S0-A	S1-A	S2-A	S3-A	S4-A
F_1		0	0,335	0,67	0,65
V_{tot-A} [kN]		**39,9**	**58,4**	**81,9**	**75,3**

S1-B	S2-B	S3-B	S5-B
0	0,335	0,67	0,325
43,2	**65,1**	**85,7**	**65,2**

B: Nemegeer 1996 - Dramix design rules

$\tau_u=\tau_{cd}+\tau_{fd}+\tau_{wd}=[0.12k(100\rho\cdot f_{ck})^{1/3}+0.15\sigma_{cp}] + k_f\cdot 0.54f_{ctk,ax}(R_t/1.5)+\tau_{wd}$

where the concrete contribution and the contribution from stirrups are determined from Eurocode

	S0-A	S1-A	S2-A	S3-A	S4-A
f_{c28} [Mpa]	51,6	51,6	48,9	54,1	47,1
$f_{fctk,ax}$[N/mm^2]	2,91	2,91	2,81	3,00	2,74
V_{cd} [kN]	35,3	35,3	34,7	35,9	34,3
V_{fd} [kN]	0,0	0,0	23,1	34,9	31,5
V_{wd} [kN]	22,8	-	-	-	-
V_{tot-B} [kN]	**58,2**	**35,3**	**57,8**	**70,8**	**65,8**

S1-B	S2-B	S3-B	S5-B
60,3	60,7	59,2	62,295
3,23	3,24	3,19	3,30
37,2	37,3	37,0	37,6
0,0	26,7	37,1	26,7
-	-	-	-
37,2	**64,0**	**74,1**	**64,4**

where b_w= 150 mm

d= 222 mm

$\rho=A_s/b_wd$=0,018 ≤2 % $k=1+(200/d)^{0.5}$= 1,949 ≤2

$$V_f = \tau_f \cdot b \cdot d = 0.54 \cdot f_{fctk,ax} \cdot \frac{1{,}1 w_f \lambda_f}{3600 + w_f \lambda_f} \cdot b \cdot d$$

and $$f_{fctk,ax} = 0{,}7 f_{fctm,ax} = 0{,}7 \cdot 0{,}3 f_{fck}^{\frac{2}{3}}$$

w_f= 38,5 kg/m^3 for 0,5 % fibres and 77 kg/m^3 for 1 % fibres

λ_f= 60/0.9 Dramix 65/60, and λ_f= 35/0,54 for Dramix 65/35

Stirrups, beam S0-A: $V_{wd}=A_{sw}/s*0{,}9d*f_{ywd}$

where f_{yw}= 606,3 N/mm^2

A_{sv}= 28,27 mm^2

s= 150 mm

C) Narayanan & Darwish 1987

$$V_{tot} = V_c + V_f = \left[e\left(A' f_{sp,cyl} + B' \rho_s \frac{d}{a} \right) + 0{,}41 \tau_f F_f \right] bd$$

$$e = \begin{cases} 1{,}0 - if\_a/d > 2{,}8 \\ 2{,}8 - if\_a/d \le 2{,}8 \end{cases}$$

$F_f=(l_f/d_f)v_f\beta$ T_f= 4,15 N/mm^2

a/d= 2,97 e= 1

A'= 0,24 ρ_s= 0,016

B'= 80 Mpa β=1 for hooked-end fibres

$f_{sp}=f_{cu}/(20-F^{0.5})+0.7+F^{0.5}$

	S0-A	S1-A	S2-A	S3-A	S4-A
F_f=	0	0	0,335	0,670	0,650
f_{sp}=	3,28	3,28	3,797	4,339	3,96
V_{tot-C} [kN]	**0,0**	**40,6**	**63,7**	**87,1**	**82,9**

S1-B	S2-B	S3-B	S5-B
0	0,335	0,670	0,325
4,3	4,1	4,8	4,7
49,1	**65,8**	**90,5**	**70,0**

D) Proposed in this thesis: $\tau_u=\tau_{cd}+ 0.9\cdot 1/3 v_f \sigma_{average}$.

where τ_{cd} is calculated from the Norwegian standard code NS3473.

Concrete contribution [NS3473]:

$$V_{cd} = 0.3 \cdot \left(f_{td} + \frac{k_A \cdot A_s}{\gamma_c \cdot b_w \cdot d} \right) \cdot b_w \cdot d \cdot k_v \leq 0{,}6 f_{td} \cdot b_w \cdot d \cdot k_v \qquad \text{[NS3473 12.3.2.1]}$$

where:

k_A= 100 N/mm^2

A_s 603 mm^2

k_v= 1,28 for all beams without stirrups. k_v=1 for beam S0-A

γ_c= 1

$\sigma_{average}$ = 500 N/mm^2

	S0-A	S1-A	S2-A	S3-A	S4-A
f_{tn}=	2,17	2,17	2,1	2,33	2,05
V_{cd} [kN]	39,8	50,8	49,9	52,9	49,3
V_{fd} [kN]	0,0	0,0	25,0	50,0	50,0
V_{tot-D} [kN]	**62,6**	**50,8**	**74,9**	**102,8**	**99,2**

S1-B	S2-B	S3-B	S5-B
2,38	2,39	2,36	2,43
53,5	53,7	53,2	54,2
0,0	25,0	50,0	25,0
53,5	**78,6**	**103,1**	**79,2**

SUMMARY

	S0-A	S1-A	S2-A	S3-A	S4-A
P_U [kN]	69,65	53,96	79,46	110,9	103
P_U/V_A	0,00	1,35	1,36	1,35	1,37
P_U/V_B	1,20	1,53	1,37	1,56	1,57
P_U/V_C	0,00	1,33	1,25	1,27	1,24
P_U/V_D	1,11	1,06	1,06	1,08	1,04

S1-B	S2-B	S3-B	S5-B
59	81	103	83
1,36	1,25	1,20	1,28
1,58	1,27	1,39	1,30
1,20	1,24	1,14	1,19
1,10	1,04	1,00	1,05

APPENDIX C

Fibre counting on cylinders: Slabs with concentrated load - Chapter 9

	Whole cross-section				Lower half of cross-section					
	v_f	v_f	η_0	η_0	$v_{f,lower}$	$v_{f,lower}$	$\eta_{0,lower}$	$\eta_{0,lower}$	σ	f_{res}
S1A-1	0,79		0,27		0,76		0,26			
S1A-2	0,77	0,78	0,34	0,32	0,83	0,84	0,35	0,34	400	1,13
S1A-3	0,75		0,39		0,77		0,47			
S1A-4	0,79		0,29		0,98		0,27			
S2A-1	0,94		0,33		1,02		0,34			
S2A-2	0,63	0,71	0,43	0,37	0,78	0,84	0,42	0,38	500	1,58
S2A-3	0,52		0,45		0,57		0,50			
S2A-4	0,76		0,27		0,99		0,25			
S3A-1	0,57		0,29		0,57		0,25			
S3A-2	0,58	0,58	0,32	0,33	0,59	0,57	0,32	0,30	400	0,70
S3A-3	0,61		0,41		0,62		0,34			
S3A-4	0,56		0,30		0,53		0,31			
S4A-1	0,80		0,25		0,97		0,24			
S4A-2	0,68	0,65	0,34	0,31	0,80	0,73	0,37	0,31	500	1,13
S4A-3	0,61		0,32		0,71		0,25			
S4A-4	0,52		0,33		0,45		0,37			
S1B-1	0,96		0,43							
S1B-2	0,83	0,87	0,43	0,43	-	0,95	-	0,43	400	1,65
S1B-3	0,89		0,44							
S1B-4	0,81		0,43							
S2B-1	1,04		0,45							
S2B-2	0,90	0,93	0,45	0,44	-	0,93	-	0,44	250	1,03
S2B-3	0,90		0,41							
S2B-4	0,89		0,45							
S3B-1	0,79		0,46							
S3B-2	0,70	0,74	0,43	0,43	-	0,81	-	0,43	500	1,74
S3B-3	0,69		0,43							
S3B-4	0,79		0,41							
S4B-1	0,87		0,41							
S4B-2	0,76	0,80	0,43	0,44	-	0,87	-	0,44	500	1,92
S4B-3	0,86		0,45							
S4B-4	0,71		0,46							
S5B-1	1,39		0,45							
S5B-2	1,35	1,28	0,41	0,45	-	1,39	-	0,45	500	3,10
S5B-3	1,26		0,46							
S5B-4	1,10		0,46							
S6B-1	1,05		0,43							
S6B-2	0,82	0,99	0,42	0,45	-	1,08	-	0,45	500	2,40
S6B-3	1,10		0,43							
S6B-4	0,98		0,50							
S7B-1	0,99		0,54		1,00		0,55			
S7B-2	0,90	0,97	0,48	0,45	0,84	0,94	0,52	0,46	250	1,09
S7B-3	0,99		0,47		0,87		0,50			
S7B-4	0,98		0,30		1,04		0,28			
S8B-1	1,47		0,50		1,48		0,60			
S8B-2	1,07	1,17	0,49	0,49	0,98	1,18	0,60	0,55	250	1,61
S8B-3	1,08		0,46		1,20		0,55			
S8B-4	1,06		0,50		1,06		0,44			

DEPARTMENT OF STRUCTURAL ENGINEERING
NORWEGIAN UNIVERSITY OF SCIENCE AND TECHNOLOGY

N–7491 TRONDHEIM, NORWAY
Telephone: +47 73 59 47 00 Telefax: +47 73 59 47 01

"Reliability Analysis of Structural Systems using Nonlinear Finite Element Methods",
C. A. Holm, 1990:23, ISBN 82-7119-178-0.

"Uniform Stratified Flow Interaction with a Submerged Horizontal Cylinder",
Ø. Arntsen, 1990:32, ISBN 82-7119-188-8.

"Large Displacement Analysis of Flexible and Rigid Systems Considering Displacement-Dependent Loads and Nonlinear Constraints", K. M. Mathisen, 1990:33, ISBN 82-7119-189-6.

"Solid Mechanics and Material Models including Large Deformations",
E. Levold, 1990:56, ISBN 82-7119-214-0, ISSN 0802-3271.

"Inelastic Deformation Capacity of Flexurally-Loaded Aluminium Alloy Structures",
T. Welo, 1990:62, ISBN 82-7119-220-5, ISSN 0802-3271.

"Visualization of Results from Mechanical Engineering Analysis",
K. Aamnes, 1990:63, ISBN 82-7119-221-3, ISSN 0802-3271.

"Object-Oriented Product Modeling for Structural Design",
S. I. Dale, 1991:6, ISBN 82-7119-258-2, ISSN 0802-3271.

"Parallel Techniques for Solving Finite Element Problems on Transputer Networks",
T. H. Hansen, 1991:19, ISBN 82-7119-273-6, ISSN 0802-3271.

"Statistical Description and Estimation of Ocean Drift Ice Environments",
R. Korsnes, 1991:24, ISBN 82-7119-278-7, ISSN 0802-3271.

“Properties of concrete related to fatigue damage: with emphasis on high strength concrete”,
G. Petkovic, 1991:35, ISBN 82-7119-290-6, ISSN 0802-3271.

"Turbidity Current Modelling",
B. Brørs, 1991:38, ISBN 82-7119-293-0, ISSN 0802-3271.

"Zero-Slump Concrete: Rheology, Degree of Compaction and Strength. Effects of Fillers as Part Cement-Replacement",
C. Sørensen, 1992:8, ISBN 82-7119-357-0, ISSN 0802-3271.

"Nonlinear Analysis of Reinforced Concrete Structures Exposed to Transient Loading",
K. V. Høiseth, 1992:15, ISBN 82-7119-364-3, ISSN 0802-3271.

"Finite Element Formulations and Solution Algorithms for Buckling and Collapse Analysis of Thin Shells", R. O. Bjærum, 1992:30, ISBN 82-7119-380-5, ISSN 0802-3271.

"Response Statistics of Nonlinear Dynamic Systems",
J. M. Johnsen, 1992:42, ISBN 82-7119-393-7, ISSN 0802-3271.

"Digital Models in Engineering. A Study on why and how engineers build and operate digital models for decisison support", J. Høyte, 1992:75, ISBN 82-7119-429-1, ISSN 0802-3271.

"Sparse Solution of Finite Element Equations",
A. C. Damhaug, 1992:76, ISBN 82-7119-430-5, ISSN 0802-3271.

"Some Aspects of Floating Ice Related to Sea Surface Operations in the Barents Sea",
S. Løset, 1992:95, ISBN 82-7119-452-6, ISSN 0802-3271.

"Modelling of Cyclic Plasticity with Application to Steel and Aluminium Structures",
O. S. Hopperstad, 1993:7, ISBN 82-7119-461-5, ISSN 0802-3271.

"The Free Formulation: Linear Theory and Extensions with Applications to Tetrahedral Elements
with Rotational Freedoms", G. Skeie, 1993:17, ISBN 82-7119-472-0, ISSN 0802-3271.

"Høyfast betongs motstand mot piggdekkslitasje. Analyse av resultater fra prøving i Veisliter'n",
T. Tveter, 1993:62, ISBN 82-7119-522-0, ISSN 0802-3271.

"A Nonlinear Finite Element Based on Free Formulation Theory for Analysis of Sandwich Structures", O. Aamlid, 1993:72, ISBN 82-7119-534-4, ISSN 0802-3271.

"The Effect of Curing Temperature and Silica Fume on Chloride Migration and Pore Structure of High Strength Concrete", C. J. Hauck, 1993:90, ISBN 82-7119-553-0, ISSN 0802-3271.

"Failure of Concrete under Compressive Strain Gradients",
G. Markeset, 1993:110, ISBN 82-7119-575-1, ISSN 0802-3271.

"An experimental study of internal tidal amphidromes in Vestfjorden",
J. H. Nilsen, 1994:39, ISBN 82-7119-640-5, ISSN 0802-3271.

"Structural analysis of oil wells with emphasis on conductor design",
H. Larsen, 1994:46, ISBN 82-7119-648-0, ISSN 0802-3271.

"Adaptive methods for non-linear finite element analysis of shell structures",
K. M. Okstad, 1994:66, ISBN 82-7119-670-7, ISSN 0802-3271.

"On constitutive modelling in nonlinear analysis of concrete structures",
O. Fyrileiv, 1994:115, ISBN 82-7119-725-8, ISSN 0802-3271.

"Fluctuating wind load and response of a line-like engineering structure with emphasis on motion-induced wind forces",
J. Bogunovic Jakobsen, 1995:62, ISBN 82-7119-809-2, ISSN 0802-3271.

"An experimental study of beam-columns subjected to combined torsion, bending and axial actions", A. Aalberg, 1995:66, ISBN 82-7119-813-0, ISSN 0802-3271.

"Scaling and cracking in unsealed freeze/thaw testing of Portland cement and silica fume concretes", S. Jacobsen, 1995:101, ISBN 82-7119-851-3, ISSN 0802-3271.

"Damping of water waves by submerged vegetation. A case study of laminaria hyperborea", A. M. Dubi, 1995:108, ISBN 82-7119-859-9, ISSN 0802-3271.

"The dynamics of a slope current in the Barents Sea", Sheng Li, 1995:109, ISBN 82-7119-860-2, ISSN 0802-3271.

"Modellering av delmaterialenes betydning for betongens konsistens", Ernst Mørtsell, 1996:12, ISBN 82-7119-894-7, ISSN 0802-3271.

"Bending of thin-walled aluminium extrusions", Birgit Søvik Opheim, 1996:60, ISBN 82-7119-947-1, ISSN 0802-3271.

"Material modelling of aluminium for crashworthiness analysis", Torodd Berstad, 1996:89, ISBN 82-7119-980-3, ISSN 0802-3271.

"Estimation of structural parameters from response measurements on submerged floating tunnels", Rolf Magne Larssen, 1996:119, ISBN 82-471-0014-2, ISSN 0802-3271.

“Numerical modelling of plain and reinforced concrete by damage mechanics”, Mario A. Polanco-Loria, 1997:20, ISBN 82-471-0049-5, ISSN 0802-3271.

“Nonlinear random vibrations - numerical analysis by path integration methods”, Vibeke Moe, 1997:26, ISBN 82-471-0056-8, ISSN 0802-3271.

“Numerical prediction of vortex-induced vibration by the finite element method”, Joar Martin Dalheim, 1997:63, ISBN 82-471-0096-7, ISSN 0802-3271.

“Time domain calculations of buffeting response for wind sensitive structures”, Ketil Aas-Jakobsen, 1997:148, ISBN 82-471-0189-0, ISSN 0802-3271.

"A numerical study of flow about fixed and flexibly mounted circular cylinders", Trond Stokka Meling, 1998:48, ISBN 82-471-0244-7, ISSN 0802-3271.

“Estimation of chloride penetration into concrete bridges in coastal areas”, Per Egil Steen, 1998:89, ISBN 82-471-0290-0, ISSN 0802-3271.

“Stress-resultant material models for reinforced concrete plates and shells”, Jan Arve Øverli, 1998:95, ISBN 82-471-0297-8, ISSN 0802-3271.

“Chloride binding in concrete. Effect of surrounding environment and concrete composition”, Claus Kenneth Larsen, 1998:101, ISBN 82-471-0337-0, ISSN 0802-3271.

“Rotational capacity of aluminium alloy beams”, Lars A. Moen, 1999:1, ISBN 82-471-0365-6, ISSN 0802-3271.

“Stretch Bending of Aluminium Extrusions”, Arild H. Clausen, 1999:29, ISBN 82-471-0396-6, ISSN 0802-3271.

“Aluminium and Steel Beams under Concentrated Loading”,
Tore Tryland, 1999:30, ISBN 82-471-0397-4, ISSN 0802-3271.

"Engineering Models of Elastoplasticity and Fracture for Aluminium Alloys",
Odd-Geir Lademo, 1999:39, ISBN 82-471-0406-7, ISSN 0802-3271.

"Kapasitet og duktilitet av dybelforbindelser i trekonstruksjoner",
Jan Siem, 1999:46, ISBN 82-471-0414-8, ISSN 0802-3271.

“Etablering av distribuert ingeniørarbeid; Teknologiske og organisatoriske erfaringer fra en norsk ingeniørbedrift”, Lars Line, 1999:52, ISBN 82-471-0420-2, ISSN 0802-3271.

“Estimation of Earthquake-Induced Response”,
Símon Ólafsson, 1999:73, ISBN 82-471-0443-1, ISSN 0802-3271.

“Coastal Concrete Bridges: Moisture State, Chloride Permeability and Aging Effects”
Ragnhild Holen Relling, 1999:74, ISBN 82-471-0445-8, ISSN 0802-3271.

”Capacity Assessment of Titanium Pipes Subjected to Bending and External Pressure”,
Arve Bjørset, 1999:100, ISBN 82-471-0473-3, ISSN 0802-3271.

“Validation of Numerical Collapse Behaviour of Thin-Walled Corrugated Panels”,
Håvar Ilstad, 1999:101, ISBN 82-471-0474-1, ISSN 0802-3271.

“Strength and Ductility of Welded Structures in Aluminium Alloys”,
Miroslaw Matusiak, 1999:113, ISBN 82-471-0487-3, ISSN 0802-3271.

“Thermal Dilation and Autogenous Deformation as Driving Forces to Self-Induced Stresses in High Performance Concrete”,
Øyvind Bjøntegaard, 1999:121, ISBN 82-7984-002-8, ISSN 0802-3271.

“Some Aspects of Ski Base Sliding Friction and Ski Base Structure”,
Dag Anders Moldestad, 1999:137, ISBN 82-7984-019-2, ISSN 0802-3271.

"Electrode reactions and corrosion resistance for steel in mortar and concrete",
Roy Antonsen, 2000:10, ISBN 82-7984-030-3, ISSN 0802-3271.

"Hydro-Physical Conditions in Kelp Forests and the Effect on Wave Damping and Dune Erosion. A case study on Laminaria Hyperborea",
Stig Magnar Løvås, 2000:28, ISBN 82-7984-050-8, ISSN 0802-3271.

"Random Vibration and the Path Integral Method",
Christian Skaug, 2000:39, ISBN 82-7984-061-3, ISSN 0802-3271.

"Buckling and geometrical nonlinear beam-type analyses of timber structures",
Trond Even Eggen, 2000:56, ISBN 82-7984-081-8, ISSN 0802-3271.

”Structural Crashworthiness of Aluminium Foam-Based Components”,
Arve Grønsund Hanssen, 2000:76, ISBN 82-7984-102-4, ISSN 0809-103X.

“Measurements and simulations of the consolidation in first-year sea ice ridges, and some aspects of mechanical behaviour”, Knut V. Høyland, 2000:94, ISBN 82-7984-121-0, ISSN 0809-103X.

”Kinematics in Regular and Irregular Waves based on a Lagrangian Formulation”, Svein Helge Gjøsund, 2000-86, ISBN 82-7984-112-1, ISSN 0809-103X.

”Self-Induced Cracking Problems in Hardening Concrete Structures”, Daniela Bosnjak, 2000-121, ISBN 82-7984-151-2, ISSN 0809-103X.

"Ballistic Penetration and Perforation of Steel Plates", Tore Børvik, 2000:124, ISBN 82-7984-154-7, ISSN 0809-103X.

"Freeze-Thaw resistance of Concrete. Effect of: Curing Conditions, Moisture Exchange and Materials", Terje Finnerup Rønning, 2001:14, ISBN 82-7984-165-2, ISSN 0809-103X

Structural behaviour of post tensioned concrete structures. Flat slab. Slabs on ground", Steinar Trygstad, 2001:52, ISBN 82-471-5314-9, ISSN 0809-103X.

"Slipforming of Vertical Concrete Structures. Friction between concrete and slipform panel", Kjell Tore Fosså, 2001:61, ISBN 82-471-5325-4, ISSN 0809-103X.

"Some numerical methods for the simulation of laminar and turbulent incompressible flows", Jens Holmen, 2002:6, ISBN 82-471-5396-3, ISSN 0809-103X.

“Improved Fatigue Performance of Threaded Drillstring Connections by Cold Rolling”, Steinar Kristoffersen, 2002:11, ISBN: 82-421-5402-1, ISSN 0809-103X.

"Deformations in Concrete Cantilever Bridges: Observations and Theoretical Modelling", Peter F. Takâcs, 2002:23, ISBN 82-471-5415-3, ISSN 0809-103X.

"Stiffened aluminium plates subjected to impact loading", Hilde Giæver Hildrum, 2002:69, ISBN 82-471-5467-6, ISSN 0809-103X.

"Full- and model scale study of wind effects on a medium-rise building in a built up area", Jónas Thór Snæbjørnsson, 2002:95, ISBN82-471-5495-1, ISSN 0809-103X.

“Evaluation of Concepts for Loading of Hydrocarbons in Ice-infested water”, Arnor Jensen, 2002:114, ISBN 82-417-5506-0, ISSN 0809-103X.

”Numerical and Physical Modelling of Oil Spreading in Broken Ice”, Janne K. Økland Gjøsteen, 2002:130, ISBN 82-471-5523-0, ISSN 0809-103X.

”Diagnosis and protection of corroding steel in concrete”, Franz Pruckner, 20002:140, ISBN 82-471-5555-4, ISSN 0809-103X.

“Tensile and Compressive Creep of Young Concrete: Testing and Modelling”, Dawood Atrushi, 2003:17, ISBN 82-471-5565-6, ISSN 0809-103X.

“Rheology of Particle Suspensions. Fresh Concrete, Mortar and Cement Paste with Various Types of Lignosulfonates”,

Jon Elvar Wallevik, 2003:18, ISBN 82-471-5566-4, ISSN 0809-103X.

“Oblique Loading of Aluminium Crash Components”, Aase Reyes, 2003:15, ISBN 82-471-5562-1, ISSN 0809-103X.

“Utilization of Ethiopian Natural Pozzolans”, Surafel Ketema Desta, 2003:26, ISSN 82-471-5574-5, ISSN:0809-103X.

“Behaviour and strength prediction of reinforced concrete structures with discontinuity regions”, Helge Brå, 2004:11, ISBN 82-471-6222-9, ISSN 1503-8181.

“High-strength steel plates subjected to projectile impact. An experimental and numerical study”, Sumita Dey, 2004:38, ISBN 82-471-6281-4 (elektr. Utg.), ISBN 82-471-6282-2 (trykt utg.),
ISSN 1503-8181.

“Alkali-reactive and inert fillers in concrete. Rheology of fresh mixtures and expansive reactions.”
Bård M. Pedersen, 2004:92, ISBN 82-471-6401-9 (trykt utg.), ISBN 82-471-6400-0 (elektr. utg.),
ISSN 1503-8181.

“On the Shear Capacity of Steel Girders with Large Web Openings”. Nils Christian Hagen, 2005:9 ISBN 82-471-6878-2 (trykt utg.), ISBN 82-471-6877-4 (elektr. utg.), ISSN 1503-8181.

”Behaviour of aluminium extrusions subjected to axial loading”. Østen Jensen, 2005:7, ISBN 82-471-6872-3 (elektr. utg.) , ISBN 82-471-6873-1 (trykt utg.), ISSN 1503-8181.

”Thermal Aspects of corrosion of Steel in Concrete”. Jan-Magnus Østvik, 2005:5, ISBN 82-471-6869-3 (trykt utg.) ISBN 82-471-6868 (elektr.utg), ISSN 1503-8181.

”Mechanical and adaptive behaviour of bone in relation to hip replacement.” A study of bone remodelling and bone grafting. Sébastien Muller, 2005:34, ISBN 82-471-6933-9 (trykt utg.) (ISBN 82-471-6932-0 (elektr.utg), ISSN 1503-8181.

“Analysis of geometrical nonlinearities with applications to timber structures”. Lars Wollebæk, 2005:74, ISBN 82-471-7050-5 (trykt utg.), ISBN 82-471-7019-1 (elektr. Utg.), ISSN 1503-8181.

“Pedestrian induced lateral vibrations of slender footbridges”, Anders Rönnquist, 2005:102, ISBN 82-471-7082-5 (trykt utg.), ISBN 82-471-7081-7 (elektr.utg.), ISSN 1503-8181.

“Initial Strength Development of Fly Ash and Limestone Blended Cements at Various Temperatures Predicted by Ultrasonic Pulse Velocity”, Tom Ivar Fredvik, 2005:112, ISBN 82-471-7105-8 (trykt utg.), ISBN 82-471-7103-1 (elektr.utg.), ISSN 1503-8181.

“Behaviour and modelling of thin-walled cast components”, Cato Dørum, 2005:128, ISBN 82-471-7140-6 (trykt utg.), ISBN 82-471-7139-2 (elektr. utg.), ISSN 1503-8181.

“Behaviour and modelling of selfpiercing riveted connections”, Raffaele Porcaro, 2005:165, ISBN 82-471-7219-4 (trykt utg.), ISBN 82-471-7218-6 (elektr.utg.), ISSN 1503-8181.

”Behaviour and Modelling og Aluminium Plates subjected to Compressive Load”, Lars Rønning,
2005:154, ISBN 82-471-7169-1 (trykt utg.), ISBN 82-471-7195-3 (elektr.utg.), ISSN 1503-8181

”Bumper beam-longitudinal system subjected to offset impact loading”, Satyanarayana Kokkula, 2005:193, ISBN 82-471-7280-1 (trykt utg.), ISBN 82-471-7279-8 (elektr.utg.), ISSN 1503-8181.

“Control of Chloride Penetration into Concrete Structures at Early Age”, Guofei Liu, 2006:46, ISBN 82-471-7838-9 (trykt utg.), ISBN 82-471-7837-0 (elektr. utgave), ISSN 1503-8181.

“Modelling of Welded Thin-Walled Aluminium Structures”, Ting Wang, 2006:78,
ISBN 82-471-7907-5 (trykt utg.), ISBN 82-471-7906-7 (elektr.utg.), ISSN 1503-8181.

”Time-variant reliability of dynamic systems by importance sampling and probabilistic analysis of ice loads”, Anna Ivanova Olsen, 2006:139, ISBN 82-471-8041-3 (trykt utg.), ISBN 82-471-8040-5 (elektr.utg.), ISSN 1503-8181.

“Fatigue life prediction of an aluminium alloy automotive component using finite element analysis of surface topography”. Sigmund Kyrre Ås, 2006:25, ISBN 82-471-7791-9 (trykt utg.), ISBN 82-471-7791-9 (elektr.utg.), ISSN 1503-8181.

”Constitutive models of elastoplasticity and fracture for aluminium alloys under strain path change”, Dasharatha Achani, 2006:76, ISBN 82-471-7903-2 (trykt utg.), ISBN 82-471-7902-4 (elektr.utg.), ISSN 1503-8181.
“Simulations of 2D dynamic brittle fracture by the Element-free Galerkin method and linear fracture mechanics”, Tommy Karlsson, 2006:125, ISBN 82-471-8011-1 (trykt utg.), ISBN 82-471-8010-3 (elektr.utg.), ISSN 1503-8181.

“Penetration and Perforation of Granite Targets by Hard Projectiles”, Chong Chiang Seah, 2006:188, ISBN 82-471-8150-9 (printed ver.), ISBN 82-471-8149-5 (electronic ver.) ISSN 1503-8181.

“Deformations, strain capacity and cracking of concrete in plastic and early hardening phases”, Tor
Arne Hammer, 2007:234, ISBN 978-82-471-5191-4 (trykt utg.), ISBN 978-82-471-5207-2 (elektr.utg.) ISSN 1503-8181.

“Crashworthiness of dual-phase high-strength steel: Material and Component behaviour”, Venkatapathi Tarigopula, 2007:230, ISB 82-471-5076-4 (trykt utg.) ISBN 82-471-5093-1 (elektr.utg.) ISSN 1503-8181.